Study of Lithium and other related elements among Evolved Stars

A thesis

submitted for the degree of

Doctor of Philosophy

in

The Department of Physics,
Pondicherry University,
Puducherry - 605 014, India

by

Anohita Mallick
Indian Institute of Astrophysics,
Bangalore - 560 034, India

Jan 2025

Study of Lithium and other related elements among Evolved Stars

Anohita Mallick
Indian Institute of Astrophysics

Indian Institute of Astrophysics
Bangalore - 560 034, India

Title of the thesis	:	**Study of Lithium and other related elements among Evolved Stars**
Name of the author	:	**Anohita Mallick**
Address	:	Indian Institute of Astrophysics II Block, Koramangala Bangalore - 560 034, India
Email	:	anohita.mallick@iiap.res.in
Name of the supervisor	:	**Prof. B. Eswar Reddy**
Address	:	Indian Institute of Astrophysics II Block, Koramangala Bangalore - 560 034, India
Email	:	ereddy@iiap.res.in

Declaration of Authorship

I hereby declare that the matter contained in this thesis is the result of the investigations carried out by me at the Indian Institute of Astrophysics, Bangalore, under the supervision of Prof. B. Eswar Reddy. This work has not been submitted for the award of any other degree, diploma, associateship, fellowship, etc. of any other university or institute.

Signed: Anohita Mallick

Date: 27/01/2025

Certificate

This is to certify that the thesis entitled **'Study of Lithium and other related elements among Evolved Stars'** submitted to the Pondicherry University by Ms. Anohita Mallick for the award of the degree of Doctor of Philosophy, is based on the results of the investigations carried out by her under my supervision and guidance, at the Indian Institute of Astrophysics. This thesis has not been submitted for the award of any other degree, diploma, associateship, fellowship, etc. of any other university or institute.

Signed: 

Date: 27/01/2025

List of Publications

Refereed Publications

1. Probing infrared excess connection with Li enhancement among red clump giants (*Chapter 3*)

   Mallick, A., Reddy, B. E., & Muthumariappan, C. 2022, *Mon. Not. Roy. Astron. Soc.*, 511, 3741. doi: 10.1093/mnras/stac224

2. Study of a Red Clump Giant, KIC 11087027, with High Rotation and Strong Infrared Excess—Evidence of Tidal Interaction for High Lithium Abundance (*Chapter 4*)

   Singh, R., **Mallick, A.**, Reddy, B. E., et al. 2024, *Astrophys. J. Lett.*, 971, L3. doi:10.3847/2041-8213/ad62f6

3. Lithium Abundances in Giants as a Function of Stellar Mass: Evidence for He Flash as the Source of Li Enhancement in Low-mass Giants (*Chapter 5*)

   Mallick, A., Singh, R., & Reddy, B. E. 2023, *Astrophys. J. Lett.*, 944, L5. doi: 10.3847/2041-8213/acb5f6

4. High Lithium Abundance Connection with the Chromospheric Helium in Red Giants: Spectroscopic and Asteroseismic analyses (*Chapter 6*)

   Mallick, A., Sneden, C., Afsar, M., & Reddy, B. E. 2025, ApJ (in press)

5. The Active Chromospheres of Lithium-rich Red Giant Stars

   Sneden, C., Afşar, M., Bozkurt, Z., , Adamów M., **Mallick A.**, Reddy B. E., Janowiecki S., et al., 2022, *Astrophys. J.*, 940, 12. doi: 10.3847/1538-4357/ac922e

6. Mining the GALAH Data. I. Study of Five Super Lithium-rich Metal-poor Giants

   Susmitha, A., **Mallick, A.**, & Reddy, B. E. 2024, *Astrophys. J.*, 966, 109. doi: 10.3847/1538-4357/ad35b9

Under Preparation

7. Stellar Evolution and Mixing Across the RGB Tip: Insights from High-Resolution Spectroscopy

   Mallick, A. & Reddy, B. E. 2025, in preparation.

   Chapter 7

Presentations at Conferences

1. **Name:** TESS Science Conference II, *Aug 2 - 6 2021*
   Venue: Online
   Nature of participation: Poster
   Mode of Attendance: Remote
   Title: The *TESS* and *K2* synergy of Li-rich red giants

2. **Name:** 40th, Astronomical society of India, *Mar 25 - 29 2022*
   Venue: IIT Roorkee
   Nature of participation: Poster
   Mode of Attendance: In-person
   Title: Probing Li enhancement-IR excess connection in stars close to RGB tip

3. **Name:** Asteroseismology in the Era of Surveys from Space and the Ground: Stars, Planets, and the Milky Way", TASC6/KASC13 workshop, *Jul 11-15 2022*
   Venue: KU Leuven, Belgium
   Nature of participation: Oral, Flash-talk
   Mode of Attendance: Remote
   Title: Asteroseismic modeling of merger signatures from *Kepler* data

4. **Name:** TASC7/KASC14 workshop, *Jul 17-21 2023*
   Venue: University of Hawaii , Honolulu
   Nature of participation: Oral, Flash-talk
   Mode of Attendance: Remote
   Title: Testing direct and grid-based asteroseismic scaling relations

5. **Name:** 42nd, Astronomical society of India, *Jan 31 -Feb 4 2024*
   Venue: IISc Bangalore
   Nature of participation: Poster
   Mode of Attendance: In-person
   Title: Exploring the Interplay of Lithium and Chromospheric Helium in Red Giants : A *Kepler* and *TESS* mission study

6. **Name:** The Milky Way Assembly Tale, *May 27-31 2024*
   Venue: CNR Research Area, Bologna, Italy
   Nature of participation: Poster
   Mode of Attendance: Remote
   Title: Evolution of Lithium in the Galaxy - the role of evolved stars

7. **Name:** Cool Stars 22, *Jun 24-28 2024*
   Venue: UC San Diego, California, USA
   Nature of participation: Poster
   Mode of Attendance: In-person
   Title: Lithium's Labyrinth in low-mass red giants : A Mystery Explored

Acknowledgements

The journey of completing this thesis has been shaped by the support and encouragement of many wonderful individuals. Throughout my time at IIA, I have received invaluable help from colleagues, mentors, and friends, all of whom have contributed to this work in their own ways. I am truly grateful for their guidance, which has made this journey both meaningful and achievable.

I would like to begin by expressing my deepest gratitude to my supervisor, *Prof. Bacham Eswar Reddy*, for his unwavering support, guidance, and mentorship throughout my research. He has always been available when I needed guidance - whether through Zoom calls during the COVID period, casual phone calls when time was constrained, or long in-person discussions. We have had both agreements and disagreements over various approaches and ideas, but we consistently found common ground, and these exchanges have significantly refined the results of my work. He has also imparted invaluable lessons on how to write scientific papers, abstracts for conferences, and observation proposals. Despite his many responsibilities, including serving as the Dean of IIA and Head of India TMT, he always made time for me, reviewing numerous plots, raw data, reduction steps, and any new results that I presented to him.

I extend my sincere thanks to my *co-supervisor, Prof. C. Muthumariappan*, who first encouraged me to explore interstellar dust, reddening, and related topics. His enthusiasm and eagerness to help, not just with my research but also with any collaborative work, have been pivotal in shaping my academic path.

I would like to express my deepest thanks to my *Doctoral Committee members: Prof. Gajendra Pandey* and *Prof. K.V.P. Latha* (Pondicherry University), for their constructive feedback and unwavering support throughout my research. Additionally, I am grateful to *Prof. Pandey* for his assistance in exploring alternative

methods for determining helium abundances in cool stars - an area I plan to continue working on in future research. I would also like to extend my thanks to *Hema B. P.*, his student, for her assistance with this.

I would also like to acknowledge the support of my *coursework instructors: Prof. Biman Nath (RRI), Prof. Arun Mangalam, Prof. Sharanya Sur, Prof. Pravabati Chingangbam, Prof. Prateek Sharma (IISc), Prof. Banibrata Mukhopadhyay (IISc), Prof. Mousumi Das, Prof. Umanath S Kamath, Prof. Maheswar Gopinathan, Prof. C. S. Stalin, and Prof. C. Kathiravan.* Their teachings have been invaluable in shaping my understanding of astrophysical phenomena, and I am grateful for their expert guidance.

I owe my gratitude to *Dr. Dipanweeta Bhattacharyya*, my old roommate, for our silly late-night conversations and sharing fun moments. I would also like to thank other seniors, *Dr. Samrat Sen, Dr. Snehalata Sahu, Dr. Chayan Mondal, Dr. Amit K. Mandal, Dr. Piyali Saha, Dr. Swastik C., Dr. Fazlu Rahman, Dr. Sioree Ansar, Dr. Indrani Pal, Dr. Anirban Dutta, Dr. Deepthi S. Prabhu, and Sonith L. S.*, for their guidance, support, and camaraderie. We shared many lighthearted moments, from watching movies together to trekking and eating out. I was fortunate to have their company for engaging in fun, non-academic activities, as well as occasionally discussing academic matters. Their presence made my journey far more enjoyable.

I would also like to express my gratitude to my *batchmates Pallavi Saraf, Ravi Kumar Sharma*, and *Rishabh Singh Teja*, whose camaraderie and support made the journey much more enjoyable. We often found creative ways to divide our coursework assignments to save time and have some much-needed breaks!

I want to acknowledge my *senior, Dr. Raghubar Singh*, for teaching me the basics of data reduction from scratch and for his general advice on writing manuscripts,

among other things. We continue to collaborate and our mutual sharing of works and fruitful discussions have been immensely useful.

I would also like to thank my *juniors, Saili Kumari Keshri, Renu Devi, Khushbu and Lupamudra Sarmah*, for their company and support, which made this journey even more memorable.

Other than all this, I want to thank my friends from IISc - *Rachita Ghosh, Bapan Dhara, Aishita Chakraborty* and *Sandeep Mondal* - for making my weekends brighter with fun visits and impromptu cooking experiments. Special thanks to *Pratip Ghosh* for always being there for me with his unwavering support and encouragement. His presence has been a cornerstone of my strength and motivation throughout this journey, and I truly appreciate his understanding and care.

A heartfelt thanks goes to the staff at *Bhaskara hostel* for their warmth and dedication, which greatly enhanced my stay. Their care and attention, especially from *Manjunath, Chandrasekhar, Narayana*, and the *housekeeping team*, created an environment that made Bhaskara feel like home. The consistent support from the staff was invaluable, helping to make every day a little more comfortable and enjoyable.

I am deeply appreciative of the staff at the *Indian Institute of Astrophysics (IIA)* for creating a supportive and stimulating environment for my research. I would like to thank the *IIA Library* and *Arumugam Pitchai*, the *librarian*, for his assistance in providing access to numerous resources and materials that have been essential in my research.

I would also like to extend my sincere gratitude to the *administration*, especially the *Dean, Prof. Eswar Reddy*, and the *Director, Prof. Annapurni Subramaniam* for allowing me to work at this institute and providing all the resources necessary

for my research.

A special mention goes to the *Data Center*, particularly *Anish, Fayaz, Ashok* and their *team*, for their help with various software installations, which was crucial for my research. I owe my thanks to the staff at the *Centre for Research and Education in Science and Technology (CREST)*, the *Indian Astronomical Observatory (IAO)*, and the *Vainu Bappu Observatory (VBO)* for their support during my observations. I would also like to thank observers *Pramod Kumar* and *Yogita Patel* at CREST for their technical assistance.

I am also grateful to the *Department of Science and Technology (DST), India*, for providing me with the PhD fellowship that has enabled me to pursue this research.

A huge thank you to my collaborators, *Prof. Christopher Sneden, Prof. Melike Afsar, Dr. Susmitha Rani Antony*, and numerous others, including *Enrico Corsaro* and *Carlos Allende Prieto*, whose help has been influential throughout my work. Their input and expertise have contributed greatly to shaping my research.

I owe much to my family for their endless love, support, and sacrifices. I want to thank both my parents - *Santi Mallick* and *Mitali Mallick* - for all their sacrifices, encouragement, and constant belief in me. There was one particularly difficult point in my life when my father was battling cancer, and my relatives suggested that my sister and I should stop our studies. Even in his weakened condition, my father never gave in to those ideas. He and my mother gave us the freedom to choose what we wanted in our academic and professional lives. A heartfelt shout-out to my mother, who mentored me through my school years and instilled in me a love for mathematics. She has sacrificed a lot to keep my motivation and focus alive.

My elder sister, *Dr. Apabrita Mallick*, has always been there for me - whether it

was discussing my weak chemistry or offering support during tough times. I will always be grateful for her encouragement and guidance.

Finally, I would like to extend my deepest thanks to all those whose names may not have been mentioned here but who have provided support, feedback, or encouragement in various ways. Your contributions have been integral to the completion of this work.

Anohita Mallick

Data usage

The research presented in this thesis is based on data obtained from various ground-based and space-based observatories. I am sincerely grateful to the scientific institutions, organizations, and individuals who made this data accessible, as their contributions were essential to the completion of this work.

High-resolution optical spectra were collected using the Hanle Echelle Spectrograph (HESP), installed on the 2.0 m Himalayan Chandra Telescope (HCT), operated by the Indian Institute of Astrophysics, Bangalore. Observations were also conducted with the Habitable Zone Planet Finder (HPF), a high-resolution infrared spectrograph mounted on the 10 m Hobby-Eberly Telescope (HET), which is operated by the McDonald Observatory of the University of Texas at Austin.

Low-resolution spectroscopic data was primarily obtained from the LAMOST survey, carried out by the National Astronomical Observatories of China (NAOC) under the Chinese Academy of Sciences (CAS). Archival high-resolution spectra from the GALAH survey, observed using the HERMES spectrograph on the 3.9 m Anglo-Australian Telescope (AAT), complemented the LAMOST data, providing detailed insights into stellar chemical abundances.

Astrometric data from the Gaia space mission, operated by the European Space Agency (ESA), was crucial for this work. Photometric data from NASA's *Kepler* mission supported asteroseismic analysis, while additional photometric information from the $2MASS$ and $WISE$ surveys enriched the study of the sample stars.

To my parents & sister.

My roots, my support, my pride.

Abstract

The formation and evolution of elements is a fundamental problem in modern astrophysics. Lithium (Li), one of the four stable nuclides produced during Big Bang Nucleosynthesis (BBN), exhibits an observed abundance in many celestial bodies that deviates from theoretical predictions. In stars, the behavior of Li is particularly complex, as it is easily destroyed under high temperatures, where it undergoes proton capture to form stable helium nuclei. Consequently, Li cannot be preserved in the hot stellar interior, but is instead confined to the surface layers. If surface Li is transported to the interior during stellar evolution it is destroyed due to high temperatures, leading to a reduction in Li abundance in the star's atmosphere. Standard stellar evolution models predict that stars with initial Li abundances comparable to the ISM value (3.3 dex) will show a Li abundance no greater than 1.5 dex once they reach the giant stage. However, observations have revealed a small number of giant stars, known as Li-rich giants, with Li abundances exceeding this threshold. Some of these stars even display Li abundances higher than the ISM value, and are referred to as super Li-rich giants. The presence of such stars presents a significant challenge to the standard stellar evolution models, suggesting the existence of additional mechanisms that can enrich Li in stars. Understanding these mechanisms is essential for both the formation of Li and the broader theories of stellar evolution, though it remains a challenging area of research. Significant progress has been made over the past four decades in the study of Li-rich giants.

We have used large scale survey programs such as LAMOST and GALAH spectroscopic surveys, photometric survey of $Kepler$ and $TESS$ space telescopes, Gaia astrometry and high-resolution spectra using 2-m Himalayan Chandra Telescope (HCT) and the 10 m Hobby Eberly Telescope (HET). Our work discovered a number of new red

clump super-Li rich giants with proper evolutionary phases assigned based on asteroseismic analysis. The extensive systematic survey based on an unbiased sample of giants common among Kepler and LAMOST surveys' fields provided a key evidence that Li enhancement is only associated with the He-core burning phase post He-flash in low-mass stars. Another key result that emerged from this study is the location of the Li enrichment site in most Li-rich stars is the He-flashing phase, the transition between the evolution of stars from the end of RGB tip to the He-core burning period in the horizontal branch. Based on the analysis of spectroscopic and photometric data, we provided first-of-its-kind evidence in the form of a correlation between lithium abundances in giants and their masses derived using asteroseismology. Another significant part of this thesis is the study of photospheric Li abundances and its relation with the strength of chromospheric He I 10830Å. The subtle correlation is the another evidence that the He-flash is the source for Li enhancement and the enhanced activity in the chromosphere resulting stronger He I line among very high Li-rich giants.

Contents

List of Figures

List of Tables

Abbreviations

AGB	**A**symptotic **G**iant **B**ranch
APOGEE	**T**he **A**pache **P**oint **O**bervatory **G**alactic **E**volution **E**xperiment
BBN	**B**ig **B**ang **N**ucleosynthesis
CHeB	**C**ore **He**lium **B**urning
FDU	**F**irst **D**redge **U**p
GALAH	The **GAL**ctic **A**rcheology with the **H**ermes
HCT	**H**imalayan **C**handra **T**elescope
HESP	**H**anle **E**chelle **SP**ectrograph
HET	**H**obby **E**berly **T**elescope
HPF	**H**abitable zone **P**lanet **F**inder
IRAF	**I**mage **R**eduction and **A**nalysis **F**acility
LAMOST	**L**arge sky **A**rea **M**ulti-**O**bject fibre **S**pectroscopic **T**elescope
LTE	**L**ocal **T**hermodynamic **E**quilibrium
MESA	**M**odules for **E**xperiments in **S**tellar **A**strophysics
pRC	**p**rimary **R**ed **C**lump
PSD	**P**ower **S**pectral **D**ensity
RGB	**R**ed **G**iant **B**ranch
RC	**R**ed **C**lump
SED	**S**pectral **E**nergy **D**istribution
SLO	**S**olar **L**ike **O**scillators
SLR	**S**uper **L**ithium **R**ich
SNR (S/N)	**S**ignal to **N**oise **R**atio
sRC	**s**econdary **R**ed **C**lump
TESS	**T**ransiting **E**xoplanet **S**urvey **S**atellite

Chapter 1

Low-Mass Stellar Evolution and the Lithium anomaly in Red Giants

1.1 Overview

The primary objective of this thesis is to investigate the processes occurring in the cores of red giant and core helium-burning red clump stars that lead to alterations in photospheric lithium (Li) and other elements. These changes serve as indicators of stellar mixing. Additionally, we have explored alternative mechanisms, such as interactions in binary star systems or stellar mergers, that could influence Li abundances. The initial section of this chapter offers a detailed explanation of the evolutionary stages of low-mass stars, while the latter section examines the role of lithium in understanding mixing processes within these stars and the peculiar puzzle it presents.

1.2 Evolution of Low-Mass Stars

Lifecycle of low-mass stars (which are defined as stellar masses ranging from about 0.8 to 2.0 $M_{\odot}$) follows a well-defined path through various stages, each marked by distinct changes in their structure and energy generation. The Hertzsprung-Russell (HR) diagram is a key tool for visualizing these stages. By plotting stellar luminosity against surface temperature, the HR diagram reveals the positions of stars at different phases of their evolution.

The two key factors that influence a star's properties are initial mass and composition. Spectroscopic studies reveal that most stars are approximately 70% hydrogen and 28% helium by weight. Heavier elements initially make up a small fraction, varying from 2-3% in solar type stars to as low as 0.1-0.01% in globular clusters. Stars rich in heavy elements, like our Sun, are termed **population I** stars, whereas those poor in heavy elements, such as globular cluster stars, are known as **population II** stars. Population I stars are considered a later generation, formed after enrichment of interstellar gas clouds, while population II stars are thought to be from an earlier generation, when heavier elements beyond hydrogen and helium were rare. Population I stars are located in the Galaxy's disk, following near-circular orbits close to the mid-plane. In contrast, Population II stars occupy the spheroidal component, halo, of the galaxy.

1.2.1 Main Sequence

Main sequence stars begin their formation in dense regions of molecular clouds known as nebulae, where gravitational forces cause the clouds to collapse, forming a dense core called a protostar. During the protostar phase, the collapsing material heats up, and the protostar accumulates mass from the surrounding gas and dust.

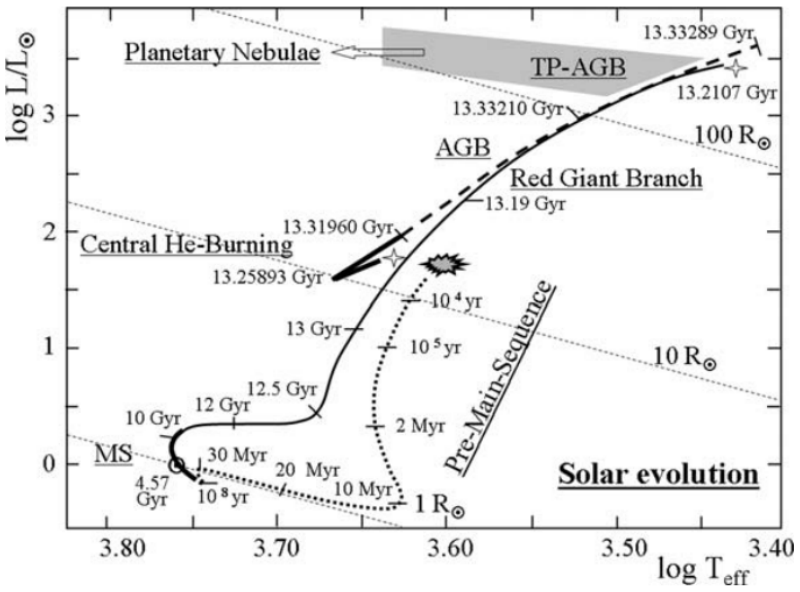

FIGURE 1.1: HR diagram of a $1M_{\odot}$ star with solar composition ($X_{\odot}$ = 0.72, $Y_{\odot}$= 0.266, $Z_{\odot}$ = 0.014), showing its evolution from the PMS phase to the planetary nebula stage. Ages are indicated along the track. The two 4-point stars mark the onset and conclusion of the He flash, which leads to the central He-burning phase. [Adapted from Fig. 25.11 by Maeder (2009)]

As the protostar keeps contracting and increasing in temperature, it progresses into the pre-main sequence stage, marked by ongoing gravitational compression and a steadily warming core. Stars during the main sequence are generally chemically homogeneous and convert hydrogen to helium inside their cores. A star spends majority of its lifespan in this stable state, where the fractional composition of hydrogen, helium, and other elements is consistent throughout the star (except for some nuclear processing in the core). In 1.1 main sequence (MS) is shown in the bottom left corner as diagonal line. A main sequence star's position on the HR diagram is mainly influenced by its mass. Stars with greater mass evolve faster than their lower mass counterparts. Figure 1.1 illustrates the HR diagram for a star with a mass of 1 $M_{\odot}$. On the main sequence, the luminosity L of stars, governed by the rate of heat loss via radiative diffusion, scales roughly with the mass M raised to the exponent four ($L \propto M^4$), and the radius R scales with the mass ($R \propto M$) (Eddington 1926). Plugging in the Stefan-Boltzmann law $L = 4\pi R^2 \sigma T_{\rm eff}^4$ (where $T_{\rm eff}$ represents the temperature of a theoretical blackbody that radiates the same

total energy as the star), more massive stars exhibit greater luminosity and higher temperatures during their main sequence phase. Main sequence stars maintain hydrostatic equilibrium by counteracting the gravitational pull acting inwards with the outward force produced by nuclear reactions in their cores. Nucleosynthesis in main sequence stars occur through two channels -

1. **Proton-proton (PP) chain :**

   Applying conservation principles, the first proton-proton chain (PP I) is a series of reactions that converts hydrogen into helium. This chain ultimately transforms four protons into helium-4, producing two positrons, two neutrinos, and two gamma rays:

$$4\,{}^{1}_{1}\mathrm{H} \rightarrow {}^{4}_{2}\mathrm{He} + 2\,e^{+} + 2\,\nu_e + 2\,\gamma$$

   The entire PP I sequence involves

$${}^{1}_{1}\mathrm{H} + {}^{1}_{1}\mathrm{H} \rightarrow {}^{2}_{1}\mathrm{H} + e^{+} + \nu_e$$

$${}^{2}_{1}\mathrm{H} + {}^{1}_{1}\mathrm{H} \rightarrow {}^{3}_{2}\mathrm{He} + \gamma$$

$${}^{3}_{2}\mathrm{He} + {}^{3}_{2}\mathrm{He} \rightarrow {}^{4}_{2}\mathrm{He} + 2\,{}^{1}_{1}\mathrm{H}$$

   ^{3}He nuclei from PP I chain can combine with ^{4}He causing an alternative PP II chain.

$${}^{3}_{2}\mathrm{He} + {}^{4}_{2}\mathrm{He} \rightarrow {}^{7}_{4}\mathrm{Be} + \gamma$$

$${}^{7}_{4}\mathrm{Be} + e^{-} \rightarrow {}^{7}_{3}\mathrm{Li} + \nu_e$$

$${}^{7}_{3}\mathrm{Li} + {}^{1}_{1}\mathrm{H} \rightarrow 2\,{}^{4}_{2}\mathrm{He}$$

   Another possible branch is the PP III chain, where an electron is captured by ^{7}Be in the PP II chain (see Fig. 1.2). In the Sun, the PP I branch occurs with a frequency of 69%, the PP II branch with 31%, and the PP III branch

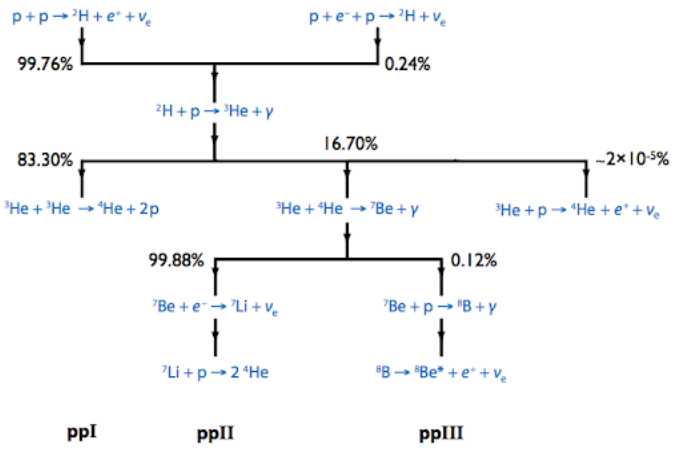

FIGURE 1.2: The three main cycles of the pp chain (ppI, ppII, and ppIII), with their corresponding branching percentages. [Adapted from Adelberger et al. (2011)]

with 0.3% (Kippenhahn et al. 2013; Carroll & Ostlie 2017). The significance of each proton-proton chain branch is determined by branching ratios, which are influenced by the stellar material's temperature, composition and density.

2. **CNO cycle:**

   The PP chain is dominant in less massive stars ($\lesssim 1.5 M_\odot$) since they have cooler cores. In higher mass stars, H-fusion occurs through the CNO cycle since it is highly temperature-sensitive, requiring higher central temperatures. It is a cyclic process where C, N and O act as nuclear catalysts. Like the PP chain, it also proceeds through several branches.

   The first branch is as follows:

$$^{12}_{6}\mathrm{C} + {}^{1}_{1}\mathrm{H} \rightarrow {}^{13}_{7}\mathrm{N} + \gamma$$

$$^{13}_{6}\mathrm{N} \rightarrow {}^{13}_{6}\mathrm{C} + e^{+} + \nu_e$$

$$^{13}_{6}\mathrm{C} + {}^{1}_{1}\mathrm{H} \rightarrow {}^{14}_{7}\mathrm{N} + \gamma$$

$$^{14}_{7}\mathrm{N} + {}^{1}_{1}\mathrm{H} \rightarrow {}^{15}_{8}\mathrm{O} + \gamma$$

$$^{15}_{8}\mathbf{O} \rightarrow {}^{15}_{7}\mathbf{N} + e^{+} + \nu_e$$

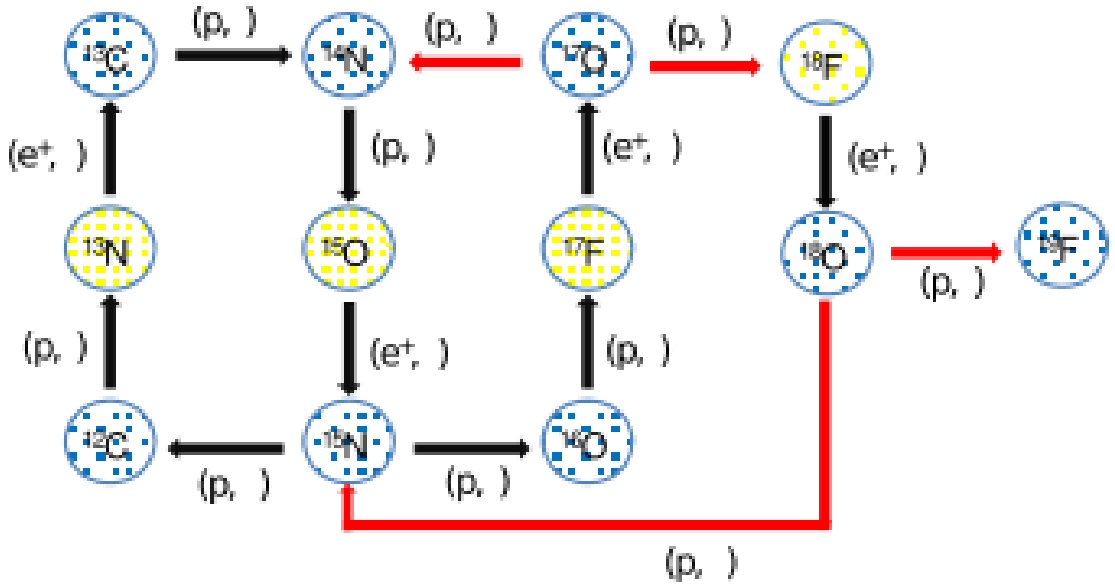

FIGURE 1.3: Diagram of the nuclear reaction network within the CNO cycle [adapted from Lebzelter et al. (2012)]

$$^{15}_{7}\mathrm{N} + {}^{1}_{1}\mathrm{H} \rightarrow {}^{12}_{6}\mathrm{C} + {}^{4}_{2}\mathrm{He}$$

The second branch occurs rarely ($\sim 0.4\%$)

$$^{15}_{7}\mathrm{N} + {}^{1}_{1}\mathrm{H} \rightarrow {}^{16}_{8}\mathrm{O} + \gamma$$

$$^{16}_{8}\mathrm{O} + {}^{1}_{1}\mathrm{H} \rightarrow {}^{17}_{9}\mathrm{F} + \gamma$$

$$^{17}_{9}\mathrm{F} \rightarrow {}^{17}_{8}\mathrm{O} + e^{+} + \nu_{e}$$

$$^{17}_{8}\mathrm{O} + {}^{1}_{1}\mathrm{H} \rightarrow {}^{14}_{7}\mathrm{N} + {}^{4}_{2}\mathrm{He}$$

Lower mass main sequence stars develop radiative cores since lower energy generation rates create insufficient temperature gradients to drive convection. In contrast, higher mass stars have convective cores due to higher energy production rates, which establish steep temperature gradients that facilitate convective energy transport. As hydrogen in the core is converted to helium, either via the CNO

cycle or the proton-proton chain, the mean molecular weight (μ) increases. According to the ideal gas law, if the temperature and gas density remain unchanged, the central pressure decreases. This results in the loss of hydrostatic equilibrium and initiates core collapse. The collapse then causes an increase in both density and temperature to compensate for the rise in μ. Main sequence evolution ends when core Hydrogen is entirely depleted.

1.2.2 Subgiants

Increase in μ during H-fusion impacts the star's hydrostatic equilibrium. To support expansion of outer layers, the core contracts, leading to a rise in temperature in the inner regions. Although the core temperature is insufficient to initiate He burning, energy transfer to the outer layers creates a chemically stratified structure, with hydrogen fusion occurring in a broad shell surrounding a non-reactive helium core. For low-mass stars ($\lesssim$ **2.1** $\mathbf{M_\odot}$), electron degeneracy pressure is dominant in the core. Thus, they maintain hydrostatic equilibrium with a thermally uniform, degenerate core as they evolve into the hydrogen shell fusion phase. They evolve to the giant phase gradually, with a much longer timescale compared to higher-mass stars. Initially, shell burning takes place in a broad zone surrounding the core. Over time, the mass of the core grows as the byproducts of hydrogen fusion accumulate within it. Due to the degeneracy of the core, this results in its shrinking and a subsequent expansion of the outer layers. The interface between compression and expansion is found close to the hydrogen fusion shell. Temperature at the H-shell is higher and the CNO cycle dominates.

1.2.3 Red Giant Branch

The shell-burning region becomes progressively narrower as the star evolves. The outer layers expand and cool as the star approaches the Hayashi track in the HR diagram. As the star gets closer to this line, further growth in radius leads to an increase in luminosity.The envelope develops a large convective zone as a result of increased opacity in the photosphere at cooler temperatures, influenced by hydrogen ions. At this stage, a star is situated on the red giant branch (RGB), with a broadened convective envelope ($\sim$ 80% of the stellar radius) over a smaller ($\sim$ 10% of the star's radius) radiative core. The convective envelope progressively moves towards the core. At these lower temperatures, convection takes over as the primary method of energy transfer due to the higher opacity. The convective envelope reaches layers where chemical composition was altered by main sequence H-burning. Chemical elements from the inner layers are brought to the photosphere, raising the associated abundances till the envelope reaches its deepest point. This stage is referred to as the **"first dredge-up"**.

- The surface He abundance increases, and ^{3}He and CNO elements get mixed in.
  - A twofold increase in the surface ^{14}N abundance.
  - A decrease in ^{12}C of approximately 30%.
  - A ^{12}C/^{13}C ratio of approximately 20-30.
  - A decrease in surface Be and Li abundances by several orders of magnitude.

Following this, the hydrogen-burning shell moves outward as a result of the growing helium core mass, and the convective envelope recedes. A chemical discontinuity is formed at this point as a result of the mixing of hydrogen-burning byproducts

from the inner regions with hydrogen from the outer envelope. Mean molecular weight in this region is lower than the interiors. Luminosity during this period varies as L $\propto \mu^7 M_{core}^7$ (Refsdal & Weigert 1970). When H-shell reaches the region of chemical discontinuity, luminosity of the star decreases for a brief period. This is known as the **"RGB luminosity bump"**. This corresponds to about 20% of the total RGB lifetime. As the H-shell crosses this region, molecular weight becomes constant and luminosity rises steadily again as core mass increases. The luminosity bump is observed in stars with masses up to around 2.2$M_\odot$. In stars with higher masses, the hydrogen-burning shell does not reach the chemical composition discontinuity before core He fusion starts.

RGB stars $\lesssim$ 2$M_\odot$:

Gravitational contraction results in a hot, massive and dense core. The core's density rises until the electrons become degenerate, causing the core to behave more like a liquid than a gas. The pressure of a degenerate gas depends solely on its density. Shell burning further raises temperature of the degenerate core with no effect on its pressure and core contraction stops. When core temp reaches $\sim$ 100MK, the helium nuclei possess enough kinetic energy to overcome the intense Coulomb repulsion and fuse, resulting in the formation of carbon-12 through a two-step process. Since three helium nuclei, or alpha particles, are involved, it is referred to as the triple-alpha process. Nuclear reaction around the degenerate core tend to be explosive. The triple α process raises the core's temperature, which subsequently accelerates the rate of fusion. At $\sim$ 300MK, which causes a thermal runaway - the "Helium - Flash". This is a transient event during which the star releases energy billions of times greater than the Sun in just several minutes. The energy does not reach the surface but is instead utilized to remove electron degeneracy pressure within the core. The core again behaves as an ideal gas and He-burning continues in a slow, stable manner. Stars which undergo He-flash are

known as **primary Red Clump (pRC) stars**.

RGB stars $\gtrsim$ 2M$_\odot$:

In massive stars, the temperature is sufficiently high for the triple-α process to begin before electron degeneracy sets in. As a result, there is no helium flash, but rather a smooth transition to a phase with helium burning at the core accompanied with hydrogen fusion in a surrounding shell. These are known as **secondary Red Clump (sRC) stars**.

1.2.4 Horizontal Branch

Following the onset of helium burning, whether initiated by a helium flash or occurring gradually, stars exhibit similar behaviors. In low-mass stars, the helium flash eliminates core degeneracy, allowing stars to behave akin to an ideal gas - leading to expansion and cooling. While energy transfers result in a hotter T_{eff}, the overall size of the star diminishes such that luminosity of the star remains relatively constant. Stars settle in the horizontal branch and exhibit He core-burning alongside H-shell burning. Stars of low metallicity exhibit a prolonged horizontal branch (HB), which is affected by the mass of the H-rich outer layer. Clump stars reside on the metal-rich side of the HB. During core He-burning, convective core becomes rich in carbon and oxygen, which increases opacity due to free-free transitions. This creates steeper temperature gradient followed by a chemical discontinuity at the core-envelope boundary. This might be smoothed out or additional discontinuities may be introduced by processes like semiconvection or convective overshoot. At this point, thermal pressure dominates over electron degeneracy pressure and the core expands again.This reduces gravitational force at the core's boundary, weakening the H-shell burning. The star now has two nuclear energy sources - core He burning and H shell burning — but the dominant

shell source is significantly weakened. As a result stellar luminosity decreases and is insufficient to maintain the star's extended red-giant state, leading to both a reduction in size and a decrease in intrinsic brightness. On the HB, stellar core is composed of a non-degenerate He plasma that is steadily fusing He into carbon encircled by a Hydrogen fusing shell. Intensity of the shell fusion is influenced by the convective envelope mass. The HB phase ends when core He is converted to Carbon and Oxygen.

1.2.4.1 Asymptotic Giant Branch

The core contracts, raising the pressure and temperature in the surrounding layers. Consequently, Helium begins fusing in a layer adjacent to the core, while hydrogen continues to burn in the outer shell. The star now enters the double-shell-burning phase. The inert carbon-oxygen core becomes massive and shrinks, mirroring the behavior of the helium core during the initial red-giant branch phase. Energy production in the two shell sources must increase rapidly, leading to a significant rise in luminosity that expands the envelope again. As a result, the star ascends the red-giant branch once more, and this double-shell-burning stage is known as the asymptotic giant branch (AGB). The phase is termed "asymptotic" because during this stage stars' position on the HR diagram approaches the same upper-right region it occupied during the earlier RGB phase asymptotically (Ledoux & Walraven 1958).

An early AGB (EAGB) star features two shell burning, with the He-burning shell being the primary energy source while the H-burning shell contributes minimally. At first, a significant portion of the helium shell's energy is absorbed by the growing outer layers. As $T_{\rm eff}$ decreases, the convective envelope extends further, reaching the transition zone between the hydrogen-dominated outer layers and the helium-rich core. This leads to the formation of a chemical discontinuity, initiating the

second dredge-up. This results in an enhancement of nitrogen and helium in the outer layers, driven by the CNO cycle and triple-alpha reactions occurring in the stellar interior.

In the following Thermal-Pulse Asymptotic Giant Branch (TPAGB) phase, the previously inactive hydrogen-burning shell reactivates and takes over as the primary source of energy. However, in this phase, the helium-burning shell starts to activate and deactivate in a quasi-periodic manner, driven by the buildup of helium products from the hydrogen-burning shell. As the helium layer's mass increases, its base begins to show slight degeneracy, leading to a He shell flash similar to earlier helium core flashes in low-mass stars but less energetic. These flashes drive the hydrogen-burning shell outward, causing it to cool and temporarily shut down. This cycle of He shell flashes and H shell recovery, known as thermal pulses, occurs at intervals that depend on the star's mass. Following a He shell flash, the stellar radius and luminosity decrease while $T_{\rm eff}$ increases. Eventually, the He shell's energy output diminishes, the H-burning shell resumes, and the star's properties return to near pre-flash values. These pulses also lead to the **third dredge-up**, where interior material is brought to the outer layers, enriching the star's composition. Despite these fluctuations, the star's overall evolution on the TPAGB track trends towards higher luminosity and lower $T_{\rm eff}$.

1.2.5 White Dwarf

During the TPAGB phase, thermal pulses play a crucial role in shedding the outer layers of a low-mass star. These periodic pulses cause significant instability within the star. Each thermal pulse increases the star's luminosity and drives strong stellar winds, which blow off the outer layers into space. The repeated cycles of expansion and contraction due to thermal pulses gradually lead to the ejection of the star's outer envelope, forming a **planetary nebula**. The exposed core, now

devoid of its outer envelope, heats up and ionizes the ejected material, causing the nebula to glow. Over time, the core contracts and cools, eventually becoming a white dwarf. This white dwarf, composed mainly of carbon and oxygen, represents the final evolutionary stage of a low-mass star. It will slowly cool and fade over billions of years, radiating away its residual thermal energy.

1.3 Lithium anomaly in Red Giant Stars

Lithium (Li), an element that is relatively rare in the universe, plays a significant role in astrophysics. It is the most massive element formed in the process of Big Bang nucleosynthesis (BBN), alongside ^{1}H, ^{2}H, ^{3}He and ^{4}He. Li primarily exists as its heavier isotope, ^{7}Li, with ^{6}Li present only in minimal amounts (^{6}Li/^{7}Li = 10^{-5}). Other than BBN, Li in the stars and interstellar medium (ISM) comes from cosmic ray spallation, and stellar production through processes like nova explosions and nucleosynthesis. Li is crucial in stellar astrophysics because its abundance can provide insights into the internal processes of stars, particularly those related to stellar mixing and nucleosynthesis. The presence and depletion of Li in stars offer valuable clues about stellar evolution, as Li is easily destroyed at relatively low temperatures in stellar interiors. Therefore, observing Li levels in stars, especially red giants, helps astronomers understand the history of mixing processes, the transport of material within stars, and the broader chemical evolution of galaxies.

1.3.1 First cosmological Li problem

From BBN and baryonic density from WMAP, the primordial Li abundance A(Li) $\simeq 2.72^{+0.05}_{-0.06}$ (Cyburt et al. 2008). Old, metal-poor stars undergo minimal stellar processing and should reflect primordial abundances. To distinguish ^{7}Li produced

in BBN from subsequent astrophysical processes, A(Li) in metal-poor halo stars in our Galaxy should be studied. Spite & Spite (1982) demonstrated that halo main sequence stars with temperatures $T_{\rm eff} \gtrsim 6000$K exhibit a constant A(Li) ~ 2.1 dex that does not vary with metallicity. This "Spite plateau" represents the initial lithium abundance if no destruction had occurred in the stars. So the observed primordial A(Li) is around four times lower than predicted value.

1.3.2 Second cosmological Li problem

The second lithium puzzle centers on the amount of ^{6}Li produced during Big Bang nucleosynthesis via the $^2\mathrm{H}(\alpha,\gamma)^6\mathrm{Li}$ reaction. In stars, ^{6}Li is rapidly depleted by other processes. It is also generated through cosmic ray interactions and might exist in the atmospheres of low metallicity, warm dwarf stars within the halo of the Galaxy. However, these assumptions are debated as they should simultaneously preserve ^{7}Li nuclei. The puzzle involves the mismatch between BBN predictions of the $^6\mathrm{Li}/^7\mathrm{Li}$ ratio, approximately 10^{-5}, and observations showing a ratio of $\sim 5 \times 10^{-2}$.

There are various potential solutions to the cosmological Li problems. One idea is that stellar evolution changes the lithium content in old stars over their lifetimes. For stellar evolution to be the only explanation, ^{7}Li would need to be depleted while ^{6}Li is produced in the same star. This is difficult because ^{7}Li and ^{6}Li have similar nuclear characteristics, so any process that depletes ^{7}Li would also deplete ^{6}Li. Thus, solutions to the cosmological Li problem often exacerbate the second Li issue. Additionally, other theories include non-standard Big Bang models, altered nuclear reaction rates, and the existence of unknown fundamental particles.

1.3.3 Li problem in Red Giants

Li is a fragile element that undergoes significant changes during stellar evolution, largely due to its tendency to be depleted at temperatures exceeding 2×10^6 K. ^{7}Li captures a proton and ultimately decomposes; $^7_3\mathrm{Li} + {}^1_1\mathrm{H} \rightarrow {}^8\mathrm{Be} \rightarrow 2\,{}^4_2\mathrm{He}$. Hence Li cannot survive in the hot stellar interior but only in a thin layer near the cooler photosphere. Many stars exhibit lithium depletion during the main sequence phase. When stars evolve off the main sequence, the First Dredge Up (FDU) takes place, mixing surface Li into the star's interior where it is destroyed by high temperatures, resulting in a rapid decrease in surface lithium abundance. This is predicted by standard stellar evolution models and also supported by observations.

Typically for Population I low-mass stars ($\lesssim 2\mathrm{M}_\odot$), starting with an initial A(Li) similar to the interstellar medium (ISM) value of 3.2 dex are expected to have a A(Li) of no more than 1.5 dex upon reaching the giant star stage (Iben 1967; Charbonnel & Balachandran 2000). However, some giant stars have been observed with lithium abundances exceeding 1.5 dex, termed Li-rich giants, and in some cases, the abundance even surpasses the ISM value, resulting in super Li-rich (SLR) giants.

Li abundance: Preservation vs Production

1. As stars progress to the RGB stage, alongside the FDU, various alternative mixing mechanisms, including rotation-induced mixing and thermohaline mixing, may enhance the depletion of lithium. Additionally, observational data (Charbonnel & Balachandran 2000) indicates that simply preserving lithium is inadequate to explain the observed abundances, especially in SLR stars that surpass the lithium levels found in the ISM.

2. An alternative explanation for the presence of lithium-rich stars involves the production of fresh lithium within the stars. There are three possibilities for Li production - First, lithium might be generated within the star itself, independent of external factors, known as “internal enrichment." Second, lithium could be acquired directly from external sources, like neighboring stars, a process known as “external enrichment." Third, external bodies may initiate an internal self-enrichment mechanism within the star, such as tidal locking leading to rotational acceleration and enhanced mixing, termed “combined enrichment". In many cases, lithium-rich giants could arise from a mix of these processes.

One known production mechanism is the Cameron-Fowler process (Cameron & Fowler 1971a). In red giants, hydrogen-shell burning generates significant amounts of ^{3}He. This ^{3}He can be converted into beryllium through reactions with helium and then into lithium via electron capture. For this mechanism to produce detectable lithium, ^{7}Be must be created and quickly moved to cooler regions where it can transform into ^{7}Li before undergoing proton capture. In red giants, the Cameron-Fowler mechanism occurs in two scenarios: when hot bottom burning (HBB) occurs, where the base of the convective outer layer reaches temperatures high enough for ^{7}Be production, which is then transported to cooler zones to form ^{7}Li. The HBB can explain Li enrichment in massive AGB stars where the mixing zone is deeper. If HBB is not occuring, a radiative layer forms between the convective envelope and the shell, requiring some non-standard mixing to transport matter to the shell where ^{7}Be is produced, and then to distribute ^{7}Be through the radiative layers towards the convective envelope. Various mechanisms proposed to explain this mixing, collectively known as ‘deep mixing’ or ‘extra mixing,’ remain under discussion. Additionally, because the same conditions that produce ^{7}Li can also lead to its destruction, the degree of lithium enrichment from this mixing depends on factors like the rate and pattern of mixing. There are many theories regarding the enrichment mechanism. For the internal enrichment scenario,

possible triggers could be thermohaline instability, rapid rotation, and magnetic field-induced asymmetrical mixing. In the case of joint enrichment mechanism, external factors like tidal locking with neighboring stars, planetary engulfment, or binary star mergers can trigger the Cameron-Fowler mechanism in the primary star, leading to Li production.

For identifying the driving mechanism behind extra mixing, another crucial question is where lithium enrichment occurs along the RGB. This is important since different evolutionary stages during the RGB phase are often distinguished by unique physical environments and internal stellar configurations. Palacios et al. (2001) suggested that internal disturbances close to the luminosity bump might generate additional lithium. In this scenario, ^{7}Be formed internally can be moved to an adjacent convective zone where ^{7}Li is created, but is quickly destroyed by proton capture. This process creates a narrow region where lithium burning occurs, with the reaction ^{7}Li(p, α)α dominating, raising the temperature in the vicinity and enhancing meridional circulation. This situation eventually disrupts the gradient of molecular weights, enabling deep mixing to occur. While it shows potential, this model necessitates a substantial and arbitrary adjustment in diffusion rates. This scenario is also expected to cause significant mass loss and an excess in infrared colors. Also this internal enrichment model will only explain the Li-rich giants near the RGB bump and not in the RC phase.

The external enrichment mechanism offers an alternative to the Cameron-Fowler process for Li enhancement. This process often has associated effects like rotational acceleration due to the increase in angular momentum, unusual elemental abundances, and infrared excess. These characteristics are observed in numerous Li-enriched giants. Nonetheless, the external enhancement model has several drawbacks. A study by Delgado Mena et al. (2016) indicated that for nearby planets to be engulfed by a Li-rich giant, they must orbit extremely close to the star,

within $\sim$ 0.4 AU. Additionally, simulations by Aguilera-Gómez et al. (2016) suggested that even in cases of companion star engulfment, the maximum achievable lithium abundance is around 2.2 dex, which is insufficient to explain the highly Li-rich giants observed. Super meteoritic Li abundances due to planetary engulfment might be observed at the main-sequence turnoff or subgiant phase, but not in RGB stars (Soares-Furtado et al. 2021). Moreover, these stars show no significant anomalies in other elemental abundances, a challenge for theories involving accretion from supernova remnants or AGB ejecta. Given that $A(Li)_{\rm ISM} \sim 3.2$ dex, its accretion cannot explain super Li-rich giants either. Thus, it is unlikely that the external enrichment mechanism alone is adequate for explaining the high levels of lithium observed in these stars.

Adding to the problem of Li rich giants, an increasing number of such stars have been discovered recently which are in the RC phase Singh et al. (2021); Yan et al. (2021). Approximately 80% of low-mass giants exhibiting high lithium are in the clump phase. Additionally, Li-rich stars in the RC phase show significantly higher lithium levels than those in the RGB phase, with the frequency of Li-rich RGB stars declining rapidly as the lithium content increases. The combined enrichment mechanism might be an answer to Li-rich RC giants. Li is universally generated between the RGB tip and RC phases, as demonstrated by Kumar et al. (2020). This was not anticipated by theoretical models, indicating that an unknown process may be occurring during the transition between the RGB tip and the clump stage. It implies that not just Li-enriched giants, but possibly every low-mass star approaching or within the RC stage, could generate Li via a common mechanism. This finding has prompted considerable interest in understanding the process behind Li production in RC stars. Schwab (2020) proposed that Helium flashes could trigger extra-mixing, leading to Li enrichment, but his model predicts an increase to around 0.7 dex, insufficient to explain the high Li levels observed. Zhang et al. (2020b) proposed that these objects could be the outcome of a red giant star merging with a helium white dwarf (HeWD), with simulations revealing post-merger

lithium levels consistent with observational data. According to Casey et al. (2019), tidal synchronization with companion stars accelerates the primary star's rotation, inducing extra-mixing that enhances Li production. Mori et al. (2021) suggested that Li enhancement during the clump phase could be associated with energy dissipation from escaping neutrinos, altering the stars' internal structure. However, this model also predicts Li abundances of only around 0.3 dex, which does not explain the high levels seen in Li-rich RC stars. Following the serendipitous discovery

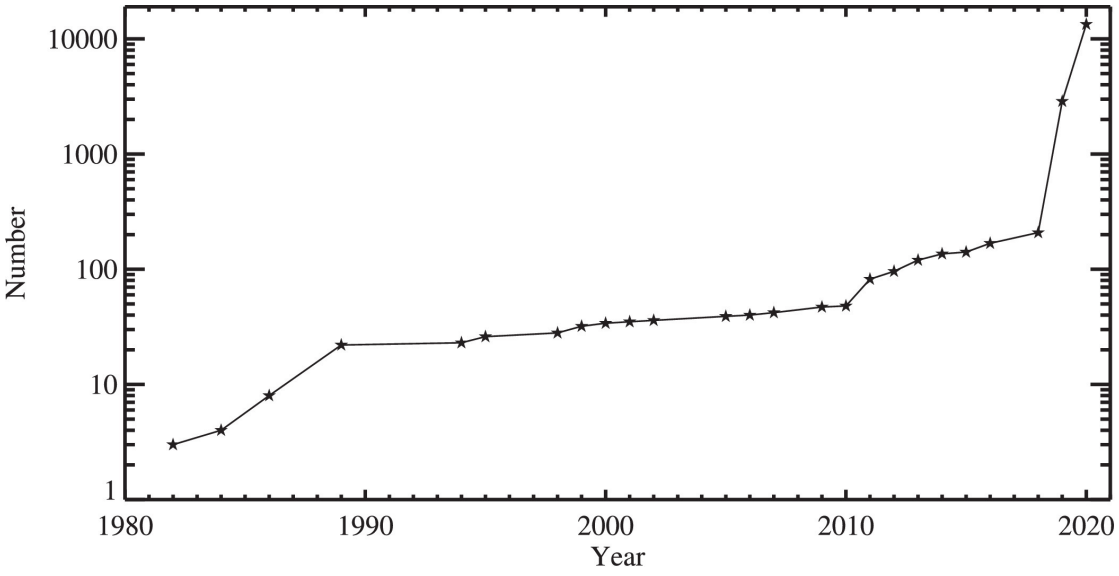

FIGURE 1.4: Cumulative number of known Li-rich giants over the years, with the vertical axis on a logarithmic scale. Pentagrams mark the total number of Li-rich giants identified up to each year.Adapted from Yan & Shi (2022)

of HD 112127, the first red giant exhibiting high levels of Li (A(Li) $\sim$ 3.01 dex) by Wallerstein & Sneden (1982), numerous Li-rich giants have since been identified (see Fig. 1.4). The presence of Li-rich giants challenges the standard stellar evolution model, indicating an additional mechanism for lithium enrichment in stars. While we do know about the conditions required for producing Li in stars, the mechanism driving Li production and its transport to the stellar photosphere are still unclear. Understanding this mechanism is crucial for comprehending lithium formation and refining stellar evolution theories, although it remains a challenging task. Understanding the actual process will also help to assess stellar contribution to the overall Li enrichment of the Galaxy. In the last four decades, considerable

advancements have been achieved in the study of Li-rich giants. However, a comprehensive theory that fully explains the lithium enhancement across all Li-rich stars is still lacking. Further observations and theoretical research are expected to offer additional insights on this topic.

Chapter 2

Observation & Methodology

2.1 Overview

This chapter provides an overview of the observational data and methodologies employed in this study. It outlines the various data sources, including high and low-resolution spectra, photometric measurements, and astrometric data, which were analyzed to investigate lithium-rich giants. High resolution optical spectra were collected for a group of lithium-enhanced giant stars with the Himalayan Echelle Spectrograph (HESP) mounted on the 2-meter Himalayan Chandra Telescope. Additionally, optical spectra with low and medium resolution were collected through the LAMOST Sky Survey project. Time-resolved photometric data, essential for asteroseismology, were gathered from the TESS and *Kepler* space telescopes. The study also incorporated astrometric data from the Gaia mission, as well as photometric observations from WISE and 2MASS. The chapter further discusses the analysis techniques applied to these diverse datasets to address the research objectives.

2.2 Spectroscopic data

Spectroscopy examines how matter interacts with radiation. It is one of the most significant tools in astronomy, as much of our understanding of the universe comes from spectroscopic studies. It provides insights into an object's temperature, composition, and velocity, and can also help deduce its mass, distance, size and various other characteristics.

2.2.1 Absorption and Emission Spectra

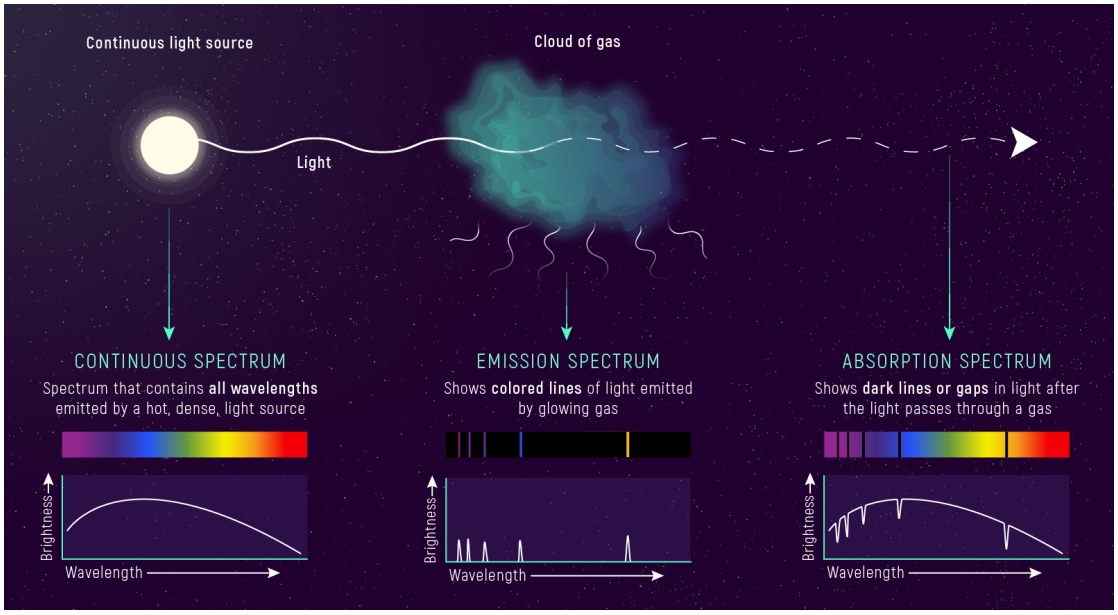

FIGURE 2.1: Different types of spectra from a continuous light source like a star. *Credit: NASA, ESA, and L. Hustak (STScI).*

White light, comprising all visible wavelengths, creates a continuous spectrum when dispersed by a prism. However, if white light passes through atoms, electrons in the ground state can absorb specific energy and transition to higher states. Each absorbed energy corresponds to a particular frequency or wavelength. As a result, certain wavelengths appear missing from the otherwise continuous spectrum, forming absorption lines. This pattern is referred to as an absorption spectrum. Since

electrons can transition to different excited states by absorbing varying energy amounts, atoms of the same element often produce multiple absorption lines. The excited electrons return to lower levels as electromagnetic waves with energy energy corresponding precisely to the difference between the energy states, producing light of specific frequencies or wavelengths. This generates an emission spectrum, characterized by bright lines of particular wavelengths against a dark background. A schematic diagram of the different types of stellar spectrum is shown in Fig. 2.1.

Each element has a distinctive absorption and emission spectrum due to differences in atomic structure. Variations in energy levels among elements mean that hydrogen's energy states, for instance, differ from those of helium. Consequently, the energy absorbed or released during transitions varies, resulting in unique spectral patterns for each element. These unique patterns enable the identification of elements through their spectra.

2.3 Insights from Astronomical Spectra

Astronomical spectra provide critical information about the physical properties, motions, and chemical compositions of celestial objects. This section explores the types of data that can be extracted from spectra and the methods used for their analysis.

2.3.1 Effective Temperature and Wien's Law

Stars generally behave like black body radiators, emitting energy across a range of wavelengths with a peak at a specific wavelength. In the 1890s, Wilhelm Wien

established that the wavelength corresponding to peak energy emission inversely correlates with the temperature of the body. This relationship, known as **Wien's Law**, is expressed as:

$$\lambda_{\max} \propto \frac{1}{T}$$

where $\lambda_{\max}$ is the peak wavelength, T is temperature, and W is Wien's constant, valued at 2.898×10^{-3} when $\lambda_{\max}$ is in meters and T in kelvins.

Wien used this principle to estimate the Sun's temperature at approximately 6,000 K—significantly closer to modern values compared to earlier estimates. Measuring the peak wavelength from a spectrum enables astronomers to calculate a star's effective temperature, even accounting for absorption lines that modify the ideal black body curve.

2.3.2 Radial velocity and Rotational Velocity

Radial velocity of stars is measured using wavelength shifts in the spectra which is known as the Doppler effect.

For stars, uniform red-shifted lines suggest recession, while blue-shifted lines indicate approach. The extent of the shift depends on the velocity component in the direction of the observer's line of sight. The Doppler effect also provides estimate of rotational velocity. When a star rotates, light from the side moving toward us undergoes blue-shift, while light from the receding side is red-shifted. This causes rotational broadening of spectral lines. The measurement of such broadening provides estimates of stellar rotation rates, accounting for the angle of the star's rotational axis with respect to an observer.

2.3.3 Pressure Broadening and Stellar Density

Spectral line widths vary due to differences in stellar density and atmospheric pressure. High-pressure environments in smaller, denser stars result in broader spectral lines, a phenomenon known as pressure broadening. For instance, main-sequence stars exhibit broader lines compared to larger, less dense giants of the same spectral class. Line broadenning is used to differential stars between the main-sequence dwarfs and giants.

2.3.4 Chemical Composition and other applications

Spectra reveal the presence of specific ions, elements, and molecules, enabling astronomers to identify a star's chemical makeup. The first detection of helium occurred in the Sun's spectrum before its discovery on Earth. Modern spectrographs not only detect elements but also allow for the calculation of relative abundances, defining a star's metallicity —the fraction of elements heavier than helium. Periodic splitting of spectral lines indicates binary stars orbiting a common center of mass. The gravitational pull of orbiting planets induces periodic shifts in a star's spectral lines. This technique, known as Doppler wobble, has led to the discovery of numerous exoplanets, including the first around a Sun-like star in 1995.

2.4 Data Reduction

Data reduction is inherently a complex process in astronomy. Since observational data are typically collected using charge coupled devices (CCDs), raw images require corrections to address detector-specific effects. Initially, the spectral data

are spread over a two-dimensional array and must be properly extracted to yield a 1-D flux profile along the wavelength axis.

2.4.0.1 Bias Correction

During observations, bias frames are taken as part of calibration. These are generally zero-second exposures captured with the shutters closed, which help in determining the bias level. Bias frames are needed to remove electrical signal noises from the CCD. Since pixel signals exhibit stochastic variations, robust results are achieved by averaging multiple bias frames into a master bias.Images are then corrected by applying the master bias. At this stage, images may also be trimmed to eliminate under or overscan regions of the detector. These virtual pixel rows or columns, located at the image edges, are sometimes used to estimate the bias level.

2.4.0.2 Flat Normalization

Flat fielding compensates for pixel efficiency variations using images of uniform light sources. In spectroscopy, flat calibration is performed using a continuous reference lamp spectrum along the dispersion axis. Flat field exposures are combined to create a master flat. The master flat is subsequently employed to generate a continuous response curve along the dispersion axis, effectively removing the lamp's spectral signature. This ensures that only high-frequency variations, such as pixel-to-pixel differences, are corrected. The flat field exposures, bias-corrected and trimmed, are merged into one image, known as the master flat.

2.4.0.3 Fitting the Spectrum of the Flat Lamp

The master flat is utilized to identify and correct variations between individual pixels. This is done by collapsing the flat along the spatial direction, allowing a one-dimensional regression to model the spectral profile of the flat lamp. High-frequency variations, distinct from the lamp's smooth spectral profile, are retained. This variation map is then utilized to adjust the science data, ensuring that every feature present in the flat field frames, excluding the fitted spectral distribution, are corrected.

2.4.0.4 Image Stacking

Flat-normalized exposures of the target are merged into a single image. Weighting is applied based on the exposure times provided in the image headers. Median combining of the images helps reduce noise effectively, increasing the signal-to-noise ratio (SNR) in the final spectra. This method also removes stray pixels with extremely high count values, which can occur when a cosmic ray hits a pixel, ensuring that these outliers do not affect the final result.

2.4.0.5 Spectrum Extraction

Once Bias frames are subtracted from and flat master frame divided into the science frames extraction of the spectra along the dispersion axis takes place. The extraction process involves locating this trace and isolating the target spectrum within a specified aperture width.

1. Trace Detection : The pixel values along the dispersion direction are added to estimate an approximate spectrum position.

2. Aperture Placement and Fitting: A smooth function is fitted to the spectrum trace, ensuring precise extraction. The aperture is centered on the trace, and background flux, sampled from regions adjacent to the aperture, is modeled and subtracted to isolate the target spectrum.

2.4.1 Wavelength Solution

Once target spectra are extracted, they are initially plot flux against pixel positions along the dispersion direction. To transform this into a wavelength-calibrated spectrum, a conversion from pixel space to wavelength space is required, termed as the wavelength solution. For this, emission line spectra of calibration lamps, with known line positions, are used.

2.4.1.1 Processing Emission Lamp Spectra

Emission line spectra are extracted in a similar manner as object spectra. Multiple exposures for each lamp type, as well as various lamp types, are combined. The combined spectra are inspected, and emission lines are identified for establishing the wavelength solution.

1. Extraction of Lamp Spectra: Since arc lamp spectra display emission lines at specific positions, they lack the spectral continuum seen in target spectra. The aperture and trace position from a science target serve as references for extracting lamp spectra.

2. Line Identification and Wavelength Fitting: Once lamp spectra are combined, they are compared against reference spectra to identify lines. Known line wavelengths are then mapped to pixel positions, creating a wavelength solution, which is subsequently applied to the target science spectra.

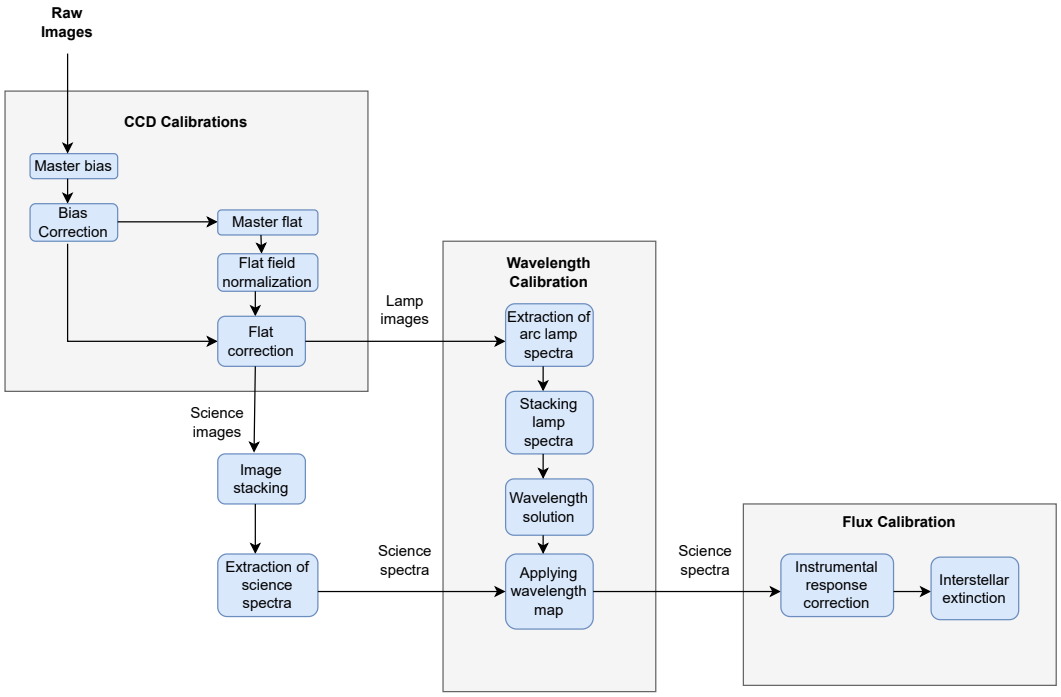

FIGURE 2.2: Schematics of spectroscopic data reduction process

2.5 Spectral Analysis

2.5.1 Continuum Normalization

Continuum normalization plays a crucial role in spectroscopic data processing, especially when assessing stellar characteristics and elemental abundances. Stellar atmospheric and abundances are derived using the relative strengths of absorption lines with respect to the continuum. Here, we normalized the observed

bias and flat corrected spectra by fitting the pseudo-continuum using the smooth curve—typically a polynomial or cubic spline—to selected continuum points in the spectrum. These points, chosen in regions free of prominent spectral lines, define the shape of the continuum. The entire spectrum is then divided by this fitted curve to normalize it to unity. While this approach is simpler and more automated, it requires careful selection of continuum points to avoid biases, especially in spectra with dense line features.

2.5.2 Estimation of stellar parameters

2.5.2.1 Equivalent Width

The equivalent width (W) provides a quantitative assessment of a spectral line's strength. It is represented by the width of a rectangle that has the same area as the line profile, with the rectangle's height set to the continuum value. The mathematical expression for this is:

$$W = \int_0^\infty \left(1 - \frac{F_\lambda}{F_c}\right) d\lambda$$

In this expression, F_λ denotes the flux at a specific wavelength λ within the line and F_c indicates the continuum flux at that wavelength. Equivalent width (EW) provides a normalized measure of line strength, making it independent of the instrument resolution or observational setup.. A larger EW indicates a stronger absorption or emission feature.

In absorption lines, the opacity at a specific wavelength determines the line's depth. The center of a line forms at cooler photospheric temperatures, where atoms and ions absorb light most effectively. At lower temperatures, increased opacity

results in deeper absorption lines, while higher temperatures reduce opacity due to ionization, leading to weaker lines.

The relationship between EW and elemental abundance is described by the curve of growth (CoG). The CoG can be divided into three regions, as illustrated in Fig. 2.3 :

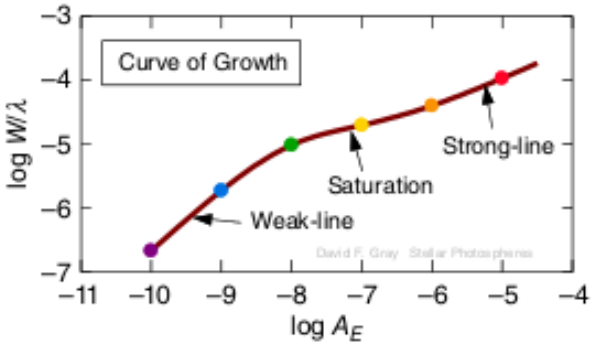

FIGURE 2.3: Schematic diagram of a general Curve of Growth (Adapted from Gray (2008))

1. **Linear Region:** When the central optical depth (τ_0) is less than 1, the equivalent width (W) increases linearly with the column density (N). In this optically thin regime, W provides a sensitive measure of N, independent of the Doppler parameter ($b = \sqrt{2}\sigma$, where σ is the velocity dispersion of the absorbing atoms).

2. **Logarithmic (Saturation) Region:** For $10 \lesssim \tau_0 \lesssim 10^3$, the absorption line becomes optically thick, and W grows more slowly, following W $\propto b\sqrt{\ln(N/b)}$. In this region, W is less sensitive to N but is influenced by the Doppler parameter.

3. **Square Root (Damping) Region:** When $\tau_0 \gtrsim 10^4$, W increases as $\sqrt{N}$, driven by the contribution from the damping wings of the line. This regime provides an accurate estimate of N based on the optical depth in the wings.

To avoid errors in calculating elemental abundances due to saturation effects of strong lines, weaker lines are used for which

$$\log \frac{W}{\lambda} \approx \log \left(constant \frac{\pi e^2}{m_e c^2} \frac{N_r/N_E}{u(T)} N_H \right) + \log \lambda + \log(g_n f A_E) - 5040 \frac{\chi_N}{T} - \log \kappa_\nu$$

Here, $A_E = \frac{N_E}{N_H}$ represents the ratio of the number of atoms of element E to those of hydrogen. $\frac{N_r}{N_E}$ is the same elemental fraction in the r-th stage of ionization. $u(T)$ denotes the partition function, representing how particles are distributed across energy levels at a specific temperature T. κ_ν represents the absorption coefficient at the spectral line frequency, while g_n denotes the statistical weight of the energy level. χ_N is the excitation potential of this level, representing the energy required to excite an electron to that state. f denotes the oscillator strength of the energy level, while λ represents the wavelength of the spectral line (see Gray (2022) for more details).

2.5.2.2 Effective temperature (T_{eff})

The effective temperature describes the temperature of a star, assuming it emits radiation like a perfect blackbody. It relates the star's luminosity (L) and radius (R) via the Stefan-Boltzmann relation:

$$L = 4\pi R^2 \sigma T_{\text{eff}}^4$$

with σ being the Stefan-Boltzmann constant. In practice, T_{eff} is derived from the overall shape of the spectral energy distribution or specific color indices (e.g., B-V), calibrated using stellar models. In spectra, the intensity of hydrogen Balmer lines (Hα, Hβ, etc.) provides sensitive diagnostics of T_{eff} for hot stars, as these lines depend on the population of hydrogen's second energy level, governed by temperature. For cooler stars, molecular features such as TiO and VO bands become prominent indicators, as they are sensitive to temperature variations.

2.5.2.3 Surface gravity ($\log g$)

Surface gravity measures the gravitational acceleration on the star's surface and is expressed as:

$$g = \frac{GM}{R^2}$$

Here G is the gravitational constant, M represents the stellar mass, and R denotes its radius. In practice, it is usually presented as $\log g$, the logarithm (base 10) of g in cgs units. Surface gravity influences line broadening, and it can be estimated through spectroscopic line profiles or derived indirectly using mass-radius relationships. It particularly affects the wings of prominent lines. Spectral features like the Mg I b triplet (5167–5183 Å) and the Ca II triplet (8498–8662 Å) are particularly useful for estimating $\log g$. In cooler stars, the balance of neutral (e.g., Fe I) and ionized (e.g., Fe II) iron lines can constrain $\log g$, as the ionization state depends on electron pressure, linked to gravity.

2.5.2.4 Metallicity ([Fe/H])

Metallicity quantifies the abundance of elements heavier than hydrogen and helium in a star, often expressed relative to the Sun.

$$[Fe/H] = \log_{10}\left(\frac{N_{\mathrm{Fe}}}{N_{\mathrm{H}}}\right)_{\star} - \log_{10}\left(\frac{N_{\mathrm{Fe}}}{N_{\mathrm{H}}}\right)_{\odot}$$

This represents the logarithmic ratio of the number densities of iron (N_{Fe}) and hydrogen (N_{H}) in a star ($\star$) compared to the Sun ($\odot$). Weak iron lines (Fe I and Fe II) in the optical spectrum are ideal for deriving metallicity, as they are less prone to saturation effects.

2.5.2.5 Microturbulence (ξ)

Microturbulence is a non-thermal velocity component that influences the formation of spectral lines, particularly in their wings. It is introduced to account for the broadening of lines beyond what thermal and pressure effects can explain. Correctly estimating ξ is essential for accurately deriving chemical abundances, as it affects the saturation of stronger lines. The microturbulence parameter adjusts the Doppler width ($\Delta\lambda$):

$$\Delta\lambda = \frac{\lambda}{c}\sqrt{v_{th}^2 + \xi^2}$$

where v_{th} is the thermal velocity, ξ denotes the microturbulent velocity, and c is the speed of light. v_{th} is the characteristic velocity of particles in a gas owing to thermal motion and is related to the temperature of the gas. It is given by the equation:

$$v_{th} = \sqrt{\frac{2kT}{m}}$$

Here, k denotes the Boltzmann constant, T represents the gas temperature, and m refers to the particle's mass (e.g., for a neutral atom, this would be the atomic mass).

In stellar spectra, v_{th} is inferred from the width of atomic absorption lines, particularly for elements like hydrogen or iron, whose line broadening is primarily due to thermal motion of atoms. By comparing the observed line profiles to theoretical models of thermal broadening, v_{th} can be estimated. The measurement of line broadening involves fitting observed spectral lines with a profile that incorporates the Doppler shift caused by thermal motion, typically using high-resolution spectroscopic data.

The microturbulence is derived by ensuring consistent abundances from lines with different equivalent widths. Specifically, if stronger, saturated lines yield higher

abundances than weaker lines, ξ is adjusted to correct the discrepancy. The diagnostic lines for ξ are typically neutral iron (Fe I), as their large number and varying strengths provide reliable sensitivity to microturbulent effects.

2.5.2.6 Rotational velocity ($\mathbf{v} \sin i$)

The parameter $v \sin i$ describes the component of the star's rotational velocity along the line of sight, where v is the equatorial rotational velocity and i is the angle between the star's rotation axis and the observer's view. It provides a measure of how fast a star rotates, as seen from Earth. When $i = 90°$, vsin i equals the actual rotational velocity., but if i is smaller, the measured value underestimates the true velocity. This rotational motion causes Doppler broadening in spectral lines, as parts of the star rotating toward or away from the observer introduce blueshifts and redshifts, respectively. This effect results in wider and shallower absorption lines, particularly evident in well-isolated features like Fe I, Fe II, or the Ca II triplet. The observed line profile also incorporates other broadening mechanisms, such as thermal motion of atoms (thermal Doppler broadening) and macroturbulence, which arises from large-scale convective motions in the stellar atmosphere. Distinguishing vsin i from these components requires fitting the observed profile with synthetic models that include contributions from both thermal and turbulent velocities. Rotational broadening becomes dominant for higher vsin i, whereas macroturbulence is more significant in slowly rotating stars, particularly cool giants.

2.5.3 Spectrum synthesis

Spectroscopic analysis can be carried out using two main approaches: equivalent width measurements or synthetic spectra. In this work, we applied the synthetic

spectrum fitting technique to derive stellar parameters and elemental abundances. Spectrum synthesis involves solving the radiative transfer equation for a stellar atmosphere model, calculating line profiles for various spectral features, and combining them to create a synthetic spectrum.

A comprehensive spectral synthesis tool capable of determining stellar parameters must include several components:

1. **radiative transfer solver :** Determines the number density of different atomic and/or molecular species across atmospheric layers, calculates the absorption coefficients at various wavelengths and layers accounting for both line and continuum absorption, and solves the radiative transfer equation using the total absorption coefficients to compute the emergent flux at the stellar photosphere.

2. **Atmospheric model grids :** Spectroscopic techniques typically rely on models of stellar atmospheres that describe the variation of physical properties—such as temperature, electron density, opacity, and gas and radiation pressure—across different atmospheric layers or optical depths. Since these methods derive parameters indirectly, their precision depends heavily on the reliability of the models used. Creating a model atmosphere from scratch can be computationally intensive; hence, pre-computed grids of models are often employed for a range of parameters like $T_{\rm eff}$, $\log g$ and [Fe/H], with interpolation applied as necessary.

3. **Atomic/molecular line list :** Spectral synthesis requires detailed and accurate atomic and molecular data for all lines within the wavelength range. The lines chosen for parameter determination should be selected carefully, as their sensitivity to stellar parameters can vary. Different approaches are used to define spectral regions for synthesis: some studies analyze wide

wavelength intervals (e.g., Spectroscopy Made Easy(SME); Valenti & Fischer (2005)), while others focus on masking regions around specific lines (e.g., iSpec;Blanco-Cuaresma et al. (2014)). In creating an accurate linelist we must consider the various broadening mechanisms that influence the final line profile, each with its own associated coefficient, often referred to as atomic data. The most crucial data for simulating an atomic line are the transition probabilities (oscillator strengths, $\log gf$), typically derived from laboratory or semi-empirical methods. Despite recent improvements, significant discrepancies still exist when comparing these values to those derived from astrophysical calibrations. To address these discrepancies and minimize uncertainties, astrophysical $\log gf$ values are used for the line list, which also helps reduce systematic errors caused by imperfections in model atmospheres. A common method for calibrating atomic data involves using high-resolution spectra from stars with well-constrained parameters.

4. **An optimization routine :** The parameter optimization procedure addresses the non-linear least-squares problem, determining the parameters that minimize the χ^2 value.

$$\chi^2 = \sum_{i=1}^{N} \frac{(Obs_i - Synth_i)^2}{\sigma_i^2}$$

Here, Obs represents the observed flux points, Synth refers to the synthetic flux points, σ denotes the error associated with the observed flux, and N is the total number of flux points within the specified wavelength interval.

2.5.3.1 Methodology

For derivation of stellar parameters, we start by supplying a line list of Fe I and Fe II lines, along with a parameter file containing initial estimates. These first-guess

values, preferably obtained through photometric measurements or trustworthy references in the literature, are chosen to be close to the expected final values, as this iterative process benefits from reduced computation time when starting near the solution.

The initial atmospheric parameters are supplied to a code designed for interpolating atmospheric models, with the Kurucz models (Castelli & Kurucz 2004) being used in this thesis. Based on the provided inputs, the code constructs an atmospheric model. This model atmosphere, along with the linelist, is then processed by MOOG. A preliminary run of MOOG is performed, followed by a σ based clipping of the Fe I and Fe II lines to exclude outliers. Once the EWs are refined, MOOG is executed once more with the updated list.

An iterative process is then undertaken to satisfy three equilibrium conditions: excitation balance, ionization balance, and reducing the slope relating log n(Fe I) (or n(Fe II)) to the reduced equivalent widths [log(W/λ)] (or wavelength or excitation potential). Here, log n(Fe I) and log n(Fe II) refer to the logarithmic abundance of neutral and ionized iron respectively. If necessary, the stellar parameters are adjusted iteratively until these conditions are met.

1. **Excitation equilibrium :** $T_{\rm eff}$ is determined by ensuring no correlation exists between neutral iron abundances (log n(Fe I)) and excitation potential (EP).The abundance of Fe I increases with $T_{\rm eff}$.

$$\log n(\mathrm{FeI}) \propto e^{-EP_i/kT_{\rm eff}}$$

   EP_i represents the excitation potential of each iron line. Variations in temperature affect Fe I abundances across a range of EP values, allowing us to derive $\mathrm{T}_{\rm eff}$ by ensuring that the abundance obtained from Fe I lines is independent of EP (Takeda et al. 2002; Gray 2022).

2. **Ionization equilibrium :** $\log g$ is set by matching the abundances of Fe I and Fe II, as the surface gravity influences ionization. The relationship between surface gravity and Fe II abundance is given by:

$$\log n(\mathrm{FeII}) \propto \log g^{n/3}$$

Here, n is 1 when iron is mostly ionized and 2 when iron is predominantly neutral. Ionization equilibrium requires that neutral (Fe I) and ionized (Fe II) iron lines yield identical abundances, allowing us to directly measure the surface gravity by comparing their abundances. When the condition $\log n(\mathrm{Fe\ I}) = \log n(\mathrm{Fe\ II})$ is met, $\log g$ can be accurately determined (Saha-Boltzmann equation).

3. **Microturbulence equilibrium :** Microturbulence (ξ) is adjusted by minimizing the slope relating log n(Fe I) to $\log(\mathrm{W}/\lambda)$. This minimizes the effect of ξ on line strength, especially for moderate to strong lines. To prevent overestimation of ξ, theoretical equivalent widths are often used instead of observed ones, as random errors in the observed EWs can lead to systematic biases (Magain 1984).

The three steps are interconnected, with changes in $\mathrm{T_{eff}}$ influencing ionization balance and $\log g$ adjustments. Typically, microturbulence is the last parameter to be adjusted after $\mathrm{T_{eff}}$ and $\log g$ are optimized. The basic procedure of our method involves generating a synthetic spectrum based on an initial set of stellar parameters and a given line list. The observed and synthetic spectra are compared by calculating the χ^2, and the optimal parameters are obtained by reducing the disparity between the two.

Elemental Abundances

Once the convergence criteria are satisfied, the final stellar parameters are determined. A line list covering a specified wavelength range is then input into MOOG, which utilizes these parameters to produce a model atmosphere and compute a synthetic spectrum over the specified wavelength interval. A comparison is made between the computed spectrum and the observed one by calculating the χ^2, and the abundances of the desired elements are derived by minimizing the discrepancies between selected absorption lines in the synthetic and observed spectra.

2.5.4 Data sources

1. **Himalayan Chandra Telescope (HCT)**

   The Himalayan Chandra Telescope (HCT) is a 2-meter optical-infrared telescope located at an altitude of 4,500 meters in Hanle, Ladakh, India, with coordinates $32°46'46''\text{N}, 78°57'51''\text{E}$. Managed by the Indian Institute of Astrophysics (IIA), this observatory ranks among the world's highest, benefiting from clear skies, minimal light pollution, and stable atmospheric conditions. The HCT is equipped with state-of-the-art instruments, including the Himalayan Faint Object Spectrograph Camera (HFOSC) for optical imaging and spectroscopy. Notably, it also houses the Hanle Echelle Spectrograph (HESP), which provides high-resolution spectroscopy ($R \approx$ 30,000–60,000) essential for precise radial velocity measurements and detailed chemical abundance studies. It covers a continuous wavelength range of 350 to 1000 nm. Remote operations are conducted through a dedicated satellite link at the Centre for Research and Education in Science and Technology (CREST), located near Hoskote Bengaluru, facilitating year-round access to the facility. These capabilities make HCT a versatile and powerful tool for observing faint stars, transient events, and exoplanetary systems.

2. **Large Sky Area Multi-Object Fiber Spectroscopic Telescope (LAMOST)**

LAMOST, also known as the Guo Shoujing Telescope, is located at Xinglong Station in Hebei Province, China, at an altitude of 900 meters and coordinates 40°23′39″N, 117°34′30″E. This 4-meter quasi-meridian reflecting Schmidt telescope is designed for large-scale spectroscopic surveys, utilizing 4,000 fibers in its focal plane to capture spectra of thousands of objects simultaneously. LAMOST covers a wide field of view (5° in diameter) and is equipped with multi-object spectrographs optimized for low- to medium-resolution spectroscopy. The telescope has revolutionized stellar and galactic studies by providing a vast dataset of high-quality stellar spectra, enabling precise determination of stellar parameters, chemical compositions, and radial velocities.

3. **Galactic Archaeology with HERMES (GALAH)**

   The GALAH survey utilizes the High Efficiency and Resolution Multi-Element Spectrograph (HERMES), installed on the 3.9-meter Anglo-Australian Telescope at Siding Spring Observatory in New South Wales, Australia, at an altitude of 1,165 meters and coordinates 31°16′24″S, 149°3′54″E. HERMES is designed for high-resolution spectroscopy (R $\approx$ 28,000), with four simultaneous spectral bands covering the optical range (471-789 nm). This allows for detailed chemical abundance analysis of up to 32 elements per star. With the exception of 2,935 spectroscopic observations conducted in 2014 using the high-resolution mode of HERMES ($R \sim 42,000$), the majority of observations were performed in the low-resolution mode ($R \sim 28,000$). Total exposure times varied depending on the observing program but were generally between 60 and 90 minutes. The GALAH survey leverages Gaia astrometric data, enabling precise kinematic and chemical tagging of stars to unravel the formation history and evolution of the Milky Way.

2.5.5 Software/Codes

For spectroscopic data reduction and analysis we used the following :

1. **IRAF :** IRAF[1] (Image Reduction and Analysis Facility) is a comprehensive software suite developed by the National Optical Astronomy Observatory (NOAO) for the reduction and analysis of astronomical data, particularly in optical and infrared wavelengths. Widely used in the astronomical community, IRAF provides tools for a range of tasks, including image calibration, spectral analysis, and data visualization. In echelle spectroscopy, IRAF is commonly employed to extract 1D spectra from 2D images, correcting for radial velocity shifts, and performing continuum normalization. Some key IRAF tasks include `rvcorrect`, which corrects for radial velocity shifts in spectra, `ccdproc`, used for bias subtraction, flat-field correction, and trimming of images. For spectral calibration, IRAF includes tasks such as `identify`, which is used for wavelength calibration, and `fluxcal`, which applies flux calibration to spectroscopic data. The `continuum` task is used to perform continuum normalization of the spectra

2. **MOOG :** MOOG is a Fortran-based radiative transfer program designed for various tasks such as line analysis, spectrum synthesis, and estimation of equivalent widths, stellar fluxes, and chemical abundances. MOOG functions based on the principles of local thermodynamic equilibrium (LTE) and one-dimensional geometry. The program takes three files as input: one specifying parameters, another containing the atmospheric model, and a third with spectral line data. MOOG is limited to using model atmospheres calculated under the assumption of plane-parallel geometry. Since MOOG only supports the SuperMONGO plotting package for graphical output, we have employed two Python wrappers, pyMOOGi[2] (Adamów et al. 2014) and

FASMA[3] (Tsantaki et al. 2018), to facilitate the execution of MOOG for our work.

3. **Linemake :** Linemake[4] (Placco et al. 2021) is a utility program designed to generate synthetic spectrum input line lists by combining Kurucz's atomic and molecular line database with refined transition probabilities, as well as detailed hyperfine and isotopic structure information. It generates line lists compatible with the requirements of the line analysis software MOOG. The process begins with the Kurucz line compendium, which is then enhanced or modified with atomic data from the Wisconsin group (Lawler et al. 2009) and molecular datasets contributed by the Old Dominion group (Bernath 2020). Linemake, implemented in standard FORTRAN, Linemake is compatible with any UNIX or Linux operating system. The output line list produced includes details such as the excitation potential (eV) of the line, wavelength, oscillator strength (gf or $\log gf$), element code, van der Waals damping constant, and dissociation energy for molecular features. When using Linemake, the user specifies which molecules should be included in the calculations, along with which elements have altered abundances compared to the standard.

4. **q2 :** q2[5] is a Python package (qoyllur-quipu, or q2) developed by Ramírez et al. (2014) to streamline the handling of MOOG's input and output files, as well as simplify iterative processes. This code allows the use of the 2019 version of MOOG (in SILENT mode) to compute stellar elemental abundances and determine atmospheric parameters, relying on the standard methods of excitation and ionization equilibrium for iron lines. In the present study, we utilized q2 to generate model atmospheres by interpolating ATLAS9 (Castelli & Kurucz 2004) model atmosphere grids. Our model atmosphere is computed across 72 plane-parallel layers. The model file contains the stellar parameters and the microturbulence velocity (either estimated or determined), along with the following five quantities for $(\rho x, T, P_g, N_e, \kappa_{Ross})$

each layer. In this context, ρx represents the mass of matter above 1 cm^2 of the atmosphere at a specific depth (g/cm^2). It is computed using the integral $R_x = \int_0^z \rho(z)\, dz$, where $\rho(z)$ denotes the matter density at depth z. T is the electronic temperature at the relevant level. P_g is the gas pressure (in dyne/cm^2).N_e is the electronic density, (in particles/cm^3) and κ_{Ross} is the Rosseland opacity,(in cm^2/g). Additionally, the number of elements ($natoms$) and their logarithmic abundances should be explicitly provided if any elements differ from the default solar values (Asplund et al. 2009). The file should also specify the number of molecules ($nmol$) and their names if they are included in molecular equilibrium calculations.

[1] https://github.com/iraf-community/iraf
[2] https://github.com/madamow/pymoogi
[3] https://github.com/MariaTsantaki/FASMA-synthesis
[4] https://github.com/vmplacco/linemake
[5] https://github.com/astroChasqui/q2

2.6 Asteroseismology: Probing Stellar Interiors through Oscillations

Asteroseismology explores the physics and internal structure of stars by analyzing their pulsations. Sound waves produced by vibrating vocal cords in humans depend on factors like density, temperature, and air's composition. Similarly natural oscillation frequencies of a star's pulsations are influenced by its mass, radius, age, and elemental composition. These frequencies constrain internal physical phenomena in stars, such as the layers where nuclear fusion occurs and the primary energy transport mechanisms.

The resonant oscillation modes of stars, which are self-excited, represent minor disturbances to their hydrostatic equilibrium structures. The core information in asteroseismology consists of the eigen frequencies of a star. These represent oscillation modes (or standing waves), each characterized by a unique frequency and a specific spherical harmonic structure. In the case of stars that are not magnetic or rotating, the wave functions can be divided into two components: one for the radial part and the other for the angular part. The radial component depends on the radial index n, representing the count of internal regions that act as nodes. For the angular part, the degree ℓ defines the count of nodal lines on the star's surface, while the azimuthal index m indicates how many nodal lines on the surface correspond to the longitudinal lines, with the condition $|m| \leq \ell$.

The primary objective of asteroseismology is identifying oscillation frequencies of stars and corresponding spherical harmonic structures and then compare these with theoretical predictions to comprehend stellar physical properties and chemical compositions using rigorous statistical methods. Different stellar structures provide the necessary conditions for exciting distinct pulsation modes, resulting in oscillations being observed throughout the HR diagram. An asteroseismic HR

diagram labeling the primary types of pulsating stars is illustrated in Fig. 2.4. The following subsections outline the various pulsation modes that can explain

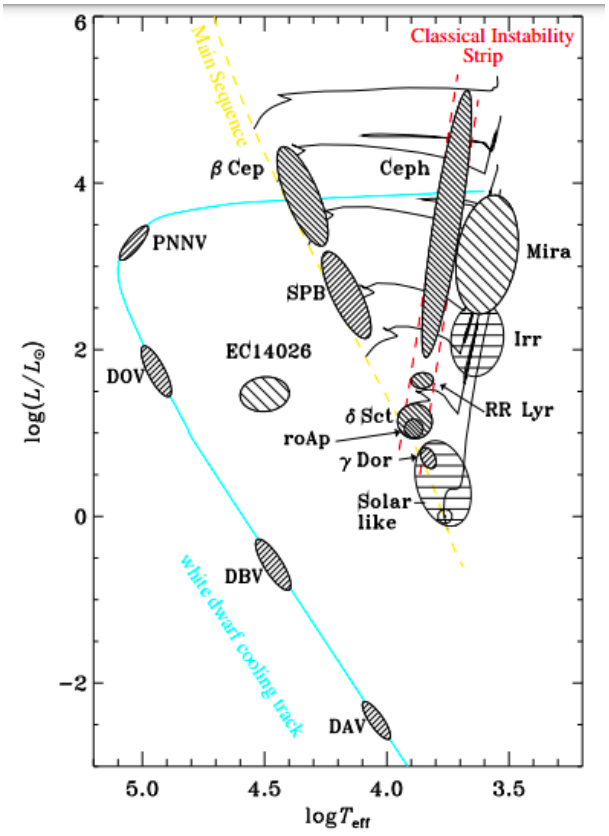

FIGURE 2.4: H-R diagram illustrating the various types of pulsating stars. Adapted from Kim et al. (2006)

the wide array of pulsating stars across the HR diagram.

2.6.1 Pressure Modes

Pressure modes refer to oscillations where pressure gradients serve as the main restoring force. These modes can take radial forms (when $\ell = 0$) or non-radial forms (when $\ell \geq 1$). In the case of radial pressure modes, the pulsation involves the entire stellar radius with no angular dependence. Conversely, non-radial pressure modes are confined to specific depths beneath the surface, with the penetration depth determined by the local adiabatic sound speed, c_s, given by:

$$c_s = \sqrt{\frac{\gamma P}{\rho}},$$

where γ denotes the adiabatic index, P is the pressure, and ρ is the density of the gas. The pulsation cavity of a pressure mode is connected to its frequency exceeding the Lamb frequency S_ℓ, defined as:

$$S_\ell = \frac{\ell(\ell+1)c_s^2}{r^2}.$$

By rearranging the equation for the radius r, the "turning radius" for a non-

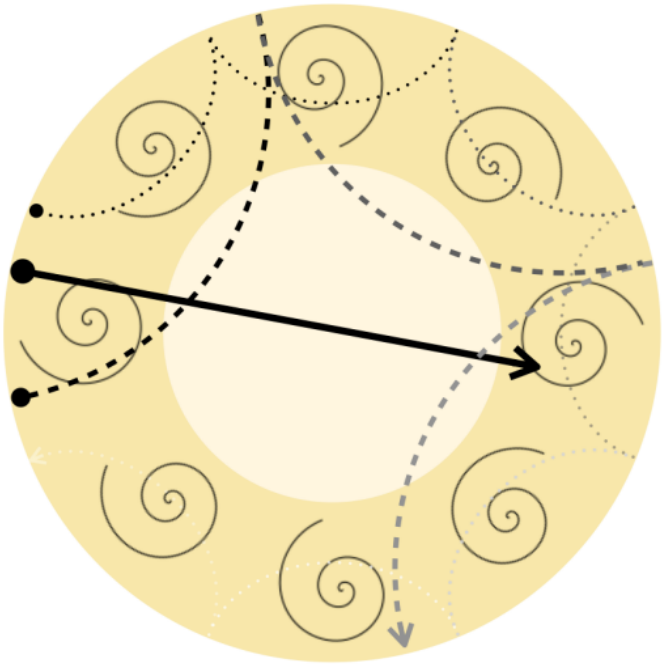

FIGURE 2.5: Example showing wave propagation in a low-mass star on the main sequence, similar to the Sun. The convective envelope is depicted in dark yellow with vortex marks, while the radiative interior is shown in light yellow. Each ray-tracing path corresponds to a distinct pulsation mode, beginning at the black circle. The solid arrow represents a radial mode ($\ell = 0$), the dashed arrow shows a quadrupole mode ($\ell = 2$), and the dotted arrow illustrates the movement of a high-radial order, high-angular degree mode, confined closer to the star's surface. Adapted from Bowman & Bugnet (2024)

radial pressure mode can be derived. This turning radius marks the farthest point

a non-radial pressure mode can propagate when excited near the star's surface. Pressure modes with higher values of ℓ correspond to shallower pulsation cavities, as turning radius is inversely proportional to $\sqrt{\ell(\ell+1)}$. This results in these modes being more sensitive to the outer layers of the star, as shown in Fig. 2.5

For pressure modes with large radial orders ($n \gg \ell$), typically ranging from $n = 5$ to $n = 15$ and with angular degrees $\ell = 0, 1, 2$, the mode frequencies follow an asymptotic pattern. For modes with successive radial orders n, the same angular degree ℓ, and azimuthal order m, the frequencies exhibit a regular spacing. The difference in frequency between consecutive modes in this sequence is known as the large frequency separation:

$$\Delta\nu = \left(2\int_0^R \frac{\mathrm{d}r}{c_s}\right)^{-1},$$

which is linked to the mean density of the star, as it reflects the star's sound-crossing time. An additional important quantity in the analysis of pressure modes of large radial orders is the frequency at which maximum power occurs, denoted as $\nu_{\max}$. Although the exact mechanism of mode excitation by turbulent convection remains uncertain, solar-like oscillators (SLOs) exhibit a roughly energy profile concentrated within a particular frequency range. SLOs include solar-like main-sequence stars, subgiants and RGBs (reviews: Chaplin & Miglio (2013); Hekker & Christensen-Dalsgaard (2017); García & Ballot (2019). The power excess is typically modeled by a Gaussian centered around ν_{max}.

As stars evolve, such as during ascension of the red giant branch (RGB) with hydrogen-shell burning, ν_{max} decreases due to the star's growing radius. Theory and observations confirm $\nu_{max} \propto \nu_{ac} \propto gT_{\mathrm{eff}}^{-1/2}$, where ν_{ac} is the acoustic cut-off frequency. Using solar ν_{max} as a reference, this relationship can be expressed as:

$$\nu_{max} = \frac{M/M_\odot}{(R/R_\odot)^2\sqrt{T_{\rm eff}/T_{\rm eff,\odot}}}\nu_{max,\odot},$$

where $\nu_{max,\odot} = 3050\,\mu$Hz and $T_{\rm eff,\odot} = 5772\,$K. However, this assumes a stellar structure similar to the Sun (Hekker 2020).

High-radial-order pressure modes exhibit a regular pattern of equally spaced frequencies centered around a particular $\nu_{\rm max}$. This is most evident in the frequency spectra of stars like the Sun and RGBs. Younger stars generally have higher $\nu_{\rm max}$ compared to older stars of the same mass.

For stars exhibiting regular pressure modes, methods for determining $\Delta\nu$ and spherical harmonic geometry include fitting the frequency spectrum or employing an échelle diagram (Chaplin & Miglio 2013; Hekker & Christensen-Dalsgaard 2017; García & Ballot 2019). Spectrum fitting directly matches theoretical predictions to observed frequencies, but it can be computationally demanding. Conversely, an échelle diagram offers a more visual and practical approach. This technique divides the oscillation spectrum into segments of equal width, corresponding to the large frequency separation $\Delta\nu$. Frequencies are plotted against their modulo $\Delta\nu$, causing modes of same angular degree ℓ to align vertically. The échelle diagram serves as a powerful tool for identifying oscillation modes and their geometric properties. Regular patterns emerge when the frequency spectrum displays evenly spaced modes, making it particularly useful for solar-like oscillators, red giants, and subgiants. In such diagrams, the vertical alignment of ridges is a direct representation of modes with identical angular degrees. This visual alignment simplifies the task of assigning ℓ and m values to each mode.

2.6.2 Gravity Modes

Gravity modes are oscillatory patterns where buoyancy, or gravity, serves as the primary force restoring equilibrium, leading to lower frequencies compared to pressure modes. These modes are exclusively non-radial ($\ell \geq 1$) and have a spherical harmonic structure. The frequencies of gravity modes lie below the Brunt–Väisälä frequency, N, also referred to as the buoyancy frequency, which is defined by:

$$N^2 = g\left(\frac{1}{\gamma P}\frac{dP}{dr} - \frac{1}{\rho}\frac{d\rho}{dr}\right).$$

Similar to the large frequency separation ($\Delta\nu$) seen in pressure modes, gravity modes of high radial order within the asymptotic limits exhibit regular period spacing, denoted by $\Delta\Pi_0$:

$$\Delta\Pi_0 = 2\pi^2\left[\int_{r_1}^{r_2}\frac{N(r)}{r}dr\right]^{-1},$$

where r_1 and r_2 represent the inner and outer radial positions within the cavity where gravity mode pulsations occur. Alternatively, the asymptotic period spacing $\Delta\Pi_{n\ell}$ can be obtained by fitting the individual periods of gravity modes ($\Pi_{n\ell}$) using:

$$\Pi_{n\ell} = \frac{\Delta\Pi_0}{\sqrt{\ell(\ell+1)}}(|n| + \alpha)$$

where α denotes a phase constant that does not depend on the angular degree of the mode. The asymptotic period spacing is expressed as :

$$\Delta\Pi_{n\ell} = \Pi_{n+1\ell} - \Pi_{n\ell} = \frac{\Delta\Pi_0}{\sqrt{\ell(\ell+1)}}$$

Since gravity modes of higher radial order exhibit equal spacing in period, a gravity-mode period spacing diagram is a widely used diagnostic tool in asteroseismology. This diagram displays the differences in period between successive radial orders (n) of modes with identical angular degree (ℓ) and azimuthal order (m) plotted against the pulsation period. Two primary features of such diagrams are leveraged in analysis. First, rotation causes a gradient in the pattern, with faster rotation resulting in steeper 'tilts.' Second, perturbations in the uniform period spacing pattern, in addition to rotation effects, appear as dips or irregularities ('wiggles') due to trapping of modes in regions with chemical composition gradients. These dips and the individual mode periods provide valuable insights into stellar ages, as the extent of chemical gradient zones evolves over time.

Gravity modes are most often utilized in the study of intermediate and higher mass stars as they are evanescent in convection zones. In low-mass stars, their amplitudes decay rapidly before reaching the surface due to thick convective envelopes. In contrast, main-sequence intermediate- and high-mass stars, with radiative envelopes, exhibit detectable surface amplitudes of gravity modes. Gravity modes show heightened sensitivity in the area immediately beyond the convective hydrogen-burning core in these stars, which diminishes in size during the main sequence.

This sensitivity arises since the Brunt–Väisälä frequency (N) has a value of zero within the convective core but becomes non-zero just outside it due to chemical gradients and energy transport mechanisms at the convective-radiative boundary. This localized peak in N, often referred to as the N-spike, leads to mode trapping, making gravity modes particularly responsive to the region separating the central

core from the outer radiative layer. Therefore, the variations observed in gravity-mode period spacings offer valuable insights into a star's age and the degree of mixing occurring at this interface.

2.6.3 Mixed Pressure-Gravity Modes

The implications of the previously discussed Lamb and Brunt-Väisälä frequencies are as follows: an oscillation having a frequency greater than both ($\omega > S_l, N$) is primarily influenced by pressure (p-mode) where pressure serves as the restoring force in the relevant stellar region. Conversely, an oscillation having a frequency smaller than both ($\omega < S_l, N$) is predominantly governed by buoyancy (g-mode). In regions within the star's interior where ω lies in the range defined by the Lamb and Brunt-Väisälä frequencies, the wave's amplitude diminishes exponentially as it moves away from the propagation zones of p-modes and g-modes, which are referred to as evanescent regions. When the evanescent region separating the p-mode and g-mode cavities is thin enough, couplings may arise, leading to mixed modes that display features of both p- and g-modes. Most mixed modes exhibit significantly larger amplitudes within the core compared to the stellar envelope, and these are called gravity dominated mixed modes. Similar to pure g-modes, their periods are approximately uniform in spacing (quasi-constant). Unfortunately, their high inertia (total interior mass influenced by the oscillation) results in very small amplitudes on the surface of the stars, making them almost undetectable. However, as a result of resonance between the two cavities, certain mixed modes exhibit increased amplitude within the envelope, causing them to resemble pressure modes. Such pressure-dominated mixed modes possess reduced inertia compared to gravity-dominated counterparts, enabling their amplitudes to become sufficiently high for observation. The interval between successive periods of these mixed modes (ΔP, representing the average of neighboring pairs) aligns

closely with the asymptotic spacing for gravity-dominated mixed modes but is significantly smaller for pressure-dominated ones.

Asteroseismic study of mixed modes in evolved stars like red giants has been remarkably successful. In red giants with radiative cores, the g-mode spacing is markedly reduced compared to clump stars that have convective cores. This phenomenon is due to convection in the central regions of helium-burning cores. In the convective region, the buoyancy frequency (N) is nearly zero. Helium-burning stars with convective cores have a restricted g-mode cavity, which reduces the buoyancy frequency integral, leading to an increase in the asymptotic period spacing(Christensen-Dalsgaard 2014). Additionally, the dense radiative cores of RGB stars lead to a higher Brunt-Väisälä frequency. However, in RC stars undergoing helium ignition, the core undergoes expansion, lowering the local gravitational pull which in turn, reduces buoyancy frequency. Since the period spacing is inversely proportional to the integral over N, this expansion results in a greater period spacing compared to stars without a convective core region.

It is to be noted that typically, dipole modes (ℓ =1) are preferred over quadrupole modes (those with degree ℓ=2) for examining the internal conditions of stars. This is due to two factors: first, higher-degree modes have weaker coupling, resulting in significantly reduced amplitudes for modes with a prominent g-mode component. Second, as the degree increases, the spacing between mixed components decreases, making it more challenging to distinguish quadrupole mixed modes and their period intervals. In RGBs, directly measuring period intervals of pure g-modes, $\Delta\Pi_{n\ell}$, is often not feasible because non-radial modes become mixed during this evolutionary phase. However, period interval for mixed modes, ΔP can be easily measured and acts as an effective substitute for $\Delta\Pi_{n\ell}$.

2.6.4 Asteroseismic Scaling Relations

For solar-like oscillations (SLOs), identifying $\Delta\nu$ and $\nu_{\max}$ enables the derivation of radius and mass of stars from asteroseismic scaling relations. These relations are expressed as:

$$\frac{M}{M_\odot} \simeq \left(\frac{\nu_{\max}}{\nu_{\max,\odot}}\right)^3 \left(\frac{\Delta\nu}{\Delta\nu_\odot}\right)^{-4} \left(\frac{T_{\rm eff}}{T_{\rm eff,\odot}}\right)^{3/2},$$
$$\frac{R}{R_\odot} \simeq \left(\frac{\nu_{\max}}{\nu_{\max,\odot}}\right) \left(\frac{\Delta\nu}{\Delta\nu_\odot}\right)^{-2} \left(\frac{T_{\rm eff}}{T_{\rm eff,\odot}}\right)^{1/2},$$

Here $\Delta\nu_\odot = 134.9\,\mu$Hz represents solar large frequency spacing.

Asteroseismology provides highly precise measurements of stellar surface gravity and stellar age, often surpassing spectroscopic estimates. However, these scaling relations are calibrated to solar properties and exclude other stellar characteristics like metallicity or specific microphysics. Variations in frequency spacings observed in spectra or echelle diagrams may arise due to factors such as rotation, chemical gradients, or magnetic fields inside the pulsation zone. These deviations can complicate the use of these formulae for certain stars, requiring in-depth asteroseismic analysis to account for underlying physics.

2.6.5 Analysis techniques

This section outlines the practical steps involved in data analysis for asteroseismology. Before identifying pulsation mode frequencies based on their spherical harmonic geometry, the frequencies must first be extracted. This process begins with gathering time-series observations of the surface features of a star. These

data can take one of two forms: (i) spectroscopic measurements, where periodic changes in spectral line profiles are analyzed, or (ii) time-series photometry, where variations in the star's overall brightness over time, often referred to as a light curve, are examined.

Frequency spectra are generated from time-series data. For a time-dependent function $f(t)$, methods based on Fourier analysis are applied to derive the amplitude as a function of frequency, $F(\omega)$. The oscillation power spectrum is obtained by squaring this amplitude across frequencies. When the ratio of signal to noise is sufficiently large, analyzing the data in the frequency domain reveals oscillation modes with amplitudes exceeding the noise level at their respective frequencies.

For time series containing multiple signals, such as those produced by solar-like oscillations, the resulting Fourier spectrum is often complex. However, time-series data are rarely perfect, as observations are sampled at discrete intervals and are not continuous. Gaps in the time series can introduce additional frequencies, called aliases, which contaminate the true oscillation signals. To minimize this issue, gaps must be avoided as much as possible.

The sampling rate is a critical consideration, as it determines the highest resolvable frequency in the power spectrum for the target under study. Additionally, the total duration of the data set affects frequency resolution—the longer the time series, the finer the resolution. For example, in the case of the Sun, at least one month of continuous observations is required to measure fundamental characteristics of its oscillation spectrum, including the lifetimes of its modes. The power spectrum is typically computed until the Nyquist frequency, ν_{Nyquist}, defined as:

$$\nu_{\mathrm{Nyquist}} = \frac{1}{2\Delta t}$$

Here, Δt represents the time interval between successive observations in the data

set. The Nyquist frequency sets the maximum frequency which can be accurately resolved without encountering undersampling issues.

2.6.5.1 Frequency Analysis

To analyze stellar oscillations in the frequency domain, the power spectrum is derived from the light curve. The primary features of the power spectrum include: rotational modulation peaks and their harmonics, granulation-induced continuum, the p-mode resonant oscillation envelope, and the photon noise level (García & Ballot 2019). In astronomy, time series data often suffer from irregular sampling due to observational constraints. For instance, data obtained from space telescopes, such as those from the Kepler mission (Borucki et al. 2010), collected across Q0–Q16 quarters, each lasting approximately three months, frequently encounter gaps and uneven sampling. The latter arises from converting evenly sampled time stamps into Barycentric Julian Date, leading to nonuniform observation intervals. To address the challenges posed by irregular sampling, the Lomb–Scargle (LS) periodogram (Lomb 1976; Scargle 1982) is frequently employed as a reliable method for estimating the power spectrum. In the next stage, individual oscillation modes are identified and extracted in a process known as “peakbagging"

1. **Background Determination**

   A solar-like oscillator's power spectrum of a solar-like oscillator typically consists of a mix of power laws to model the granulation noise in the background along with a Gaussian envelope to represent the excess oscillation power. This approach is based on models proposed by Harvey (1985). The overall model for the power density spectrum in terms of ν, is expressed as:

$$\mathcal{M}_{\mathrm{PSD}}(\nu) = [P_{\mathrm{gran}}(\nu) + P_{\mathrm{Gauss}}(\nu)] \cdot R(\nu) + W$$

where each component is defined as follows:

The background signal due to granulation ($P_{\rm gran}(\nu)$) is modeled by the sum of r Lorentzian-type profiles:

$$P_{\rm gran}(\nu) = \sum_{i=1}^{r} \frac{2\pi a_i^2/b_i}{1 + (\nu/b_i)^{c_i}}$$

where a_i, b_i, and c_i are the amplitude, characteristic frequency, and slope for each component, respectively. Typically, two or three terms are used to represent granulation processes occurring at various timescales.

Harvey (1985) initially proposed using a Lorentzian function to describe solar granulation. Later, Carrier et al. (2010) and Kallinger et al. (2010) introduced an alternative model with a super-Lorentzian shape, featuring slopes greater than two, which provided a better fit. Kallinger et al. (2014) recommended using a slope of four for red giants, but allowed the value to vary between two and four, treating it as a free parameter during their fitting procedure to improve the model's accuracy.

The additional power resulting from oscillations($P_{\rm Gauss}(\nu)$) is modeled using a Gaussian function:

$$P_{\rm Gauss}(\nu) = P_g \exp\left(-\frac{(\nu - \nu_{\rm max})^2}{2\sigma_g^2}\right)$$

Here P_g, $\nu_{\rm max}$, and σ_g denote the amplitude, central frequency, and extent of the oscillation envelope, respectively. The constant instrumental Noise is denoted by W. To account for the effect of discrete sampling, the response function ($R(\nu)$) is included:

$$R(\nu) = \mathrm{sinc}^2\left(\frac{\pi\nu}{2\nu_{\rm Nyq}}\right)$$

This accounts for signal discretization, which may diminish the strength of both granulation and oscillation signals (see studies like Karoff et al. (2013)

and Kallinger et al. (2014)). Initial estimates of the parameters in the PSD model are obtained using a least-squares minimization approach. These estimates are further refined with a Markov Chain Monte Carlo (MCMC) method based on Bayesian inference algorithm for ensuring a more precise fit.

2. **Determining ν_{max} and $\Delta\nu$**

   The PSD was normalized by the noise spectrum to create the signal-to-noise ratio (SNR) periodogram. The autocorrelation function (ACF) of the PSD was used across multiple segments of the frequency spectrum to identify the range corresponding to the Gaussian envelope encompassing the power excess. This process involved several steps: first, the background was subtracted from the smoothed spectrum; second, the autocorrelation was applied to a segment of the smoothed background spectrum; third, a Gaussian curve was fitted to the average collapsed correlation within each segment; and finally, the frequency of the peak in the fitted Gaussian curve (ν_{max}) was identified. The next step involves calculating the large frequency spacing, denoted as $\Delta\nu$. To achieve this, the ACF of the power density spectrum was evaluated across a defined range of frequencies focused on $\nu_{\rm max}$. This range was determined by using some factor of an initial guess of $\Delta\nu$, which was obtained from a scaling relation using the previously obtained $\nu_{\rm max}$. This scaling relation, calibrated on a broad stellar sample by Stello et al. (2009), is expressed as :

$$\Delta\nu_{\rm estimate} = (0.263 \pm 0.009)\ \nu_{\rm max}^{0.772 \pm 0.005}.$$

   In this formula, $\Delta\nu_{\rm estimate}$ serves as the estimated value of $\Delta\nu$ from the scaling relation. A frequency range defined as $\nu_{max} \pm 2\Delta\nu_{\rm estimate}$ is subsequently directed into the ACF calculation for obtaining a refined measurement. Restricting the analysis to this range minimizes the impact of $\Delta\nu$ variations across different frequencies.

The next step involves identifying the ACF's maximum within a region around $\Delta\nu_{\text{estimate}}$ and refining it further by fitting a Lorentzian profile. This ensures that the final $\Delta\nu$value is independent of the ACF's frequency resolution. Similar to the PSD modeling, initial parameter estimates for the Lorentzian fit are obtained using least-squares (LS) minimization. These initial values are again refined through a Bayesian MCMC method, applying uniform priors on the parameters and using the likelihood function to guide the fitting process.

3. **Determining the average dipole period spacing**

After determining ν_{max} and $\Delta\nu$ with precision, individual oscillation modes are extracted and identified. Using the SNR periodogram as in the previous step, the modes are fitted for each radial order individually. Specifically, only the prominent modes within two successive radial-mode orders, n_p and $n_p + 1$, are considered. Any mode peak is deemed significant if its SNR exceeds seven times the mean SNR within the frequency band corresponding to that radial-mode order. The oscillation modes in SLOs are modeled using a Lorentzian profile (Kumar et al. 1988; Anderson et al. 1990), expressed as:

$$P_{\text{mode}}(\nu) = \frac{A^2/\pi\Gamma}{1 + 4\left(\frac{\nu-\nu_0}{\Gamma}\right)^2},$$

where A represents the amplitude, Γ is the full width at half maximum (FWHM), ν_0 is the peak frequency of the mode.

The PSD for s prominent oscillation modes within a radial order of a given mode is described as:

$$\mathcal{M}_{\text{order}}(\nu) = W + R(\nu) \cdot \left[P_{\text{gran}}(\nu) + \sum_{i=1}^{s} P_{\text{mode},i}(\nu) \right].$$

This formulation facilitates the identification of p-modes in the red giant spectrum. Pure g-modes, however, are undetectable due to their low amplitudes. As noted by Dupret et al. (2009), every $\ell = 1$ peak consists of

one pressure mode encircled by mixed modes, predominantly reflecting the g-mode characteristics.

Unidentified peaks in the spectrum are treated as potential dipole g-m modes and are used to obtain the period interval. The observed period spacing, defined as the time gap (given in seconds) between successive mixed dipole modes, is expressed as:

$$\Delta P = \frac{1}{\nu_{n_{\rm m}}} - \frac{1}{\nu_{n_{\rm m}+1}}.$$

The mean of these observed period intervals (separating atleast 6-7 consecutive ℓ =1 modes) is employed to assess the star's evolutionary stage in this analysis.

2.6.6 Data sources

1. ***Kepler*** :

   The NASA *Kepler* satellite was deployed on March 7, 2009, into a heliocentric orbit trailing Earth by about 0.5 AU. It carried a Schmidt telescope with a 0.95-meter aperture and a a field of view spanning 115 square degrees (pixel size: 4"). The spacecraft was equipped with a highly sensitive photometer covering a spectral range of 400 to 850 nm. This photometer consisted of 42 science CCD modules, each containing two CCDs with dimensions of 2200×1024 pixels, as well as four fine guider sensor CCDs. Each module surveyed 5 square degrees of the sky.

   To ensure optimal coverage, the spacecraft rotated 90 degrees every 93 days, a process termed the quarterly roll, shifting stars between CCDs. The mission aimed to monitor approximately 100,000 stars brighter than 14th magnitude continuously and simultaneously. Kepler remained fixed on the constellations Cygnus and Lyra throughout its primary mission, which was

originally planned for 3.5 years. Data for all targets were captured at intervals of 6.52 seconds and aggregated 270 times, resulting in 29.4 minute intervals referred to as Long Cadence (LC) measurements. A smaller selection of up to 512 targets was aggregated 9 times to form 58.8 second measurements which are available as Short Cadence (SC) data."

The Kepler photometer's full field of view spanned 116 square degrees, focusing on a single sky region during the primary mission. Although Kepler's primary objective was detecting transiting Earth-like exoplanets, its high-precision data proved valuable for asteroseismology, including studies of low-amplitude solar-like oscillations. After the spacecraft's pointing control systems failed, the mission was re-branded as K2. Despite these challenges, it continued to detect exoplanets by observing as its field of view drifted across the sky. The mission officially concluded in 2018.

2. ***TESS*:**

The Transiting Exoplanet Survey Satellite (*TESS*; Ricker et al. (2015)), a mission funded by NASA under the Astrophysics Explorer program, is tasked with conducting a nearly complete sky survey, focusing on planets transiting stars that are relatively bright and in close proximity to our solar system. Launched on April 18, 2018, TESS aimed to monitor the brightness of hundreds of thousands of low-mass, main-sequence stars during its two-year primary mission. Observation durations ranged from one month to one year, primarily determined by a star's ecliptic latitude. Selected target stars were observed with a 2-minute cadence, while full-frame images (FFIs) were captured every 30 minutes. *TESS* targets are significantly brighter than those of *Kepler*, with brightness values ranging from 10 to 100 times greater, and are spread across an area that is nearly 300 times larger.

The mission's high photometric precision, combined with fine time resolution and extended observation periods, has facilitated asteroseismic studies of stars similar to the Sun and red giants, which exhibit oscillation periods from

a few minutes to several hours. *TESS* divided the sky into 26 observation sectors, with 13 sectors assigned to each hemisphere of the ecliptic plane, observing every region for a period of 27.4 days (equivalent to two full orbits of the spacecraft). While most of the sky (92%) was monitored for 1–2 sectors, *TESS* nearly covered the entire celestial sphere.

The *TESS* Asteroseismic Science Consortium (TASC; Lund et al. (2017)) established the "*TESS* Data for Asteroseismology" (T'DA) initiative to provide light curves suitable for asteroseismic studies. This includes data from both full-frame images and Target Pixel Files (TPFs). These light curves are processed through a custom-built, open-source pipeline, with the resulting data made accessible via the *TESS* Asteroseismic Science Operations Center (TASOC) database and the Mikulski Archive for Space Telescopes (*MAST*).

2.6.7 Software/Codes

For downloading and analyzing asteroseismic data we used the following :

1. **Lightkurve :** Lightkurve[1] is an open-source Python library created by the community, providing an intuitive tool for analyzing flux time series data. It is specifically designed to handle pixels and lightcurves collected by NASA's *Kepler* and *TESS* missions focused on exoplanets. This study utilized Lightkurve to download lightcurves from MAST for analysis or to generate custom lightcurves from target pixel files. By applying simple aperture photometry, it allows users to minimize contamination from nearby sources or enhance the desired signal relative to the background. Additionally, it facilitates tasks such as eliminating long-term trends, removing outliers through

sigma clipping, handling infinite or NaN values, folding data at a specific period, and reducing the time resolution of the dataset.

2. **pySYD :** pySYD[2] is an open-source Python tool designed to identify solar-like oscillations and measure their global characteristics automatically. It is a Python version of the original SYD code (Huber et al. 2009), which was developed in IDL.

3. **FAMED :** The FAMED[3] pipeline (Fast and Automated pEak bagging with Diamonds) works across different platforms. It is a parallelized tool designed for automatically extracting and identifying oscillation frequencies in stars exhibiting solar-like pulsations. It utilizes the DIAMONDS code, which implements Bayesian parameter estimation and model selection using a nested sampling approach based on Monte Carlo (NSMC) techniques. The pipeline is versatile and can analyze a wide range of stars, including hot F-type main-sequence and subgiant stars to the red giants, as well as stars in the helium core-burning stage, or transitioning to the early asymptotic giant branch. Organized into distinct modules, each part of the pipeline handles specific tasks with varying levels of detail.

[1] https://github.com/lightkurve/lightkurve
[2] https://github.com/ashleychontos/pySYD
[3] https://github.com/EnricoCorsaro/FAMED

Chapter 3

Investigating Infrared Excess and Lithium Enhancement in Red Clump Giants

3.1 Overview

The results discussed in this chapter are outlined in Mallick et al. (2022)). Here we focus on exploring the potential connection between Li enrichment and infrared (IR) excess among RC and upper RGB stars. Lithium enrichment in low-mass red clump stars, is a known anomaly that defies standard stellar evolution models. While the mechanism behind this enhancement remains debated, one hypothesis suggests that mass loss, triggered by mergers or interactions, may play a role. Specifically, mergers involving helium white dwarfs or other stellar companions could induce a helium flash, leading to both mass ejection and Li production.

To investigate this hypothesis, we analyze a sample of RC and upper RGB giants

drawn from the GALAH DR3 survey, which provides high-resolution optical spectra and stellar parameters, including Li abundances. Infrared photometric data from the Wide-field Infrared Survey Explorer ($WISE$) program and the Two Micron All Sky Survey ($2MASS$) are used to probe the presence of IR excess, which could indicate mass loss events. The goal of this study is to determine whether there is a relationship between lithium enrichment and infrared excess, which might suggest external events such as mergers are responsible for the observed lithium anomalies in certain giants. We also explore the rotational velocities of these stars to understand whether rapid rotation, potentially resulting from mergers, is linked to lithium enrichment.

3.2 Criteria for Sample Selection and Data Sources

The working sample consists of low mass RC and upper RGB stars from the GALAH DR3 survey, which provides high-resolution optical spectra (R=28,000), stellar parameters, and elemental abundances, including lithium. To investigate the possible link between lithium enhancement and infrared excess, we cross-matched this sample with near-IR fluxes from 2MASS and mid-IR fluxes from WISE.

To ensure data quality, the following criteria were applied to our sample:

- Uncertainty in effective temperature ($\Delta T_{\rm eff}$) $\leq$ 100 K
- Positive parallaxes with fractional parallax error ($\frac{\sigma_\omega}{\bar{\omega}}$) ≤ 0.15
- Stellar masses $\leq$ 2 $M_\odot$, estimated from the stellar parameters

The stellar mass was computed as follows:

$$\frac{M}{M_{\odot}} = 10^{\left[\log\left(\frac{L}{L_{\odot}}\right)+\log g-\log g_{\odot}+4\times\log\left(\frac{T_{\rm eff\odot}}{T_{\rm eff}}\right)\right]}$$

where $\log g_{\odot} = 4.44$ dex, $T_{\rm eff,\odot} = 5772$ K are the adopted solar values. Luminosity (L) was derived from Gaia parallaxes and G-band magnitudes using:

$$\log\left(\frac{L}{L_{\odot}}\right) = M_G + BC_G(T_{\rm eff}) - M_{bol\odot}$$

where the absolute magnitude in G-band is given as

$$M_G = G + 5 - 5\log_{10} r - A_G$$

and the temperature dependent bolometric correction is : explain below equation :

$$BC_G(T_{\rm eff}) = \sum_{i=0}^{4} a_i (T_{\rm eff} - T_{\rm eff,\odot})^i$$

$M_{bol\odot} = 4.74$ for the Sun, r denotes the distance from the star (in parsec) and A_G is the interstellar extinction in G-band. Given the lack of uniform extinction values for the sample, corrections were only applied where available from the Gaia catalogue.

The final sample included 957 RC giants and 518 upper RGB giants. The sample regions were defined in the Hertzsprung-Russell diagram as follows:

- RC: 4500 K $\leq$ $T_{\rm eff}$ $\leq$ 4800 K and 1.6 $L_{\odot}$ $\leq$ L $\leq$ 1.75 $_{\odot}$
- Upper RGB: 4100 K $\leq$ $T_{\rm eff}$ $\leq$ 4400 K and 1.65 $L_{\odot}$ $\leq$ L $\leq$ 2.2 $L_{\odot}$.

These criteria minimized contamination between RC and RGB giants. The selection is shown in Figure 3.1, where the stars' distribution is plotted on the HR diagram.

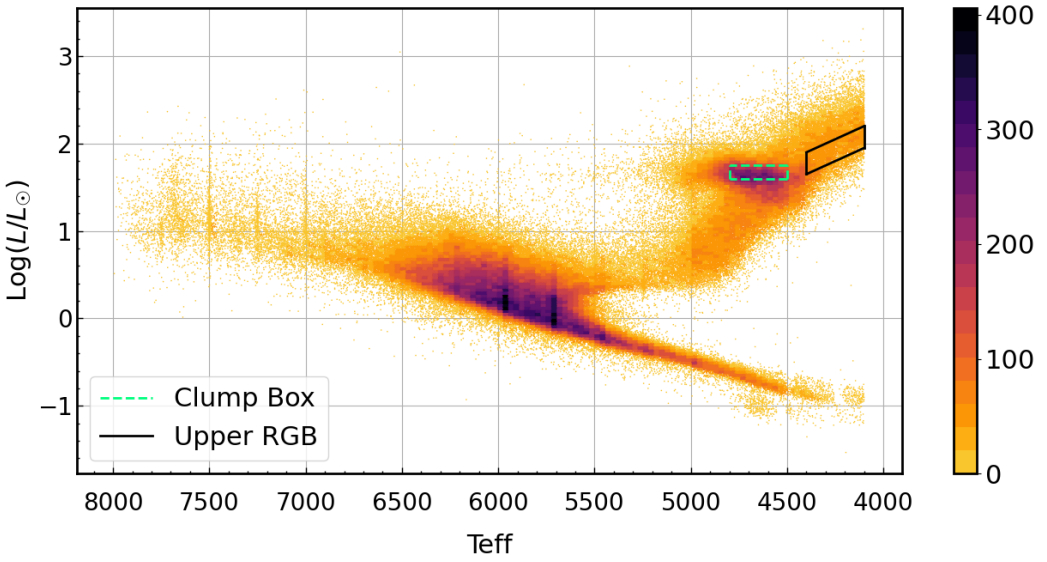

FIGURE 3.1: HR-diagram displaying the giant samples from GALAH data (green dotted box for the red clump, black box for the upper RGB).

3.3 Overlap of RGB and RC Stars in the HR Diagram

In Fig. 3.1, the color bar indicates the star density, with darker shades corresponding to regions of greater star concentration. The RC giants were selected to minimize contamination by the RGB sample. However, due to uncertainties in stellar parameters and similarities in T_{eff} and $\log g$ between RC and RGB giants, a minor overlap between the two is unavoidable. To evaluate contamination levels, we compared our RC giants with the sample from Vrard et al. (2016), which used asteroseismic analysis to determine evolutionary phases. The Vrard et al. (2016) sample is shown in a seismic diagram of g-mode period spacing (ΔP) versus large-frequency spacing ($\Delta\nu$) (see Fig. 3.2). In ΔP, RGB giants (green symbols) are distinct from RC giants (red symbols), though there is some overlap at the lower frequency end.

Our selected GALAH giants do not overlap with the Vrard et al. (2016) dataset. However, 96 RC giants from our sample match entries in a larger catalog of half a

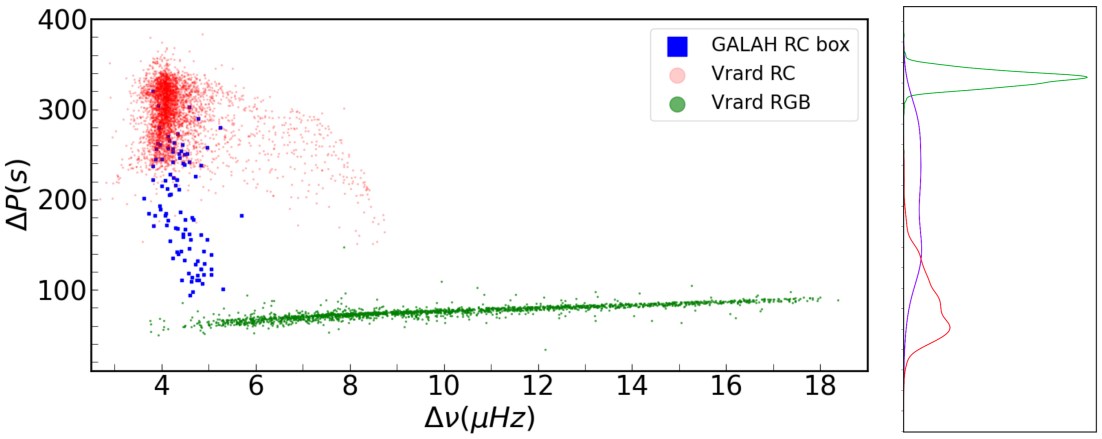

FIGURE 3.2: Evaluation of the overlap between RC and RGB samples in our GALAH selection, comparing with the RC (red) and RGB (green) data from Vrard et al. (2016), where evolutionary phases were determined through asteroseismic methods. The 96 giants (blue) from our GALAH sample, classified using secondary calibration, are marked

million RC giants (Lucey et al. 2020), where ΔP and $\Delta\nu$ were estimated using secondary calibration based on a neural network applied to stellar SEDs and spectra from LAMOST DR3 and APOGEE DR14 (Ting et al. 2018). Fig. 3.2 compares the 96 RC giants (blue symbols) from our sample with the Vrard et al. (2016) RGB giants (green) typically show a mean ΔP of approximately 80 s with a standard deviation around 20 s, suggesting that giants with $\Delta P > 100$ s are more likely to be RC stars. Of the 96 RC giants (blue) in our GALAH sample, only four to five overlap with RGB giants (green), indicating about 5% contamination of the RC sample by RGBs. Kumar et al. (2020) performed a similar analysis, estimating around 10% contamination in GALAH RC by RGB. The difference may be due to a stricter box for RC selection and better calibrated GALAH DR3 data.

3.4 Lithium Abundance in Red Clump and RGB Stars

Lithium abundances for our sample were extracted from the GALAH DR3 survey, which provides A(Li) values derived from the Li I 6707.8 Å resonance doublet. Lithium abundance A(Li) is defined as:

$$A(Li) = 12 + \log_{10} \frac{n(Li)}{n(H)}$$

where n(Li) and n(H) denote the atomic number densities for lithium and hydrogen, respectively. In GALAH DR3, Li abundances are given relative to iron ([Li/Fe]). The solar Li abundance is given as $A(Li)_{\odot} = 1.05$ dex (Buder et al. 2021). The total lithium abundance is computed as:

$$A(Li) = [Li/Fe] + [Fe/H] + A(Li)_{\odot}$$

Uncertainties in A(Li) are propagated as:

$$\sigma_{A(Li)} = \sqrt{\sigma^2_{[Li/fe]} + \sigma^2_{[Fe/H]} + \sigma^2_{A(Li)_{\odot}}}$$

Lithium abundance distributions for upper RGB giants and RC stars are shown in Figure 3.3. The RC stars exhibit a peak A(Li) of 0.62 dex, whereas RGB stars peak around 0.15 dex, consistent with expected Li depletion during their ascent up the RGB. However, about 2.3% of RC stars are classified as super Li-rich (SLR), with $A(Li) \geq 3.2$, indicating recent lithium enrichment. This distribution is in agreement with previous studies by Kumar et al. (2020) and Singh et al. (2021)

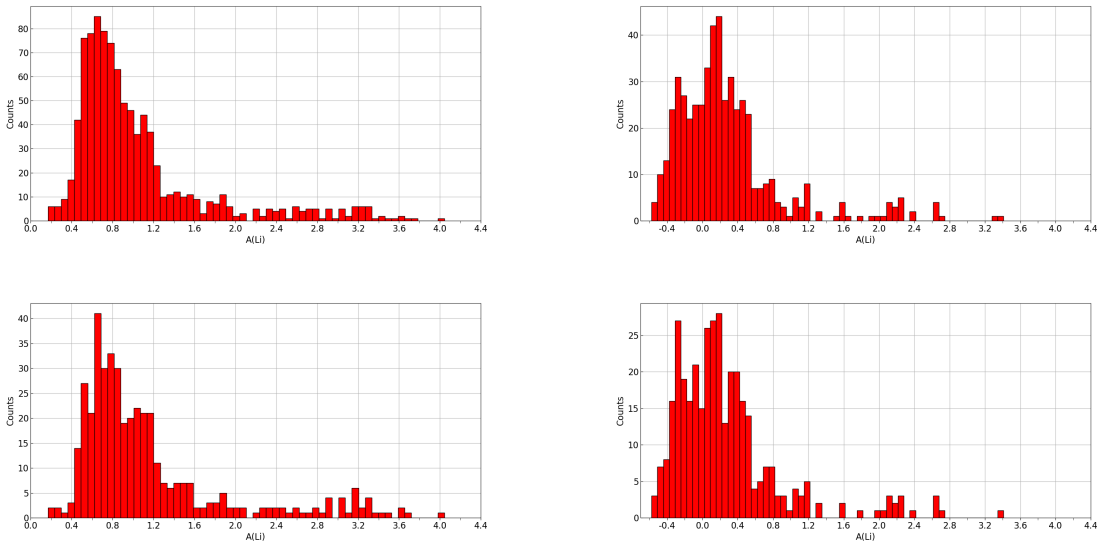

FIGURE 3.3: Li abundance distribution within our RC and RGB samples. The top panels display the Li distribution for the full RC (left) and RGB (right) samples, while the bottom panels show the distribution for RC giants (left) and RGB giants (right) with available mid IR data

3.5 Infrared Excess

We used infrared data from 2MASS and WISE to search for IR excess, which could indicate mass loss through events like mergers or binary interactions. IR excess is typically associated with circumstellar dust. We constructed color-color diagrams for both the RC and RGB stars using 2MASS J, H, and K bands, and WISE W1, W2, W3, and W4 bands (see Fig. 3.4)

Stars that fall outside theoretical zero-excess regions are considered to exhibit IR excess. The color between two wavelengths, λ_1 and λ_2 was calculated using:

$$[\lambda_1 - \lambda_2] = -\log\left[\left(\frac{\lambda_1}{\lambda_2}\right)^{\alpha}\left(\frac{B_{\lambda_1}}{B_{\lambda_2}}\right)\left(\frac{f_{\lambda_2}}{f_{\lambda_1}}\right)\right]$$

where B_{λ_1} and B_{λ_2} are the Planck functions at the corresponding wavelengths for a given $T_{\rm eff}$ and f_{λ_1} and f_{λ_2} are the zero-point flux densities. The spectral index α accounts for deviations from a blackbody spectrum and was varied to cover all

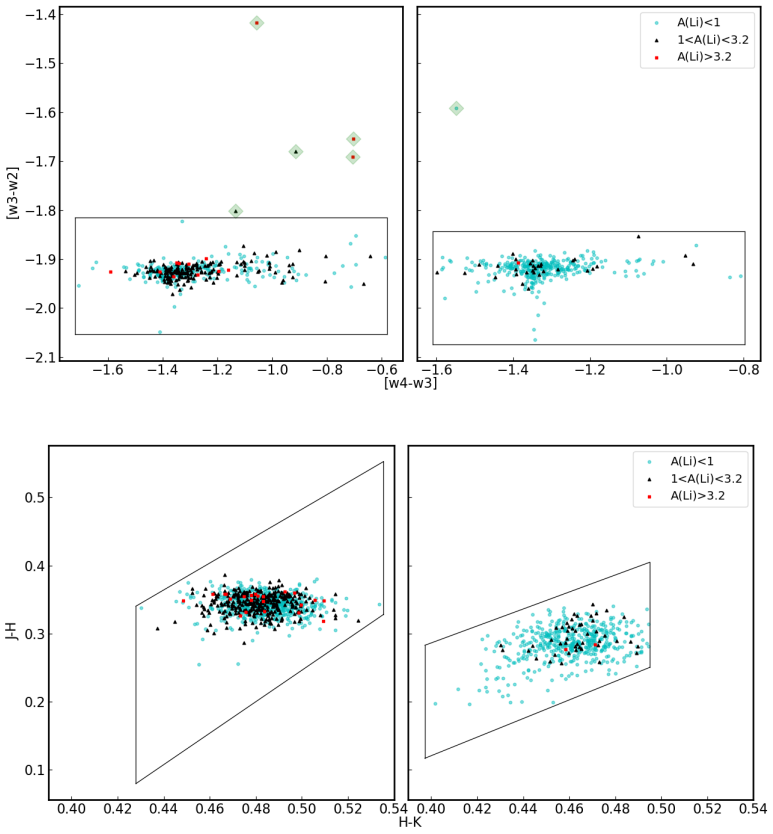

FIGURE 3.4: CCDs for WISE mid-IR (top) and 2MASS near-IR (bottom) colours. RC giants are shown in the left panels, and RGB giants in the right panels. Boxes indicate regions without IR excess. Only six giants in the mid-IR panels lie outside these boxes, showing IR excess.

zero-excess stars. The zero-excess regions were calculated by setting $\alpha = 1$ for near-IR colors and α =3 for mid-IR colors.

Out of the entire sample, 418 red clump (RC) stars and 359 red giant branch (RGB) stars had both 2MASS and WISE photometric data. However, infrared excess was detected only in the WISE data, and none of the stars from the 2MASS photometry showed signs of IR excess. Among the stars showing infrared excess, five red clump giants and one RGB giant were identified. These results suggest that infrared excess is a relatively rare phenomenon among giants. Interestingly, of the five RC stars with IR excess, three were super Li-rich and two were Li-rich (defined as A(Li) $\geq$ 1.0), reinforcing the idea that there could be a potential link between Li enhancement and the presence of circumstellar dust resulting from

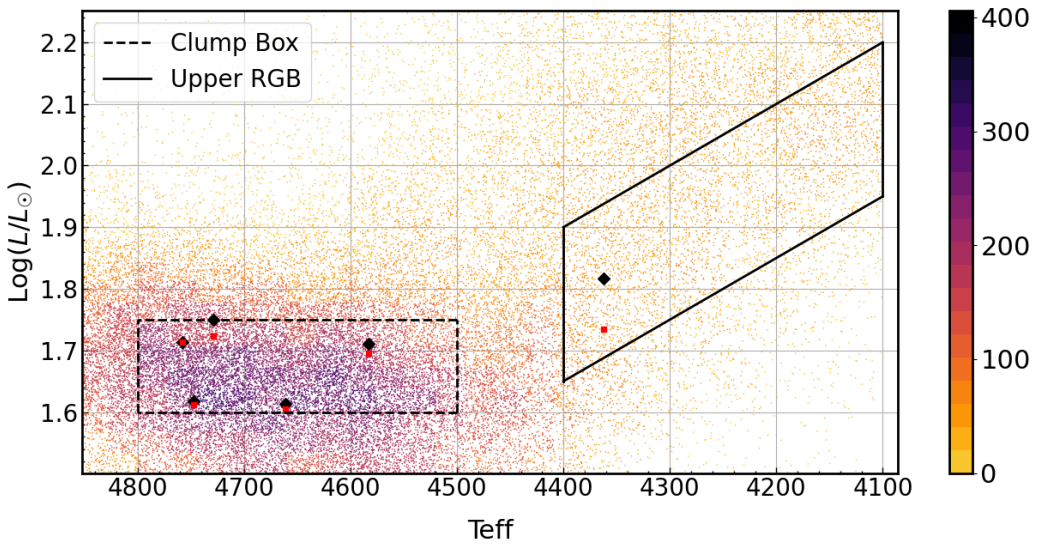

FIGURE 3.5: H–R diagram displaying sample stars, with RC and upper RGB areas marked. Six giants with IR excess are shown as red squares (before extinction correction) and black diamonds (after correction). The evolutionary status of these giants remains unaffected.

mass loss.The lack of IR excess in 2MASS data, which covers shorter wavelengths, implies that the dust surrounding these stars is cooler and more easily detectable in the mid-IR WISE bands (W3 and W4).

The presence of IR excess, especially in super Li-rich stars, implies that mass loss has occurred recently, possibly due to merger events involving helium white dwarfs. These mergers could trigger the helium flash, leading to both Li enrichment and mass loss, as suggested by Zhang & Jeffery (2013). An in-depth discussion on IR excess can be found in Section 3.6.

As mentioned earlier, interstellar extinction corrections were not applied to the sample due to the lack of A_G values for many giants. High extinction levels can lead to misidentifying the evolutionary phase of stars. Fortunately, all six giants showing IR excess have A_G values provided in the Gaia catalogue. The largest correction is for the upper RGB star BD-19 4687, with an AG of 0.98, causing an uncertainty of 0.08 in both $\log\left(\frac{L}{L_\odot}\right)$ and mass. As depicted in Fig. 3.5, none of

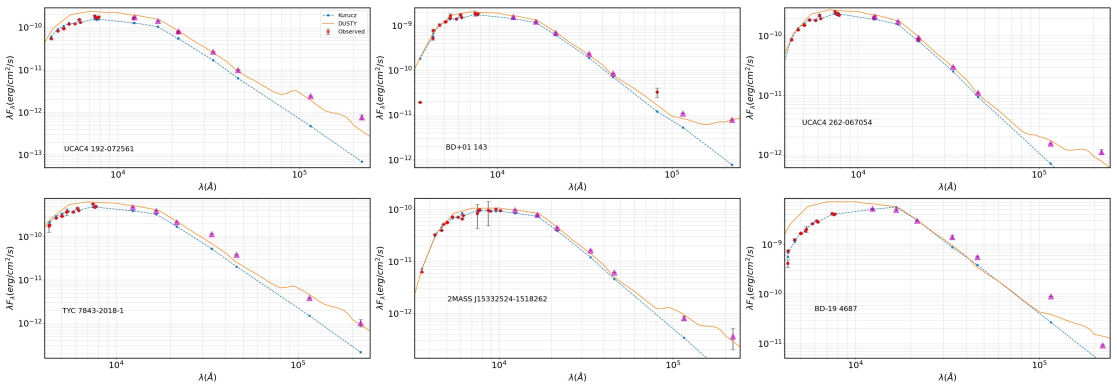

FIGURE 3.6: SEDs of giants showing IR excess, modeled with dusty fits. Stellar atmospheric SEDs use Kurucz models. Triangles represent IR bands (2MASS: J, H, K; WISE: W1, W2, W3, W4).

the six giants change their evolutionary classification after applying the extinction corrections.

3.6 Dust Shell Modeling and Mass Loss

To model the IR excess in these stars, we used DUSTY (Ivezic et al. 1999), a FORTRAN code that solves the radiative transfer equation under LTE assumptions. It assumes a spherically symmetric dust shell around the star, composed of astronomical silicates. For the six giants displaying IR excess in WISE bands, SEDs were built from observed photometric data across optical and IR bands and were compared to model SEDs. The observed SED accounts for both the stellar photosphere and surrounding dust shell. The stellar input SED was taken from Castelli & Kurucz (2004) models which are a collection of 4300 LTE photospheric models with different $T_{\rm eff}$, $\log g$, and [Fe/H]. Dust properties, including grain sizes (a_{min} = 0.005 μm, a_{max} = 0.25 μm), dust temperature at the inner edge of the dust shell (T_{inner}), and optical depth in the visible band (τ_v), were derived from the observed infrared fluxes. Fig. 3.6 presents the SEDs of these six stars with IR excess, along with photospheric model atmosphere contributions. The model

stellar parameters ($T_{\rm eff}$, $\log g$, [Fe/H]) are sourced from GALAH DR3. Optical and infrared flux densities for each star were retrieved using the filter repository of VOSA (Virtual Observatory SED Analyzer), created by the Spanish Virtual Observatory project.

The mass loss rate was estimated using the formula (de La Reza et al. 1996):

$$\dot{M} = \frac{16\pi}{3}\left(\frac{\rho_d}{\psi}\right)\left(\frac{a}{Q_\lambda}\right)\tau_v V_s R_{in}$$

where ρ_d denotes density of the grain (3 g.cm^{-3}), ψ is dust-to-gas ratio (4.3×10^{-3}), Q_λ represents the absorption coefficient, a denotes the size of the grain, V_s is the wind velocity (2km/s), and R_{in} is the inner radius of the dust shell. The expression $\left(\frac{a}{Q_\lambda}\right)$ equals $\frac{\lambda}{12.6}$ μm in the thermal infrared region. The DUSTY code-derived R_{in} corresponds to a stellar luminosity of 10^4 L$\odot$. Scaling R_{in} with ($R_{in} \propto L^{1/2}$) the actual luminosity of the giants and substituting the parameters simplifies the mass-loss relation to:

$$\dot{M} = 1.62 \times 10^{-22}\tau_v R_{in} \;\; M_\odot.yr^{-1}$$

Mass-loss rates $\dot{M}$ calculated from DUSTY models for each giant are compared against the corresponding values determined from the modified Reimers' Law (Schröder & Cuntz 2005) based on the stellar parameters (provided by GALAH or estimated in this work):

$$\dot{M}_R = \frac{\eta L_* R_*}{M_*}\left(\frac{T_{\rm eff}}{4000}\right)\left(1 + \frac{g_\odot}{4300 g_*}\right)$$

The stellar parameters (L_*, R_*, M_*, g_*, and $T_{\rm eff}$) are presented in Table 3.1.

The kinematic age of the dust shell, giving the time since the mass-loss event, is calculated using:

$$t_{kin} = \frac{R_{inner}}{V_s}$$

Star	T_{eff} (K)	logg	Luminosity ($L_\odot$) (extinction corrected)	Radius ($R_\odot$) (extinction corrected)	A(Li) (dex)	Classification
UCAC4 192-072561	4661.60	2.34	41.01	10.06	4.04	RC
BD+01 143	4747.72	2.41	40.93	9.29	3.66	RC
UCAC4 262-067054	4757.81	2.45	51.78	10.63	3.31	RC
TYC 7843-2018-1	4728.81	2.31	56.14	12.05	1.59	RC
2MASS J15332524-1518262	4583.01	2.29	49.55	10.67	1.41	RC
BD-19 4687	4362.29	1.80	65.56	16.68	0.29	RGB

TABLE 3.1: Stellar parameters of 6 IR-excess giants

Star	T_{inner} (K)	τ_v	T_d (K)	R_{in} (cm)	t_d (years)	$\dot{M}$ ($M_\odot.yr^{-1}$) (DUSTY)	$\dot{M}_R$ ($M_\odot.yr^{-1}$) (Reimer's Law)
UCAC4 192-072561	500	4.00E-2	194	5.92E14	93.85	3.83 ± 0.03E-9	5.19 ± 0.39E-11
BD+01 143	100	4.12E-2	52	2.50E16	3963.22	1.67 ± 0.01E-7	4.33 ± 0.06E-11
UCAC4 262-067054	225	3.00E-2	107	2.91E15	461.32	1.41 ± 0.01E-8	4.70 ± 0.12E-11
TYC 7843-2018-1	440	2.85E-2	179	7.40E14	117.31	3.41 ± 0.09E-9	7.58 ± 1.34E-11
2MASS J15332524-1518262	300	4.00E-2	136	1.45E15	229.87	9.39 ± 0.02E-9	5.40 ± 0.39E-11
BD-19 4687	150	1.25E-2	75	6.92E15	1097.02	1.40 ± 0.12E-8	2.79 ± 1.17E-10

TABLE 3.2: Dust shell parameters obtained from the DUSTY code for giants showing IR excess.

The calculated ages range from several hundred to a few thousand years, indicating that the mass-loss events occurred recently. Table 3.2 lists the optimal model parameters for the giants with IR excess. Mass-loss uncertainties are assessed based on the Gaia parallax uncertainties. Table 3.2 indicates that rates obtained from dusty modeling are 2–4 times greater than those predicted by Reimer's relation for the evolutionary phase of these giants. This implies that the IR-excess giants may have undergone merger events in the recent past, leading to significant mass loss. The calculated values of t_d for the dust shells suggest circumstellar envelope ages of less than 4000 years (refer to Table 3.2).

3.7 Asymmetrical Distribution of Circumstellar Dust

The DUSTY models used in this study assume that the dust shell is spherically symmetric, which is a reasonable approximation if the mass depletion is owed to internal stellar processes. However, if the mass loss is caused by external events, such as the merger of a helium white dwarf with the helium-inert core of a red giant, the geometry of the dust shell is expected to be asymmetric. This may result in torus-shaped or disk-like structures around the star, rather than a spherical distribution (Lynden-Bell & Pringle 1974).

To probe the asymmetry of the circumstellar dust, we used the flux ratios in the WISE infrared bands to fit the observed data. The relationship between the flux densities at different wavelengths, λ_1 and λ_2, is given by:

$$\frac{F_{\lambda_1}}{F_{\lambda_2}} = \left(\frac{\lambda_2}{\lambda_1}\right)^{\beta} \frac{B_{\lambda_1}(T_d)}{B_{\lambda_2}(T_d)}$$

where $B_{\lambda_1}(T_d)$ and $B_{\lambda_2}(T_d)$ are the Planck functions at wavelengths λ_1 and λ_2 for a dust temperature T_d, and β is the opacity index. By fitting the WISE flux ratios for the stars in our sample, we obtained values for β, which are listed in Table 3.3 of the study.

The value of β is typically between 1 and 2 for dust shells that are spherically symmetric with sub-micron-sized grains (Muthumariappan et al. 2006). In contrast, the observed values of β for two of the stars in our study (BD-19 4687 and BD+01 143) were much lower, with $\beta = 0.04$ and $\beta = -1.42$ respectively. Such low values of β suggest that these stars have asymmetric dust distributions, likely resulting from external events such as mergers. These asymmetrical structures could be torus-like, where dust is concentrated in the equatorial plane of the star,

Star	β	v_{sini} km.s^{-1}
This work		
UCAC4 192-072561	2.71	10.16
BD+01 143	-1.42	10.15
UCAC4 262-067054	1.53	6.07
TYC 7843-2018-1	2.44	9.42
2MASS J15332524-1518262	2.12	8.61
BD-19 4687	0.04	6.87
Kumar et.al. 2015		
HD 233517	1.41	17.6
HD 219025	2.40	23.0
HD 19745	2.18	3.0
IRAS 13539-4153	2.80	5.0
IRAS 17596-3952	2.48	35.0
IRAS 13313-5838	2.61	20.0
PDS 100	2.75	8.3

TABLE 3.3: Values for the opacity index β and v_{sini} of IR-excess giants analyzed in this study are provided. Only β values were derived for giants reported in Bharat Kumar et al. (2015). The v_{sini} data were sourced from original publications: HD 233517 (Charbonnel & Balachandran 2000), HD 219025 (Jasniewicz et al. 1999), HD 19745, IRAS 13313-5838, IRAS 13539-4153, IRAS 17596-3952 (Reddy & Lambert 2005), IRAS 13313-5838 (Drake et al. 2002), and PDS 100 (Takeda & Tajitsu 2017)

or more complex, non-spherical configurations (Lynden-Bell & Pringle 1974)

The opacity index β is distinct from the spectral index α used in spectral energy distribution (SED) fitting, though the two are related by

$$\alpha = \beta + 2$$

The majority of stars showed values of β consistent with a symmetric, spherically distributed dust shell, while the two aforementioned stars showed clear evidence of asymmetry.

3.8 Stellar Rotation and Rapid Rotators Among Li-rich Stars

Literature suggests that the additional lithium observed in certain low-mass giants could result from rotation-induced extra mixing (Charbonnel & Lagarde 2010). Additionally, merger scenario studies indicate elevated rotation rates and IR excess (Kamath et al. 2016; Ceillier et al. 2017). The potential role of stellar rotation in Li enrichment is explored by analyzing the rotational velocities (v_{sini}) of our sample. High rotational velocities are often linked to enhanced mixing in stellar interiors, which can transport lithium from deeper layers to the outer regions. GALAH DR3 provides velocity broadening parameters (v_{broad}), which include contributions from both rotational and macroturbulent velocities (v_{mac}). To isolate v_{sini}, we used:

$$v_{broad} = \sqrt{v_{sini}^2 + v_{mic}^2 + v_{mac}^2}$$

The GALAH survey provides v_{mic}, and an average v_{mac} of 3 km s^{-1} has been assumed based on Carney et al. (2008). Fig. 3.7 displays the $v \sin i$ distributions

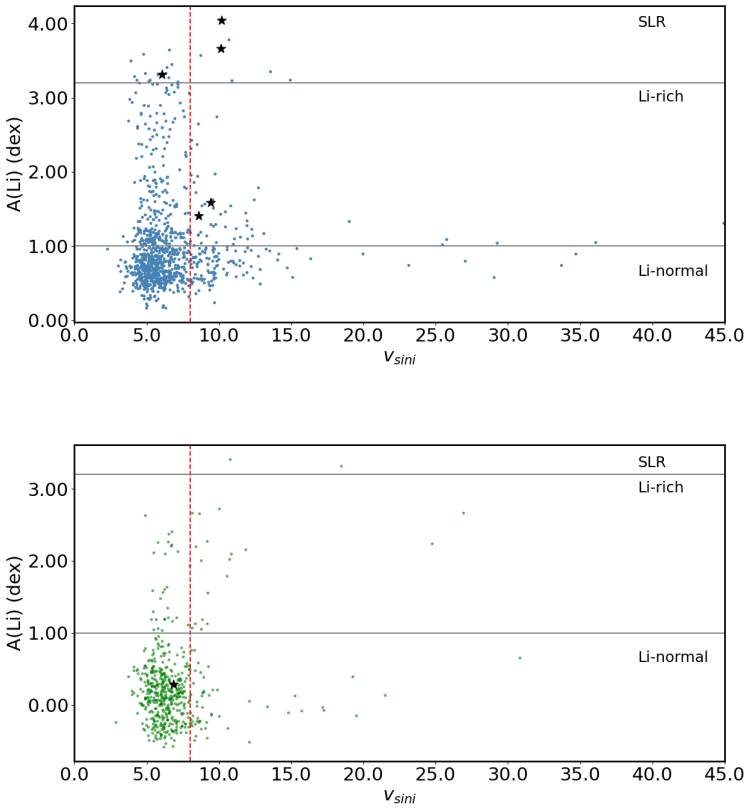

FIGURE 3.7: Distribution of Li abundances and $v \sin i$ for RC stars (top panel) and RGB stars (bottom panel). Stars with IR excess are marked with * symbols.

alongside A(Li) for both RC and RGB stars. The majority in each group falls within the range of 5 to 10 km s^{-1}. Based on Drake et al. (2002), stars with $v \sin i > 8$ km s^{-1} are classified as rapid rotators. The probability of identifying rapid rotators in RC stars is p(rr, RC) = 0.18 (168 out of 957 stars), and for RGB stars, p(rr, RGB) = 0.14 (73 out of 518 stars), aligning with findings from Martell et al. (2021). However, for sample 2 giants with WISE IR colours, the probability is 0.13 (53 out of 417) for RCs and 0.18 (64 out of 357) for RGBs (see Table 3.4). No clear pattern emerges distinguishing rapid rotators in RCs versus RGBs or those with versus without mid-IR colours. Although higher average $v \sin i$ might be expected for RCs due to post-He-flash contraction, four of the five RC giants showing IR excess are rapid rotators, making this about 5–6 times more likely compared to non-IR-excess giants. This suggests that external interactions, such as mergers, may impart angular momentum, increasing rotational velocities and

	RC	RGB	Total
With A(Li)	957	518	1475
with 2MASS (sample 1)	957	518	1475
With WISE (sample 2)	418	359	777
Sample 1			
v_{sini}	957	518	1475
rapid rotator	168	73	241
excess	0	0	0
Sample 2			
v_{sini}	417	357	774
rapid rotator	53	64	117
excess	5	1	6

TABLE 3.4: v_{sini} and excess statistics of sample giants.

enhancing mixing. Note that $v \sin i$ values might have greater uncertainty due to the relatively low resolution and underlying assumptions in their derivation. It remains essential to measure $v \sin i$ for IR-excess and Li-rich giants using high-resolution spectra (R $\geq$ 60,000).

3.9 Discussion: Mechanisms for Lithium Enhancement

To further understand the connection between lithium enrichment and infrared excess a quantitative comparison was performed to evaluate the frequency of lithium enhancement among stars with and without infrared excess. IR excess was detected in six giants, of which five were red clump (RC) stars and one was a red giant branch (RGB) star. Among the RC stars with IR excess, all five were Li-rich

Group	RC (percent)	RGB (percent)	Total
Sample 1 (having $2MASS$ fluxes)			
Li-normal	629 (65.7)	469 (90.5)	1098
Li-rich	306 (31.9)	47 (9.1)	353
SLR	22 (2.3)	2 (0.4)	24
Sample 2 (having both $2MASS$ and $WISE$ fluxes			
Li-normal	241 (57.6)	326 (90.8)	567
Li-rich	164 (39.2)	32 (8.9)	196
SLR	13 (3.11)	1(0.29)	14

TABLE 3.5: Lithium distribution among RC and RGB stars from samples 1 and 2

(A(Li) $\geq$ 1.0), including three that were super Li-rich (A(Li) $\geq$ 3.2). By contrast, among the 952 RC stars without IR excess, only 304 ($\sim$31.9%) were Li-rich and 19 ($\sim$2.0%) were super Li-rich. Among RGB stars, 47 of 517 ($\sim$9.1%) without IR excess were Li-rich and only 2($\sim$0.4%) were super Li-rich, while the single IR-excess RGB star was Li-normal. This indicates a significant over-representation of Li-rich stars in the IR-excess group. These results are summarized in Table 3.5. The contrast is particularly striking in the case of super Li-rich RC giants, where the frequency increases from $\sim$2% in the non-IR-excess group to 60% among IR-excess stars. Although the total number of IR-excess stars is small, this degree of over-representation strongly suggests a physical correlation between Li enhancement and the presence of circumstellar material. Previous studies (e.g., de la Reza et al. (1997); Bharat Kumar et al. (2015)) have shown that IR excess is generally uncommon in cool red giants. Our results support this but further reveal that when IR excess does occur, it is frequently associated with Li-rich stars, especially in the red clump phase.

In our study, infrared excess was identified in five out of 418 RC giants, resulting in a 1.2% occurrence rate for IR excess among RC stars. In contrast, only one out

of 359 RGB stars exhibited IR excess, corresponding to just 0.3%. These findings are consistent with the 1.4% RC giants and 1.3% RGB giants reported in the survey by Martell et al. (2021). However, our study shows a smaller percentage of RGB giants with IR excess, which could be attributed to differences in the sample selection criteria. While Martell et al. (2021)'s RGB sample included stars across the entire RGB phase, our study focused on upper RGB stars. Additionally, their sample contained more massive giants, which could evolve more rapidly and potentially retain some dust from their pre-main-sequence stages.

Furthermore, our findings align with those of Bharat Kumar et al. (2015), who found 0.5% of giants with IR excess and Martell et al. (2021), who reported 0.8% of giants with IR excess, using similar WISE mid-IR data. This suggests that while IR excess is relatively rare in giants, it is more commonly observed in RC stars than RGB stars, which aligns with the hypothesis that mass loss occurs more frequently during the RC phase, particularly in stars undergoing lithium enrichment.

Our findings suggest two possible mechanisms for lithium enhancement in RC giants:

1. **In-situ Li Production:** Most lithium-rich RC stars without IR excess likely experienced internal Li production during the helium flash. These stars exhibit normal rotational velocities, indicating no external interactions.
2. **Merger-induced Li Enrichment:** Zhang et al. (2020b) proposed a detailed model to explore the potential for lithium production triggered by the merger between a helium white dwarf (HeWD) and a red giant. In such mergers, the HeWD spirals inward due to drag within the common envelope. Once it merges with the He core of the giant, the merger triggers a delayed helium flash, causing energy to be released. This event initiates the Cameron–Fowler mechanism, where lithium is synthesized and the mixing

processes transport lithium to the surface of the star. These mergers could also result in rapid rotation, which enhances internal mixing, leading to the dredge-up of lithium from deeper layers of the star to its surface. The high v_{sini} values found in Li-rich giants with IR excess provide further support for this scenario. Zhang et al. (2020b) applied their binary star population synthesis (BSPS) model to a sample of stars with known Li abundances. By simulating mergers of HeWDs with the helium cores of giants, the study produced stars with lithium-rich surfaces, effective temperatures, and luminosities matching those of real-world stars. The model predicted that a significant fraction of stars in the red clump phase with masses between 0.65 and 2.0 solar masses could have undergone these mergers.

In the sample of 30 RC stars analyzed, the model provided good agreement with the observed properties of these lithium-rich stars. The stars' masses were carefully selected to lie in the range where HeWD + RGB mergers are most likely to occur, ensuring that the predicted outcomes would match their evolutionary stage. The merger model also makes predictions about the future evolution of these stars. Post-merger, the stars are expected to remain in the red clump for an extended period due to the additional energy provided by the helium flash. The surface lithium would gradually be depleted as the star evolves, but during the initial phase following the merger, the stars would display enhanced lithium abundances, as observed. The mass loss from the merger would continue to produce infrared signatures, which would persist as long as the dust remains in the circumstellar environment.

Mergers involving helium white dwarfs are a potential explanation for both Li enhancement and the observed mass loss (Zhang & Jeffery 2013). In these systems, the helium flash, triggered by the accretion of material during the merger, could lead to the creation of a lithium-enriched surface layer. The subsequent mass ejection would be observed as infrared excess in the surrounding dust shell.

3.10 Conclusion

In this chapter, we investigated the relationship between infrared excess and lithium enrichment in a sample of red clump and upper RGB stars. We found that while IR excess is rare, it is more frequently observed in super Li-rich giants, suggesting a possible link between mass loss and lithium enhancement. Furthermore, rapid rotation in some of these stars hints at the possibility that mergers or other interactions have played a role in enhancing their lithium content.

The results indicate two main pathways for lithium enrichment in RC giants: one involving in-situ production during the helium flash with little or no mass loss, and another involving external interactions, such as mergers, that lead to both mass loss and lithium production. These findings provide important information about the complex processes which govern Li abundance in evolved stars, although further observational and theoretical studies will be necessary to fully understand the origin of Li enrichment in these stars.

Chapter 4

Study of a rapidly rotating super Li-rich red clump giant with strong infrared excess - Signs of tidal interaction

4.1 Overview

This study examines KIC 11087027, an RC giant characterized by its unusually high Li abundance, rapid rotation, and significant IR excess (results are published in Singh et al. (2024)). The investigation utilized *Kepler* photometry and high-resolution spectroscopic data to determine its rotational period (P_{rot} = 30.4 ± 0.1 days) and corresponding rotational velocity (V_{rot} = 19.5 ± 1.7 km s^{-1}). Its location on the HR diagram, combined with measured values of $^{12}C/^{13}C$ (7 ± 1) and [C/N] (-0.95 ± 0.2), along with asteroseismic metrics obtained through spectral calibration, indicates it is a low mass RC giant undergoing helium-core

burning. Gaia astrometric observations revealed changes in radial velocity and proper motion, pointing to the presence of an undetected binary companion. These observations, combined with the star's large rotational velocity, point to tidal synchronization and potential He-flash effects. The co-occurrence of high rotation, strong IR excess, elevated Li abundance and stellar flare activity in the same object raises the question of whether binary interactions, particularly tidal locking, are prerequisites for the transport of substantial amounts of Li to the stellar surface during or after the He-flash.

4.2 Introduction

A subset of red giant stars exhibits exceptionally high levels of lithium, an element expected to be depleted during stellar evolution. This anomaly has puzzled astronomers ever since the identification of the first Lithium rich giant by Wallerstein & Sneden (1982). Recent research suggests that elevated lithium levels among red clump (RC) giants are relatively common and strongly linked to the core helium-flash, which precedes the RC phase (see Kumar et al. (2011); Casey et al. (2019); Singh et al. (2019); Deepak & Reddy (2019); Yan et al. (2021)). Post helium-flash, lithium abundances in RC stars are, on average, about forty times greater compared to stars located on the upper RGB (Kumar et al. 2020). Further investigations by (Singh et al. 2021) demonstrated a correlation between lithium abundance (A(Li)) and the evolution of asymptotic dipolar g-mode period spacing ($\Delta\Pi_1$). This period spacing increases during the transition from a degenerate core to convective core helium burning, and high lithium levels are predominantly observed at lower values of $\Delta\Pi_1$, immediately following the He-flash. Based on this evidence, the super Li-rich giant phase (A(Li) $>$ 3.2) is hypothesized to be short-lived, indicating that these stars have experienced lithium enrichment very recently.

Notably, studies by Mallick et al. (2023) revealed that lithium-rich red giants are mostly low mass stars (M $\leq 2M_{\odot}$), providing indirect evidence that lithium enhancement is tied to the helium-flash, which occurs exclusively in low-mass stars (Miller Bertolami et al. 2020). We also observe that investigations of cluster giants have uncovered instances of SLR giants positioned across the RGB (Sanna et al. 2020; Nagarajan et al. 2023; Tsantaki et al. 2023). If these stars are indeed experiencing their first ascent of the RGB, it suggests that multiple pathways may exist for lithium enrichment in such giants. However, the physical mechanisms behind lithium production and its subsequent transport to the stellar surface remain unclear. Proposed explanations include gravity waves within the star generated at the time of the helium-flash (Schwab 2020; Jermyn & Fuller 2022), thermohaline mixing (Gao et al. 2022), and processes driven by differential rotation (Fekel & Balachandran 1993; Simon & Drake 1989) Binary interactions, such as tidal locking, have also been posited as a potential mechanism for facilitating the required mixing (Denissenkov & Herwig 2004; Casey et al. 2019). External events like mergers or tidal encounters with nearby companions may also induce rapid rotation, triggering strong magnetic fields and circumstellar material. The simultaneous presence of these features would suggest that lithium enrichment likely occurred recently due to such interactions.

This paper presents a comprehensive analysis of KIC 11087027, a super Li-rich giant exhibiting high rotation, significant IR excess, and pronounced chromospheric activity. Observations suggest recent binary interactions as the primary driver behind these unique characteristics.

4.3 Observations and Data

KIC 11087027 was identified within a sample of 12,500 stars common to the LAMOST (Large Sky Area Multi-Object Fiber Spectroscopic Telescope) and *Kepler* fields (Zhao et al. 2006; Cui et al. 2012). This star, initially excluded from a prior study by Singh et al. (2019) due to the absence of oscillation modes in its *Kepler* Power spectral density (PSD), displayed several distinctive characteristics, such as rotational modulation, flares, and infrared excess. To supplement the photometric data, high-resolution optical spectra (R = 60,000) were obtained using the 2.0-m Himalayan Chandra Telescope (HCT), using the Hanle Echelle Spectrograph (HESP)[1]. Three frames were captured, each with a 40-minute exposure, covering a wavelength range of 3700 to 9300 Å. Calibration data, including bias, flat, and Th-Ar lamp frames, were also acquired for wavelength calibration. Additionally, spectra of hot, fast-rotating stars were collected to remove telluric lines.

Standard procedures for Echelle spectral data reduction were applied using IRAF, resulting in spectra with a signal-to-noise ratio (SNR) of 86. These spectra were then wavelength-calibrated and continuum-normalized to facilitate the analysis and derivation of stellar atmospheric parameters and elemental abundances.

4.4 Analysis and Results

4.4.1 Deriving Stellar Parameters and Abundances

The stellar parameters of KIC 11087027 ($T_{\rm eff}$, $\log g$,[Fe/H],$v_{\rm sini}$,ξ_t were derived from high-resolution spectra (see Table 4.3). The `FASMA` code (Tsantaki et al. 2018) was

[1] https://www.iiap.res.in/centers/iao/facilities/hct/hesp/

used for spectrum synthesis to calculate these parameters. Stellar luminosity was determined using the Gaia G magnitude (Gaia Collaboration et al. 2016, 2018), along with appropriate bolometric corrections (Andrae et al. 2018) and parallax measurements provided by Gaia. Extinction in the G-band (A_G) was calculated using the *dustapprox* code (Fouesneau et al. 2022)[2]. Radial velocities were derived by cross-correlating continuum-normalized spectra with a template spectrum of Arcturus.

Elemental abundances and carbon isotopic ratios were obtained by matching synthesized spectra with observations. Model spectra were generated using one-dimensional radiative transfer models (MOOG; Sneden (1973)) based on LTE and stellar atmospheric models (Castelli & Kurucz 2004). Atomic and molecular line lists were sourced using the Linemake[3] tool (Placco et al. 2021). Lithium abundance was measured from the Li I resonance line at 6707.78 Å, yielding A(Li) = 4.35 ± 0.10 dex, and from the subordinate line at 6103 Å, yielding A(Li) = 3.85 ± 0.10 dex. Non-LTE adjustments were implemented according to the method described by Lind et al. (2009). Carbon abundance was determined from atomic carbon lines at 5086 and 5384.3 Å, while nitrogen abundance was obtained from the ^{12}C^{14}N molecular line at 6486.4 Å. The carbon isotopic ratio ($^{12}C/^{13}C$) was derived using the ^{13}C^{14}N molecular feature at 8004.72 Å. Errors in lithium abundance and carbon isotopic ratio were calculated by summing in quadrature the uncertainties in stellar parameters ($T_{\rm eff}$, $\log g$, [Fe/H], ξ_t) and the signal-to-noise ratio. Abundances of other elements were determined through equivalent width measurements.

[2] https://mfouesneau.github.io/dustapprox
[3] https://github.com/vmplacco/linemake

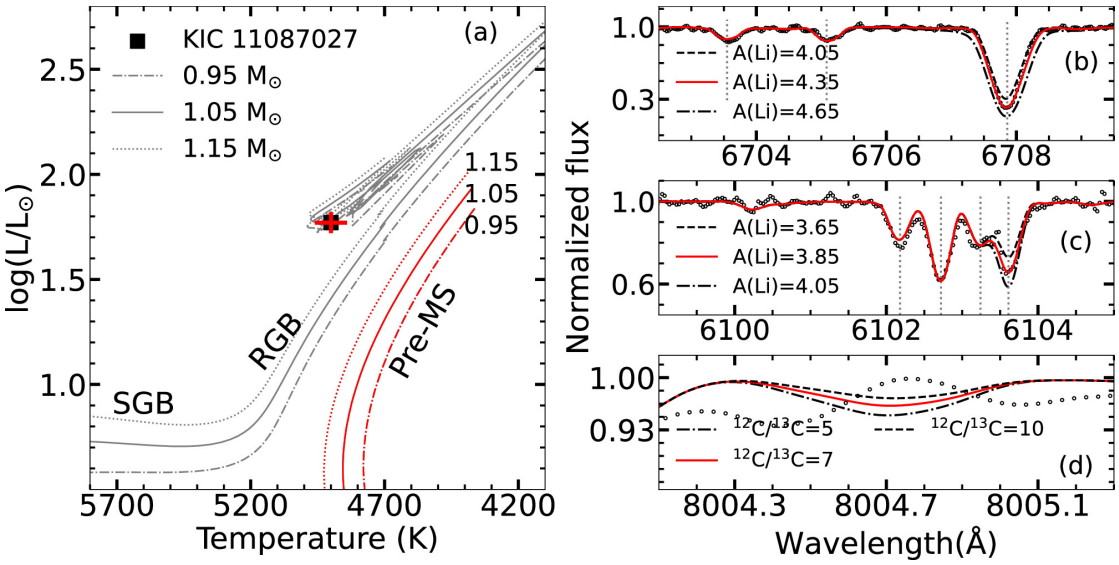

FIGURE 4.1: (a): Location of KIC11087027 (solid square), in the Hertzsprung-Russell diagram along with MESA-MIST (Paxton et al. 2011; Dotter 2016) evolutionary tracks for [Fe/H]=-0.55 dex with different masses. Panels (b),(c), and (d) are the spectral synthesis of Li resonance lines at 6707 Å Li subordinate line at 6103 Å and CN red line band near 8004 Å, respectively.

4.4.2 Evolutionary Phase

The evolutionary status of KIC 11087027 was assessed using its position in HR-diagram in conjunction with evolutionary tracks. As shown in Figure 4.1 panel (a), the luminosity and $T_{\rm eff}$ of the star places it within the RC region. Furthermore, the observed values of [C/N] = -0.95 ± 0.22 and [Fe/H] = -0.55 ± 0.05 align with RC stars when their [C/N] ratios are plotted against metallicities (e.g., Hawkins et al. (2018)). The carbon isotopic ratio, $^{12}C/^{13}C = 7 \pm 1$, indicates that the star has evolved beyond the luminosity bump. Although *Kepler* photometry spanning 18 quarters is available, the power spectral density (PSD) of KIC 11087027 lacks a Gaussian excess associated with oscillation modes. Such inhibition of oscillation modes is typically linked to enhanced magnetic activity (Chaplin et al. 2011; Gaulme et al. 2014). Consequently, asteroseismic parameters were estimated using secondary calibrations (Wang et al. 2023), yielding $\Delta\Pi_1 = 187$ s and $\Delta\nu = 4.4$ μHz. These values confirm the star's classification as an RC giant in the core helium-burning stage (Bedding et al. 2011).

4.4.3 Detection of stellar flare and measuring flare energy

Stellar flares are the result of the release of magnetic energy. While such events are frequently observed in main-sequence stars, they are less common in red giants, where the magnetic field is weaker. Occasionally, exceptionally large flares, or superflares, can occur in binary systems or as a result of interactions with planets that resemble stellar companions (Cuntz et al. 2000) For this study, we analyzed long cadence (29.4-minute) white light photometric data from the *Kepler* mission, spanning four years. Visual inspection of the light curves revealed rapid increases in brightness followed by exponential decay patterns, which are characteristic of flare events. We use FLATW·RM code (Vida & Roettenbacher 2018) for detection of stellar flare and measuring flare parameter such as equivalent duration, amplitude. We found 15 white light flares (WLFs) in KIC 11087027, see Figure 4.2 (b). Flare energy in white light is derived from equivalent duration (ED) of flare and quiescent luminosity. Quiescent luminosity in *Kepler* wavelength band is measured by integrating convolution of bolometric flux (F_λ) and *Kepler* response function (S_{Kp}).

$$E_{flare} = 4\pi R^2 \times ED \int_{\lambda_1}^{\lambda_2} F_\lambda * S_{Kp} d\lambda$$

Here λ_1 and λ_2 are lower and upper wavelength limit of *Kepler* filter. Bolometric flux F_λ for stellar parameters is retrieved from VOSA [4] and *Kepler* response function S_{Kp} from *Kepler* website [5]. Flare energy is in range from $10^{35} - 10^{37}$ erg. Energetic flares have longer duration and larger amplitude. Flare energy in most of flares is more than 10^{33}ergs^{-1} which makes it a super flaring giant.

[4] http://svo2.cab.inta-csic.es
[5] https://keplergo.github.io/KeplerScienceWebsite/

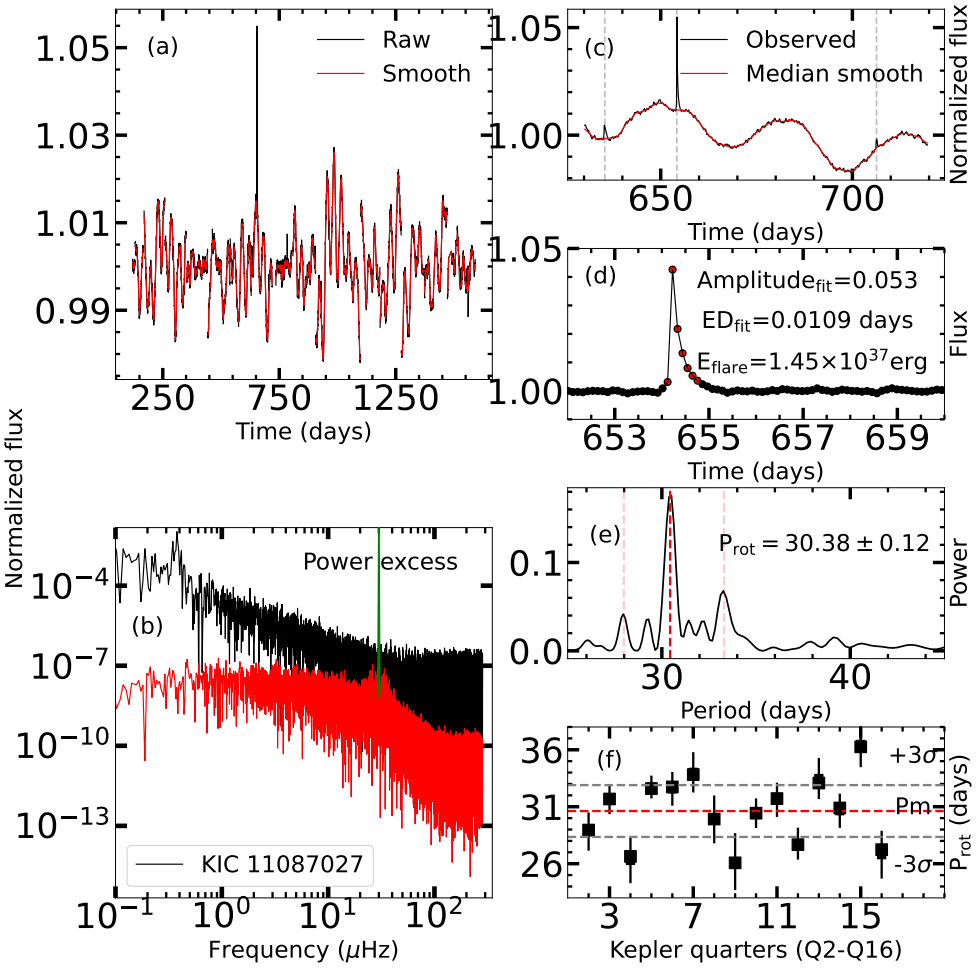

FIGURE 4.2: Rotation period measurement and flares in KIC 11087027. Top panel is 7 quarter *Kepler* light curve of KIC 11087027 in solid black line. Red solid line is median smooth flux. 3 flares are marked as vertical dashed line. Middle panel is Lomb-Scargle periodogram of entire 17 quarter light curve. Vertical red dashed line is measured period. Error is measured by fitting Gaussian to significant peak. Bottom panel is detrended light curve similar to top panel in region of a flare. Flare flux points identified in FLATWRM (Vida & Roettenbacher 2018) are marked as red square. Measured flare parameters are given in figure. bottom panel: Rotation period measured in different quarters gives different values. We have plotted P_{rot} for 2 to 16 quarters. Horizontal lines are mean and 3 sigma values of period. Individual squares are period measured in each quarters. Panel d is power density spectra of light curve presented in panel a. In PDS we see a strong peak at 30.40 days as well as two weaker but significant peaks near 28 days and 33.3 days respectively. This different rotation in individual quarters appears as different peaks in the PDS. Median absolute deviation of the periods derived from different quarters is 2.1 which clearly signal variability in the period.

4.4.4 IR excess and chromospheric activity

We searched for infrared excess to determine if the star had experienced any mass loss resulting from external merger events, the He-flash, or interactions with a binary companion. We gathered observed flux data across the near-UV to far-IR wavelength ranges. The spectral energy distribution (SED) of KIC 11087027 is presented in Figure 4.3 panel (b). This observed SED is compared with the model SED, which is based on the star's derived atmospheric model from the Kurucz grid of flux models and generated using VOSA[6]. Observed wavebands of KIC 11087027 include NUV (GALEX), optical (APASS, GAIA), near IR (2MASS), mid IR (WISE) to far IR (AKARI, IRAS). The magnitudes in different bands were converted into fluxes and compared with theoretical model flux in different wavebands. KIC 11087027 exhibits notable infrared excess in both the near-IR and far-IR wavelengths, suggesting the presence of an extended circumstellar environment resulting from episodic mass loss. To detect IR excess we have followed Kennedy & Wyatt criteria (Kennedy & Wyatt 2012):

$$X_B = \frac{(F_B - F_{\star B})}{\sqrt{\sigma_B^2 + \sigma_{\star B}^2}}$$

Here, F_B represents the photometric flux density of band B, $F_{\star B}$ is the photospheric model flux density of the same band, with each σ denoting the corresponding flux uncertainty. Stars are typically considered to show excess emission if X_B exceeds 3. For KIC 11087027, $X_B > 3$ in wise W4, AKARI, and IRAS 12 μm.

We obtained optical spectra covering the H_α region at low and medium resolutions from LAMOST and at high resolution from HESP, with data collected at different times. Strong emission is observed in all the spectra, with emission level exceeding the continuum. A double-peak structure is evident in the medium and high-resolution spectra. To investigate any asymmetry in the H_α line, we applied the

[6] http://svo2.cab.inta-csic.es/theory/vosa/

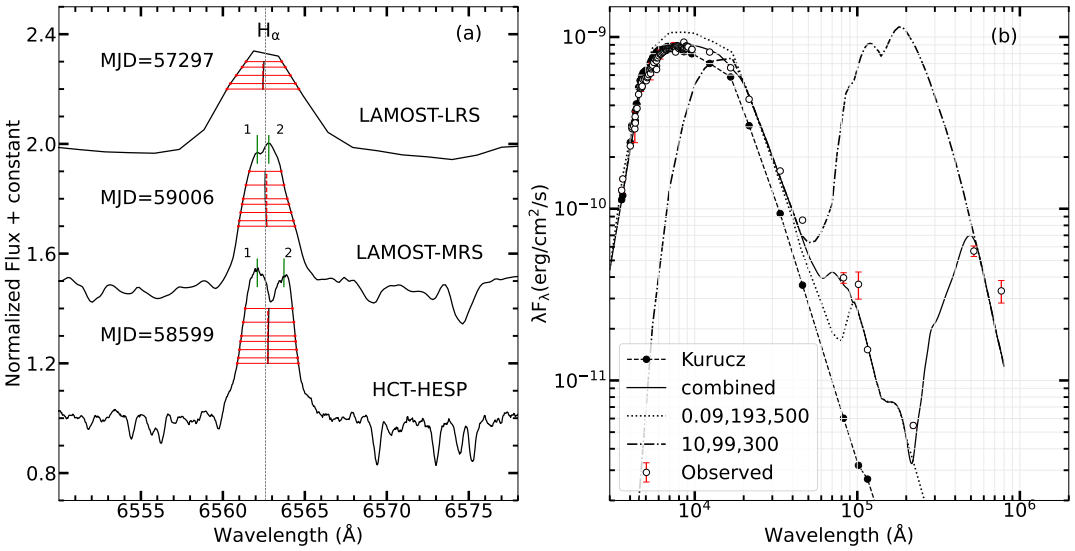

FIGURE 4.3: (a): H_α emission in KIC 11087027. Three spectra are taken at different time and resolution. Top level spectra is LAMOST low resolution spectra, middle one is LAMOST medium resolution spectra and bottom one HCT-HESP high resolution spectra. In LRS double peaks are not visible because of low resolution. In MRS we can see double peak, with more strength on red side and in HRS double peaks are clearly visible with more strength on blue side. (b): SED fitting to observed fluxes. After WISE W1 band this star has excess fluxes than expected for stellar models. Model flux is derived using Kurucz model atmosphere in VOSA.

bisector method. Asymmetry is clearly present in the H_α feature, as illustrated in Figure 4.3a. The asymmetric and variable H_α profile indicates the presence of chromospheric activity and mass motion in the stellar atmosphere (Dupree et al. 1984).

4.4.5 SED modelling

The DUSTY code (Ivezic et al. 1999), a one-dimensional radiative transfer program in conjunction with Kurucz model fluxes, was employed to determine dust parameters based on a given set of stellar parameters and an assumed dust grain distribution. A spherically symmetric dust shell is assumed in our model. The following input parameters were carefully tailored to achieve an optimal model fit.

1. Stellar Spectrum: The input flux incorporated the model stellar spectrum derived from Kurucz models, anchored by the derived stellar parameters ($T_{\rm eff}$, $\log g$ and metallicity)

2. Dust composition: KIC 11087027 is a post-RGB object (see sec 4.4.2) and is expected to have oxygen-rich circumstellar envelope. The IR flux values are indicative of warm silicate (Sil-Ow) dust particles (Draine & Lee 1984)

3. Grain size (a) dispersion : We applied the Mathis, Rumpl, & Nordsieck size distribution (MRN) (Mathis et al. 1977) where the grain count $n(a) \propto a^{-q}$, where n represents the quantity of grains within the size range $(a, a + da)$, $q = 3.5$, $a_{\rm min} \approx 0.005\,\mu m$, and $a_{\rm max} \approx 0.25\,\mu m$.

4. Dust Temperature: Temperature T_{in} at inner radius of dust envelope (R_{in}).

5. Relative Thickness: Defined by the relative thickness parameter Y= $\left(\frac{R_{out}}{R_{in}}\right)$

6. Optical Depth: Optical depth (τ_v) was specified for a fiducial wavelength (λ_0 = 0.55 μm).

Model SED was computed by varying T_{in}, Y and τ_v. The SED was normalized to the 2MASS Ks band flux value since this band exhibits lower susceptibility to extinction and variability compared to optical bands like the V-band. The optimal fit was determined through the computation of a modified minimum chi-square (χ^2) given by :

$$\chi^2 = \sum \left(\frac{f_{obs} - fmod}{\sigma_{obs}}\right)^2 /(N - p - 1)$$

where f_{obs}, f_{mod} and σ_{obs} are observed flux, model flux and error in observed flux respectively. $N - p - 1$ represents the degrees of freedom, where N corresponds to the number of observed data points, and p signifies the number of independent parameters. Initially, the SED was fit using a single-shell (one-component) model, with the input parameters adjusted accordingly. However, this model was unable to adequately fit the observed SED, particularly the points showing infrared excess.

As a result, a two-component model was then adopted. In this approach, an inner hot component and a cooler outer dust shell were introduced, and the input parameters were adjusted to minimize the χ^2 statistic. The two-component best fit model using DUSTY is shown in Fig. 4.3b. DUSTY outputs are based on the assumption of a stellar luminosity of 10^4 $L_\odot$. The shell inner radii and expansion velocities were obtained from DUSTY models using the scaling relations $R_{in} \propto L^{1/2}$, $V_s \propto L^{1/4} \left(\frac{\rho_d}{\psi}\right)^{-1/2}$. Mass loss rate from the dust shells (inner/outer) is given by Chan & Kwok (1988)

$$\dot{M} = \frac{16\pi}{3} \left(\frac{\rho_d}{\psi}\right) \left(\frac{a}{Q_\lambda}\right) \tau_\lambda V_s R_{in}$$

where grain density $\rho_d = 3$ g.cm^{-3}, dust to gas mass ratio $\psi = 4.3\times10^{-3}$, continuum dust absorption coefficient Q_λ , grain radius a , opacity at wavelength λ is τ_λ and V_s is the expansion velocity of dust shell. Value of $\left(\frac{Q_\lambda}{a}\right)$ is given by Draine's (1985) model for astronomical silicates as 1.3 μm^{-1} at $\lambda = 9.7$ μm. Using $\tau_{9.7\mu m}$ from DUSTY models, mass loss rates were obtained. Mass of each dust shell is calculated as :

$$M_d = \frac{16\pi}{3} \left(\frac{\rho_d}{\psi}\right) \left(\frac{a}{Q_\lambda}\right) \pi \tau_\lambda R_{in}^2$$

Kinematic age of dust shells is given as :

$$t_d = \frac{R_{in}}{V_s}$$

We also computed expected mass-loss rate using modified Reimer's Law (Reimers 1975) :

$$\dot{M}_R = \frac{\eta L_* R_*}{M_*} \left(\frac{T_{eff}}{4000}\right) \left(1 + \frac{g_\odot}{4300 g_*}\right)$$

where luminosity (L_*), radius (R_*), mass (M_*), $T_{\rm eff}$, g_* are taken from Table 4.3. Solar reference value $\log g_\odot = 4.44$ dex and $\eta = (8 \pm 1)\times 10^{-14}$ $M_\odot$.yr^{-1}. All derived values for KIC 11087027 are given in Table 4.1.

Stellar flares on a star's surface, can lead to the formation of distinct inner warm

	$\dot{M}_R$ ($M_\odot.yr^{-1}$) (Reimer's Law)	T_{inner} (K)	τ_v	T_d (K)	V_s (km.s^{-1})	R_{in} (cm)	t_d (years)	$\dot{M}$ ($M_\odot.yr^{-1}$) (DUSTY)	M_d ($M_\odot$)
Inner Shell	6.68×10^{-11}	500	0.09	193	5.48	4.87×10^{13}	2.82	5.78×10^{-9}	8.26×10^{-8}
Outer Shell		300	10	99	1.41	2.45×10^{14}	55.09	8.29×10^{-7}	2.32×10^{-4}

TABLE 4.1: Dust shell parameters of KIC 11087027.

and outer cool dust shells, coupled with episodic mass loss. During a flare, rearrangement of magnetic fields results in the release of energetic particles and radiation. Increased radiation pressure and localized heating in the outer layers of the star can drive enhanced stellar winds, expelling material into space. The expelled material, composed of dust and gas, forms an outer cool dust shell. Simultaneously, the intense stellar radiation can lead to the sublimation of dust grains closer to the star, creating an inner warm dust shell. These episodic events, shaped by flare variability, contribute to episodic mass loss from the two dust shells.

4.4.6 Rotational velocity

Rotational velocity $V_{\rm rot}$ of KIC 11087027 was calculated both from spectra and light curve. The observed spectral width is influenced by line blending in the region, instrumental broadening, and stellar factors such as macroturbulence and rotation. To isolate the rotational component of the line width, two well-defined Fe I lines at 6703 and 6705 Å were used. A series of line profiles were computed based on given line abundances, stellar parameters, and instrumental broadening, the latter measured using Th-Ar calibration lines in the same region. The macroturbulence velocity ($V_{\rm mac} = 3.9\,{\rm km\ s^{-1}}$) was determined using a calibration relation involving $T_{\rm eff}$ and $\log g$ (Hekker & Meléndez 2007). A χ^2 test identified the best fit to the observed profiles with $V_{\sin i} = 10.1\,{\rm km\ s^{-1}}$.

Additionally, *Kepler* photometric data were analyzed to estimate the star's period. Modulation in the light curve, likely caused by large stellar spots co-rotating with the stellar surface, was observed. A periodogram analysis using the Lomb Scargle technique (Lomb 1976; Scargle 1982) was conducted on 4 years of *Kepler* data. Periods ranging from 26 to 33 days were found in different quarters, with an average period of 30.38 ± 0.12 days (see Figure 4.2f, bottom panel). Using the star's estimated radius ($R = 11.69 \pm 1\, R_{\odot}$) and treating this period as the rotational period ($P_{\rm rot}$), an average rotational velocity of $\mathrm{V_{rot}} = 19.5 \pm 1.7\,\mathrm{km\ s^{-1}}$ was derived, an unusually high value for evolved stars like KIC 11087027. The quarter-to-quarter variations, with a median absolute deviation of 2.1, likely result from latitudinal differential rotation (Suto et al. 2022). We also derived the stellar magnetic field using theoretical turnover timescale (Charbonnel et al. 2017) and rotation period from present study4.3. We found that a core He-burning star of this mass has a convective turnover timescale of 38 days. For derived period of 30.38 days we estimated Rossby number = 0.8 and a corresponding magnetic field of 3.91 Gauss (Aurière et al. 2015).

4.4.7 Binarity

No resolved binary for KIC 11087027 was found within $10''$ in the Gaia survey, and no evidence of an eclipse is seen in the *Kepler* light curve. The star was observed at four different epochs using APOGEE, LAMOST, and HCT-HESP over a period of 7 years, revealing a small difference in its radial velocity. Hence, the possibility of an unresolved companion cannot be excluded.

Binarity introduces complications in astrometric measurements. In systems with shorter periods ($\sim$ 10 years) where a substantial number of orbits can occur during the observation period of the observing instrument, the astrometric motion of the center of mass (c.o.m.) is effectively captured. In unresolved binary systems,

the motions of the center of mass and the center of light diverge. The apparent motion of a single star in the sky is characterized by five free parameters: parallax, RA, DEC, and proper motion along RA and DE (pmRA, pmDE). While this 5-parameter model is sufficient for describing the barycentric motion, the trajectory of the center of light now introduces an additional component stemming from the binary orbital motion. This change in position of the photocenter can be assessed by analyzing the reduced χ^2 value obtained from fitting the single source 5-parameter astrometric model to observational values. Essentially, a closely associated metric GAIA renormalized unit weight error (RUWE) was employed for gauging deviations from a single source fit. RUWE value > 1.4 is a threshold indicating a poor astrometric solution, suggestive of the presence of stellar multiplicity. GAIA RUWE for KIC 11087027 is 4.38. To complement the RUWE excess we made a comparative study of its proper motion estimates across multiple epochs. Faint or unresolved companions have the potential to cause a displacement of the barycenter relative to the photocenter, a phenomenon detectable through the comparison of proper motion estimates over different epochs, known as the proper motion anomaly (PMa) method. Proper motion information about this star was compiled from two long term surveys -Tycho 2 (Høg et al. 2000) (epoch J2000.0) and UCAC5 (epoch J2001.0) catalogues (Zacharias et al. 2017) and from GAIA DR2 (Gaia Collaboration et al. 2016) (epoch J2015.5) and DR3 (Gaia Collaboration et al. 2018) (epoch J2016.0), both covering a span of a few years. As indicated in Table 4.2, significant disparities exist in the proper motion components between different epochs. A notable acceleration is detected in the δ direction, indicating

Tycho 2 (J2000.0)		UCAC5 (J2001.0)		Gaia DR2 (J2015.5)		Gaia DR3 (J2016.0)	
pmRA	pmDE	pmRA	pmDE	pmRA	pmDE	pmRA	pmDE
-2.0 ± 2.9	-3.6 ± 2.7	-1.1 ± 1.3	-5.4 ± 1.3	-1.839 ± 0.148	-7.511 ± 0.131	-1.547 ± 0.067	-7.289 ± 0.059

TABLE 4.2: Proper motion (pmRA and pmDE) comparison

that the star could be an unresolved binary or part of a multiple system. The lack

Name	KIC11087027	reference	Name	KIC11087027	reference
ra	19:33:14.212		τ_c (days)	38	this work
dec	+48:35:17.322		Rossby no	0.80	this work
Vmag	11.23 ± 0.09	APASS	B (Gauss)	3.91	this work
A_G	0.11	this work	XYZ (kpc)	(-7.9, 1.1, 0.3)	this work
plx	0.7946 ± 0.0668	Gaia DR3	UVW (km s^{-1})	(-48.5, 216.03, -8.1)	this work
RUWE	4.38	Gaia DR3	Pericenter (kpc)	7.1±0.003	this work
P_{rot} (Days)	30.47 ± 0.16	this work	Apocenter (kpc)	8.3±0.001	this work
v(km s^{-1})	20.5	this work	Eccentricity	0.07±0.001	this work
vsini (km s^{-1})	10.7 ± 0.2	this work	Energy (kpc^2/Myr^2)	-0.14	this work
Inclination angle	0.57	this work	Angular momentum(kpc^2/Myr)	-1.82	this work
Number of flares	15	this wok	Radius (kpc)	7.98	this work
Teff [K]	4920 ± 60	this work			
log g	2.64 ± 0.05	this work			
$[Fe/H]$	-0.54 ± 0.05	this work			
ξ_t(km s^{-1})	0.95 ± 0.05	this work			
$\log(L/L_\odot)$	1.77 ± 0.05	this work			
Mass ($M_\odot$)	1.014 ± 0.2	this work			
Radius ($R_\odot$)	11.69 ± 1	this work			
rv_{gaia} (km s^{-1})	26.68 ± 0.6	Gaia DR3			
rv_{lamost} (km s^{-1})	22.71 ± 4.11	Luo+2018			
RV_{HESP} (km s^{-1})	19.98 ± 0.26	this work			
A(Li)	4.0 ± 0.1	this work			
$^{12}C/^{13}C$	7 ± 1	this work			
Age (Gyr)	5.4 ± 3.2	this work			
Mass ($M_\odot$)	1.038 ± 0.142	this work			
Radius ($R_\odot$)	9.92 ± 0.52	this work			
log g	2.48 ± 0.11	this work			

TABLE 4.3: Stellar parameters of KIC 11087027.

of oscillation modes (refer to Fig. 4.2b) and the presence of strong magnetic activity in this low-mass, fast-rotating evolved star (Gaulme et al. 2014) indicate that KIC 11087027 is probably part of a tidally synchronized system. Further evidence comes from its high rotational velocity projection ($V_{sini} = 10$ km.s^{-1}), which is notably large given its color ($B - V = 1.04$ (De Medeiros et al. 2002). These observations indicate that KIC 11087027 is tidally locked with an unresolved close binary companion, having an orbital period of 30.4 days.

4.5 Discussion

Red giants exhibiting both exceptionally high lithium and significant infrared (IR) excess are uncommon, as these characteristics are transient and follow different evolutionary paths. While information on IR excess in such stars remains limited, large-scale surveys have generally found no evidence of IR excess among red giants (Bharat Kumar et al. 2015). Just a limited number of lithium-rich giants and SLR stars were observed with IR excess (Mallick et al. 2022). This scarcity suggests either that mass ejection during lithium enrichment events is minimal, or that any resulting IR excess diminishes faster than lithium depletion.

In this context, KIC 11087027 stands out as an unusual case, displaying both a remarkably high lithium abundance and significant IR excess. This implies that lithium enrichment occurred relatively recently, assuming that both features originate from a single event responsible for the lithium enhancement observed in red clump (RC) giants. Furthermore, the period spacing ($\Delta\Pi_1$) serves as a marker of the evolutionary stage where a degenerate core transitions to a convective zone. Older RC giants with typical lithium levels generally exhibit higher $\Delta\Pi_1$ values (Singh et al. 2021). For KIC 11087027, the estimated $\Delta\Pi_1 = 187\,\mathrm{s}$ (Wang et al. 2023) confirms it as a young RC star, reinforcing the likelihood of recent lithium enrichment.

Additionally, the star's elevated rotational velocity ($V_{\mathrm{rot}} = 19.5\,\mathrm{km\ s^{-1}}$) contributes to pronounced chromospheric activity, including flares. However, the underlying mechanism linking these features remains unclear. If a single event, such as the He-flash, is responsible for generating these properties, which evolve over different timescales, it would explain why such stars are exceedingly rare.

It is also noteworthy that Sneden et al. (2022) identified a subtle relationship between the strength of the chromospheric He I 10830 Å line and elevated lithium

abundance in giants. Their findings also indicate a higher binary fraction among lithium-rich giants compared to their lithium-poor counterparts, suggesting that binary interactions could play a role in driving both lithium production and enhanced chromospheric activity. The optical spectra of KIC 11087027 has strong H_α emission feature across low, medium, and high resolutions, signifying chromospheric activity (Dupree et al. 1984). The asymmetric H_α profile, characterized by a red-shifted core and stronger emission in the red wing compared to the blue wing, suggests radial mass motion within the stellar atmosphere. The presence of emission in both the blue and red wings of the H_α line points to a thin stellar envelope and a lower mass-loss rate than typically observed in P Cygni-type stars.

For KIC 11087027, we explore two potential explanations. The first involves an internal mechanism during single-star evolution, while the second considers binary evolution, where orbital synchronization induces rapid rotation, facilitating high lithium levels. It is widely believed that the helium flash plays a pivotal role in the lithium anomaly observed among RC giants (Casey et al. 2019; Singh et al. 2019; Deepak & Reddy 2019; Singh et al. 2021; Mallick et al. 2023). However, understanding certain extremely lithium-rich giants identified in clusters is equally essential. These giants seem to be located on the RGB, well before reaching the RGB tip (Sanna et al. 2020; Nagarajan et al. 2023), which precedes the helium flash event. Investigating cluster lithium-rich giants through asteroseismology to determine whether they are ascending the RGB remains a key objective for future work.

For RC lithium-rich giants, a critical question concerns the mechanism that transports lithium from its production site to the outer layers. Is the helium flash solely responsible, or do external influences, such as tidal locking, contribute? To support the significant lithium levels among RC giants, Schwab (2020) developed models where strong gravity waves generated during the helium flash promote extensive

convection. These models require a diffusion coefficient $D_{\rm mix} = 10^{11}\,{\rm cm^2\,s^{-1}}$, several orders of magnitude higher than expected for RGB stars.

Assuming lithium forms within the star via the Cameron–Fowler mechanism (Cameron & Fowler 1971b) and the helium flash drives large-scale mixing, mass loss due to the flash may explain the IR excess observed in some cases. While models predict no noticeable IR excess from a central helium flash, it is plausible that any mass loss triggered by the flash depends on its intensity. Since the resulting IR excess is a transient, one-time occurrence, it could dissipate faster than lithium depletion, making RC giants with IR excess rare. Notably, not all SLRs or lithium-rich giants exhibit IR excess, as their evolution may proceed at different rates. However, RC giants showing infrared excess are often SLRs or lithium-rich (Mallick et al. 2022), indicating that IR excess vanishes more quickly than lithium does.

Regarding KIC 11087027's elevated rotational velocity, the He-flash, followed by a reduction in stellar radius by approximately a factor of 10, would naturally spin up the star. For giants at the RGB tip with $V_{\rm rot} \sim 0.7\,{\rm km\ s^{-1}}$, a young RC giant would be expected to have $V_{\rm rot} \sim 7\,{\rm km\ s^{-1}}$, given the size reduction. However, the observed $V_{\rm rot}$ of $19.5\,{\rm km\ s^{-1}}$ is significantly higher. Such discrepancy suggests that rapid rotation in KIC 11087027 and other lithium-rich RC stars reported in the literature may result from external factors like mergers or tidal locking.

If a primary giant nearing the RGB tip is tidally locked with a binary companion, its rotational velocity would be greater than that of a single star. For KIC 11087027, the observed $V_{\rm rot} = 19.5\,{\rm km\ s^{-1}}$ might combine the effects of tidal locking and the post-helium flash spin-up. Assuming a tidally locked star with a slightly elevated $V_{\rm rot}$, around $2\,{\rm km\ s^{-1}}$ instead of the expected $0.7\,{\rm km\ s^{-1}}$, the post-flash rotational velocity aligns with the observed value. A high rotational velocity increases the diffusion coefficient to $D_{\rm mix} = 10^{11}\,{\rm cm^2\,s^{-1}}$ since $D_{\rm mix} \propto \Omega^2$. Such an increase in $D_{\rm mix}$, as shown in models (Casey et al. 2019), could explain the

enhanced lithium levels in the photosphere (Denissenkov & VandenBerg 2003).

4.6 Conclusion

This study presents findings derived from high resolution spectroscopy and *Kepler* photometric light curves. From variations in radial velocity and Gaia astrometric information, we propose that KIC 11087027 possesses an unresolved companion. The observed high rotational velocity of $V_{\rm rot} = 19.5\,{\rm km\ s^{-1}}$ is likely attributable to a combination of tidal synchronization within a binary system and the influence of the helium flash. Elevated rotational velocity may result in an increased diffusion coefficient, thereby explaining the star's enhanced lithium levels.

The presence of several transient characteristics, including exceptionally high lithium abundance, multiple dust shells, rapid rotation, and strong flares, suggests that the star might have experienced a merger-triggered helium flash (Mallick et al. 2022) or that the tidally locked primary recently underwent a helium flash. Furthermore, to gain deeper insights into the origin of lithium-enriched giants, it is essential to investigate lithium-rich giants in clusters that are reported to be ascending the RGB.

Name	KIC11087027	reference	Name	KIC11087027	reference
ra	19:33:14.212		τ_c (days)	38	this work
dec	+48:35:17.322		Rossby no	0.80	this work
Vmag	11.23 ± 0.09	APASS	B (Gauss)	3.91	this work
A_G	0.11	this work	XYZ (kpc)	(-7.9, 1.1, 0.3)	this work
plx	0.86 ± 0.05	Gaia DR3	UVW (km s^{-1})	(-48.5, 216.03, -8.1)	this work
RUWE	4.38	Gaia DR3	Pericenter (kpc)	7.1±0.003	
phot_gof_al	67.29	Gaia DR3			
astrometric_excess_noise_sig	458.01	Gaia DR3			
P_{rot} (Days)	30.38 ± 0.12	this work	Apocenter (kpc)	8.3±0.001	this work
V_{rot}(km s^{-1})	20.5	this work	Eccentricity	0.07±0.001	this work
Vsini (km s^{-1})	10.7 ± 0.2	this work	Energy (kpc^2/Myr^2)	-0.14	this work
Inclination angle	35°	this work	Angular momentum(kpc^2/Myr)	-1.82	this work
Number of flares	15	this wok	Radius (kpc)	7.98	this work
T_{eff} [K]	4920 ± 60	this work			
log g	2.64 ± 0.05	this work			
[Fe/H]	-0.54 ± 0.05	this work			
ξ_t(km s^{-1})	0.95 ± 0.05	this work			
$\log(L/L_\odot)$	1.77 ± 0.05	this work			
Mass ($M_\odot$)	1.014 ± 0.2	this work			
Radius ($R_\odot$)	11.69 ± 1	this work			
RV_{Gaia} (km s^{-1})	26.70 ± 0.38	Gaia DR3			
RV_amplitude_robust	5.29	Gaia DR3			
RV_{LAMOST} (km s^{-1})	22.71 ± 4.11	Luo+2018			
$RV_{HESP,Helio}$ (km s^{-1})	19.98 ± 0.26	this work			
$A(Li)_{NLTE}$(6103 Å)	3.95 ± 0.1	this work			
$A(Li)_{NLTE}$(6707 Å)	3.85 ± 0.1	this work			
[CI/Fe]	-0.18 ± 0.1	this work			
[NI/Fe]	0.77 ± 0.2	this work			
[NaI/Fe]	0.01 ± 0.15	this work			
[MgI/Fe]	0.03 ± 0.05	this work			
[AlI/Fe]	0.01 ± 0.25	this work			
[SiI/Fe]	-0.02 ± 0.3	this work			
[KI/Fe]	0.61 ± 0.2	this work	one line		
[CaI/Fe]	-0.03 ± 0.3	this work			
[ScII/Fe]	-0.09 ± 0.1	this work			
[TiII/Fe]	0.0 ± 0.1	this work			
[VI/Fe]	0.13 ± 0.22	this work			
[CrI/Fe]	-0.02 ± 0.3	this work			
[MnI/Fe]	0.77 ± 0.15	this work	one line		
[CoI/Fe]	-0.28 ± 0.18	this work	one line		
[NiI/Fe]	-0.34 ± 0.21	this work			
[ZnI/Fe]	0.23 ± 0.2	this work			
[SrI/Fe]	-0.51 ± 0.2	this work	one line		
[BaII/Fe]	0.04 ± 0.06	this work			
[NdII/Fe]	0.22 ± 0.1	this work	one line		
[EuII/Fe]	0.15 ± 0.08	this work	one line		
$^{12}C/^{13}C$	7 ± 1	this work			
Age (Gyr)	5.4 ± 3.2	this work			
Mass ($M_\odot$)	1.038 ± 0.142	this work			
Radius ($R_\odot$)	9.92 ± 0.52	this work			
log g	2.48 ± 0.11	this work			

TABLE 4.4: Stellar parameters and elemental abundances of KIC 11087027

Chapter 5

Lithium Enrichment in Red Giants: Stellar Mass and Helium Flash Dynamics

5.1 Overview

This chapter (Results of this study are published in Mallick et al. (2023)) explores the variation of Li abundances in giant stars based on their masses, with a particular focus on the role of the He flash as a possible origin of lithium enrichment in low mass red giants. Using a sample of 1,240 stars that overlap between the Kepler photometric data and medium-resolution spectra obtained from the LAMOST project, we aim to provide insights into the Li content of stars at different stages of their evolution.

The asteroseismic parameters, particularly period spacing (ΔP) and frequency spacing ($\Delta\nu$), have been crucial in distinguishing core helium-burning RC giants

from those on the RGB with inert helium cores. Li abundances for this sample have been derived using spectral synthesis methods. A combination of asteroseismic data and spectroscopic analysis allowed us to categorize these giants based on mass: primary red clump (pRC) giants, which are low-mass stars ($\leq 2M_{\odot}$) experiencing a helium flash, and secondary red clump (sRC) giants, which are more massive stars ($> 2M_{\odot}$).

Our results provide evidence that Li enrichment is primarily observed in low-mass pRC giants. We found no SLR stars among the high-mass sRC stars. This supports the hypothesis that the He flash — a runaway thermonuclear event that occurs in low mass giants at the tip of the RGB is responsible for the lithium enhancement observed in some low-mass red clump stars. This discovery places limitations on theoretical models aiming to clarify the mechanism behind lithium enhancement in such stars, as it implies that only stars with masses lesser than $\approx 2M_{\odot}$ undergo the degenerate helium-core flash that triggers this phenomenon.

5.2 Sample selection

Identifying the evolutionary phase of giant stars—particularly distinguishing helium-core burning RC stars from those in the RGB phase—can be challenging based solely on their positions in the Hertzsprung-Russell Diagram. This difficulty arises from the overlap between the luminosity bump of the RGB and the region occupied by RC stars. For this reason, independent indicators, such as asteroseismic parameters, are essential in determining a star's evolutionary phase.

The Kepler space mission has provided high-cadence photometric data, making it possible to perform detailed asteroseismic analyses of giant stars. In this study, we adopted a sample of 16,094 giants provided in Yu et al. (2018), that includes

stars with detectable oscillations. The sample consists only of stars with log(g) $\geq$ 1.5 and log(L/L$_\odot$) $\leq$ 2.24, effectively restricting it to RC and RGB stars. Stars with $\nu_{max} < 5$ μHz and $\nu_{max} \geq 275$ μHz were excluded to ensure that the sample omitted both supergiants and dwarfs. The sample is displayed in the HRD (Fig. 5.1), overlaid on the complete Kepler dataset as the background.

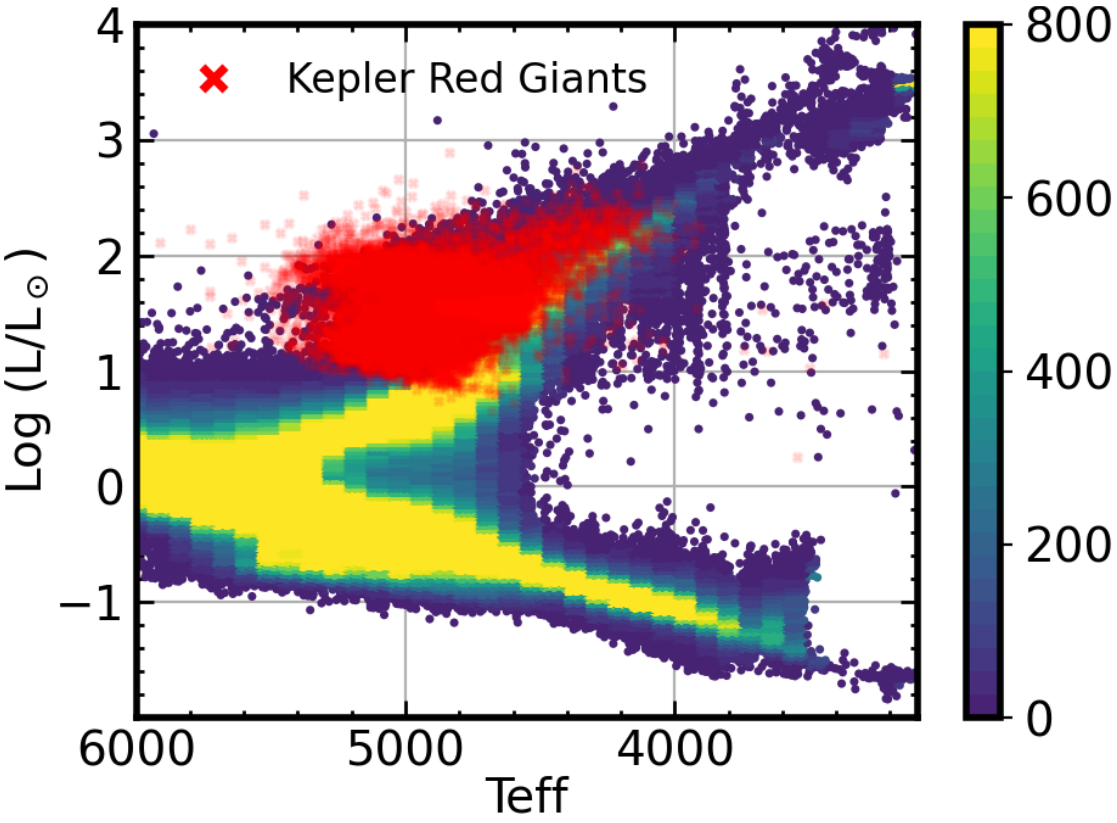

FIGURE 5.1: The sample of 16,094 RC and RGB giants (red symbols) from Yu et al. (2018), plotted against the full Kepler sample as the background.

We cross-referenced this sample with medium-resolution spectra from the LAMOST survey (Data Release 7), resulting in 1,240 stars common to both catalogues. The working sample of these 1,240 giants are displayed in the ΔP versus $\Delta\nu$ diagram (see Fig. 5.2), with the background including RC and RGB samples from Vrard et al. (2016).

All spectra exhibit a signal-to-noise ratio (SNR) exceeding 30, with the majority having an SNR greater than 50, ensuring good data quality. For the 584 stars

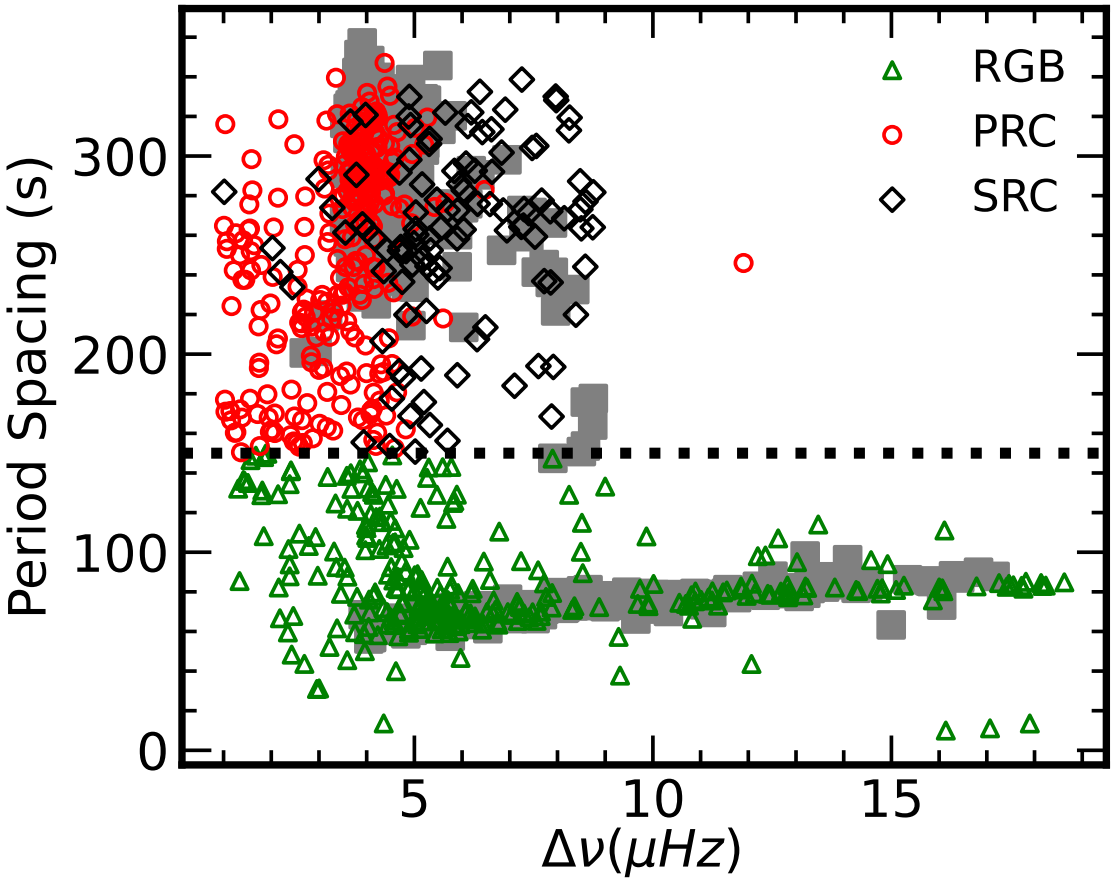

FIGURE 5.2: Asteroseismically identified RGB and RC stars from this study displayed alongside the giant star sample from (Vrard et al. 2016)

where direct estimates of the mixed-mode period interval (ΔP or $\Delta\Pi_1$) were available from literature sources (Vrard et al. 2016; Singh et al. 2019), these values were adopted. For the remaining 656 stars, ΔP values were derived using Kepler light curves in this study (see Table 5.1 for ΔP values of some stars derived in this work)

The sample was further classified based on the period spacing. Stars with ΔP (or $\Delta\Pi_1$) values of 150 seconds or greater were identified as RC stars, while those with smaller values were categorized as RGB stars. This threshold divides the sample into 777 RC giants and 463 RGB giants. While a small amount of contamination is possible due to some overlap between RC and RGB regions in the ΔP - $\Delta\nu$ diagram, especially near $\Delta\nu \approx 5\ \mu Hz$ (Fig. 5.2), the RC sample with ΔP $\geq$ 150 s

is expected to be the least contaminated. This is because the RC cut-off at ΔP is approximately 3-σ away from the typical RGB trend in the diagram.

5.3 Analysis

5.3.1 Stellar Mass Estimation

Traditional methods for estimating stellar mass based on evolutionary tracks often face complications in the RC and RGB regions, where tracks can degenerate. In this study, we utilized scaling relations derived from asteroseismic parameters, which have been shown to provide reliable mass estimates. The stellar masses for this study were taken from Yu et al. (2018), who used updated scaling relations from Sharma et al. (2016).

The mass of a star was estimated using the formula:

$$\frac{M}{M_{\odot}} = \left(\frac{\nu_{max}}{f_{\nu_{max}}\nu_{max,\odot}}\right)^{3} \left(\frac{\Delta\nu}{f_{\Delta\nu}\Delta\nu_{\odot}}\right)^{-4} \left(\frac{T_{eff}}{T_{eff,\odot}}\right)^{1.5}$$

Here, the parameters ν_{max} and $\Delta\nu$ denote the frequency corresponding to the peak oscillation power and the large frequency separation between oscillation modes, respectively, while $T_{\rm eff}$ is the effective temperature. The factors $f_{\nu_{\rm max}}$ and $f_{\Delta\nu}$ are correction terms for the scaling relations, with $f_{\nu_{\rm max}}$ set to 1.0 for this study, and $f_{\Delta\nu}$ derived using the ASFGRID code (Sharma et al. 2016). The solar reference values were adopted as $\nu_{max,\odot} = 3090 \pm 30$ μHz, $\Delta\nu_{\odot} = 135.1 \pm 0.1$ μHz, and $T_{\rm eff,\odot} = 5777$ K (Huber et al. 2011)

For the purpose of our analysis, we divided the red clump sample into two mass

categories: low-mass giants ($\leq 2M_{\odot}$), classified as primary red clump (pRC) stars, and high-mass giants ($> 2M_{\odot}$), categorized as secondary red clump (sRC) stars. Similarly, the RGB stars were grouped into low-mass and high-mass categories, with the $2M_{\odot}$ threshold used to distinguish between stars which are predicted to experience the Helium flash and those that are not. The final sample consisted of 668 pRC stars, 109 sRC stars, 10 high-mass RGB stars, and 453 low-mass RGB stars. The smaller proportion of high-mass secondary RC stars in the sample is due to the faster evolutionary timescales of high-mass giants compared to lower mass stars.

5.3.2 Lithium Abundances

For the entire sample of 1,240 giants, we extracted spectra from the LAMOST DR7 survey, focusing on those with SNR greater than 50. In a few cases, spectra with lower SNR were still sufficient to derive lithium abundances. All spectra were continuum normalized and corrected for radial velocity using IRAF tasks. The lithium abundances were derived using spectral synthesis, accounting for line blending with the Li 6707 Å resonance line. The stellar parameters $T_{\rm eff}$, log(g), and [Fe/H] were adapted from Yu et al. (2018), and the microturbulent velocity (ξ_t) was calculated using an empirical formula for giants based on their metallicities.

For giants with [Fe/H] > -1.0 dex, ξ_t was computed as:

$$\xi_t = 10^{\left(0.226 - 0.0228 \log g + 0.0297 (\log g)^2 - 0.0113 (\log g)^3\right)} \qquad \text{(Holtzman et al. 2018)}$$

For stars with [Fe/H] $\leq$ -1.0 dex, ξ_t was calculated as:

$$\xi_t = 2.478 - 0.325 \log g \qquad \text{(García Pérez et al. 2016)}$$

The *linemake* code (Placco et al. 2021) was used to generate atomic and molecular data around the Li I 6707.8 Å feature. The model atmospheres assuming local thermodynamic equilibrium (LTE) were constructed with the ATLAS9 software (Castelli & Kurucz 2003). An updated version of the MOOG radiative transfer code (Sneden 1973) was utilized to produce synthetic spectra for every object by adjusting their Li abundances. The Li abundance corresponding to the best match to the observed spectrum (minimized chi-square) was selected as the final abundance for that star. Figure 5.3 displays sample synthetic spectra compared with observed spectra. Among them, the third spectrum has one of the lowest signal-to-noise ratios, approximately 30.

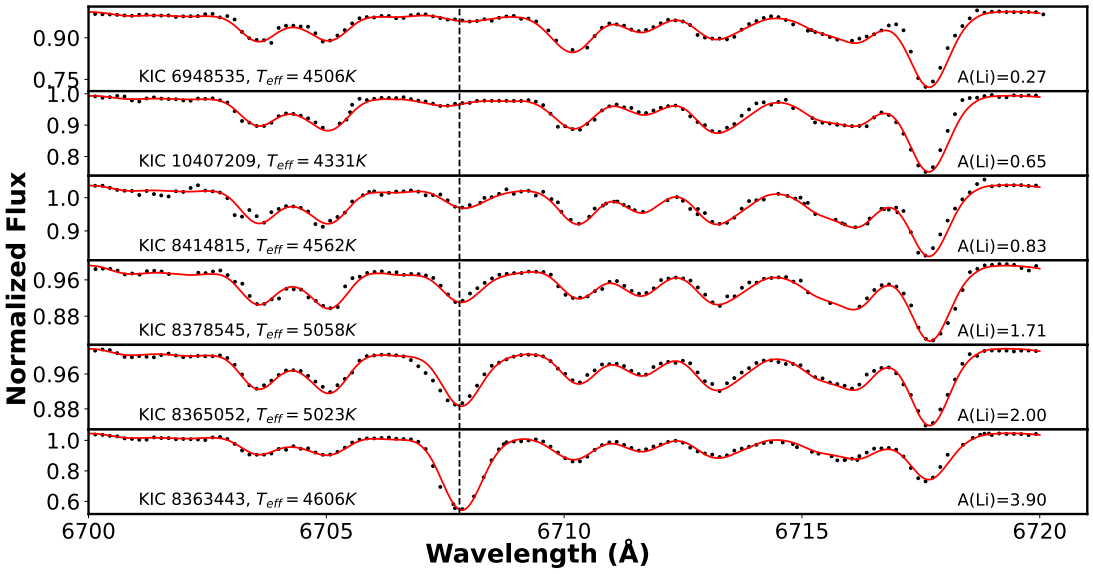

FIGURE 5.3: Li abundances derived for select representative giants through spectrum synthesis near the Li 6707.8 Å resonance line.

To assess the reliability of the Li abundance measurements, we estimated the errors in equivalent widths using Cayrel's formula (Cayrel 1988). The weakest detectable lines in our spectra yielded equivalent widths ranging from 0.62 to 17.5 mÅ, leading to a detection limit of lithium abundances between approximately 0.2 to 0.9 dex, contingent on T_{eff} and log$g$. All giants in our sample exhibited Li abundances above this detection threshold.

In addition to LTE lithium abundances, corrections based on non-local thermodynamic equilibrium (NLTE) were applied, using values from Lind et al. (2009). The NLTE corrections accounted for the effects of inhomogeneous stellar atmospheres and provided more accurate estimates of Li abundances in our sample.

A comparison of our derived Li abundances with those reported in previous studies revealed that our findings align well with the established trends. Specifically, lithium measurements calculated in the current work were compared against values obtained from high-resolution spectra of 41 common stars analyzed by Yan et al. (2021) and found a mean difference of 0.35 dex with a standard deviation of 0.02 dex. This comparison confirms that our results are consistent with their observations and that the derived Li values are reliable.

The overall error in the lithium abundance was determined by summing the individual uncertainties in quadrature, as shown below:

$$\Delta A(Li) = \sqrt{\Delta A(Li)^2_{S/N} + \Delta A(Li)^2_{T_{eff}} + \Delta A(Li)^2_{[Fe/H]} + \Delta A(Li)^2_{\xi}}$$

Each component of this equation represents the contributions to the total uncertainty:

- The term due to S/N is given by:

$$\Delta A(Li)_{S/N} = a_0 + a_1 \times S/N$$

- The term due to effective temperature is expressed as:

$$\Delta A(Li)_{T_{eff}} = b_0 + b_1 \times T_{eff} + b_2 \times T^2_{eff} + b_3 \times T^3_{eff}$$

TABLE 5.1: Derived and adopted parameters of Secondary RC sample of 110 stars

KIC	T_{eff} (K)	log g (dex)	[Fe/H] (dex)	ξ (km/s)	Mass ($M_\odot$)	A(Li)$_{LTE}$ (dex)	Δ_{NLTE} (dex)	$\Delta\nu$ (μHz)	ΔP ($\Delta\pi_1$) [a] (s)
4995956	4855±80	2.652±0.01	1.458±-0.003	0.12±0.15	2.56±0.19	1.1±0.17	0.15	4.917±0.026	238.7±14.54(2)
5181651	4858±80	2.623±0.01	1.468±-0.003	0.35±0.15	2.41±0.19	1.27±0.12	0.15	4.745±0.037	320.74±3.15(1)
5184199	5011±80	2.912±0.008	1.357±-0.003	0.17±0.15	2.31±0.15	1.87±0.15	0.13	7.912±0.033	241.3±19.87(2)
5439339	5082±80	2.919±0.009	1.354±-0.004	0.03±0.15	2.5±0.17	1.43±0.2	0.15	7.876±0.055	248.27±23.63(1)
5603916	4910±145	2.512±0.014	1.503±-0.004	0.2±0.3	2.2±0.22	1.03±0.19	0.16	4.01±0.028	306.13±4.82(1)
5866138	5034±80	2.867±0.008	1.376±-0.003	0.14±0.15	2.41±0.15	1.46±0.18	0.15	7.253±0.044	272.5±36.58(2)
5943345	4893±80	2.631±0.017	1.465±-0.006	0.07±0.15	2.68±0.32	1.54±0.17	0.15	4.688±0.036	292.5±2.85(2)
6115650	5112±161	2.629±0.018	1.466±-0.006	0.09±0.3	2.24±0.33	1.26±0.18	0.15	4.894±0.092	305.1±31.86(1)
6188215	5203±100	2.976±0.007	1.328±-0.003	0.03±0.15	2.43±0.14	1.51±0.15	0.15	8.739±0.024	164.2±21.18(2)
6188269	4958±100	2.726±0.009	1.431±-0.003	-0.13±0.15	2.45±0.16	1.07±0.18	0.15	5.648±0.023	189.33±1.83(1)

[a] (1) ΔP (This work) (2) $\Delta\pi_1$ (Vrard et al. 2016)

NOTE - A subset of this table is presented here to illustrate its structure and details.

- The term related to metallicity is:

$$\Delta A(Li)_{[Fe/H]} = c_0 + c_1 \times [Fe/H] + c_2 \times [Fe/H]^2 + c_3 \times [Fe/H]^3$$

- Finally, the term due to microturbulent velocity is:

$$\Delta A(Li)_{\xi} = d_0 + d_1 \times \xi$$

The coefficients a_i, b_i, c_i, d_i were adapted from Gao et al. (2021), ensuring that our calculations reflect reliable empirical relationships for estimating uncertainties. The derived A(Li) values of a few sRC stars are provided in Table 5.1

5.4 Discussion

The primary focus of this work is to investigate how Li abundances in giant stars change with stellar mass. The results are shown in Figure 5.4, which plots lithium abundance against stellar mass for both pRC and sRC stars, as well as RGB stars.

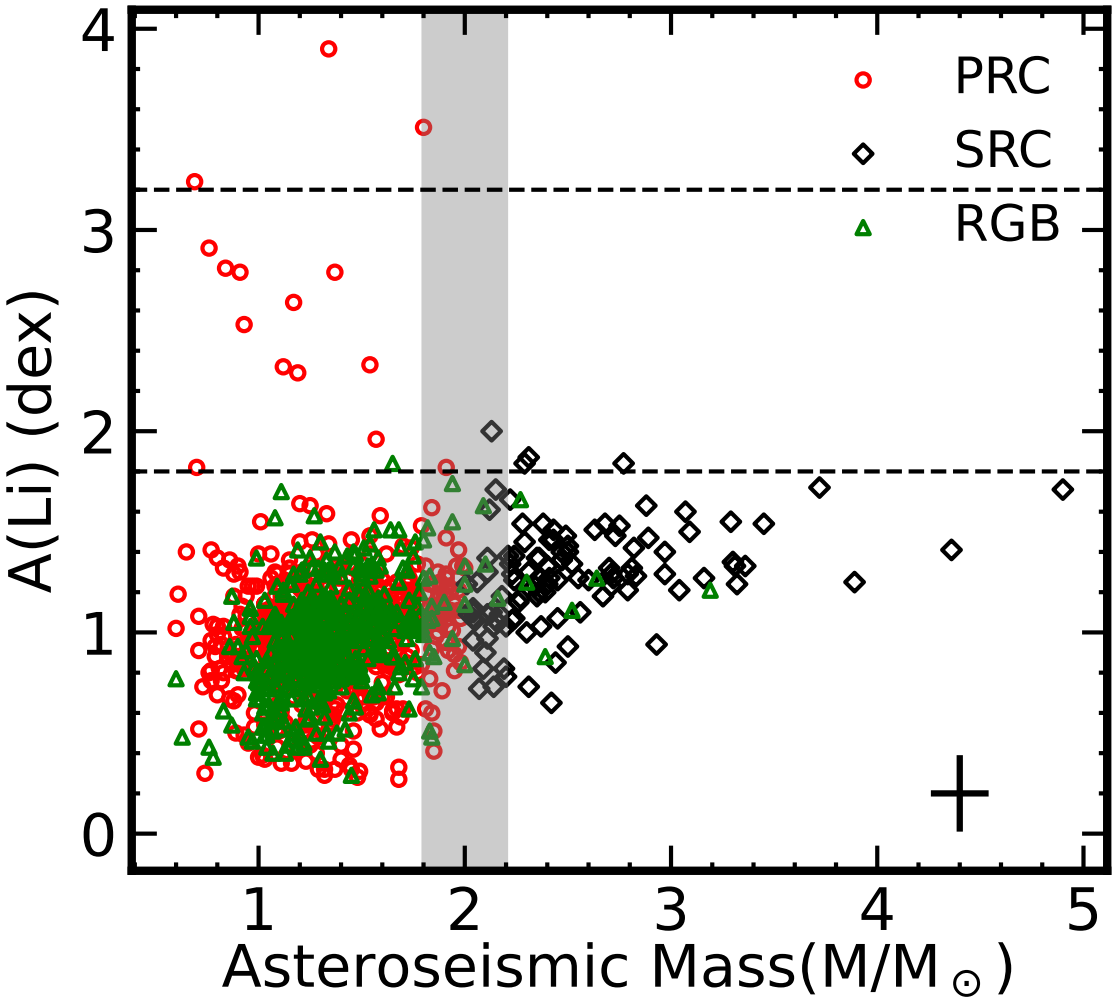

FIGURE 5.4: Lithium abundances of pRC, sRC, and RGB giants as a function of stellar mass. The horizontal lines represent the theoretical upper limits for the first dredge-up: A(Li) = 1.8 for a 1.5 $M_{\odot}$ giant and A(Li) = 3.2 for SLR giants. The error bar in the lower-right corner represents the mean uncertainties in A(Li) and stellar mass.

The boundary between pRC and sRC stars is determined by the helium flash, which occurs in stars with masses less than approximately 2 $M_{\odot}$. This distinction helps explain the significantly different Li abundances observed in these groups.

The theoretical predictions indicate that low-mass stars, which develop degenerate He cores, undergo a He flash at the RGB tip, releasing an enormous amount of energy. This energy manifests as a sharp decline in luminosity and an upsurge of Li in the outer layers. The energy emitted during the helium flash is primarily

consumed to lift the hydrogen-burning shell upwards, while only a fraction escapes into the surrounding layers. As a result, Li can be transferred from the core towards the photosphere, leading to an observable enhancement.

We utilized the Modules for Experiments in Stellar Astrophysics (MESA) models following the methodology outlined by Schwab (2020) to simulate the Li evolution of both pRC and sRC stars. The MESA models predicted lithium abundances for high-mass giants ranging from approximately 0.7 to 1.6 dex (see Fig. 5.5), depending on mass. These theoretical predictions align closely with our observed lithium values for pRC stars

The observed transition mass M_{HeF} delineates two groups of stars: primary red clump (pRC) giants, which develop degenerate helium cores and undergo helium flashes, and secondary red clump (sRC) giants, which are more massive and do not experience a helium flash. In our sample, we found that all pRC giants, including three super lithium-rich giants (SLRGs) and 11 stars with A(Li) $>$ 1.8 dex, exhibit lithium abundances significantly higher than what is predicted by standard evolutionary models and their counterparts on the upper RGB. This discrepancy suggests that the helium flash serves as a crucial process for lithium enrichment in low-mass giants. In contrast, high-mass stars ($> 2M_{\odot}$) experience He burning under non-degenerate conditions and do not undergo a He flash. This explains why Li abundances in sRC stars remain consistent with the theoretical maximum for first dredge-up, which typically limits to A(Li) = 1.8 dex. A comparison of the observed Li values with the theoretical predictions for sRC stars shows a good agreement, with only a few exceptions, where some stars have slightly higher A(Li) values than expected (by 0.1-0.3 dex). These slight differences could be attributed to uncertainties in the measurements rather than fresh Li production.

Importantly, none of the sRC stars in our sample exhibit SLR characteristics (A(Li) $>$ 3.2), further reinforcing the idea that the helium flash is a key process

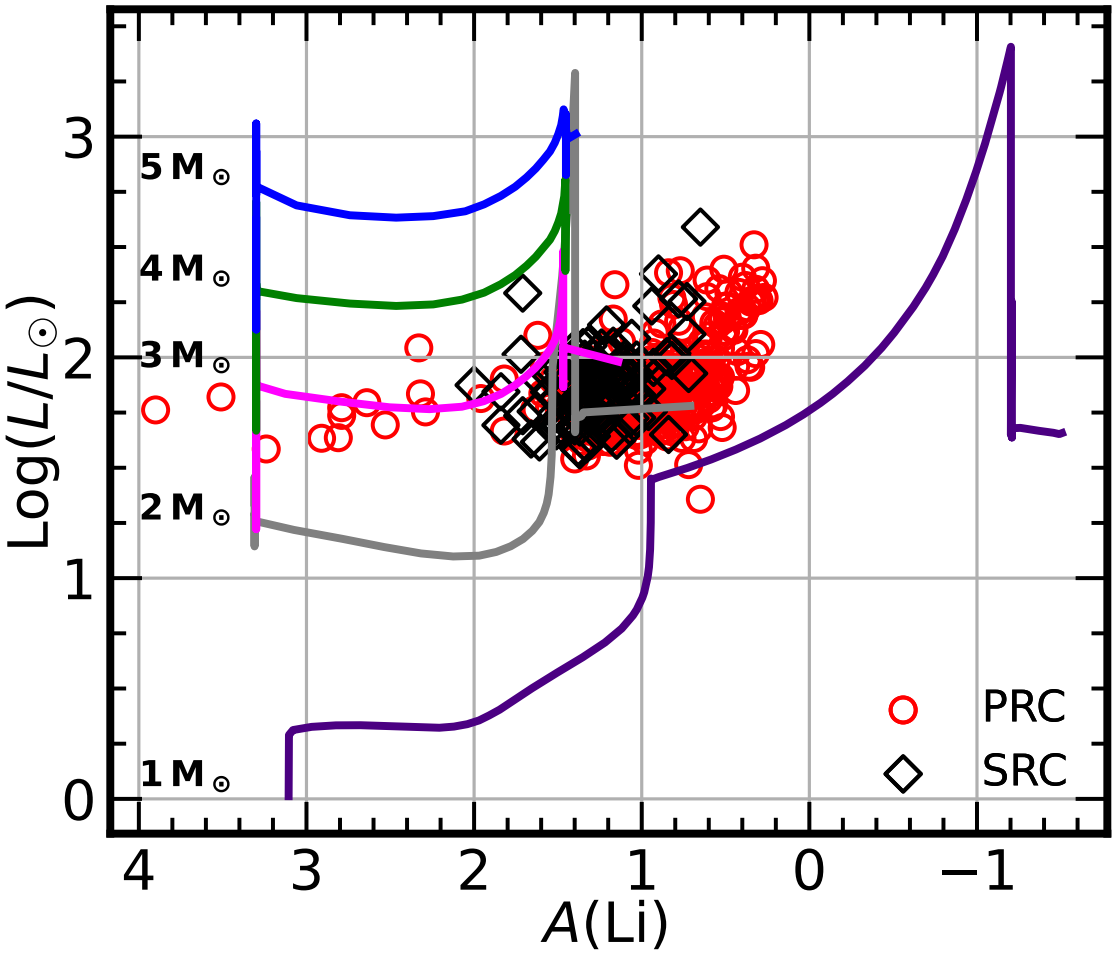

FIGURE 5.5: The pRC and sRC giants are shown in a Luminosity vs. A(Li) plot, with MESA models for 1-5 $M_{\odot}$ giants superimposed. Many LRGs, including SLRGs, are found among the pRC giants, while none are present among the sRC giants. The models indicate that pRC giants undergo substantial Li depletion during the first dredge-up and at the luminosity bump.

in Li enrichment. By contrast, several pRC stars, which have undergone a helium flash, exhibit super lithium-rich behavior. The range of lithium abundances among pRC giants is also larger compared to the sRC stars, likely due to more pronounced lithium depletion through the first dredge-up and extra mixing in the former group.

The findings of this study align with previous work by Deepak & Reddy (2019) and Deepak & Lambert (2021), which emphasized the role of mass in Li enrichment. Our study builds on these efforts by utilizing a large sample that combines data from the Kepler and LAMOST catalogues, overcoming limitations related

to small sample sizes and inaccurate mass determinations. Furthermore, while some earlier studies (Martell et al. 2021; Zhou et al. 2022) have suggested that giants with large Li abundances exist across a variety of masses and evolutionary phases, our results indicate that most Li enriched giants have low stellar masses which have experienced a He flash. These differences may stem from variations in sample selection and methods of classifying the stars' evolutionary stages. Unlike previous studies that relied on stellar parameters alone, our analysis is based on direct asteroseismic measurements of ν_{max} and ΔP, providing more reliable phase identification.

While the He flash remains the most likely source of Li enrichment in low-mass stars, further research is needed to fully understand the mixing mechanisms that transport Li from the stellar core to the surface. The absence of Li-rich giants among sRC stars, despite their similar evolutionary status to pRC stars, suggests that the flash itself plays a crucial role in Li production.

5.4.1 Statistical Trends in Lithium-Rich Stars Across Evolutionary Groups

To further examine the evolutionary origin of Li enrichment, we quantified the frequency of Li-normal(LN), Li-rich(LR), and super Li-rich (SLR) stars across the three evolutionary groups: pRC, sRC, and RGB stars. These categories were defined using two physically motivated phase-sensitive schemes outlined in Liu et al. (2014); Singh et al. (2021). Based on this classification, the Li distribution in our sample is tabulated in Table 5.2 :

These trends indicate that lithium enrichment (A(Li) $>$ 1.0 dex) is significantly more common in sRC stars than in pRC stars. This is consistent with their higher masses and the absence of mixing processes such as the RGB bump, which depletes

TABLE 5.2: Distribution of lithium abundances among red giants, separated by evolutionary phase.

Category	Li-normal	Li-rich	Super Li-rich (SLR)
pRC (668)[a]	308 (46.1%)	357 (53.4%)	3 (0.45%)
sRC (109)[a]	14 (12.8%)	95 (87.2%)	0 (0%)
RGB (463)[b]	461 (99.6%)	2 (0.43%)	0 (0%)

[a] For RC → Li-normal: A(Li) ≤ 1.0; Li-rich: 1.0 < A(Li) < 3.2; SLR: A(Li) ≥ 3.2.

[b] For RGB → Li-normal: A(Li) ≤ 1.7; Li-rich: A(Li) >1.7; SLR: A(Li) ≥ 3.2.

Li in lower-mass stars. MESA models further support slower depletion in sRCs (see Fig. 5.5) Conversely, RGB stars are predominantly low-mass and have not undergone a core helium flash. The rarity of Li-rich stars and the absence of SLR stars in this group is therefore expected.

Of particular interest is the distribution of super Li-rich stars. All three SLR stars are found exclusively in the pRC population, and none are detected in either the sRC or RGB samples. Given the observed SLR frequency in pRC stars (∼0.45%), one would statistically expect ∼0 SLR stars in the sRC (109 stars) and ∼2 in the RGB (463 stars). While the absence in the sRC is statistically consistent, the lack of SLR stars in the RGB population, where some are expected, is more significant.

These results strongly support the hypothesis that SLR stars are produced via an internal mechanism activated by the helium flash, which occurs only in low-mass stars. Since SLR abundances exceed the primordial lithium level, such enrichment cannot be explained by preservation or inefficient depletion alone. The exclusive presence of SLR stars in the pRC group underscores the role of the helium flash as a critical process in Li production.

The extremely low frequency of LR stars in the RGB population is also noteworthy. While two RGB stars in our sample exhibit $A(\mathrm{Li}) > 1.7\,\mathrm{dex}$, both remain below the theoretical FDU limit of 1.8 dex, with measured values in the range

of ∼1.75–1.78 dex. Given our abundance uncertainties of approximately 0.2 dex, derived from medium-resolution spectra, we adopted a conservative approach in interpreting these cases. It is therefore possible that some low-level LR RGB stars exist in the broader population, particularly due to variations in initial lithium abundance or differing depletion levels. However, their occurrence is clearly rare in comparison to both RC groups.

To summarize:

- Li-rich stars (A(Li) > 1.0 dex) appear more frequently in sRC stars than in pRC stars, consistent with their higher masses and the absence of depletion at the RGB bump.
- Stars with A(Li) > 1.7 dex are rarely found among RGB stars, likely due to their low masses, Li depletion during bump crossing, and the absence of core helium ignition.
- Super Li-rich stars (A(Li) ≥ 3.2 dex) are detected only among pRC stars. Their occurrence is absent in both sRC and RGB populations, reinforcing the interpretation that such extreme Li enhancement likely originates from He-flash-induced mixing events.

These results are also relevant in the context of an earlier work by Yan et al. (2021), who identified seven RGB stars with A(Li) > 2.0 dex in their LAMOST low-resolution sample. However, since their data are from lower-resolution spectra and do not include error estimates, it is difficult to compare directly with our results. In their high-resolution spectroscopic follow-up of 26 stars, only one source (KIC 9596106) was properly classified as an RGB star using asteroseismic data and found to be Li-rich (A(Li) = 2.18 ± 0.06 dex). Unfortunately their study sample did not provide stellar mass estimates publicly, and it is plausible that some of their identified Li-rich RGB stars belong to higher-mass regimes that do

not undergo depletion at the RGB bump. In contrast, our work employs medium-resolution spectroscopy, well-defined seismic classifications, and evolutionary mass constraints, along with more cautious treatment of abundance thresholds. Hence, our conclusions are not inconsistent with those of Yan et al. (2021), but reflect a more conservative and physically constrained sample.

5.4.2 Measurement of Mixed-Mode Period Spacing

In order to determine the evolutionary phase of the stars in our sample more precisely, we calculated their period spacing, which plays a vital role in distinguishing between stars in different stages of evolution. Although the stars in the Yu et al. (2018) catalogue already had known evolutionary phases, deriving their period spacing allowed us to refine their classification based on the asteroseismic diagram of ΔP versus $\Delta\nu$ (Bedding et al. 2011).

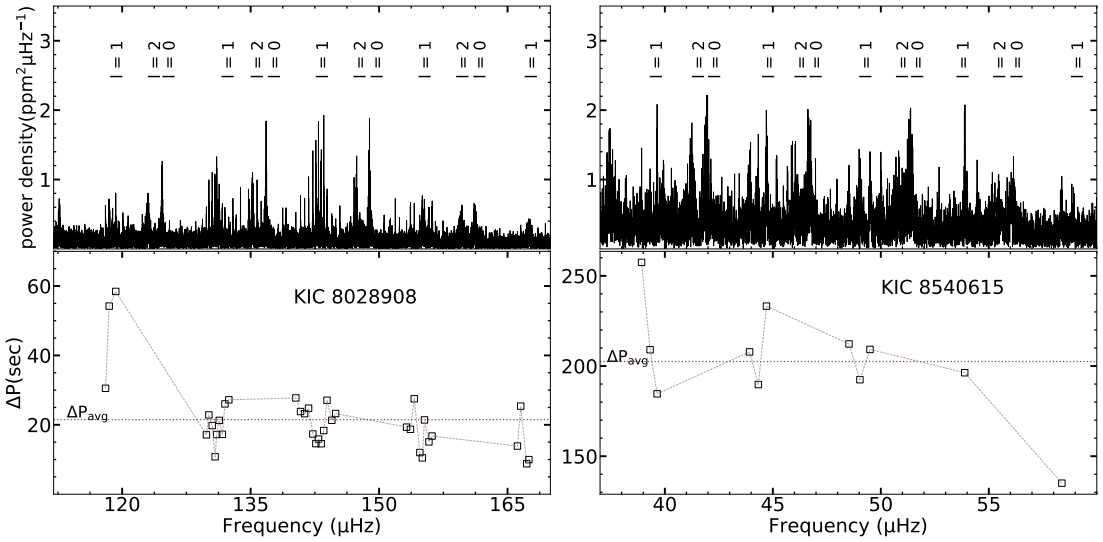

FIGURE 5.6: Upper left panel displays the PSD of an RGB star KIC 8028908, while the upper right panel shows the PSD of an RC star KIC 8540615. Oscillation modes corresponding to l = 0, 1, and 2 are labeled in the figure. The lower panel illustrates the process of measuring mixed-mode period spacing (ΔP), with the red dashed horizontal line indicating the average period spacing in each bottom panel.

Evolved stars exhibit a wide range of oscillation modes, including radial, dipole, and quadruple modes. The dipole modes, in particular, are of mixed nature, arising from interactions between pressure modes in the outer layers and gravitational modes in the inner core. These mixed dipole modes exhibit approximately equal spacing in period, which allows for the identification of a star's evolutionary phase (Tassoul 1980).

For this study, we obtained Kepler photometric observations from the Mikulski Archive for Space Telescopes (MAST) and transformed the time-series into frequency domain utilizing the Lomb-Scargle periodogram technique. We visually inspected the power density spectra to identify radial ($\ell = 0$), dipole ($\ell = 1$), and quadruple ($\ell = 2$) modes in each star. Three to five sequences of mixed modes were identified (refer to the upper panels of Figure 5.6). Period spacing was determined from successive mixed dipole modes. The average value was adopted as the period spacing of the star, with the standard deviation representing the associated error.

To ensure accuracy, we compared our derived period spacing values with those provided by Vrard et al. (2016) for six stars—two each from the RGB, primary RC, and secondary RC phases. The comparison as illustrated in Figure 5.7 showed strong agreement, with a linear regression coefficient of r = 0.99, confirming the reliability of our period spacing measurements.

5.4.3 Variation in the Transition Mass for Helium Flash Events

The mass at which stars experience the helium flash can vary slightly depending on their composition. The typical range for stars to undergo helium flash falls between 1.8 and 2.2 $M_{\odot}$ (Chiosi et al. 1992), with other studies suggesting a range

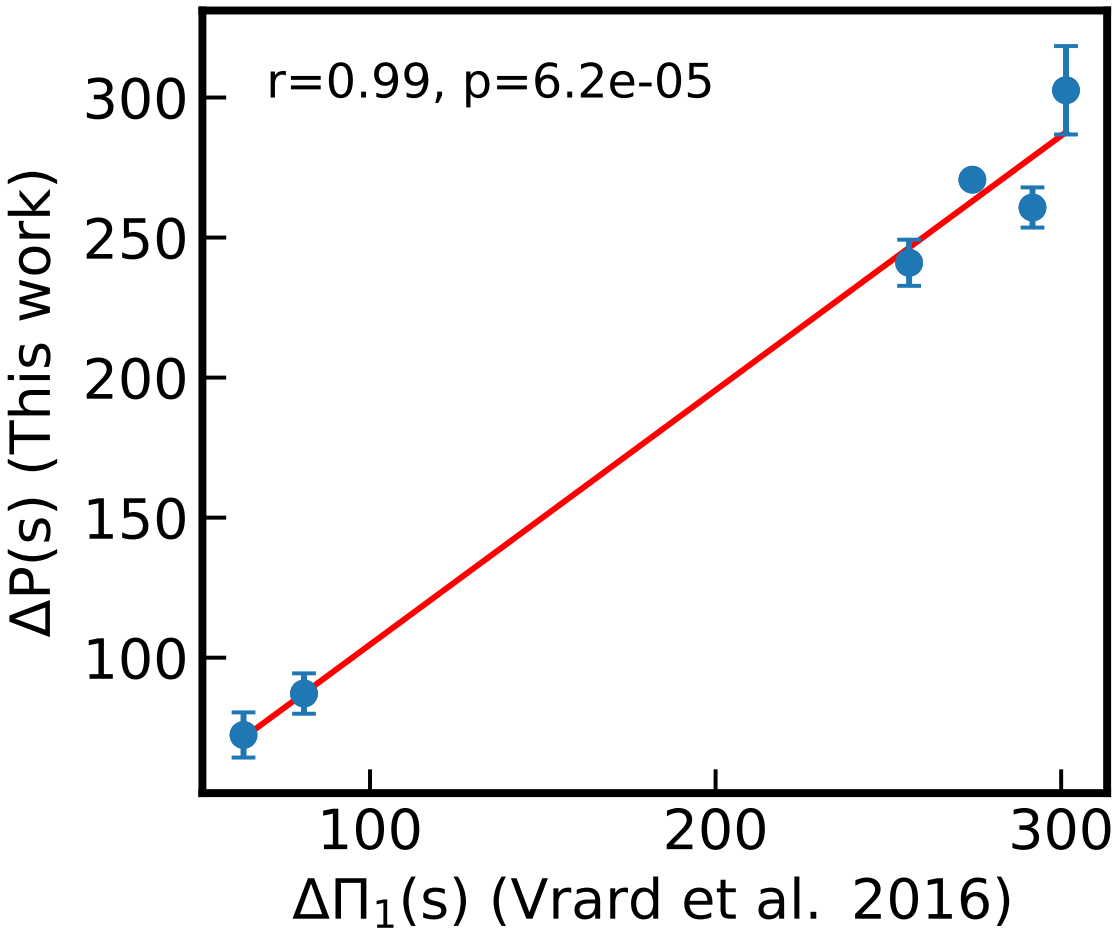

FIGURE 5.7: Comparison of average period spacing determined in this study with values reported by Vrard et al. (2016)

extending to 2.5$M_\odot$ (Girardi 1999). For the purpose of this analysis, we used a median value of 2$M_\odot$ to differentiate between pRC and sRC stars.

In Figure 5.4, one super lithium-rich star appears near the $M_{HeF} = 2M_\odot$ boundary. To further verify its evolutionary status, we plotted the helium core mass (M_c) and stellar luminosity (L) from the main sequence to the end of the core helium-burning phase using MESA model of [Fe/H] = 0.14. The minima of M_c and L, plotted against the asteroseismic mass (M_{cl}), are used to determine the M_{HeF} value. As seen in Figure 5.8, for KIC 8879518 (M_{cl} = 1.80 $M_\odot$ and [Fe/H] = 0.14) the M_{HeF} is found to be 2.1 $M_\odot$. Since $M_{Cl} < M_{HeF}$, it is confirmed that it underwent a He flash and can be unambiguously classified as a pRC star.

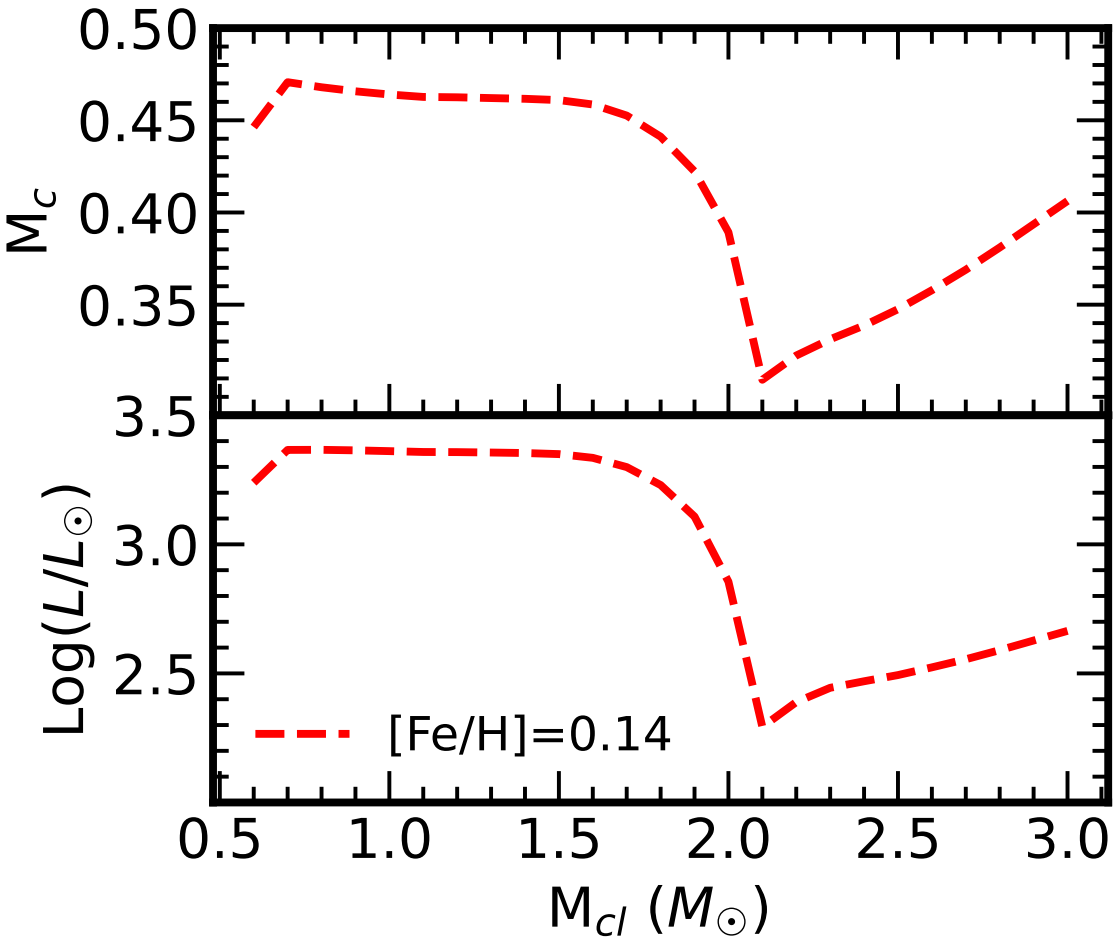

FIGURE 5.8: He-core mass and luminosity as a function of stellar mass for two metallicities, spanning both main sequence and core helium-burning phases.

5.5 Conclusion

This study has utilized a large sample of RGB and RC stars, whose evolutionary phases were determined using direct asteroseismic measurements of period spacing (ΔP) and frequency spacing ($\Delta\nu$). Li abundances were derived from LAMOST spectra using spectral synthesis methods, allowing us to compare observed values with theoretical predictions for stars at different evolutionary stages.

Our findings indicate that Li enhancement is predominantly observed in low-mass primary red clump (pRC) stars, which have undergone a He flash. In contrast, high-mass secondary red clump (sRC) stars do not show significant Li enrichment,

with their Li abundances remaining consistent with the theoretical expectations for first dredge-up. This lack of Li enriched giants in sRC population strengthens the notion that the helium flash, which only occurs in low-mass stars, is the key event responsible for lithium enrichment.

Our results further contribute to the growing body of evidence that links Li enrichment to the He flash in low-mass stars. However, the exact transport and mixing mechanisms involved in bringing Li from the stellar core to the surface remain uncertain. Future studies that combine Li data with other indicators, such as carbon isotopic ratios ($^{12}C/^{13}C$), may help shed light on the underlying processes responsible for this enhancement.

Chapter 6

High Lithium Abundance and Strong Chromospheric Helium in Red Giants: A combined Asteroseismic and Spectroscopic Perspective

6.1 Overview

This study (Results of this study are published in Mallick et al. (2025), ApJ) investigates the correlation between elevated lithium abundances and the prominent absorption strength of the chromospheric He I 10830 Å feature among field

giants from the Kepler mission. The sample consists of 84 red giants exhibiting detectable solar-like oscillations in their light curves. Lithium abundances were either sourced from prior studies or determined using LAMOST medium-resolution spectra. Asteroseismic analyses were employed to determine evolutionary phases, with the mixed-mode period spacing (ΔP) providing insights into the temporal evolution of red clump (RC) giants. Observations of the He I λ10830 line were carried out using the Habitable-zone Planet Finder (HPF) spectrograph mounted on the 10-m class Hobby–Eberly Telescope (HET).

Both elevated lithium abundances and increased He I absorption are seen exclusively in RC giants, with their absence in red giant branch (RGB) stars pointing to a possible connection with the helium flash. Among RC stars, the He I line strength diminishes steadily with decreasing lithium levels, suggesting a clear relationship. Older, lithium-normal RC giants exhibit weaker helium activity, while younger, super lithium-rich RC stars display stronger He I absorption.

The findings propose that the core helium flash and its subsequent sub-flashes could explain both the heightened lithium in the photospheres of RC giants and the increased chromospheric activity responsible for strong He I absorption in younger RC stars. Over time, as the effects of the helium flash fade, chromospheric activity weakens, resulting in older RC stars exhibiting normal lithium levels and reduced helium absorption.

6.2 Introduction

According to standard cosmological nucleosynthesis models, the expected primordial lithium abundance is approximately A(Li) $\simeq$ 2.6 dex (Mitler 1972; Romano et al. 2001). However, observations show higher abundances, with values such as

A(Li) $\simeq$ 3.2 dex found in early age stars and the interstellar medium, indicating that lithium has been enhanced significantly since the Big Bang. Two key processes—cosmic ray spallation (CRS) and stellar nucleosynthesis—are thought to contribute to this enrichment. While CRS alone is insufficient to explain the observed fourfold increase in lithium, standard stellar evolution models consider stars as lithium sinks rather than sources (Iben 1968; Pinsonneault et al. 2000). Observations largely support this theoretical framework.

However, spectroscopic studies over the past several decades have identified rare cases of evolved stars with unusually elevated lithium levels. These include intermediate-mass stars (M $\geq$ 3M$_\odot$ on the asymptotic giant branch (AGB) and low-mass stars on the red giant branch (RGB). For AGB starsof intermediate mass, the hot bottom burning (HBB) process is believed to explain the observed lithium enrichment (Holanda et al. 2020). Nevertheless, the source of lithium enhancement in low-mass giants remains an open question, persisting since its initial discovery (Wallerstein & Sneden 1982).

The development of all-sky spectroscopic surveys has advanced this field significantly. These surveys have identified numerous lithium-rich giants (LRGs) for which A(Li) $>$ 1.5 dex, exceeding the theoretical upper limit for evolved stars. Among these, a subset of SLR stars with A(Li) $\geq$ 3.2 has also been identified (Kumar et al. 2011; Singh et al. 2019; Deepak & Reddy 2019; Magrini et al. 2021; Yan et al. 2021). Building on the work of Kumar et al. (2011), which proposed that lithium production might be linked with the helium flash at the tip of the RGB, subsequent studies have shown that most LRGs are RC stars burning He in their cores. All known SLRs confirmed through asteroseismology have also been identified as RC stars.

The evidence strongly suggests that the helium flash may play a pivotal role in lithium enhancement among RC stars (Casey et al. 2019; Kumar et al. 2020;

Martell et al. 2021; Singh et al. 2021; Sneden et al. 2022; Mallick et al. 2023). However, the physical mechanisms responsible for producing lithium and its mixing during the helium flash remain unclear. Furthermore, the possibility of multiple sites or mechanisms for lithium enrichment in giants cannot be excluded. Although a few RGB stars have been documented with high lithium levels (Ruchti et al. 2011; Kirby et al. 2016; Magrini et al. 2021; Tsantaki et al. 2023), their evolutionary states were often determined using HR diagrams or machine-learning approaches rather than asteroseismology, necessitating further study.

In addition to lithium enrichment, this study explores whether Li-rich giants exhibit distinctive chromospheric characteristics. The He I λ10830 line was first noted as unusually strong in a Li enhanced star (A(Li) $>$ 1.5 dex) by Sneden et al. (2021). A subsequent survey by Sneden et al. (2022) concluded that approximately 56% of their observed Li-rich field giants displayed strong 10830 Å absorption. This paper aims to examine the relationship between lithium abundance, helium line strength, and the evolutionary phases of 84 red giants observed by Kepler.

6.3 Sample Selection

Our investigation focused on acquiring high-resolution spectra of the He I 10830 Å profile in RGB stars that also have lithium abundances and asteroseismic data available. Following the advancements in asteroseismology initiated by the MOST (Walker et al. 2003) and CoRoT (Catala & COROT Team 2001) missions, the Kepler mission (Borucki et al. 2010) surveyed over 500,000 giants, primarily located within a 115-degree field in Cygnus. From its final data release (DR25) (Coughlin et al. 2017), Kepler identified solar-like pulsations in nearly 22,000 RGB stars (Hon et al. 2019).

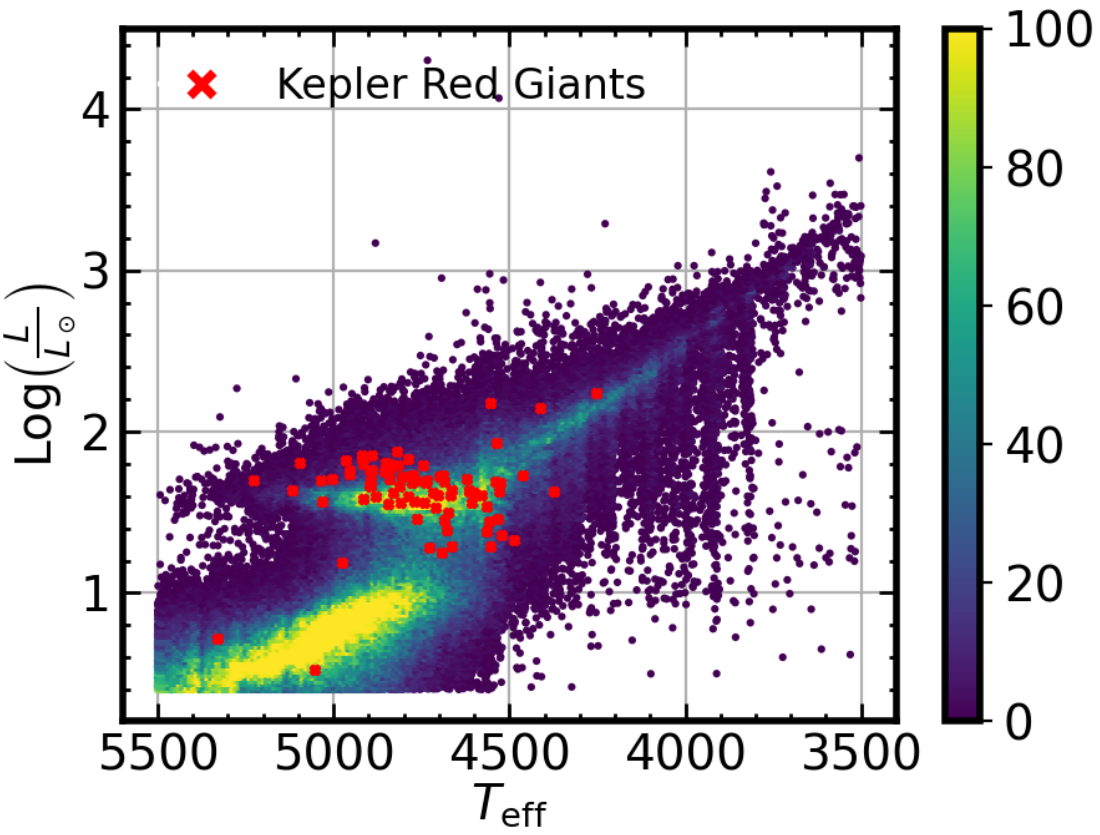

FIGURE 6.1: HR diagram showing the 84 red giants in the sample (marked as red crosses) with the complete *Kepler* Input Catalog displayed in the background.

To compile the sample, we searched for Kepler giants with previously published lithium abundances from four major spectroscopic studies:

1. Singh et al. (2019): Investigated 24 lithium-rich Kepler giants using low-resolution spectra (R ≈ 1800) from the LAMOST survey.

2. Singh et al. (2021): Provided medium-resolution (R ≈ 7500) lithium measurements for 12 stars using LAMOST MRS data.

3. Yan et al. (2021): Measured lithium abundances for 29 giants using high-resolution spectra from multiple telescopes, including the Lijiang 2.4m and Subaru.

4. Takeda & Tajitsu (2017): Published detailed lithium measurements for 103 Kepler stars.

Additionally, lithium abundances for several giants from the LAMOST medium-resolution survey (DR10) were included, provided that the Li I 6707.8 Å line could be measured. The final sample consists of 11 stars from Yan et al. (2021), 12 from Takeda & Tajitsu (2017), 10 from Singh et al. (2021), 12 from Singh et al. (2019), and independent measurements for 39 stars from LAMOST DR10, culminating in a total of 84 stars.

High-resolution near-infrared spectra (zyJ band, 8400–12500 Å) were collected using the HET equipped with the Habitable Zone Planet Finder (HPF) spectrograph. To ensure optimal signal-to-noise ratios (SNR), the sample was limited to stars with a brightness range of $3 < \mathrm{Jmag} < 13$. Further details regarding the spectra and reduction process are discussed in Section 6.5. Figure 6.1 presents the HR diagram of the sample, showcasing the stellar distribution within the Kepler field analyzed in this work.

6.4 Lithium Measurements from LAMOST

Medium-resolution spectra ($R \approx 7500$) were analyzed for 39 giants using data from the LAMOST survey. Each observation yielded two spectral bands: a blue band spanning 4950–5350 Å and a red band covering 6300–6800 Å. Since the red band includes the Li I resonance line located at 6707.8 Å, it was utilized for this study. All spectra were coadded to improve quality, achieving signal-to-noise ratios exceeding 35 in the red band, sufficient for lithium abundance determinations.

The spectra were corrected for radial velocity shifts using data from Gaia DR3 (Katz et al. 2023) and normalized using standard IRAF routines. Stellar parameters, including T_{eff}), log g and [Fe/H], were adapted from the LAMOST MRS

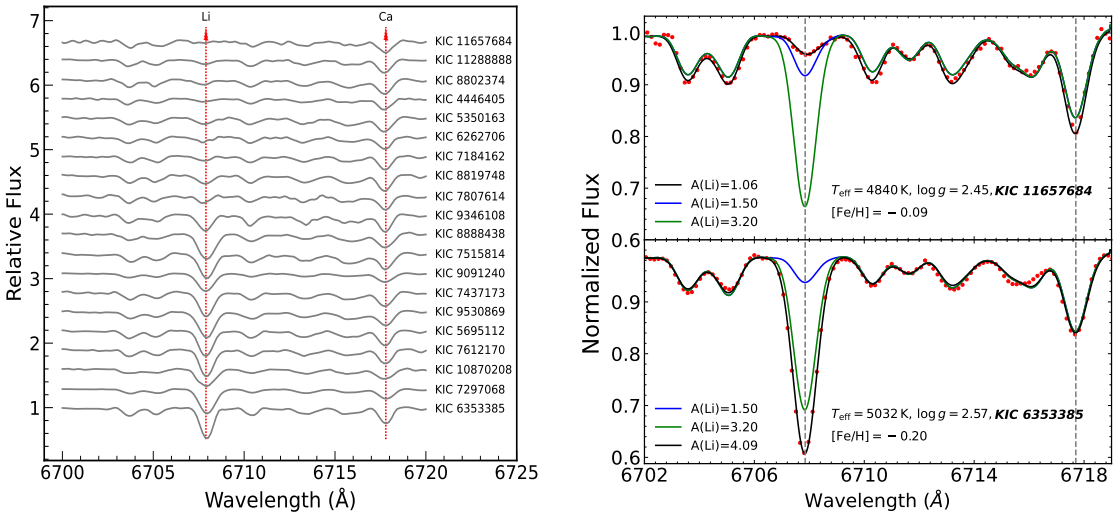

(a) (b)

FIGURE 6.2: Panel (a) shows spectra of several giants from *LAMOST* with Li abundances determined in this study. Panel (b) presents the spectrum synthesis for two *Kepler* giants, representing the lowest and highest Li abundances observed. The vertical dashed lines mark the positions of the Li resonance line at 6707.8 Å and a prominent Ca line at 6717.7 Å. The solid black line represents the best fit to the observed spectrum

parameter catalog (Xiang et al. 2015). Microturbulent velocities (ξ) are calculated from empirical relations defined by Holtzman et al. (2018) and García Pérez et al. (2016).

Stellar atmospheric models were constructed using the ATLAS9 code (Castelli & Kurucz 2003), and synthetic spectra were generated with pyMOOGi, a Python interface for the MOOG radiative transfer code (Sneden 1973). Lithium abundances were iteratively adjusted in the synthetic models to best match the observed spectra by minimizing the chi-square statistic. Figure 6.2 presents the spectra of selected giants analyzed in this work. Panel (a) displays representative spectra from LAMOST, emphasizing the Li resonance line at 6707.8 Å along with a prominent Ca line at 6717.7 Å. In panel (b), spectrum synthesis for stars with the lowest and highest Li abundances is shown, illustrating the spectral features utilized to determine A(Li). A(Li) values for some reference stars are presented in Table 6.1.

6.5 HPF Observations and Reductions

We acquired high-resolution spectra of 84 Kepler field giants using the Habitable Zone Planet Finder (HPF) spectrograph mounted on the Hobby–Eberly Telescope (HET). The HPF is a near-infrared spectrograph that operates across the zyJ photometric bands (8100–12750 Å) with a resolving power R ≈ 55,000 (Mahadevan et al. 2012, 2014).

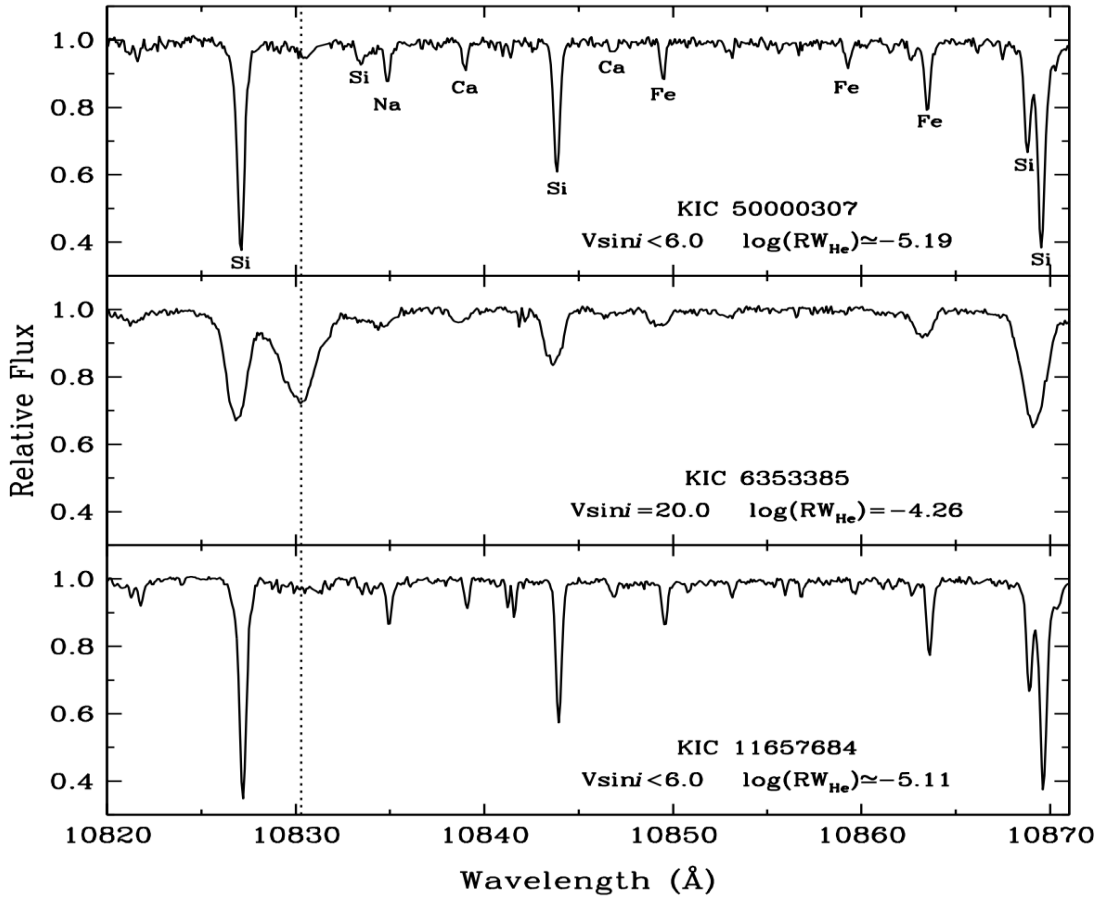

FIGURE 6.3: Spectra of He I 10830.3 Å for three program stars, also shown in other figures of this chapter. The HPF spectral order covering the λ10830 line ranges from approximately 10820 Å to 10960 Å, placing the λ10830 feature near the blue end of the order. Key atomic features, attributed to transitions of neutral species, are labeled by element, with the He I feature marked by a dotted vertical line.

These spectra were obtained over a two-year period, during which we employed a reduction process described by Sneden et al. (2022). A brief outline of the

reduction steps follows: The raw data frames were processed using the HPF facility's automatic reduction package, *Goldilocks*[1]. This package performed initial corrections and prepared the spectra for further analysis. The reduction steps included sky emission subtraction, order-by-order continuum normalization, division by telluric absorption lines, wavelength calibration, and radial velocity correction for each star.

The final 2D echelle spectra were used for analysis. The analysis focused on the He I λ10830 Å line, with its rotational velocity and equivalent width as the primary measurable quantities. We followed the techniques outlined in Sneden et al. (2022) for measuring the EW and rotational broadening of the λ10830 Å line. These measurements were essential for exploring the connection between the chromospheric activity and photospheric lithium abundance.

In Figure 6.3, we show example spectra for three of our program stars, which represent a range of lithium abundances and He I λ10830 Å line strengths.

6.6 Asteroseismic Investigation of Kepler Red Giants

6.6.1 Stellar Pulsation Theory

Solar-like pulsations occur in stars that have cooler outer convective regions. Such oscillations are driven by turbulent activity within the convective zones, which trigger pulsations that deform the stellar surface. Such oscillations are commonly observed in main-sequence stars, subgiants, red giants, and asymptotic giant branch

[1]https://github.com/grzeimann/Goldilocks_Documentation

(AGB) stars, all of which possess unstable outer convective zones.

The oscillation modes can be radial or non-radial. Radial modes are characterized based on the radial order n, which indicates the count of nodal lines along the radius. Non-radial modes are characterized using spherical harmonics Y_ℓ^m, where ℓ denotes the angular degree (indicating how many nodal lines exist on the surface), and m represents the azimuthal order (indicating how many nodal lines intersect the poles).

Due to the point-like nature of distant stars and the resulting cancellation effects, only modes with higher radial orders n and lower angular degrees l are typically observable. Under these conditions, stellar oscillations can be well described in the asymptotic regime ($n \gg \ell$) (Tassoul 1980).

Solar-like oscillations, also called p-modes, have pressure as the force that acts to restore equilibrium. Additionally, g-modes, which travel through the inner radiative region, have gravity as the restoring force. In evolved stars like subgiants and RGBs, a sharp density gradient across the core and the outer convective layers divides the star into two distinct wave cavities:

- An inner cavity, where g-modes propagate.
- An external cavity, where p-modes dominate.

Coupling between the two modes occurs in the evanescent region between these cavities, giving rise to mixed modes. These modes exhibit acoustic characteristics in the outer layers and g-mode characteristics in the inner layers (Kjeldsen & Bedding 1995). In red giants, mixed modes are primarily g-dominated (Dupret et al. 2009).

Consequently, RGB stars exhibit a complex frequency spectrum with evenly spaced peaks due to p-modes. Additional peaks occur with a less structured arrangement, arising from mixed modes and other peaks uniformly spaced in period corresponding to g-modes. Three global seismic parameters are crucial for describing these oscillations:

1. Peak frequency (ν_{max}): The frequency at which acoustic modes (p-modes) reach maximum amplitude.

2. Large frequency spacing ($\Delta\nu$): The variation in frequency between p-modes of the same angular degree ℓ and adjacent radial orders n.

3. Average period spacing (ΔP): The spacing in periods between g-modes of successive radial orders n of same angular degree ℓ

In the RGB stage, stars of mass $\geq$ 0.8 $M_{\odot}$ experience a rapid descent in the HR diagram, characterized by the core helium flash, before reaching a stable phase where He continues to fuse in the core (Iben 1968). The core mass at the beginning of the helium flash is approximately 0.45 $M_{\odot}$ for all stars, resulting in a narrow luminosity range and minor temperature variations due to differences in stellar mass and composition. Clump stars overlap with giants ascending the RGB, particularly in field stars.

Bedding et al. (2011) demonstrated that asteroseismology can distinguish RGB stars from core helium-burning stars using two key parameters: the p-mode large frequency spacing ($\Delta\nu$) and the average period interval (ΔP) of dipole mixed modes. RC stars have significantly higher ΔP values compared to RGB stars.

6.6.2 Data Preparation

The Kepler mission observed a variety of pulsating stars with photometric variations monitored at two cadences: the short cadence (SC) of 58.9 seconds and the long cadence (LC) of approximately 29.4 minutes. Evolved RGB stars, which exhibit $\nu_{max} \sim 20\mu$Hz (corresponding to half-day periods), are well-suited to the LC sampling rate.

In this study, we utilized LC light curves because long-duration data are essential for detecting low-frequency oscillations and resolving modes. The Kepler dataset provides two types of flux:

1. Simple Aperture Photometry (SAP) flux: Raw pixel data, calibrated and photometrically analyzed, but still containing instrumental effects.
2. Pre-search Data Conditioning (PDC) flux: Corrected flux where instrumental perturbations have been removed (Smith et al. 2012).

Three stars in our sample lacked Kepler time-series data, so we used TESS LC data with a similar cadence of 30 minutes. Both Kepler and TESS light curves were processed using the Python-based Lightkurve package ((Lightkurve Collaboration et al. 2018).

Although the PDC flux mitigates most instrumental artifacts, some issues persist, including flux fluctuations caused by cosmic rays, zero-crossing events, detector saturation, pointing losses, and rolling band artifacts from detector electronics. To address these anomalies, a stringent 4.5-sigma clipping technique was applied, as described by Handberg & Lund (2014). This method removed outliers during momentum desaturation.

Only data points with quality flags set to zero were retained. To fill gaps caused by data removal, random white Gaussian noise was introduced (see Fig. 6.4). The corrected light curves from different quarters were normalized and stitched together, producing a dataset suitable for asteroseismic analysis.

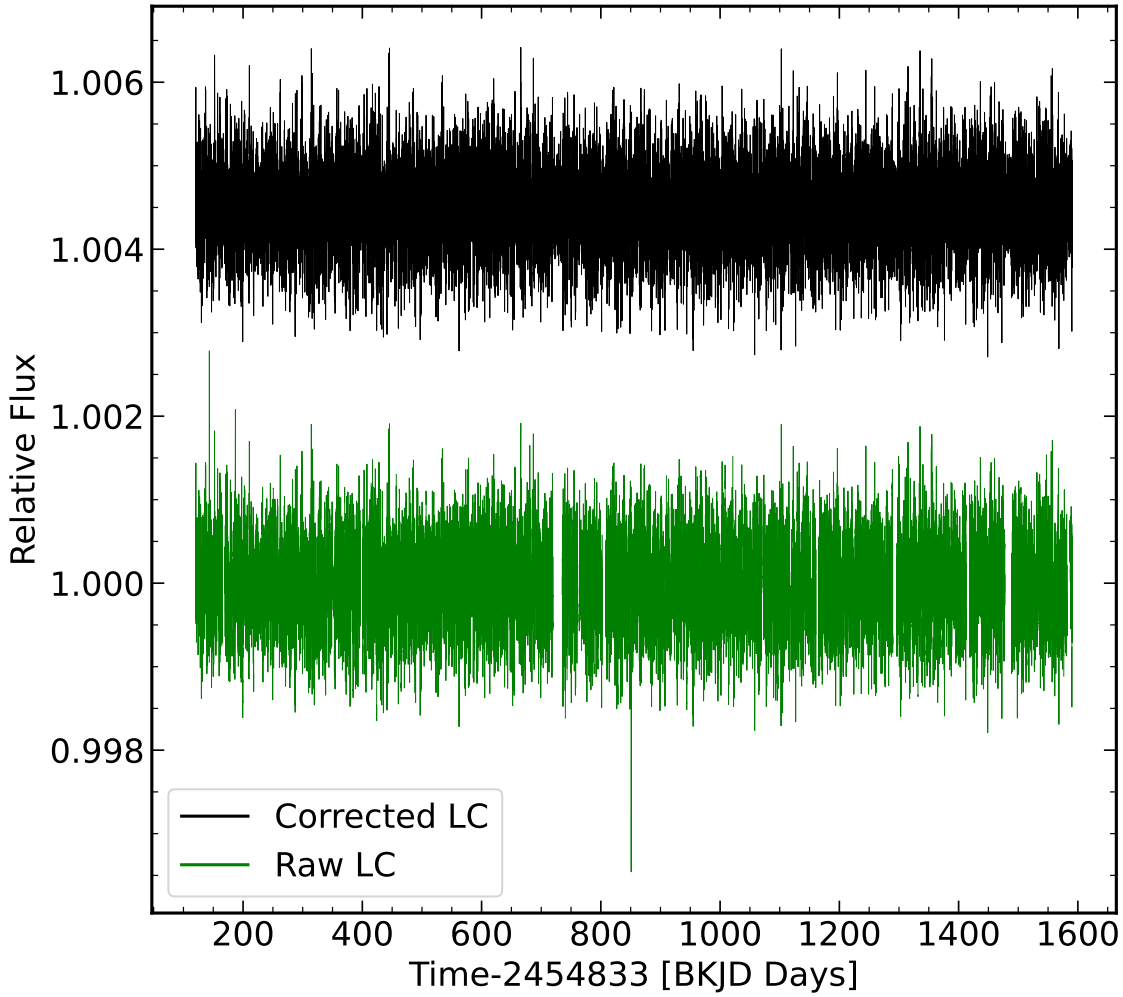

FIGURE 6.4: The raw(green) and corrected(black) lightcurves from *Kepler* for KIC 5000307

6.6.3 Seismic Parameters

In asteroseismology, light curve data is analyzed in the frequency domain by evaluating the power spectral density (PSD). To handle irregularly sampled data, the

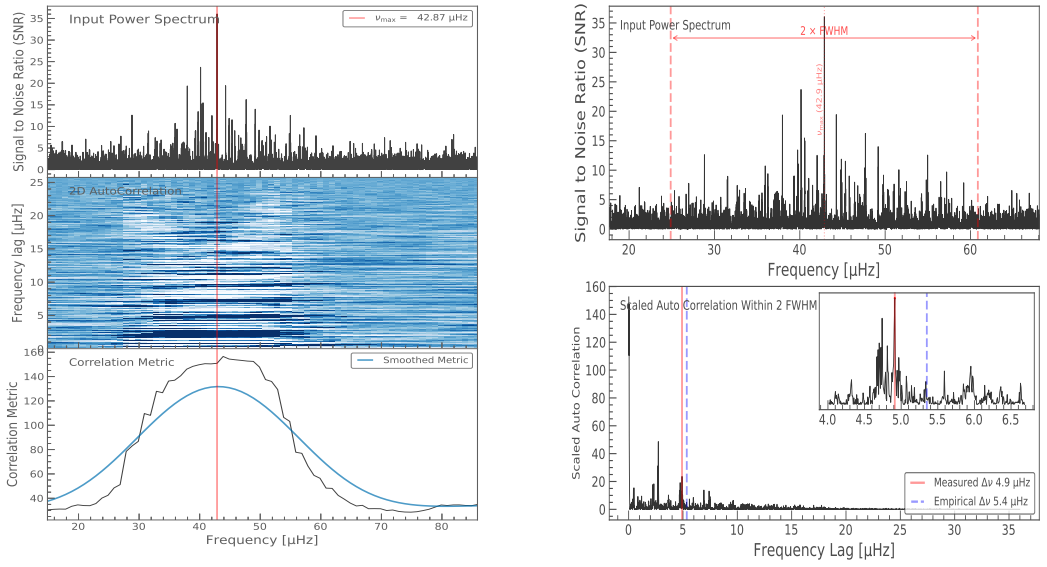

(a) (b)

FIGURE 6.5: Results of Lightkurve analysis for KIC 5000307. In panel (a) estimation of ν_{max} using a smoothed 2D ACF over background corrected PSD. In panel (b) Peaks in ACF in the region near empirical $\Delta\nu$ for calculating $\Delta\nu$

Lomb-Scargle periodogram method is applied to estimate the PSD (Lomb 1976; Scargle 1982). The PSD reveals signal amplitudes across a range of frequencies. This signal consists of solar-like oscillations along with background noise from both instrumental and stellar sources, as well as random photon noise. The stellar convective background is removed using a logarithmic median filter, and the PSD is normalized by dividing it by the background noise to generate a "signal-to-noise spectrum."

To determine $\nu_{\max}$, a segment of the corrected PSD displaying strong power excess is selected. Solar-like oscillations within this region exhibit amplitudes modulated by a broad Gaussian profile, where the peak frequency of this distribution corresponds to $\nu_{\max}$. An empirical formula introduced by Stello et al. (2009) provides

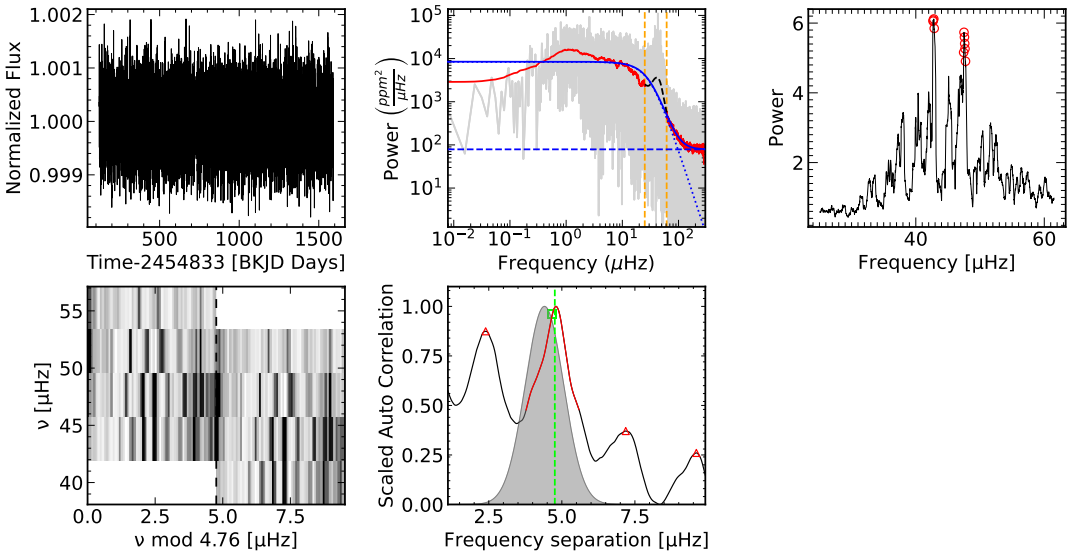

FIGURE 6.6: pySYD results for KIC 5000307. 1st panel shows the corrected lightcurve, 2nd panel is the PSD where original PSD is shown in gray, the red curve is the smoothed PSD using a boxcar filter of 5 μHz, black dashed line indicates the Gaussian power-excess superposed on the smoothed PSD. The blue dashed line indicates the white noise, blue dotted line shows stellar granulation and solid blue line is the overall best fit to the background. In 3rd panel, a zoomed-in region of the background-corrected PSD with several peaks close to ν_{max} is shown. In 4th panel, an echelle diagram of the PSD with background correction with $\Delta\nu$ modulated frequencies. In the last panel is an ACF of panel 3. Black solid line is smoothed background-corrected PSD, red region indicates the extracted ACF peak. Gray shading represents the Gaussian weighting function to define the red region and the center of the Gaussian fit (green dashed line) provides the estimated value of $\Delta\nu$.

a first-order estimate for $\Delta\nu$:

$$\Delta\nu_{\rm est} = (0.263 \pm 0.009)\nu_{\rm max}^{(0.772\pm0.005)}\ \mu{\rm Hz}.$$

A two-dimensional auto-correlation function (ACF) is calculated over the same region, correlating the data with temporally shifted versions of itself. Peaks in the ACF occur where oscillation modes overlap, and `Lightkurve` reports the frequency of the peak closest to $\Delta\nu_{\rm est}$ as $\Delta\nu$.

However, `Lightkurve` does not provide error estimates for $\nu_{\rm max}$ or $\Delta\nu$. Additionally, when examining stars with low $\nu_{\rm max}$, choosing a frequency window narrower than $\nu_{\rm max}$ is essential to avoid over-smoothing the PSD. The software struggles to accurately fit Gaussians in these narrower windows, which in turn affects the computation of the ACF.

To address these limitations and validate the derived parameters, the entire dataset was reanalyzed using `pySYD`[2], an open-source Python adaptation of the well-established SYD pipeline implemented in IDL (Huber et al. 2009), developed by Chontos et al. (2022). The key difference between `pySYD` and `Lightkurve` lies in how they handle background noise modeling. `pySYD` employs Harvey-like functions (up to three components) combined with white noise to fit background contributions arising from stellar granulation. The algorithm iterates through $2(n_{\rm law}+1)$ models, selecting the one that minimizes the Bayesian Information Criterion (BIC). The methods for estimating $\nu_{\rm max}$ and $\Delta\nu$ from the corrected PSD remain consistent between `pySYD` and `Lightkurve`.

To estimate uncertainties, a Monte Carlo approach is utilized, introducing stochastic noise to the PSD and refitting the background iteratively. Global seismic parameters are recalculated approximately 200 times, and the resulting statistical distribution is used to derive robust uncertainty values from the standard deviation. Figures 4 and 5 compare the global seismic parameters determined using `Lightkurve` and `pySYD`.

For determining ΔP, the background-corrected PSD is further smoothed using a Gaussian filter with $\sigma \approx 2$. Initial guesses for the frequencies of mixed dipole modes ($l = 1$) are made by manually identifying peaks in the smoothed flux data. Regions containing at least 4–5 consecutive $l = 1$ modes are selected, and the periods between these consecutive frequencies are calculated. The average and

[2] https://github.com/ashleychontos/pySYD

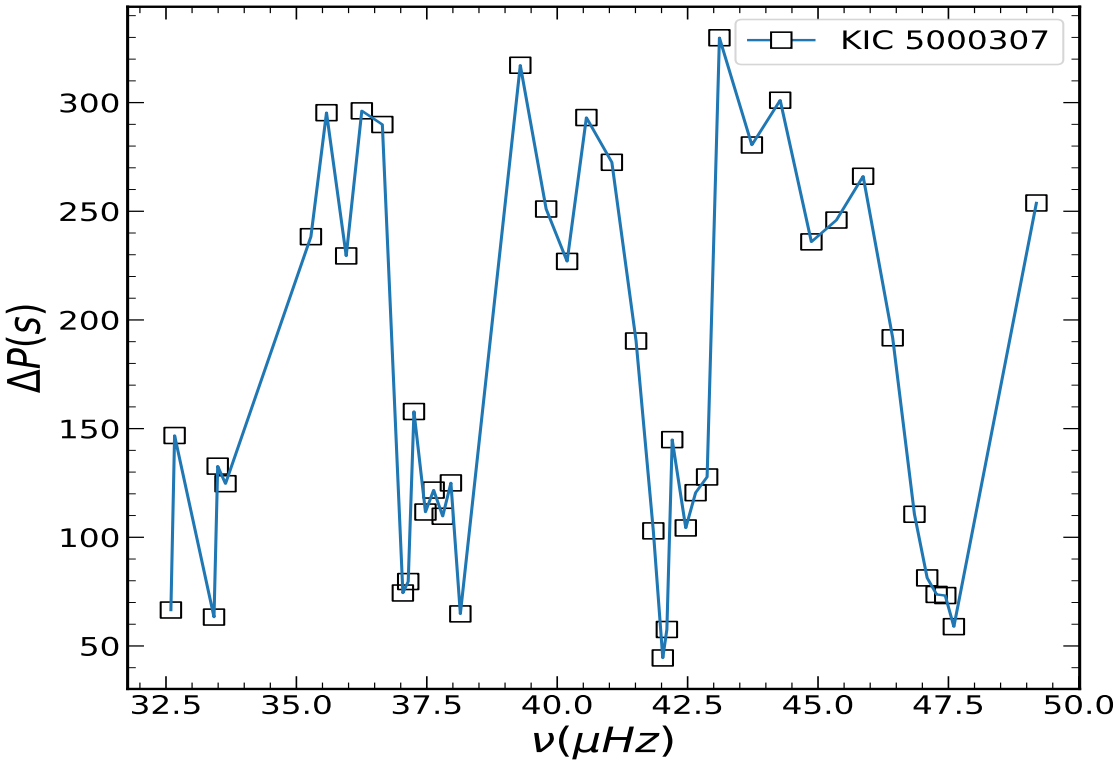

FIGURE 6.7: Measurement of average ΔP from consecutive dipole modes for KIC 5000307

its associated standard error are propagated to provide the mean mixed-mode period spacing (ΔP) and its uncertainty (see Figure 6.7 for ΔP measurements of KIC 5000307). Seismic parameters for some representative stars in the sample are summarized in Table 6.1.

6.6.4 Evolutionary Status

In the ΔP-$\Delta\nu$ diagram (Fig. 6.8), stars on the RGB are located in the region with lower ΔP values. Based on the classification criteria established by Vrard et al. (2016) and Ting et al. (2018), giants with $\Delta P < 150$ s are identified as being in the hydrogen-burning (H-burning) phase, while those with $\Delta P \geq 150$ s are classified as in the CHeB phase.

In the H-burning category, there are 24 RGB stars and one subgiant star, as identified following the methodology described by Mosser et al. (2014). Overall, the sample comprises 59 CHeB stars, 24 RGB stars, and one subgiant.

Seismic stellar masses were determined using the corrected scaling relations proposed by Sharma et al. (2016), expressed as:

$$\frac{M}{M_{\odot}} \approx \left(\frac{\nu_{\rm max}}{f_{\nu_{max}}\nu_{\rm max,\odot}}\right)^{3} \left(\frac{\Delta\nu}{f_{\Delta\nu}\Delta\nu_{\odot}}\right)^{-4} \left(\frac{T_{\rm eff}}{T_{\rm eff,\odot}}\right)^{3/2}.$$

The evolutionary stages of all giants in the sample are visualized in Fig. 6.8.

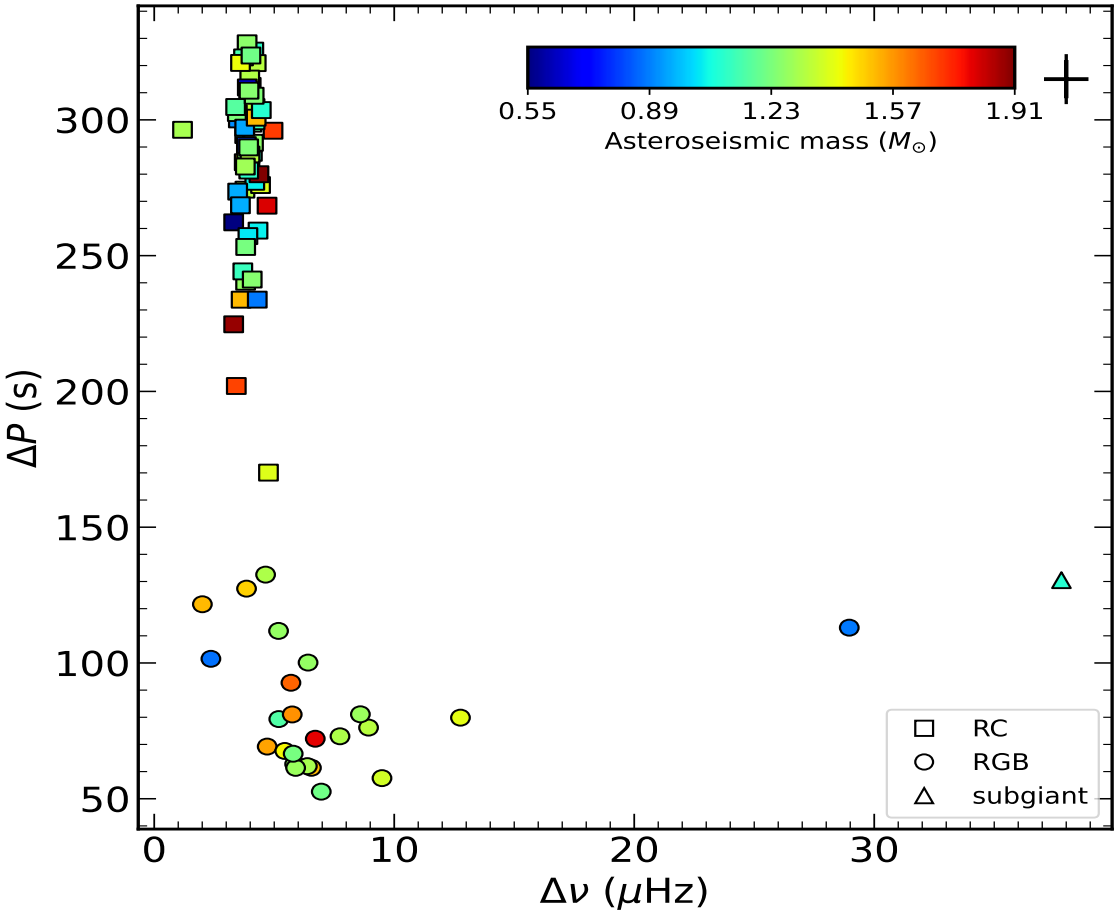

FIGURE 6.8: Average ΔP plotted against $\Delta\nu$ for all stars, with the error cross at the top right illustrating typical uncertainties in both parameters.

TABLE 6.1: Derived and Adopted Parameters of the *Kepler* Sample

KIC	T_{eff}	log g	[Fe/H]	A(Li)	Source [a]	EW_{He}	RW_{He}	RUWE	ν_{max}	$\Delta\nu$	ΔP	Evol stage [b]	Mass	$\log\left(\frac{L}{L_\odot}\right)$	(B-V)	$\log R'_{HK}$
	(K)	(dex)	(dex)	(dex)		(mÅ)	(dex)	(dex)	(μHz)	(μHz)	(s)		($M_\odot$)	($L_\odot$)	(dex)	(dex)
1726211	4965±95	2.24±0.06	-0.61±0.03	-0.03±0.17	3	105±15	-5.01	0.90	30.40±0.63	3.72±0.05	321.66±6.50	1	1.44±0.35	1.82	0.98±0.19	-5.43±0.50
2305930	4879±25	2.47±0.06	-0.39±0.03	3.90±0.03	4	290±10	-4.56	0.91	27.92±0.94	3.77±0.10	297.12±10.00	1	0.74±0.13	1.60	1.18±0.20	-5.36±0.29
2449858	4840±30	2.50±0.10	-0.15±0.00	3.30±0.28	1	195±10	-4.74	0.95	26.76±0.45	3.46±0.05	215.00±6.60	1	1.23±0.12	1.80	1.18±0.02	-5.37±0.03
2714397	5003±100	2.44±0.01	-0.62±0.15	0.00±0.19	3	50±10	-5.34	1.02	33.08±0.52	4.18±0.04	319.22±3.46	1	1.10±0.06	1.71	1.04±0.15	-5.40±0.28
3748691	4954±100	2.50±0.01	0.07±0.15	0.00±0.26	3	69±10	-5.20	0.84	38.71±0.79	4.24±0.05	321.61±3.97	1	1.63±0.07	1.76	0.81±0.36	-5.40±1.84
3751167	4914±80	2.33±0.03	-0.76±0.15	4.00±0.57	1	330±15	-4.52	1.02	26.14±1.59	3.59±0.12	268.52±17.60	1	0.95±0.22	1.80	1.23±0.20	-4.82±0.28
3858850	4375±14	2.23±0.03	0.29±0.02	2.95±0.09	4	195±10	-4.74	0.96	25.92±0.69	3.48±0.07	285.00±15.70	1	0.95±0.11	1.63	1.32±0.14	-5.62±0.25
4044238	4702±164	2.44±0.01	0.00±0.30	1.08±0.35	3	95±8	-5.06	1.05	34.55±0.75	4.01±0.05	296.40±3.06	1	1.33±0.21	1.61		
4161005	4897±40	2.35±0.10	-0.52±0.00	3.30±0.36	1	415±15	-4.42	1.02	29.10±0.96	3.90±0.12	257.20±1.89	1	1.03±0.18	1.67	1.09±0.03	-5.38±0.06
4446405	4846±100	2.69±0.01	-0.13±0.15	1.37±0.19	5	165±10	-4.82	0.89	59.96±0.65	5.75±0.02	81.04±3.90	0	1.58±0.09	1.55	1.33±0.51	-5.66±0.76

[a] (1) Singh et al. (2019) (2) Singh et al. (2021) (3) Takeda & Tajitsu (2017) (4) Yan et al. (2021) (5) Present Work

[b] 0-RGB, 1-RC, 2-subgiant

NOTE - A segment of this table is presented here to illustrate its structure and content.

6.7 Lithium and Helium Variations in RGB and CHeB Stars

The equivalent widths of the He I λ10830 lines were determined by analyzing the relevant spectrum from the HPF order using the `SPECTRE`[3] software tool (Fitzpatrick & Sneden 1987). Given the significant variation in the EWs observed across the sample (ranging from 25 to 750 mÅ), we chose to use logarithmic reduced widths (RW_{He}) for subsequent analyses:

$$RW_{He} = \log_{10}\left(\frac{EW_{He}}{\lambda}\right),$$

with EW expressed in Å. A threshold of RW_{He} = -4.85 was used to distinguish stars with weak or strong λ10830 absorption lines, as defined by Sneden et al. (2022).

To investigate the relationship between chromospheric He I strength and photospheric lithium abundance in RGB and CHeB stars, the stars were grouped according to their lithium content. For RC stars, we used the classification scheme from Singh et al. (2021) to divide them into three categories: Li-normal (LN) (A(Li) $\leq$ 1.0), Li-rich (LR) (1.0 $<$ A(Li) $<$ 3.2), and SLR (A(Li) $\geq$ 3.2). For RGB stars, two groups were formed: Li-normal (A(Li) $\leq$ 1.7 dex) and Li-rich (A(Li) $>$ 1.7 dex) based on Liu et al. (2014).

It is important to highlight that no SLR RGB stars with determined asteroseismic phases have been reported thus far, although there are instances of SLR giants in clusters (Hill & Pasquini 1999; Magrini et al. 2021). To clarify their evolutionary status, asteroseismological analysis is needed.

[3] `http://www.as.utexas.edu/~chris/spectre.html`

In Fig. 6.9, the correlation between lithium abundance A(Li)) and $\mathrm{RW_{He}}$ is shown for both RC and RGB stars.

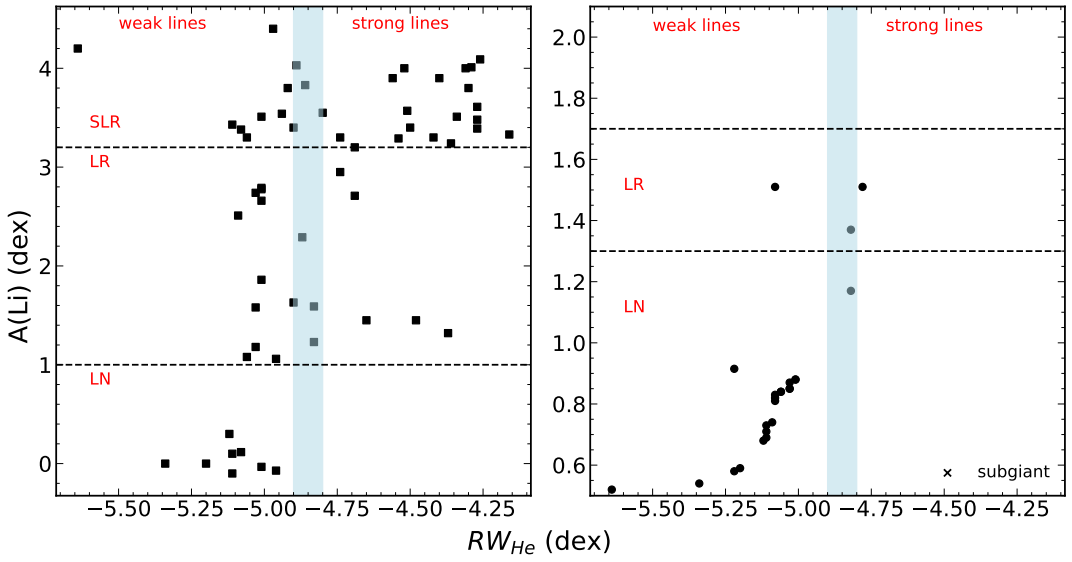

FIGURE 6.9: Correlation between RW_{He} and lithium abundances (A(Li)). The left panel represents RC stars, and the right panel shows RGB stars. Both plots feature a vertical blue-shaded region that marks the boundary between weak and strong λ10830 absorption strengths. Black dashed lines delineate the groups into Li-normal, Li-rich, and SLR categories. Additionally, the right panel identifies a subgiant among the RGB stars, indicated by a $\times$.

Of the 59 CHeB stars, 31 show weaker He lines, while 27 have stronger He lines. In the SLR group (31 stars), most giants (20) exhibit stronger He II profiles, whereas 11 have weaker He I lines. Among the 19 LR stars, 12 display weaker He lines, and 7 show stronger He lines. The subgiant star exhibits weak He absorption. All members of the LN group exhibit weaker He lines. Among the 24 RGB stars, three are situated within the vertical shaded region, while the remaining 20 stars show weaker signals.

6.8 Infrared Excess and Binary Signatures

Numerous studies (Kumar et al. 2011; Deepak & Reddy 2019; Kumar et al. 2020; Magrini et al. 2021) have consistently shown that the majority of Li-rich giants are located within the red clump. This suggests that the helium-core flash, a critical stellar phenomenon that precedes red clump formation, plays a significant role in lithium enhancement. However, some giants with elevated lithium levels may achieve such enrichment due to binary interactions or mergers. Two recent studies propose mechanisms by which lithium abundance can increase during binary evolution. According to Casey et al. (2019), tidal acceleration caused by a neighboring binary star can lead to internal circulation of matter, triggering production of lithium through the Cameron-Fowler mechanism (Cameron & Fowler 1971b). This process could potentially occur at various stages, either on the RGB or during the clump phase. Alternatively, Zhang et al. (2020b) suggest that mergers in systems involving an RGB star and a helium white dwarf may produce Li-rich stars during the CHeB phase. Angular momentum transfer in such scenarios can result in both increased stellar rotation and the ejection of material from the star. As the expelled material cools, it may condense into dust grains, leading to excess infrared emission in the circumstellar environment.

We explored the possibility of binary companions and infrared excess in our sample by investigating photometric and astrometric variations.

6.8.1 Infrared Excess

To examine IR excess, we gathered optical, near-infrared (NIR), and mid-infrared (MIR) photometry using the SED Analyzer from the Virtual Observatory (VOSA), a tool created by the Spanish Virtual Observatory project. This photometric data

was used to construct spectral energy distributions (SEDs) for each star. Photospheric contributions to the SEDs were modeled using stellar atmospheres provided by Castelli & Kurucz (2003). Stellar parameters were obtained either from the literature or calculated via LASP for stars with determined lithium abundances.

VOSA determines the SED slope by iteratively incorporating additional infrared data points and performing a linear regression. If the slope is found to be significantly smaller than expected (< 2.56), the object is flagged as exhibiting IR excess. Furthermore, VOSA refines this detection by comparing observed fluxes with synthetic fluxes at each photometric point, flagging any deviations greater than 3σ as indicative of IR excess. Detailed information on this methodology can be found in the VOSA documentation.[4]

None of the sample giants showed evidence of NIR or MIR excess. However, due to the lack of far-infrared observations, the possibility of cooler dust around these stars cannot be ruled out entirely.

6.8.2 Binary Signatures

To search for binary companions, we investigated both astrometric and eclipsing signatures in the sample. The Gaia Renormalized Unit Weight Error (RUWE) metric serves as a useful indicator for detecting astrometric binaries, with values exceeding 1.4 suggesting the presence of unresolved binary systems (Halbwachs et al. 2023). Two stars from the sample, KIC 10716853 and KIC 10404994, displayed RUWE values greater than 1.4.

[4] http://svo2.cab.inta-csic.es/theory/vosa/helpw4.php?otype=star&action=help&what=&seeall=1

We also cross-referenced the sample with the Hipparcos–Gaia Catalog of Accelerations (HGCA) (Brandt 2021), which uses a longer baseline to identify binaries with slightly wider separations. Among the stars in our sample, only four were found in the HGCA catalog. The catalog provides χ^2 values based on a model with constant proper motion and two degrees of freedom, which we converted into a RUWE-like metric. Following Sneden et al. (2022), HGCA RUWE values greater than 3 indicate long-term astrometric variability. Both stars with elevated Gaia RUWE values also exhibited HGCA RUWE values above 3. Notably, these two stars are in the RC phase, with weak He lines and low lithium abundances.

For potential eclipsing binaries, we cross-checked the sample against the Kepler Eclipsing Binary Catalog[5] (Kirk et al. 2016), which contains 2920 binaries identified from the complete Kepler mission (Q0–Q17). No evidence of eclipsing binaries was detected among the giants in our sample.

A dedicated time-domain radial velocity survey could provide additional insights into the spectroscopic binary characteristics of these stars.

6.9 Other Chromospheric Activity Indicators

Chromospheric activity arises from additional heating mechanisms in the stellar atmosphere that cause deviations from radiative equilibrium. These mechanisms include magnetic effects, such as Alfvén waves (transverse or torsional magnetohydrodynamic waves), mechanical heating from shocks and pulsations, and acoustic heating, where sound waves driven by pulsations generate hydrodynamic shocks.

[5] http://keplerebs.villanova.edu/

Additional contributors include turbulence and ambipolar diffusion, the latter resulting from the separation of oppositely charged species in a plasma in the presence of an external electric field.

A prominent indicator of chromospheric activity among cool stars (spanning early-F to M-type) is the non-thermal emission reversals observed within the cores of the Ca II H and K absorption features, located at wavelengths of 3968.470 Å and 3933.663 Å, respectively. Non-thermal heating mechanisms elevate the emission in the line cores, as described by Linsky & Avrett (1970). Chromospheric activity for these stars is often expressed using the S-index, which is a dimensionless quantity comparing the core fluxes of the Ca II H and K lines against the fluxes in two nearby pseudocontinuum windows located on the blue and red sides of these lines. Pseudocontinua are regions within a spectrum that resemble the continuum but are interspersed with absorption lines. The S-index is calculated as:

$$S_{\mathrm{CaII}} = \frac{F_H + F_K}{F_B + F_R},$$

where F_H, F_K, F_B, and F_R are the integrated fluxes over specific bandpasses: a triangular passband (full width at half maximum, FWHM, of 1.09 Å) for the Ca II H and K lines, and rectangular passbands, 20 Å wide) for the blue and red pseudocontinuum centered at 3901.070 Å and 4001.070 Å, respectively.

Since both the pseudocontinuum fluxes as well as core emissions from the Ca II H and K lines depend on stellar temperature, the S-index is not the best metric for assessing chromospheric activity across stars of varied T_{eff} (Linsky & Avrett 1970; Noyes et al. 1984). To enable reliable comparisons, the contribution from the stellar photosphere (primarily from the wings of the Ca II lines) must be subtracted, and the fluxes' dependence on temperature must also be corrected. This led to the development of a modified metric, R'_{HK}, defined as:

$$R'_{\mathrm{HK}} = R_{\mathrm{HK}} - R_{\mathrm{phot}},$$

where $R_{\rm HK}$ is a photosphere-corrected version of the S-index, calculated as:

$$R_{\rm HK} = 1.34 \times 10^{-4} C_{\rm cf} \times S_{\rm MW}.$$

Here, $C_{\rm cf}$, a coefficient dependent on the star's $(B-V)$ color, adjusts for temperature-related variations in the B and R fluxes. For evolved stars, $C_{\rm cf}$ is given by Rutten (1984):

$$\log C_{\rm cf} = -0.066(B-V)^3 - 0.25(B-V)^2 - 0.49(B-V) + 0.45,$$

and $R_{\rm phot}$, the photospheric contribution, is defined as per Noyes et al. (1984):

$$\log R_{\rm phot} = -4.898 + 1.918(B-V)^2 - 2.893(B-V)^3.$$

The S-index derived from observations is converted to the Mount Wilson S-index ($S_{\rm MW}$) using the relation provided by Vaughan et al. (1978):

$$S_{\rm MW} = \alpha \times 8 \times \frac{\Delta\lambda_{\rm HK}}{\Delta\lambda_{\rm BR}} \times S_{\rm CaII},$$

where $\alpha = 1.8$ is taken from Hall et al. (2007), and the factor of 8 arises from the design of the original Mount Wilson spectrophotometer.

This study uses LAMOST low-resolution spectra. Accurately determining integrated fluxes requires high-quality data, so only spectra with negative fluxes below 1% within the Ca II H and K line regions were included, as recommended by Gomes da Silva et al. (2021). Additionally, a signal-to-noise ratio (S/N) threshold of $\mathrm{S/N}_g > 10$ in the g-band was applied, following Zhang et al. (2020a). Out of 84 stars, 76 met these criteria, and their $S_{\rm CaII}$ values were computed using ACTIN[6] (Gomes da Silva et al. 2021). Before measuring the emission fluxes, the LAMOST

[6] https://github.com/gomesdasilva/ACTIN2

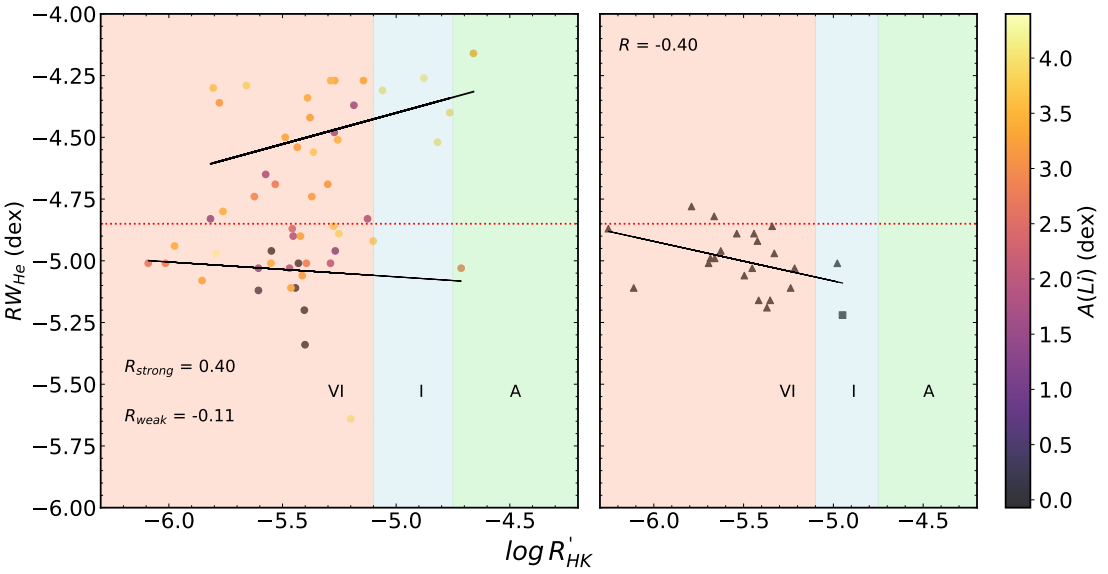

FIGURE 6.10: Relationship between $RW_{\rm He}$ and $\log R'_{\rm HK}$ for RC (left) and RGB (right) stars. Data points are color-coded based on A(Li) values, with a square marking the lone subgiant. Chromospheric activity levels follow Henry et al. (1996), and a red vertical line separates weak and strong He I 10830 Å absorptions (Sneden et al. 2022). Black solid lines indicate trends in the data.

spectra were adjusted to the rest frame with radial velocity corrections using values from LASP. A comparison with the dataset of Gehan et al. (2022), containing 37 common stars, showed a mean difference of 0.07 and a standard deviation of 0.003. The $S_{\rm CaII}$ values were then converted to $\log R'_{\rm HK}$ using the relationships described earlier.

To investigate potential correlations between $RW_{\rm He}$ and $\log R'_{\rm HK}$, we plotted these parameters in Fig. 6.10. Following Henry et al. (1996), chromospheric activity levels were classified into four groups: (i) very active ($\log R'_{\rm HK} > -4.20$), (ii) active ($-4.75 \leq \log R'_{\rm HK} < -4.20$), (iii) inactive ($-5.10 \leq \log R'_{\rm HK} < -4.75$), and (iv) very inactive ($\log R'_{\rm HK} < -5.10$). Most stars fall into the very inactive category, which aligns with expectations for evolved stars.

In RC stars, a moderate positive correlation ($R = 0.40$) is observed in the helium-strong group, suggesting transient shocks from the He flash may enhance chromospheric activity, increasing emissions in both the Ca II and He I lines. Jian

et al. (2024) similarly found a positive correlation ($R = 0.89$) in RC stars from the Stock 2 cluster, though their smaller sample of nine stars likely contributed to the stronger correlation. Conversely, helium-weak RC stars exhibit a weak negative correlation ($R = -0.11$), suggesting minimal upper chromospheric disturbances or a stable state following earlier shocks.

For RGB stars, a moderate negative correlation ($R = -0.4$) is found. Since these stars have not undergone the He flash, their chromospheres are likely influenced by stable long-term activity drivers, suppressing any significant Ca II line enhancements.

The Ca II H and K features provide complementary understanding of the He I 10830 Å line, offering a more detailed view of chromospheric activity across different layers. Observing these lines over time helps establish baseline activity levels, enabling differentiation between regular chromospheric phenomena and disturbances caused by events like the He flash.

6.10 Discussion

A recent study investigating the relationship between A(Li) and the chromospheric He I 10830 Å line analyzed a large set of red giants (Sneden et al. 2022). Their findings hinted at a connection between higher lithium abundances and stronger chromospheric He line strengths. Specifically, giants classified as Li-rich (A(Li) $>$ 1.5) were found to more frequently exhibit enhanced He I strengths compared to their Li-poor (A(Li) $\leq$ 1.5 dex) counterparts.

A key distinction between the present study and the work of Sneden et al. (2022) is the availability of evolutionary phase information for the sample stars in this

study. Although the current sample is smaller, it is better constrained with respect to evolutionary status.

Here, the sample is divided into two main groups: red clump (RC) stars undergoing core helium burning and RGB stars with inert helium cores ascending the RGB for the first time. The results for these groups are presented in Fig. 6.9, which shows a plot of A(Li) versus $RW_{\rm He}$. Additionally, both RC and RGB groups are further subdivided into three lithium-based categories (as described in Section 6.7), denoted by horizontal lines. The broad vertical line in the figure separates stars into groups with strong and weak He I absorption (Sneden et al. 2022). Based on this figure, the following observations can be made: 1. No Li-normal stars in either the RC or RGB groups (as per Section 6.7) display strong He I lines, defined as $RW_{\rm He} > -4.80$ dex (Sneden et al. 2022). 2. Among the 18 Li-rich ($1.0 \leq$ A(Li) ≤ 3.2) RC stars, nine exhibit weak He lines, five are He-strong, and four fall within the uncertainty range. No Li-rich RGB stars display clear He-strong characteristics. 3. The majority (20 out of 29) of super Li-rich RC stars exhibit strong He line strengths. Four fall within the uncertainty range, while the remaining stars are He-weak.

A notable result is the clear absence of strong He I lines and high Li abundance among RGB giants, contrasted with their prevalence in RC stars. This provides strong evidence that the helium flash is likely the key process responsible for lithium enrichment in RC stars. The findings also suggest a potential shared origin for both high Li abundances and strong He I lines in RC stars, likely tied to the helium flash. However, it remains unclear why RGB and RC giants are distinctly separated in terms of both Li abundance and chromospheric He I line strength. One possibility is that the helium flash induces increased chromospheric activity, leading to stronger He lines. Alternatively, material enriched in helium, dredged from the H-burning shell, may reach the photosphere and subsequently the chromosphere.

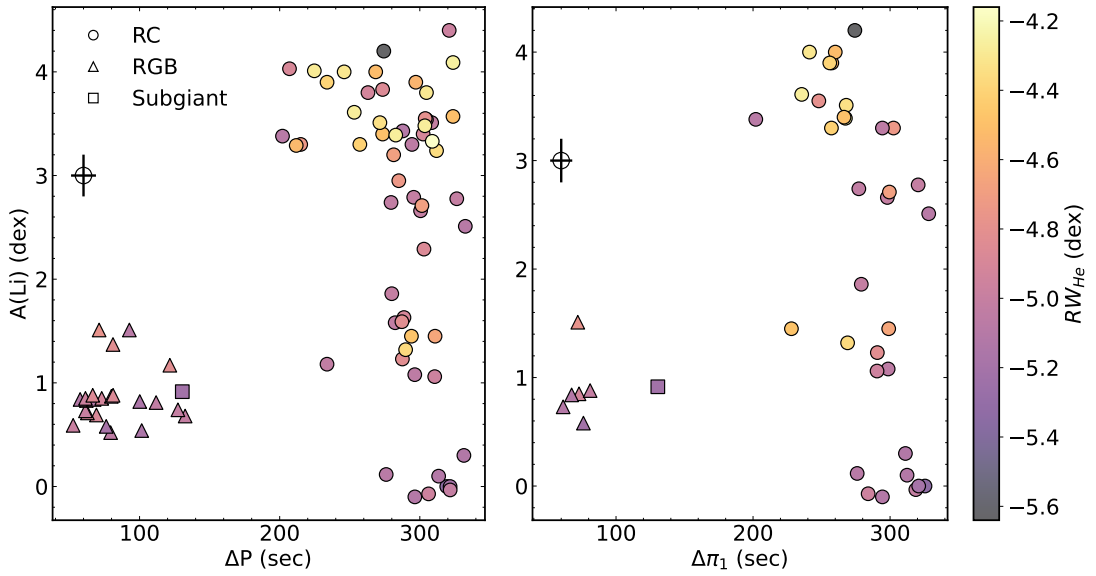

FIGURE 6.11: Comparison of A(Li) with ΔP (left panel) and A(Li) with $\Delta\Pi_1$ (right panel). ΔP is available for all stars in this study, while $\Delta\Pi_1$, which reflects information about the stellar core and is more sensitive to time evolution after the He flash, is available for 41 stars from the literature. Data points are color-coded based on $RW_{\rm He}$ values.

The He I 10830 Å line has been extensively studied in evolved giants (Obrien & Lambert 1986; Smith et al. 2004; Dupree et al. 2011), but its behavior in response to the helium flash has not been thoroughly explored. The core helium flash generates a thermal pulse that significantly increases the core temperature, causing a rapid expansion of the star's outer layers. This expansion may produce shock waves as material moves outward and interacts with overlying layers. These shocks could disrupt the chromosphere, creating transient disturbances that enhance He I absorption. Additionally, intense shocks may contribute to mass loss by ejecting material from the outer layers.

These processes—thermal pulses, expansion, and shock waves—may collectively explain the enhanced He I 10830 Å line in RC stars. In contrast, the absence of He-strong giants on the RGB could be due to reduced chromospheric activity and cooler temperatures compared to post-helium-flash stars.

The formation of the He I 10830 Å absorption feature is primarily driven by

photoionization-recombination processes, as described by Sanz-Forcada & Dupree (2008). The shock-induced heating following the helium flash raises chromospheric temperatures, producing photons with energies in the X-ray and EUV range. These high-energy photons ionize helium atoms, and subsequent recombination populates the metastable 2^3S_1 state, which interacts with the adjacent IR continuum to produce the absorption feature. Alternatively, in hotter and denser chromospheres, non-thermal electron collisions can populate this state, contributing to absorption.

In RGB stars, lower temperatures reduce thermal motion, leading to fewer collisions between neutral helium atoms and high-energy photons, thus decreasing the rate of photoionization. This results in weaker He I absorption features.

In summary, the results indicate that the helium flash and subsequent sub-flashes play a crucial role in the enhanced He I 10830 Å line observed in RC giants. Conversely, RGB stars lack such strong He lines, likely due to their cooler temperatures and lower chromospheric activity. The evolution of chromospheric helium and lithium abundance post-helium flash, as inferred from these results, warrants further investigation using asteroseismic data.

6.10.1 Li Abundance - Chromospheric He I Strength Correlation and Their Evolution Post He-flash

In addition to the distinct separation between giants before and after the helium flash, Fig. 6.9 reveals a steady decline in the number of He-strong giants as lithium abundance decreases. This trend is also apparent for RGB stars, which primarily exhibit weak absorption profiles. Notably, super Li-rich stars show high prevalence of strong He I lines, whereas Li-normal (LN) and Li-rich (LR) giants display little to no evidence of strong He I absorption. This observation is significant, as super

Li-rich stars correspond to younger RC giants that have experienced the helium flash more recently, while LN giants represent older RC stars (Singh et al. 2021).

If the helium flash serves as the trigger for both increased lithium abundance and stronger He I line strengths, these properties are expected to evolve over time. Specifically, older RC stars should exhibit lower chromospheric activity and reduced Li abundances, while younger RCs are expected to retain high lithium levels and strong chromospheric activity. Previous studies have demonstrated that lithium depletes rapidly among RC giants, making the Li-rich phase relatively short-lived (Kumar et al. 2020; Singh et al. 2021). The results in Fig. 6.9 provide evidence of a connection between chromospheric He I line strength and lithium abundance, suggesting that both evolve over time.

To further explore the evolution of Li abundance alongside chromospheric activity, Fig. 6.11 illustrates the relationship between ΔP, A(Li), and $RW_{\rm He}$. The g-mode period spacing (ΔP) is known to track core evolution as stars move from the RGB phase to the clump phase. In Fig. 6.9, RGB stars are distinctly separated in the A(Li) versus ΔP plot, showing low lithium abundance and weak He I lines. Although the A(Li) versus ΔP relation is not strongly defined, younger RC stars (with relatively smaller ΔP values) display a higher frequency of super Li-rich and He-strong giants compared to older RC stars, which typically have $\Delta P \sim 320\,$s and are predominantly Li-normal with weak He I lines.

The dominant mechanism for the formation of the He I λ 10830 Å line in cool red giants is photoionization-recombination (Sanz-Forcada & Dupree 2008). The chromospheric temperatures in RGB stars are generally cooler than those of RC stars, leading to diminished thermal motion and a reduced likelihood of collisions between neutral helium atoms and high-energy photons. This results in lower photoionization rates and weaker absorption features in RGB stars.

For core helium-burning stars, the primary mechanism responsible for populating the metastable 2^3S_1 state remains unclear. Shock waves produced during the helium flash induce both heating and compression as they travel through the star's outer layers, raising the chromospheric temperature. However, as these shock waves move outward, the material undergoes rarefaction and cooling. Variations in the properties of these shock waves—such as their strength, duration, and interaction with the outer layers—lead to differences in chromospheric density and temperature among stars.

6.10.2 Formation of the He I λ 10830 Å Line

The He I triplet at 10830 Å arises from the higher layers of the chromosphere in late-type stars and has no contribution from the photosphere. As a purely chromospheric feature, it provides a powerful diagnostic for investigating hot chromospheres, unaffected by photospheric interference. The asymmetry or core shifts of this line can also offer insights into stellar mass outflows. This spectral line has been extensively studied in late-type stars (Vaughan & Zirin 1968; Dupree et al. 1992).

Helium atoms in excited states can exist in two configurations, based on the alignment of electron spins. These are parahelium (antiparallel spins, $S = 0$, singlet state) and orthohelium (parallel spins, $S = 1$, triplet state). The lowest energy level of the triplet state, 2^3S_1, is both the longest-lived neutral atomic state ($\tau \sim 7800\,\mathrm{s}$) and the highest-energy metastable state among all atomic species ($\sim 19.2\,\mathrm{eV}$ above the ground state).

Three mechanisms have been proposed for populating electrons from the ground 1^1S_0 state to the metastable 2^3S_1 state:

1. **Collisional activation:** Ground-state helium atoms interact with thermal or non-thermal electrons (Goldberg 1939).

2. **Photoionization-recombination:** Coronal heating ionizes helium atoms, followed by recombination (Centeno et al. 2009).

3. **Collisional ionization:** Helium atoms are ionized via collisions and subsequently recombine (Andretta & Jones 1997).

In collisional activation, interactions between neutral helium atoms and electrons result in the population of the 2^3S_1 state. For the other two pathways, helium atoms are ionized by high-energy photons or collisions, with recombination populating the triplet state.

The He I λ10830 absorption line is formed by resonance scattering from the 2^3S_1 to 2^3P state. The 2^3P state has three sublevels ($J = 0, 1, 2$), producing three spectral lines. Two of these transitions (from $J = 2$ and $J = 1$) occur at 10830.34 Å and 10830.25 Å, respectively, but are indistinguishable at chromospheric temperatures, forming a single blended feature at 10830.3 Å. The third transition occurs at 10829.1 Å.

The mechanism responsible for populating the triplet state depends on the star's evolutionary stage and chromospheric properties, such as temperature and density. A combination of these mechanisms may also be at play, influencing the He I λ 10830 Å line in stars at different stages of evolution.

6.11 Conclusion

To investigate the origin of high lithium abundances in red clump giants, we carried out an analysis involving asteroseismic parameters, the chromospheric He I line at 10830 Å, and photospheric lithium measurements for a sample of 84 giants. The findings reveal a clear distinction between giants ascending the RGB and those in the red clump phase, both in terms of their lithium abundance and chromospheric He I strength.

Giants on the RGB exhibit relatively lower chromospheric activity, weaker He I absorption, and a lack of high lithium levels. In contrast, red clump giants are characterized by strong He I lines and elevated lithium abundances. A notable trend observed is a decrease in the number of He-strong giants as lithium abundance decreases. Since high lithium content among red clump giants is known to diminish rapidly, the He-strong giants with high lithium levels are likely associated with younger red clump stars. Conversely, giants with weaker He I lines and lower lithium abundances are more likely to represent older red clump stars.

Interestingly, the presence of some super Li-rich giants with weak He I lines suggests that these two properties may evolve on different timescales and could be influenced to varying degrees by the helium flash. Nevertheless, the results of this study provide additional evidence that the brief, highly energetic helium flash not only contributes to lithium enrichment but also impacts chromospheric activity.

The exact physical mechanism responsible for lithium enrichment in red clump giants remains uncertain. However, it is plausible that a portion of the energy produced in course of the helium flash is used to rapidly expand the stellar envelope. As these layers interact with the regions above, shock waves are generated, propagating through the stellar atmosphere and disrupting the chromosphere. These

dynamic disturbances, including thermal pulses, expansion, and shock waves, may collectively enhance He I 10830 Å absorption.

Chapter 7

Stellar Evolution and Mixing Across the RGB Tip: Insights from High-Resolution Spectroscopy

7.1 Overview

In this chapter, we discuss our ongoing project on stellar evolution and mixing processes near the RGB tip using high-resolution optical spectroscopy. Additionally, we present preliminary findings related to this study and outline future directions for the project.

7.2 Mixing Mechanisms in Red Giants

During the main sequence, stars primarily experience nucleosynthesis through the pp-chain. For stars above 1.3 $M_\odot$, the CNO cycle dominates, although its impact is limited in lower-mass stars (0.7–0.9 $M_\odot$), where only partial conversion of carbon to nitrogen occurs. When central hydrogen burning transitions to a shell, the former core contains regions processed by hydrogen burning. These regions exhibit equilibrium carbon isotope ratios (e.g., 12C/13C $\approx$ 3), reduced carbon abundance, enhanced nitrogen, and significant increases in 3He (Clayton 1983). Meanwhile, fragile elements like lithium, beryllium, and boron are depleted in most of the stellar interior.

When the FDU ends, the convective zone starts retreating as the shell in which hydrogen burns shifts outward in mass. This process creates a minor gap in hydrogen and additional elemental abundance profiles at the point of maximum penetration. As the hydrogen-burning shell passes through this gap, it adapts to the altered chemical composition, causing a temporary decrease in luminosity of a star on the HR diagram before continuing its ascent along the RGB. This phase results in a temporary slowdown in evolution, observed as a concentration of stars at the corresponding luminosity, known as the RGB bump. Theoretical predictions from the FDU align well with observations for lower RGB stars (e.g., Gratton et al. (2000)), evidence has emerged for an additional mixing event at the RGB bump (Charbonnel 1994; Gratton et al. 2000). For instance, 12C/13C ratios in stars below 2.5 $M_\odot$ were found to be significantly lower than expected (Gilroy 1989).

The secondary mixing episode impacts not only carbon isotopes but also other chemical elements. Lithium depletion at the RGB bump is well-documented (Pilachowski et al. 1993; Grundahl et al. 2002), alongside declining carbon and rising nitrogen abundances in field and globular cluster stars (e.g., Gratton et al. (2000);

Bellman et al. (2001)). These changes can be attributed to additional mixing between the convective envelope's base and the hydrogen shell's outermost layers, where CNO-cycle reactions occur outside the primary energy-producing regions (Sweigart & Mengel 1979).

In the region beyond the luminosity bump on the upper RGB, low mass giants may experience additional mixing process that are non-convective occurring in the radiative layers, located between the shell burning hydrogen and the base of the convective envelope (e.g. Gilroy & Brown (1991); Gratton et al. (2000); Smith & Martell (2003); Shetrone et al. (2019)). This process depletes surface lithium along with altering $^{12}C/^{13}C$ and carbon-to-nitrogen ratios. At the RGB tip, He-flash lifts the degeneracy and establishes helium fusion within a convective core. This marks the transition of a star to the RC phase of the horizontal branch (HB). Once core helium is exhausted, The star moves off the HB and climbs the asymptotic giant branch (AGB), experiencing intermittent hydrogen and helium shell burning, with the latter occurring as thermal pulses.

In the standard model of low-mass stellar evolution, with observationally constrained rates and depths of extra mixing (Denissenkov & VandenBerg 2003), surface lithium abundances in RC stars are predicted to be significantly lower than their main-sequence (MS) values for solar composition (Asplund et al. 2009). This is probably due to some unknown extra mixing mechanisms beneath the convective envelope (Richard et al. 2005; Dumont et al. 2021).

However, Kumar et al. (2020) stated that every RC star in their study exhibited surface lithium abundances approximately 40 times higher than theoretical predictions. They found that the previously identified lithium enriched giants (classically defined as A(Li) > 1.5) were part of a broader distribution of lithium abundances in RC stars. This claim was contested in another work (Chanamé

et al. 2022) which demonstrated that considering a more accurate mass distribution and associated MS lithium values resolved most RC stars ($A(\mathrm{Li}) \leq 1.5$) with conventional stellar evolutionary models. Nevertheless, the classical lithium enriched giants ($A(\mathrm{Li}) > 1.5$) remain unexplained by current stellar evolution theories, while no definitive evidence exists to suggest widespread lithium enrichment across all RC stars.

Non-canonical extra mixing is expected to occur between the RGB bump and the core helium-burning stage, leading to an enhancement in nitrogen along with a corresponding decrease of carbon. Several mechanisms have been proposed to explain the origin of this mixing, including rotationally induced meridional circulation (Sweigart & Mengel 1979), transfer of angular momentum transport and material mixing triggered by azimuthal magnetorotational instability (Rüdiger et al. 2015; Dumont 2023), thermohaline mixing, which is one of the most widely invoked explanations (Charbonnel & Zahn 2007), magnetic-buoyancy mixing (Nucci & Busso 2014), mixing induced by internal gravity waves (Schwab 2020), and rotation-driven mixing processes in binary stars on the RGB that are in tidal synchronization (Casey et al. 2019). However, no single theory has yet achieved consensus in explaining this phenomenon.

In this study, we investigate the lithium abundances, CNO abundances, and $^{12}\mathrm{C}/^{13}\mathrm{C}$ ratios of a set of giant stars from high-resolution optical spectra to better constrain the mixing processes in giant stars. Section 7.3 outlines the sample selection and observational data. In Section 3, we detail the methods employed to derive stellar parameters and elemental abundances. A discussion on the observed abundances and potential mechanisms for extra mixing is provided in Section 5, concluded with a summary of our findings in Section 6.

7.3 Sample selection

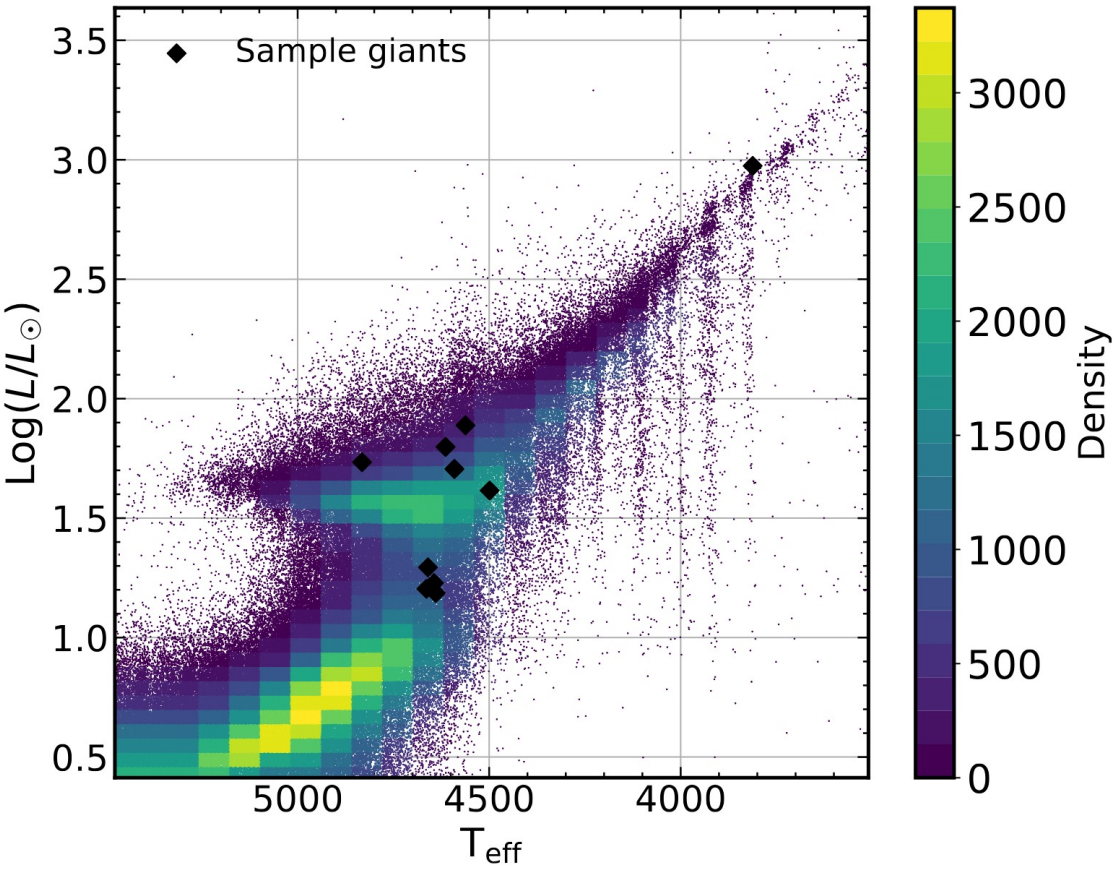

FIGURE 7.1: HR diagram of *Kepler* field giants with the sample giants marked in black diamonds. The colorbar represents the number density of the stars

To test the hypothesis that some transient extra mixing mechanism driven by the He-flash explains the existence of giants with abnormally high Li abundances, we focused on stars on the upper RGB, just before reaching the tip, as well as on core helium-burning stars immediately past the tip. Determining the precise evolutionary phase of Li-enriched giants plays a vital role in deciphering the mechanism causing their enrichment, as the physical processes capable of increasing stellar Li are predominantly confined to specific regions of the HR diagram. A target list was carefully selected from two works -Yu et al. (2018, 2020), which reported clear oscillation signals in a large number of red giants, ensuring robust evolutionary phase identification. Additional selection criteria included their location within the Himalayan Chandra Telescope (HCT's) accessible sky domain and a

brightness threshold suitable for observations, with visual magnitudes brighter than $V \sim 13$.

High-resolution spectra ($\lambda/\Delta\lambda \sim 60,000$) were acquired for all targets using the Hanle Echelle SPectrograph (HESP), mounted on the Himalayan Chandra Telescope (HCT). The spectral range spans a range of [3530-9970] Å. The instrument delivers a resolution of 60,000 when equipped with a slicer and 30,000 without one. A CCD with 4096 × 4096 pixels, each measuring 15μm, was employed for recording the spectra. Spectra of the program stars were obtained over a year, starting in July 2022, due to the limited visibility of *Kepler* field stars from HCT's location and their faintness (most have V > 10). Three frames were obtained for each object, with an exposure time of 2700 seconds per frame. The frames were combined to improve the signal-to-noise ratio, and the resulting co-added spectrum was used for subsequent analysis. All object spectra had good signal-to-noise ratio (SNR ≥ 80). A rapidly rotating bright star was observed on every night as a telluric standard to remove the atmospheric absorption lines caused by Earth's atmosphere. Calibration frames, including bias, flat, and Th-Ar lamp images, were acquired to correct pixel-to-pixel sensitivity variations in the CCD and to perform wavelength calibration. The data reduction was carried out using the standard procedures available in the IRAF echelle package (described in details in Chapter 2). The sky fiber facilitated background subtraction. Each order was wavelength calibrated, continuum normalized, corrected for radial velocity, and merged to create the final spectrum, which was then used for further analysis to determine stellar parameters and chemical abundances.

7.4 Analysis and Results

7.4.1 Stellar parameters

Each star's radial velocity was estimated by performing a cross-correlation between the observed spectrum and a synthetic template derived from Arcturus, the red giant standard. Initial guesses for the stellar parameters ($T_{\rm eff}$, $\log g$, [Fe/H]) were adopted from Mathur et al. (2017), which consolidates values derived from methods like asteroseismology, spectroscopy, photometry, and Flicker analysis.

The stellar parameters ($T_{\rm eff}$, $\log g$, [Fe/H] and ξ) for the objects were derived based on the equivalent widths of selected clean, unblended Fe I and Fe II spectral lines (line lists were compiled from Reddy et al. (2003) and Ramírez & Allende Prieto (2011)). $T_{\rm eff}$ is identified as the value where the relationship between Fe I and Fe II abundances and their excitation potentials flattens. At this point, the microturbulent velocity is fine-tuned so that any correlation between Fe I and Fe II abundances and their reduced equivalent widths is eliminated. With these constraints, $\log g$ is set to the value where Fe I and Fe II abundances match closely. Only lines with excitation potentials between 0 to 5 eV and EWs ranging from 20-180 mÅ were included in the analysis. The analysis employed α-normal photospheric models ([α/Fe] = 0) derived from the Kurucz atmospheric model grid (Castelli & Kurucz 2004). Uncertainties are determined by assessing how abundance trends are affected by small variations in the respective parameters.

7.4.2 Elemental abundances

Each element was examined using a selection of lines that are reasonably strong, devoid of significant blending, and supported by trustworthy atomic information,

as sourced from the high-resolution Arcturus spectral atlas (Hinkle et al. 2000). Abundances were derived by comparing the observed spectra with modeled spectra in the region of interest. The line lists for the synthetic spectra were generated using the `Linemake` tool (Placco et al. 2021). This line list was tested against the synthetic spectra of Arcturus using abundance values and stellar parameters from Ramírez & Allende Prieto (2011). Iterative comparisons led to adjustments in the transition probabilities and wavelengths of few transitions in the final line list. All synthetic spectra used in this work were generated using `pyMOOGi`, a Python wrapper for the current version of the LTE synthetic spectrum code MOOG (Sneden 1973).

1. **Lithium :** Two lines were selected for determining lithium abundances: the prominent resonance doublet line at 6707.8 Å and a subordinate line at 6103.6 Å. The latter is typically only detectable in stars with exceptionally high lithium levels. However, none of the program stars except one (KIC 8879518) exhibited a strong λ6103.6 Å line, so the lithium abundance was calculated solely from the resonance line. The line list was sourced from the `linemake` code (Placco et al. 2021).

2. **Carbon, Nitrogen, Oxygen and ^{12}C/^{13}C ratios:** The isotopic abundance of ^{12}C was determined by comparing the observed spectra against synthetic spectra of two C I lines at 5052.15 Å and 5380.34 Å, along with the C_2 Swan (0, 1) band heads located at 5135.5 Å and 5635.2 Å. Line lists and transition probabilities for atomic and molecular features were sourced from Wiese et al. (1996) and Gonzalez et al. (1998), respectively. The final abundance was taken as the mean of the four lines. In spectra of solar-like stars, most atomic nitrogen lines overlap with molecular CN features or lines from other elements. In stars with temperatures lower than the Sun, N I lines diminish in strength, whereas blended CN features grow more prominent, making it challenging to use atomic nitrogen lines. Consequently, the nitrogen abundance was derived from a few molecular ^{12}C^{14}N lines by

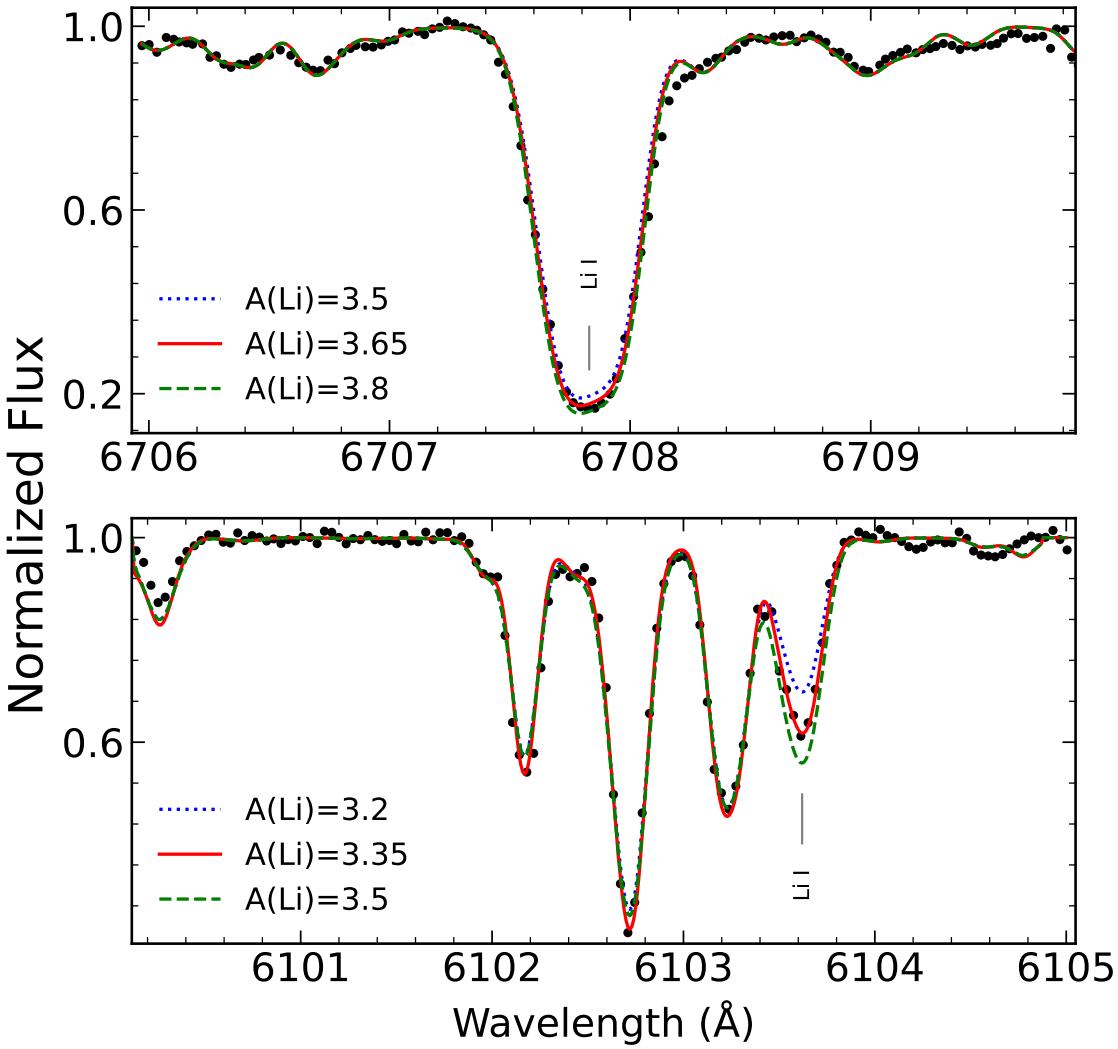

FIGURE 7.2: Examples of fits to the 6707.8Å and 6103.6Å Li I lines in the spectrum of KIC 8879518 are shown. The solid red line represents the optimal fit for a given A(Li), while the other two lines correspond to ± 0.15 dex variations in the Li abundance

comparing the observed spectrum to synthetic spectra in the 8000 Å to 8006 Å range. The $^{12}C/^{13}C$ ratio was then calculated by performing spectral synthesis on the $^{13}C^{14}N$ line at 8004.6 Å. Line lists and molecular data for the $^{12}C^{14}N$ and $^{13}C^{14}N$ lines, including dissociation energies and oscillator strengths (gf-values), were adapted from Sneden et al. (2014). Oxygen abundance was derived using the two forbidden O I transitions at 6300.30 Å and 6363.78 Å, with the line data compiled from Reddy & Lambert (2005).

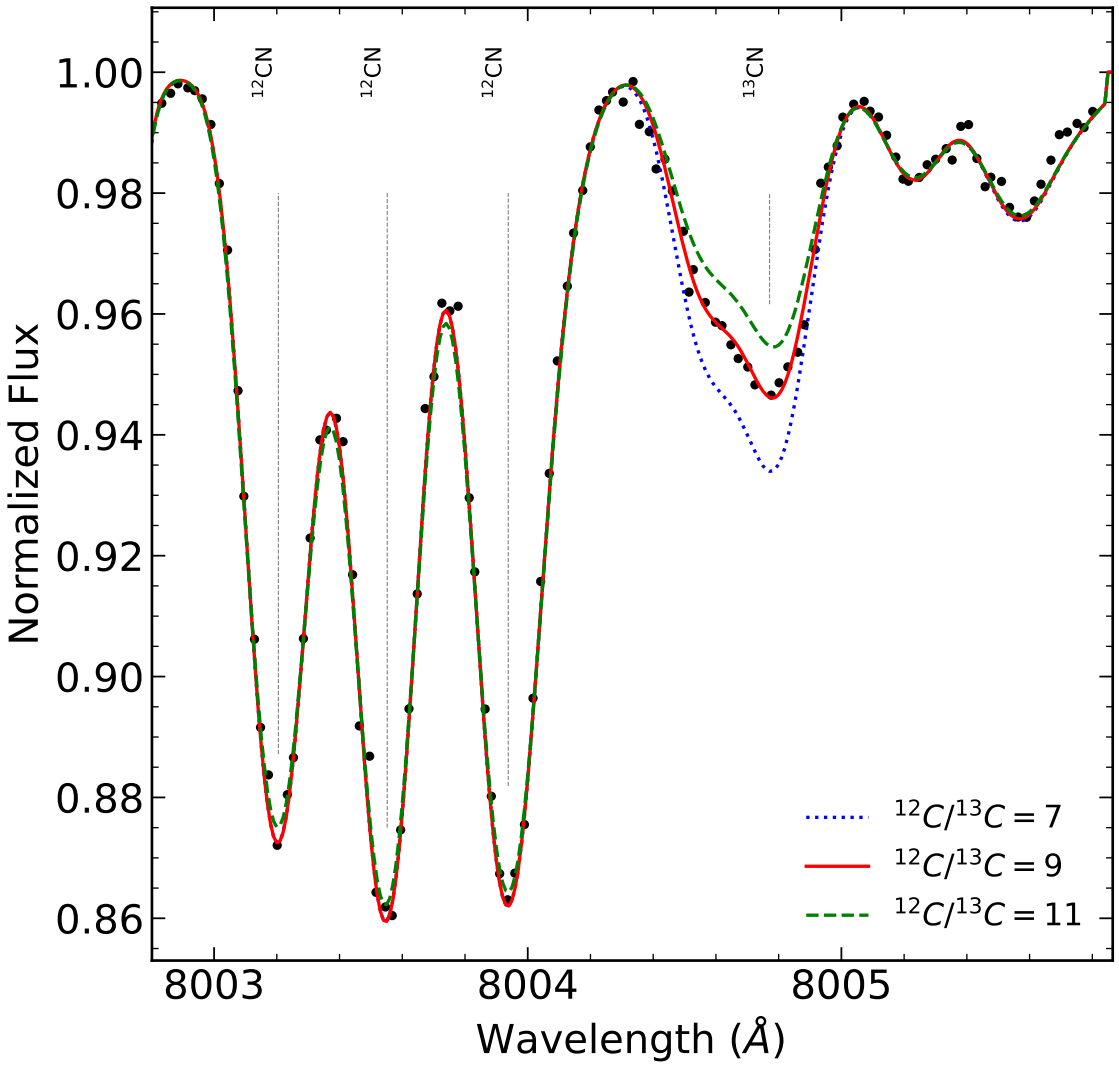

FIGURE 7.3: Example fitting for the $^{12}C^{14}N$ and $^{13}C^{14}N$ molecular lines in the KIC 8879518 spectrum are shown. The solid red line represents the optimal fit for a $^{12}C/^{13}C$ ratio of 9, while the other two lines correspond to ± 2 variations in the $^{12}C/^{13}C$ ratio.

The stellar parameters, lithium abundances, and selected elemental and isotopic ratios derived from high-resolution spectra are summarized in Table 7.1.

7.4.3 Rotational velocities and IR excess

Rotational velocity projections ($v \sin i$) were determined from two Fe I lines at 6703.5 Å and 6705.1 Å near the Li line, following the method outlined in Reddy

TABLE 7.1: Stellar parameters and abundance measurements from high-resolution spectra.

KIC	RV (km/s)	$T_{\rm eff}$ (K)	$\log g$	[Fe/H]	A(Li)	[C/Fe]	[N/Fe]	[O/Fe]	$^{12}C/^{13}C$
10976343	-74	3812 ± 4.5	0.888 ± 0.023	-0.30 ± 0.009	0.10 ± 0.10	$+0.025 \pm 0.010$	$+0.156 \pm 0.011$	$+0.124 \pm 0.009$	14 ± 3
7533995	-32	4639 ± 7.1	2.87 ± 0.021	$+0.07 \pm 0.007$	0.80 ± 0.10	$+0.061 \pm 0.010$	$+0.170 \pm 0.013$	$+0.113 \pm 0.013$	15 ± 4
7122640	-54	4660 ± 7.4	2.81 ± 0.022	-0.06 ± 0.007	0.90 ± 0.10	$+0.027 \pm 0.011$	$+0.136 \pm 0.014$	$+0.118 \pm 0.014$	26 ± 5
8158382	-62	4664 ± 10.2	2.89 ± 0.026	$+0.12 \pm 0.010$	0.90 ± 0.20	-0.003 ± 0.014	$+0.178 \pm 0.017$	$+0.068 \pm 0.018$	22 ± 7
6034166	-28	4644 ± 6.8	2.88 ± 0.019	$+0.27 \pm 0.007$	1.00 ± 0.10	$+0.008 \pm 0.009$	$+0.390 \pm 0.011$	$+0.031 \pm 0.011$	7 ± 1
7595155	-44	4499 ± 6.1	2.29 ± 0.019	$+0.27 \pm 0.007$	1.30 ± 0.10	$+0.146 \pm 0.008$	$+0.043 \pm 0.010$	$+0.067 \pm 0.010$	20 ± 7
7597056	-34	4591 ± 6.6	2.44 ± 0.019	$+0.22 \pm 0.007$	1.20 ± 0.30	$+0.025 \pm 0.009$	$+0.275 \pm 0.011$	$+0.039 \pm 0.011$	10 ± 2
11084620	-22	4562 ± 6.3	2.37 ± 0.018	$+0.33 \pm 0.007$	1.10 ± 0.10	$+0.002 \pm 0.008$	$+0.356 \pm 0.010$	-0.005 ± 0.010	10 ± 2
8506295	-13	4614 ± 6.7	2.41 ± 0.019	$+0.23 \pm 0.007$	1.00 ± 0.00	-0.046 ± 0.009	$+0.420 \pm 0.011$	$+0.003 \pm 0.011$	9 ± 3
8879518	-32	4832 ± 8.2	2.72 ± 0.021	$+0.08 \pm 0.007$	3.50 ± 0.15	-0.471 ± 0.011	$+0.608 \pm 0.014$	-0.014 ± 0.016	9 ± 2

et al. (2002). This approach simultaneously estimates macroturbulence (V_m) and $v \sin i$ corresponding to a given Fe I abundance, incorporating an instrumental broadening $\sim$ 5 km/s through a χ^2 minimization technique. The derived $v \sin i$ values were all below 8 km/s, indicating that none of the stars in the sample are rapid rotators. Additionally, all stars were examined for potential infrared excess by employing infrared photometry and filter profiles available through VOSA. An evaluation of observed infrared fluxes against model spectral energy distributions, along with the infrared excess criteria from Bharat Kumar et al. (2015), found no indications of infrared excess in any of the giants.

7.4.4 Evolutionary Status

Evolutionary stages of all sample giants were determined using the standard ΔP (or $\Delta\Pi_1$)-$\Delta\nu$ diagram (see Fig. 7.4 panel a). Asteroseismic parameters were sourced from Vrard et al. (2016); Yu et al. (2018, 2020); Mosser et al. (2024). For KIC 10976343, determining period spacing was not feasible due to its very low $\nu_{\rm max}$ = 1.03 μHz, with only four radial orders detectable in its power spectral density. Instead, an alternative method outlined by Kallinger et al. (2012) was employed. This approach utilized the large frequency spacing ($\Delta\nu_c$) surrounding

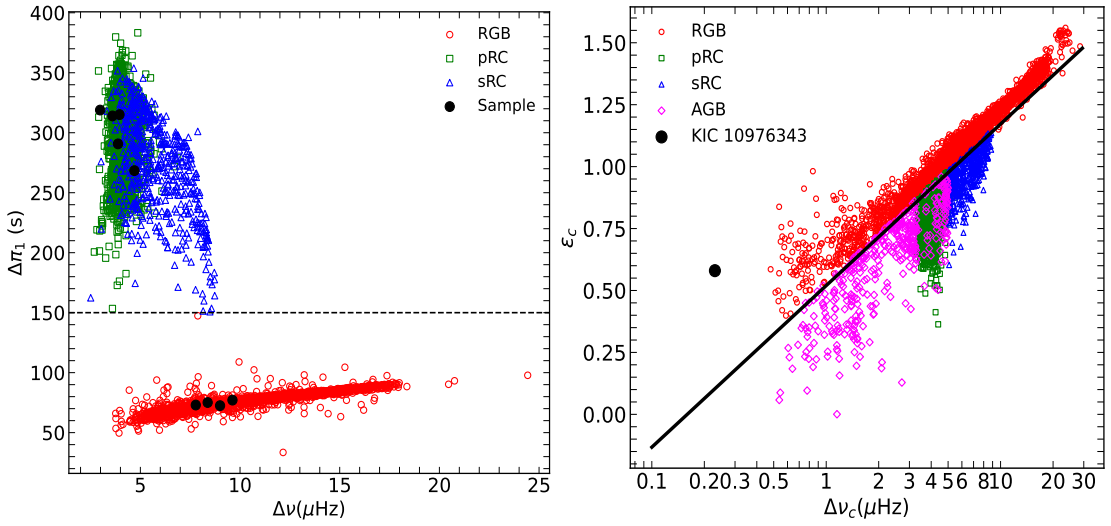

(a) (b)

FIGURE 7.4: Panel (a) shows the $\Delta\Pi_1 - \Delta\nu$ diagram for the sample giants overlaid on Vrard et al. (2016) data. Panel (b) illustrates shifts in the phases of the central radial modes as a function of $\Delta\nu_c$. The black circle indicates KIC 10976343 - only star in the sample for which $\Delta\Pi_1$ could not be determined. Background data points acquired from Kallinger et al. (2012)

the primary radial mode and the phase difference (ϵ_c) of this mode reflects the linear deviation in the asymptotic approximation applied to the acoustic modes. Although $\Delta\nu_c$ and ϵ_c do not provide direct insight into the core of stars like $\Delta\Pi_1$, these local asteroseismic indicators are equally reliable for distinguishing evolutionary stages, comparable to the period interval of mixed dipole modes. Although the values of $\Delta\nu_c$ and ϵ_c for KIC 10976343 fall outside the ranges presented in Kallinger et al. (2012) (see Fig. 7.4 panel b), according to their prescription, the star is within 2σ of the linear fit (black solid line) that separates the population. Therefore, it can confidently be classified as a red giant branch star. Extra mixing occurs along the RGB and potentially during the helium flash, leading to distinct differences in carbon and nitrogen abundances between RGB and RC stars (Masseron et al. 2017; Masseron & Hawkins 2017). This allows a star's spectrum to reveal whether it is undergoing helium burning in its core. Such mixing reduces the carbon-to-nitrogen ratio in RC stars in contrast to RGB stars having similar

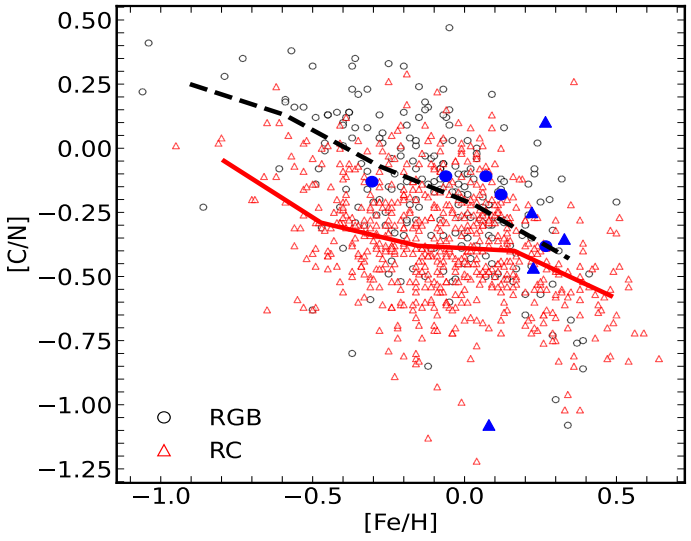

FIGURE 7.5: [C/N] ratio plotted against [Fe/H] for RGB stars (black circles) and RC stars (red triangles) from Hawkins et al. (2018) The bold red and black lines indicate the running medians for the RC and RGB populations respectively. Blue points (circles for RGB and triangles for RC) mark the stars in our sample.

stellar parameters (e.g. Lagarde et al. (2012); Hawkins et al. (2016). The measured surface [C/N] ratios among the sample giants are shown in Fig. 7.5, with RGB stars represented by blue circles and RC stars by blue triangles. Background [C/N] ratios are sourced from Hawkins et al. (2018). Our findings align with expectations: 4 out of 5 RC stars in the sample are older RC stars, as suggested by their $\Delta\Pi_1$ and A(Li) values, and most exhibit low [C/N] ratios ($\leq$ -0.25). The single SLR star shows significant carbon depletion and nitrogen enhancement, indicating a recent mixing event.

7.5 Conclusions

We obtained high-resolution optical spectra for 10 RGB and RC giants to gain deeper insights into the mechanisms at the RGB tip that lead to abrupt changes in Li, CNO abundances, and $^{12}C/^{13}C$ ratios between RGB stars undergoing hydrogen

shell fusion and clump stars that have begun helium core burning. Both $^{12}C/^{13}C$ and C/N ratios are found to be lower in RC stars compared to RGB stars.

- Our future plans include investigating how these quantities vary with stellar age, mass, and metallicity.

- We aim to perform stellar evolution simulations to align our observations with various theoretical mechanisms (discussed in Section 7.2) to determine whether one or a combination of these mechanisms is responsible for the observed changes before and after the onset of core He-burning.

Chapter 8

Conclusion and Future Directions

8.1 Conclusions

The primary focus of this thesis was to investigate the mechanisms responsible for the observed anomalies in Lithium and other related elements among evolved stars, specifically RGB and RC stars. The longstanding puzzle of Li enhancement in some giants, including some super Li-rich giants, has posed significant challenges to standard stellar evolution models. This work explored the processes driving changes in surface Li abundances, carbon-nitrogen-oxygen (CNO) abundances, and carbon isotopic ratios. Additionally, it sought to identify whether these anomalies are linked to specific evolutionary stages, such as the helium flash or extra mixing events triggered by other phenomena like rotation, and to investigate the role of external influences, such as tidal interactions or mergers, in contributing to Li enrichment.

Spectroscopic analysis of RGB and RC stars was carried out using high resolution optical and IR spectra (HCT and HPF) as well as medium resolution spectra (LAMOST), focusing on measuring elemental abundances and identifying features such as rotational velocities and infrared excess. The asteroseismic data from *Kepler* and *TESS* missions were analyzed in this study to derive the parameters necessary for accurately determining the evolutionary stages of stars and distinguishing RC stars from RGB stars and these data were coupled with photometric and astrometric information to obtain a detailed comprehension of the structural and elemental traits in these stars.

We have verified that lithium enrichment is primarily linked to the core helium–burning phase—especially the helium flash—in low-mass giants through a coherent sequence of investigations across Chapters 3–7. In Chapter 3, we demonstrate that giants showing mid-infrared excess are mostly Li-rich, suggesting that recent mass loss or circumstellar disturbances accompany Li enhancement. Chapter 4 presents a detailed case study of KIC 11087027—a rapidly rotating, SLR RC giant with strong IR excess, flare activity, and tidal interaction signatures — illustrating how individual objects can pinpoint the roles of rotation and binarity. Building on the same LAMOST and Kepler parent samples introduced in Chapter 2, Chapter 5 uses asteroseismic ΔP–$\Delta\nu$ classification to show that super Li-rich stars occur only among low-mass primary RC stars, consistent with a He-flash mixing origin. Chapter 6 connects Li abundance to chromospheric He I 10830 Å absorption in an overlapping Kepler sample, revealing that strong helium line strengths trace the same mixing processes that enhance surface lithium. Finally, Chapter 7's high-resolution HESP/HCT spectra of a targeted subset presents detailed abundance patterns of Li, CNO, and $^{12}C/^{13}$C ratios, providing direct evidence for the deep internal mixing events discussed earlier. Together, these complementary lines of evidence—from infrared photometry and chromospheric spectroscopy to asteroseismology and high-resolution abundance analysis—converge on a unified narrative: the core helium flash in low-mass giants triggers non-standard

mixing that produces and transports Li to the surface, while external processes such as rotation and tidal interactions modulate its abundance in a small population.

A comparison of observed Li abundances with theoretical predictions highlights gaps in current standard models, especially in explaining SLR giants. While internal mixing processes can account for moderate Li enrichment, external influences are necessary to explain the extreme cases. These findings provide critical constraints on theoretical models of stellar evolution, particularly regarding non-standard mixing processes and the role of external interactions in evolved stars. They also contribute to understanding the broader chemical evolution of Milky Way, as the processes studied here influence the distribution of Li and related elements in the interstellar medium.

8.1.1 Overview of Sample Selection and Chapter-wise Data Usage

To aid clarity regarding the sample selection across the thesis, we summarize here the datasets and criteria used in Chapters 3 to 7. The samples used in these chapters were independently selected based on the scientific goals of each analysis and were not drawn from a single parent catalog.

Chapter 3 used only archival GALAH data to examine the correlation between infrared excess and lithium enrichment in giants, with no seismic classification. A small subset (96 stars) overlapping with the calibrated seismic catalog of Lucey et al. (2020) was used solely to assess contamination.

Chapter 4 focused on a single SLR RC giant (KIC 11087027), independently selected from a cross-match of Kepler and LAMOST low-resolution data and unrelated to Chapter 3.

Chapters 5 and 6 both used LAMOST medium-resolution spectra combined with Kepler asteroseismic parameters, but with distinct selection criteria: Chapter 5 relied on the Yu et al. (2018) sample of stars with detectable oscillations, while Chapter 6 was restricted to objects accessible to the HET telescope and also incorporated targets from external literature with high-resolution Li abundances.

Chapter 7 employed an entirely independent sample based on Kepler photometry and sky visibility from the HCT telescope, without relying on LAMOST data.

Although all chapters draw from common surveys such as Kepler, LAMOST, or WISE, the selections were tailored separately, and any overlaps—if present—are incidental. The seismic classification method does appear in multiple chapters, but was applied independently to the relevant subsamples in each case.

8.2 Future prospects

Building on these results, future works can explore the role of metallicity in shaping Li enrichment patterns across diverse stellar populations. Expanding the sample size with data from upcoming high-resolution spectroscopic surveys will allow for better statistical characterization of Li enrichment across different evolutionary stages. Furthermore, detailed 3D hydrodynamic simulations can help model the complex interplay of mixing mechanisms, He flash, and external influences. Here are some research ideas I intend to pursue in the future:

1. **Investigating disparity between chromospheric and photospheric Helium signatures in Red giants**

   Hydrogen and helium are the most abundant elements in stellar atmospheres, making it extremely challenging to determine their precise abundances. Helium abundances can only be estimated in hotter stars where helium transitions are detectable. For the Sun, helium is measured indirectly through solar wind sampling. However, in cooler stars, neither helium lines are observable, nor can small variations in hydrogen abundance be inferred from the saturated hydrogen-Balmer lines. Accurate measurements of the He/H ratio in cooler stars are critical for determining precise elemental abundances, including helium. In such cases, a "standard" He/H ratio of 0.1 is typically assumed to derive elemental abundances.

   An alternative method, suggested by Hema & Pandey (2014), involves comparing Mg I and MgH (0,0) band measurements. Any discrepancy between magnesium abundances derived from these indicators, if not due to uncertainties in the star's effective temperature and surface gravity, could indicate either reduced hydrogen or increased helium in the stellar atmosphere. During the core helium flash, the extreme core temperatures can enhance surrounding shell hydrogen burning. If mixing is triggered by the helium flash, the helium produced in the hydrogen-burning shell could be transported to the photosphere. Since helium is stable and less easily destroyed than lithium, all core helium-burning stars are expected to exhibit helium-rich atmospheres.

   It would be valuable to investigate helium enhancement in red giants across various stages of the RGB phase, such as the RGB bump, clump, ascent, and tip, to identify when and how these enhancements occur. Preliminary studies have explored estimating photospheric helium abundances using chromospheric modeling of the He I 10830 Å line. If helium abundance in the photosphere can be reliably determined for a statistically significant sample of stars alongside He I measurements, an empirical relationship between the

two could be established. This would also help clarify how the core helium flash impacts helium distribution across different atmospheric layers.

Many normal stars are analyzed with the assumption of a standard He/H ratio of 0.1, which might not reflect the actual value. In helium-enhanced stars, deviations in the He/H ratio could influence other elemental abundances. Conducting abundance analysis based on the true He/H ratio may help resolve some of the abundance anomalies observed in such stars.

2. **Helium Abundance Estimation via Asteroseismology: Acoustic Glitches as Diagnostic Tools**

   Certain regions within stars, such as ionization zones and the boundary between radiative and convective layers, cause localized sharp variations in sound speed. These variations are referred to as "acoustic glitches." Acoustic glitches imprint distinctive signatures on stellar oscillation frequencies, making them valuable diagnostic tools. Specifically, these signatures can provide insights into the location of the second helium ionization zone and the base of the convective envelope.

   In helium ionization zones, these glitches produce a peak in the first adiabatic index, Γ_1, between the He I and He II ionization regions. The amplitude of these signatures is influenced by the amount of helium present in the ionization zones. However, the amplitudes are typically very small, requiring a large set of precisely measured oscillation frequencies to detect them reliably. This makes such analyses challenging for a broad sample of stars.

   To determine the helium abundance in the stellar envelope, the observed amplitude of the helium-related glitch signature must be calibrated against the corresponding amplitudes from model frequencies with varying surface helium abundances (Y_s). This comparison allows for an accurate estimation of the envelope helium content in stars.

Li-rich giants remain one of the most intriguing and perplexing topics in stellar physics. These stars offer valuable insights into stellar evolution, with implications for binarity, rotation, mass, metallicity, mixing, and potentially planetary influences. However, uncovering the precise mechanisms behind these phenomena has proven to be a difficult task. As the quantity of Li measurements increases, along with more accurate data on stellar masses, ages, evolutionary stages, and binary companions, the hope is that a physical explanation—or perhaps a combination of them—will eventually clarify the causes of Li enrichment, both on a population-wide scale and for individual stars.

Hopefully, this work has served as a small piece of the puzzle in understanding the enigma of Li-rich red giants, and as future research continues, more insights will emerge to further unravel this fascinating aspect of stellar physics.

"So remember to look up at the stars and not down at your feet. Try to make sense of what you see and wonder about what makes the universe exist. Be curious. And however difficult life may seem, there is always something you can do and succeed at. It matters that you don't just give up. Unleash your imagination. Shape the future."

- Stephen Hawking, Brief Answers to the Big Questions

Bibliography

Adamów, M., Niedzielski, A., Villaver, E., Wolszczan, A., & Nowak, G. 2014, The Penn State - Toruń Centre for Astronomy Planet Search stars. II. Lithium abundance analysis of the red giant clump sample, *Astron. Astrophys.*, 569, A55, doi: 10.1051/0004-6361/201423400

Adelberger, E. G., García, A., Robertson, R. G. H., et al. 2011, Solar fusion cross sections. II. The pp chain and CNO cycles, Reviews of Modern Physics, 83, 195, doi: 10.1103/RevModPhys.83.195

Aguilera-Gómez, C., Chanamé, J., Pinsonneault, M. H., & Carlberg, J. K. 2016, On Lithium-rich Red Giants. I. Engulfment of Substellar Companions, *Astrophys. J.*, 829, 127, doi: 10.3847/0004-637X/829/2/127

Anderson, E. R., Duvall, Jr., T. L., & Jefferies, S. M. 1990, Modeling of Solar Oscillation Power Spectra, *Astrophys. J.*, 364, 699, doi: 10.1086/169452

Andrae, R., Fouesneau, M., Creevey, O., et al. 2018, Gaia Data Release 2. First stellar parameters from Apsis, *Astron. Astrophys.*, 616, A8, doi: 10.1051/0004-6361/201732516

Andretta, V., & Jones, H. P. 1997, On the Role of the Solar Corona and Transition Region in the Excitation of the Spectrum of Neutral Helium, *Astrophys. J.*, 489, 375, doi: 10.1086/304760

Asplund, M., Grevesse, N., Sauval, A. J., & Scott, P. 2009, The Chemical Composition of the Sun, *Ann. Rev. Astron. Astrophys.*, 47, 481, doi: 10.1146/annurev.astro.46.060407.145222

Aurière, M., Konstantinova-Antova, R., Charbonnel, C., et al. 2015, The magnetic fields at the surface of active single G-K giants, *Astron. Astrophys.*, 574, A90, doi: 10.1051/0004-6361/201424579

Bedding, T. R., Mosser, B., Huber, D., et al. 2011, Gravity modes as a way to distinguish between hydrogen- and helium-burning red giant stars, *Nature*, 471, 608, doi: 10.1038/nature09935

Bellman, S., Briley, M. M., Smith, G. H., & Claver, C. F. 2001, Carbon Abundances of M92 Red Giant Branch Stars, *Pub. Astron. Soc. Pac.*, 113, 326, doi: 10.1086/319336

Bernath, P. F. 2020, MoLLIST: Molecular Line Lists, Intensities and Spectra, jqsrt, 240, 106687, doi: 10.1016/j.jqsrt.2019.106687

Bharat Kumar, Y., Reddy, B. E., Muthumariappan, C., & Zhao, G. 2015, Far-infrared study of K giants in the solar neighborhood: Connection between Li enrichment and mass-loss, *Astron. Astrophys.*, 577, A10, doi: 10.1051/0004-6361/201425076

Blanco-Cuaresma, S., Soubiran, C., Heiter, U., & Jofré, P. 2014, Determining stellar atmospheric parameters and chemical abundances of FGK stars with iSpec, *Astron. Astrophys.*, 569, A111, doi: 10.1051/0004-6361/201423945

Borucki, W. J., Koch, D., Basri, G., et al. 2010, Kepler Planet-Detection Mission: Introduction and First Results, Science, 327, 977, doi: 10.1126/science.1185402

Bowman, D. M., & Bugnet, L. 2024, Asteroseismology, arXiv e-prints, arXiv:2410.01715, doi: 10.48550/arXiv.2410.01715

Brandt, T. D. 2021, The Hipparcos-Gaia Catalog of Accelerations: Gaia EDR3 Edition, *Astrophys. J. Suppl.*, 254, 42, doi: 10.3847/1538-4365/abf93c

Buder, S., Sharma, S., Kos, J., et al. 2021, The GALAH+ survey: Third data release, *Mon. Not. Roy. Astron. Soc.*, 506, 150, doi: 10.1093/mnras/stab1242

Cameron, A. G. W., & Fowler, W. A. 1971a, Lithium and the s-PROCESS in Red-Giant Stars, *Astrophys. J.*, 164, 111, doi: 10.1086/150821

—. 1971b, Lithium and the s-PROCESS in Red-Giant Stars, *Astrophys. J.*, 164, 111, doi: 10.1086/150821

Carney, B. W., Latham, D. W., Stefanik, R. P., & Laird, J. B. 2008, Line Broadening in Field Metal-Poor Red Giant and Red Horizontal Branch Stars, *Astron. J.*, 135, 196, doi: 10.1088/0004-6256/135/1/196

Carrier, F., De Ridder, J., Baudin, F., et al. 2010, Non-radial oscillations in the red giant HR 7349 measured by CoRoT, *Astron. Astrophys.*, 509, A73, doi: 10.1051/0004-6361/200912749

Carroll, B. W., & Ostlie, D. A. 2017, An introduction to modern astrophysics, Second Edition (Cambridge University Press)

Casey, A. R., Ho, A. Y. Q., Ness, M., et al. 2019, Tidal Interactions between Binary Stars Can Drive Lithium Production in Low-mass Red Giants, *Astrophys. J.*, 880, 125, doi: 10.3847/1538-4357/ab27bf

Castelli, F., & Kurucz, R. L. 2003, in Modelling of Stellar Atmospheres, ed. N. Piskunov, W. W. Weiss, & D. F. Gray, Vol. 210, A20. https://arxiv.org/abs/astro-ph/0405087

Castelli, F., & Kurucz, R. L. 2004, New Grids of ATLAS9 Model Atmospheres, ArXiv Astrophysics e-prints

Catala, C., & COROT Team. 2001, Overview of the COROT mission, Journal of Astronomical Data, 7, 8

Cayrel, R. 1988, in The Impact of Very High S/N Spectroscopy on Stellar Physics, ed. G. Cayrel de Strobel & M. Spite, Vol. 132, 345

Ceillier, T., Tayar, J., Mathur, S., et al. 2017, Surface rotation of Kepler red giant stars, *Astron. Astrophys.*, 605, A111, doi: 10.1051/0004-6361/201629884

Centeno, R., Trujillo Bueno, J., Uitenbroek, H., & Collados, M. 2009, in Astronomical Society of the Pacific Conference Series, Vol. 405, Solar Polarization 5: In Honor of Jan Stenflo, ed. S. V. Berdyugina, K. N. Nagendra, & R. Ramelli, 297

Chan, S. J., & Kwok, S. 1988, The Transition from Oxygen-rich to Carbon Stars, *Astrophys. J.*, 334, 362, doi: 10.1086/166843

Chanamé, J., Pinsonneault, M. H., Aguilera-Gómez, C., & Zinn, J. C. 2022, Mass Matters: No Evidence for Ubiquitous Lithium Production in Low-mass Clump Giants, *Astrophys. J.*, 933, 58, doi: 10.3847/1538-4357/ac70c8

Chaplin, W. J., & Miglio, A. 2013, Asteroseismology of Solar-Type and Red-Giant Stars, *Ann. Rev. Astron. Astrophys.*, 51, 353, doi: 10.1146/annurev-astro-082812-140938

Chaplin, W. J., Bedding, T. R., Bonanno, A., et al. 2011, Evidence for the Impact of Stellar Activity on the Detectability of Solar-like Oscillations Observed by Kepler, *Astrophys. J. Lett.*, 732, L5, doi: 10.1088/2041-8205/732/1/L5

Charbonnel, C. 1994, Clues for non-standard mixing on the red giant branch from C-12/C-13 and C-12/N-14 ratios in evolved stars, *Astron. Astrophys.*, 282, 811

Charbonnel, C., & Balachandran, S. C. 2000, The Nature of the lithium rich giants. Mixing episodes on the RGB and early-AGB, *Astron. Astrophys.*, 359, 563, doi: 10.48550/arXiv.astro-ph/0005280

Charbonnel, C., & Lagarde, N. 2010, Thermohaline instability and rotation-induced mixing. I. Low- and intermediate-mass solar metallicity stars up to

the end of the AGB, *Astron. Astrophys.*, 522, A10, doi: 10.1051/0004-6361/201014432

Charbonnel, C., & Zahn, J. P. 2007, Thermohaline mixing: a physical mechanism governing the photospheric composition of low-mass giants, *Astron. Astrophys.*, 467, L15, doi: 10.1051/0004-6361:20077274

Charbonnel, C., Decressin, T., Lagarde, N., et al. 2017, The magnetic strip(s) in the advanced phases of stellar evolution. Theoretical convective turnover timescale and Rossby number for low- and intermediate-mass stars up to the AGB at various metallicities, *Astron. Astrophys.*, 605, A102, doi: 10.1051/0004-6361/201526724

Chiosi, C., Bertelli, G., & Bressan, A. 1992, New developments in understanding the HR diagram, *Ann. Rev. Astron. Astrophys.*, 30, 235, doi: 10.1146/annurev.aa.30.090192.001315

Chontos, A., Huber, D., Sayeed, M., & Yamsiri, P. 2022, pySYD: Automated measurements of global asteroseismic parameters, The Journal of Open Source Software, 7, 3331, doi: 10.21105/joss.03331

Christensen-Dalsgaard, J. 2014, in Asteroseismology, ed. P. L. Pallé & C. Esteban (Cambridge University Press), 194, doi: 10.48550/arXiv.1106.5946

Clayton, D. D. 1983, Principles of stellar evolution and nucleosynthesis (University of Chicago Press)

Coughlin, J., Thompson, S. E., & Kepler Team. 2017, in American Astronomical Society Meeting Abstracts, Vol. 230, American Astronomical Society Meeting Abstracts #230, 102.04

Cui, X.-Q., Zhao, Y.-H., Chu, Y.-Q., et al. 2012, The Large Sky Area Multi-Object Fiber Spectroscopic Telescope (LAMOST), Research in Astronomy and Astrophysics, 12, 1197, doi: 10.1088/1674-4527/12/9/003

Cuntz, M., Saar, S. H., & Musielak, Z. E. 2000, On Stellar Activity Enhancement Due to Interactions with Extrasolar Giant Planets, *Astrophys. J. Lett.*, 533, L151, doi: 10.1086/312609

Cyburt, R. H., Fields, B. D., & Olive, K. A. 2008, An update on the big bang nucleosynthesis prediction for ^{7}Li: the problem worsens, JCAP, 2008, 012, doi: 10.1088/1475-7516/2008/11/012

de La Reza, R., Drake, N. A., & da Silva, L. 1996, Lithium Enrichment–Mass-Loss Connection in K Giant Stars, *Astrophys. J. Lett.*, 456, L115, doi: 10.1086/309874

de la Reza, R., Drake, N. A., da Silva, L., Torres, C. A. O., & Martin, E. L. 1997, On a Rapid Lithium Enrichment and Depletion of K Giant Stars, *Astrophys. J. Lett.*, 482, L77, doi: 10.1086/310685

De Medeiros, J. R., Da Silva, J. R. P., & Maia, M. R. G. 2002, The Rotation of Binary Systems with Evolved Components, *Astrophys. J.*, 578, 943, doi: 10.1086/342613

Deepak, & Lambert, D. L. 2021, Lithium in red giants: the roles of the He-core flash and the luminosity bump, *Mon. Not. Roy. Astron. Soc.*, 507, 205, doi: 10.1093/mnras/stab2022

Deepak, & Reddy, B. E. 2019, Study of Lithium-rich giants with the GALAH spectroscopic survey, *Mon. Not. Roy. Astron. Soc.*, 484, 2000, doi: 10.1093/mnras/stz128

Delgado Mena, E., Tsantaki, M., Sousa, S. G., et al. 2016, Searching for Li-rich giants in a sample of 12 open clusters. Li enhancement in two stars with sub-stellar companions, *Astron. Astrophys.*, 587, A66, doi: 10.1051/0004-6361/201527196

Denissenkov, P. A., & Herwig, F. 2004, Enhanced Extra Mixing in Low-Mass Red Giants: Lithium Production and Thermal Stability, *Astrophys. J.*, 612, 1081, doi: 10.1086/422575

Denissenkov, P. A., & VandenBerg, D. A. 2003, Canonical Extra Mixing in Low-Mass Red Giants, *Astrophys. J.*, 593, 509, doi: 10.1086/376410

Dotter, A. 2016, MESA Isochrones and Stellar Tracks (MIST) 0: Methods for the Construction of Stellar Isochrones, *Astrophys. J. Suppl.*, 222, 8, doi: 10.3847/0067-0049/222/1/8

Draine, B. T., & Lee, H. M. 1984, Optical Properties of Interstellar Graphite and Silicate Grains, *Astrophys. J.*, 285, 89, doi: 10.1086/162480

Drake, N. A., de la Reza, R., da Silva, L., & Lambert, D. L. 2002, Rapidly Rotating Lithium-rich K Giants: The New Case of the Giant PDS 365, *Astron. J.*, 123, 2703, doi: 10.1086/339968

Dumont, T. 2023, Angular momentum and lithium transport from main sequence to sub-giant and red giant low-mass stars, *Astron. Astrophys.*, 677, A119, doi: 10.1051/0004-6361/202346915

Dumont, T., Palacios, A., Charbonnel, C., et al. 2021, Lithium depletion and angular momentum transport in solar-type stars, *Astron. Astrophys.*, 646, A48, doi: 10.1051/0004-6361/202039515

Dupree, A. K., Hartmann, L., & Avrett, E. H. 1984, Chromospheres and mass loss in metal-deficient giant stars., *Astrophys. J. Lett.*, 281, L37, doi: 10.1086/184280

Dupree, A. K., Sasselov, D. D., & Lester, J. B. 1992, Discovery of a Fast Wind from a Field Population II Giant Star, *Astrophys. J. Lett.*, 387, L85, doi: 10.1086/186311

Dupree, A. K., Strader, J., & Smith, G. H. 2011, Direct Evidence for an Enhancement of Helium in Giant Stars in Omega Centauri, *Astrophys. J.*, 728, 155, doi: 10.1088/0004-637X/728/2/155

Dupret, M.-A., Belkacem, K., Samadi, R., et al. 2009, Theoretical amplitudes and lifetimes of non-radial solar-like oscillations in red giants, *Astron. Astrophys.*, 506, 57, doi: 10.1051/0004-6361/200911713

Eddington, A. S. 1926, The Internal Constitution of the Stars (Cambridge University Press)

Fekel, F. C., & Balachandran, S. 1993, Lithium and Rapid Rotation in Chromospherically Active Single Giants, *Astrophys. J.*, 403, 708, doi: 10.1086/172242

Fitzpatrick, M. J., & Sneden, C. 1987, in Bulletin of the American Astronomical Society, Vol. 19, 1129

Fouesneau, M., Andrae, R., Sordo, R., & Dharmawardena, T. 2022, dustapprox, 0.1. https://github.com/mfouesneau/dustapprox

Gaia Collaboration, Brown, A. G. A., Vallenari, A., et al. 2018, Gaia Data Release 2. Summary of the contents and survey properties, ArXiv e-prints. https://arxiv.org/abs/1804.09365

Gaia Collaboration, Prusti, T., de Bruijne, J. H. J., et al. 2016, The Gaia mission, *Astron. Astrophys.*, 595, A1, doi: 10.1051/0004-6361/201629272

Gao, J., Zhu, C., Yu, J., et al. 2022, Li-rich and super Li-rich giants produced by element diffusion, *Astron. Astrophys.*, 668, A126, doi: 10.1051/0004-6361/202243871

Gao, Q., Shi, J.-R., Yan, H.-L., et al. 2021, The Lithium Abundances from the Large Sky Area Multi-object Fiber Spectroscopic Telescope Medium-resolution Survey. I. The Method, *Astrophys. J.*, 914, 116, doi: 10.3847/1538-4357/abf841

García, R. A., & Ballot, J. 2019, Asteroseismology of solar-type stars, Living Reviews in Solar Physics, 16, 4, doi: 10.1007/s41116-019-0020-1

García Pérez, A. E., Allende Prieto, C., Holtzman, J. A., et al. 2016, ASPCAP: The APOGEE Stellar Parameter and Chemical Abundances Pipeline, *Astron. J.*, 151, 144, doi: 10.3847/0004-6256/151/6/144

Gaulme, P., Jackiewicz, J., Appourchaux, T., & Mosser, B. 2014, Surface Activity and Oscillation Amplitudes of Red Giants in Eclipsing Binaries, *Astrophys. J.*, 785, 5, doi: 10.1088/0004-637X/785/1/5

Gehan, C., Gaulme, P., & Yu, J. 2022, Surface magnetism of rapidly rotating red giants: Single versus close binary stars, *Astron. Astrophys.*, 668, A116, doi: 10.1051/0004-6361/202245083

Gilroy, K. K. 1989, in Bulletin of the American Astronomical Society, Vol. 21, Bulletin of the American Astronomical Society, 790

Gilroy, K. K., & Brown, J. A. 1991, Carbon isotope ratios along the giant branch of M67, *Astrophys. J.*, 371, 578, doi: 10.1086/169922

Girardi, L. 1999, A secondary clump of red giant stars: why and where, *Mon. Not. Roy. Astron. Soc.*, 308, 818, doi: 10.1046/j.1365-8711.1999.02746.x

Goldberg, L. 1939, The Temperature of the Solar Chromosphere., *Astrophys. J.*, 89, 673, doi: 10.1086/144092

Gomes da Silva, J., Santos, N. C., Adibekyan, V., et al. 2021, Stellar chromospheric activity of 1674 FGK stars from the AMBRE-HARPS sample. I. A catalogue of homogeneous chromospheric activity, *Astron. Astrophys.*, 646, A77, doi: 10.1051/0004-6361/202039765

Gonzalez, G., Lambert, D. L., Wallerstein, G., et al. 1998, FG Sagittae: A Newborn R Coronae Borealis Star?, *Astrophys. J. Suppl.*, 114, 133, doi: 10.1086/313068

Gratton, R. G., Sneden, C., Carretta, E., & Bragaglia, A. 2000, Mixing along the red giant branch in metal-poor field stars, *Astron. Astrophys.*, 354, 169

Gray, D. F. 2008, The Observation and Analysis of Stellar Photospheres (Cambridge University Press)

—. 2022, The observation and analysis of stellar photospheres (Cambridge University Press), doi: 10.1017/9781009082136

Grundahl, F., Briley, M., Nissen, P. E., & Feltzing, S. 2002, Abundances of RGB stars in NGC 6752, *Astron. Astrophys.*, 385, L14, doi: 10.1051/0004-6361:20020264

Halbwachs, J.-L., Pourbaix, D., Arenou, F., et al. 2023, Gaia Data Release 3. Astrometric binary star processing, *Astron. Astrophys.*, 674, A9, doi: 10.1051/0004-6361/202243969

Hall, J. C., Lockwood, G. W., & Skiff, B. A. 2007, The Activity and Variability of the Sun and Sun-like Stars. I. Synoptic Ca II H and K Observations, *Astron. J.*, 133, 862, doi: 10.1086/510356

Handberg, R., & Lund, M. N. 2014, Automated preparation of Kepler time series of planet hosts for asteroseismic analysis, *Mon. Not. Roy. Astron. Soc.*, 445, 2698, doi: 10.1093/mnras/stu1823

Harvey, J. 1985, in ESA Special Publication, Vol. 235, Future Missions in Solar, Heliospheric & Space Plasma Physics, ed. E. Rolfe & B. Battrick, 199

Hawkins, K., Masseron, T., Jofré, P., et al. 2016, An accurate and self-consistent chemical abundance catalogue for the APOGEE/Kepler sample, *Astron. Astrophys.*, 594, A43, doi: 10.1051/0004-6361/201628812

Hawkins, K., Ting, Y.-S., & Walter-Rix, H. 2018, Photospheric Diagnostics of Core Helium Burning in Giant Stars, *Astrophys. J.*, 853, 20, doi: 10.3847/1538-4357/aaa08a

Hekker, S. 2020, Scaling relations for solar-like oscillations: a review, Frontiers in Astronomy and Space Sciences, 7, 3, doi: 10.3389/fspas.2020.00003

Hekker, S., & Christensen-Dalsgaard, J. 2017, Giant star seismology, *Astron. Astrophys. Rev.*, 25, 1, doi: 10.1007/s00159-017-0101-x

Hekker, S., & Meléndez, J. 2007, Precise radial velocities of giant stars. III. Spectroscopic stellar parameters, *Astron. Astrophys.*, 475, 1003, doi: 10.1051/0004-6361:20078233

Hema, B. P., & Pandey, G. 2014, Discovery of Relatively Hydrogen-poor Giants in the Galactic Globular Cluster ω Centauri, *Astrophys. J. Lett.*, 792, L28, doi: 10.1088/2041-8205/792/2/L28

Henry, T. J., Soderblom, D. R., Donahue, R. A., & Baliunas, S. L. 1996, A Survey of Ca II H and K Chromospheric Emission in Southern Solar-Type Stars, *Astron. J.*, 111, 439, doi: 10.1086/117796

Hill, V., & Pasquini, L. 1999, A Super Lithium Rich giant in the metal-poor open cluster Berkeley 21, *Astron. Astrophys.*, 348, L21, doi: 10.48550/arXiv.astro-ph/9907106

Hinkle, K., Wallace, L., Valenti, J., & Harmer, D. 2000, Visible and Near Infrared Atlas of the Arcturus Spectrum 3727-9300 A (Astronomical Society of the Pacific)

Høg, E., Fabricius, C., Makarov, V. V., et al. 2000, The Tycho-2 catalogue of the 2.5 million brightest stars, *Astron. Astrophys.*, 355, L27

Holanda, N., Drake, N. A., & Pereira, C. B. 2020, HD 150382: A Lithium-rich Star at the Early-AGB Stage?, *Astron. J.*, 159, 9, doi: 10.3847/1538-3881/ab5528

Holtzman, J. A., Hasselquist, S., Shetrone, M., et al. 2018, APOGEE Data Releases 13 and 14: Data and Analysis, *Astron. J.*, 156, 125, doi: 10.3847/1538-3881/aad4f9

Hon, M., Stello, D., García, R. A., et al. 2019, A search for red giant solar-like oscillations in all Kepler data, *Mon. Not. Roy. Astron. Soc.*, 485, 5616, doi: 10.1093/mnras/stz622

Huber, D., Stello, D., Bedding, T. R., et al. 2009, Automated extraction of oscillation parameters for Kepler observations of solar-type stars, Communications in Asteroseismology, 160, 74, doi: 10.48550/arXiv.0910.2764

Huber, D., Bedding, T. R., Stello, D., et al. 2011, Testing Scaling Relations for Solar-like Oscillations from the Main Sequence to Red Giants Using Kepler Data, *Astrophys. J.*, 743, 143, doi: 10.1088/0004-637X/743/2/143

Iben, Icko, J. 1967, Stellar Evolution.VI. Evolution from the Main Sequence to the Red-Giant Branch for Stars of Mass 1 M_{sun}, 1.25 M_{sun}, and 1.5 M_{sun}, *Astrophys. J.*, 147, 624, doi: 10.1086/149040

—. 1968, Low-Mass Red Giants, *Astrophys. J.*, 154, 581, doi: 10.1086/149782

Ivezic, Z., Nenkova, M., & Elitzur, M. 1999, User Manual for DUSTY, arXiv e-prints, astro. https://arxiv.org/abs/astro-ph/9910475

Jasniewicz, G., Parthasarathy, M., de Laverny, P., & Thévenin, F. 1999, Late-type giants with infrared excess. I. Lithium abundances, *Astron. Astrophys.*, 342, 831

Jermyn, A. S., & Fuller, J. 2022, Wave heating during the helium flash and lithium-enhanced clump stars, arXiv e-prints, arXiv:2206.13479, doi: 10.48550/arXiv.2206.13479

Jian, M., Fu, X., Matsunaga, N., et al. 2024, Stellar Population Astrophysics (SPA) with the TNG. Measurement of the He I 10 830 Å line in the open cluster Stock 2, *Astron. Astrophys.*, 687, A189, doi: 10.1051/0004-6361/202449476

Kallinger, T., Mosser, B., Hekker, S., et al. 2010, Asteroseismology of red giants from the first four months of Kepler data: Fundamental stellar parameters, *Astron. Astrophys.*, 522, A1, doi: 10.1051/0004-6361/201015263

Kallinger, T., Hekker, S., Mosser, B., et al. 2012, Evolutionary influences on the structure of red-giant acoustic oscillation spectra from 600d of Kepler observations, *Astron. Astrophys.*, 541, A51, doi: 10.1051/0004-6361/201218854

Kallinger, T., De Ridder, J., Hekker, S., et al. 2014, The connection between stellar granulation and oscillation as seen by the Kepler mission, *Astron. Astrophys.*, 570, A41, doi: 10.1051/0004-6361/201424313

Kamath, D., Wood, P. R., Van Winckel, H., & Nie, J. D. 2016, A newly discovered stellar type: dusty post-red giant branch stars in the Magellanic Clouds, *Astron. Astrophys.*, 586, L5, doi: 10.1051/0004-6361/201526892

Karoff, C., Campante, T. L., Ballot, J., et al. 2013, Observations of Intensity Fluctuations Attributed to Granulation and Faculae on Sun-like Stars from the Kepler Mission, *Astrophys. J.*, 767, 34, doi: 10.1088/0004-637X/767/1/34

Katz, D., Sartoretti, P., Guerrier, A., et al. 2023, Gaia Data Release 3. Properties and validation of the radial velocities, *Astron. Astrophys.*, 674, A5, doi: 10.1051/0004-6361/202244220

Kennedy, G. M., & Wyatt, M. C. 2012, Confusion limited surveys: using WISE to quantify the rarity of warm dust around Kepler stars, *Mon. Not. Roy. Astron. Soc.*, 426, 91, doi: 10.1111/j.1365-2966.2012.21621.x

Kim, A., Winget, D. E., Montgomery, M. H., & Kepler, S. O. 2006, Driving in ZZ Ceti stars - Problem solved? ., memsai, 77, 376, doi: 10.48550/arXiv.astro-ph/0510104

Kippenhahn, R., Weigert, A., & Weiss, A. 2013, Stellar Structure and Evolution (Springer Berlin, Heidelberg), doi: 10.1007/978-3-642-30304-3

Kirby, E. N., Guhathakurta, P., Zhang, A. J., et al. 2016, Lithium-rich Giants in Globular Clusters, *Astrophys. J.*, 819, 135, doi: 10.3847/0004-637X/819/2/135

Kirk, B., Conroy, K., Prša, A., et al. 2016, Kepler Eclipsing Binary Stars. VII. The Catalog of Eclipsing Binaries Found in the Entire Kepler Data Set, *Astron. J.*, 151, 68, doi: 10.3847/0004-6256/151/3/68

Kjeldsen, H., & Bedding, T. R. 1995, Amplitudes of stellar oscillations: the implications for asteroseismology., *Astron. Astrophys.*, 293, 87. https://arxiv.org/abs/astro-ph/9403015

Kumar, P., Franklin, J., & Goldreich, P. 1988, Distribution Functions for the Time-averaged Energies of Stochastically Excited Solar p-Modes, *Astrophys. J.*, 328, 879, doi: 10.1086/166345

Kumar, Y. B., Reddy, B. E., Campbell, S. W., et al. 2020, Discovery of ubiquitous lithium production in low-mass stars, Nature Astronomy, 4, 1059, doi: 10.1038/s41550-020-1139-7

Kumar, Y. B., Reddy, B. E., & Lambert, D. L. 2011, Origin of Lithium Enrichment in K Giants, *Astrophys. J. Lett.*, 730, L12, doi: 10.1088/2041-8205/730/1/L12

Lagarde, N., Decressin, T., Charbonnel, C., et al. 2012, Thermohaline instability and rotation-induced mixing. III. Grid of stellar models and asymptotic asteroseismic quantities from the pre-main sequence up to the AGB for low- and intermediate-mass stars of various metallicities, *Astron. Astrophys.*, 543, A108, doi: 10.1051/0004-6361/201118331

Lawler, J. E., Sneden, C., Cowan, J. J., Ivans, I. I., & Den Hartog, E. A. 2009, Improved Laboratory Transition Probabilities for Ce II, Application to the Cerium Abundances of the Sun and Five r-Process-Rich, Metal-Poor Stars, and Rare Earth Lab Data Summary, *Astrophys. J. Suppl.*, 182, 51, doi: 10.1088/0067-0049/182/1/51

Lebzelter, T., Uttenthaler, S., Busso, M., Schultheis, M., & Aringer, B. 2012, Lithium abundances along the red giant branch: FLAMES-GIRAFFE spectra of a large sample of low-mass bulge stars, *Astron. Astrophys.*, 538, A36, doi: 10.1051/0004-6361/201117743

Ledoux, P., & Walraven, T. 1958, Variable Stars., Handbuch der Physik, 51, 353, doi: 10.1007/978-3-642-45908-5_6

Lightkurve Collaboration, Cardoso, J. V. d. M., Hedges, C., et al. 2018, Lightkurve: Kepler and TESS time series analysis in Python, Astrophysics Source Code Library, record ascl:1812.013. http://ascl.net/1812.013

Lind, K., Asplund, M., & Barklem, P. S. 2009, Departures from LTE for neutral Li in late-type stars, *Astron. Astrophys.*, 503, 541, doi: 10.1051/0004-6361/200912221

Linsky, J. L., & Avrett, E. H. 1970, The Solar H and K Lines, *Pub. Astron. Soc. Pac.*, 82, 169, doi: 10.1086/128904

Liu, Y. J., Tan, K. F., Wang, L., et al. 2014, The Lithium Abundances of a Large Sample of Red Giants, *Astrophys. J.*, 785, 94, doi: 10.1088/0004-637X/785/2/94

Lomb, N. R. 1976, Least-Squares Frequency Analysis of Unequally Spaced Data, *Astrophys. Space Sci.*, 39, 447, doi: 10.1007/BF00648343

Lucey, M., Ting, Y.-S., Ramachandra, N. S., & Hawkins, K. 2020, From the inner to outer Milky Way: a photometric sample of 2.6 million red clump stars, *Mon. Not. Roy. Astron. Soc.*, 495, 3087, doi: 10.1093/mnras/staa1226

Lund, M. N., Handberg, R., Kjeldsen, H., Chaplin, W. J., & Christensen-Dalsgaard, J. 2017, in European Physical Journal Web of Conferences, Vol. 160, European Physical Journal Web of Conferences, 01005, doi: 10.1051/epjconf/201716001005

Lynden-Bell, D., & Pringle, J. E. 1974, The evolution of viscous discs and the origin of the nebular variables., *Mon. Not. Roy. Astron. Soc.*, 168, 603, doi: 10.1093/mnras/168.3.603

Maeder, A. 2009, Physics, Formation and Evolution of Rotating Stars (Springer Berlin, Heidelberg), doi: 10.1007/978-3-540-76949-1

Magain, P. 1984, A comment on systematic errors in determinations of microturbulent velocities, *Astron. Astrophys.*, 134, 189

Magrini, L., Smiljanic, R., Franciosini, E., et al. 2021, Gaia-ESO survey: Lithium abundances in open cluster Red Clump stars, *Astron. Astrophys.*, 655, A23, doi: 10.1051/0004-6361/202141275

Mahadevan, S., Ramsey, L., Bender, C., et al. 2012, in Society of Photo-Optical Instrumentation Engineers (SPIE) Conference Series, Vol. 8446, Ground-based and Airborne Instrumentation for Astronomy IV, 84461S, doi: 10.1117/12.926102

Mahadevan, S., Ramsey, L. W., Terrien, R., et al. 2014, in Society of Photo-Optical Instrumentation Engineers (SPIE) Conference Series, Vol. 9147, Ground-based and Airborne Instrumentation for Astronomy V, 91471G, doi: 10.1117/12.2056417

Mallick, A., Reddy, B. E., & Muthumariappan, C. 2022, Probing infrared excess connection with Li enhancement among red clump giants, *Mon. Not. Roy. Astron. Soc.*, 511, 3741, doi: 10.1093/mnras/stac224

Mallick, A., Singh, R., & Reddy, B. E. 2023, Lithium Abundances in Giants as a Function of Stellar Mass: Evidence for He Flash as the Source of Li Enhancement in Low-mass Giants, *Astrophys. J. Lett.*, 944, L5, doi: 10.3847/2041-8213/acb5f6

Mallick, A., Sneden, C., Reddy, B. E., & Afşar, M. 2025, High Lithium Abundance Connection with the Chromospheric Helium in Red Giants: Spectroscopic and Asteroseismic analyses, arXiv e-prints, arXiv:2501.08863. https://arxiv.org/abs/2501.08863

Martell, S. L., Simpson, J. D., Balasubramaniam, A. G., et al. 2021, The GALAH survey: a census of lithium-rich giant stars, *Mon. Not. Roy. Astron. Soc.*, 505, 5340, doi: 10.1093/mnras/stab1356

Masseron, T., & Hawkins, K. 2017, The spectroscopic indistinguishability of red giant branch and red clump stars, *Astron. Astrophys.*, 597, L3, doi: 10.1051/0004-6361/201629938

Masseron, T., Lagarde, N., Miglio, A., Elsworth, Y., & Gilmore, G. 2017, Nitrogen depletion in field red giants: mixing during the He flash?, *Mon. Not. Roy. Astron. Soc.*, 464, 3021, doi: 10.1093/mnras/stw2632

Mathis, J. S., Rumpl, W., & Nordsieck, K. H. 1977, The size distribution of interstellar grains., *Astrophys. J.*, 217, 425, doi: 10.1086/155591

Mathur, S., Huber, D., Batalha, N. M., et al. 2017, Revised Stellar Properties of Kepler Targets for the Q1-17 (DR25) Transit Detection Run, *Astrophys. J. Suppl.*, 229, 30, doi: 10.3847/1538-4365/229/2/30

Miller Bertolami, M. M., Battich, T., Córsico, A. H., Christensen-Dalsgaard, J., & Althaus, L. G. 2020, Asteroseismic signatures of the helium core flash, Nature Astronomy, 4, 67, doi: 10.1038/s41550-019-0890-0

Mitler, H. E. 1972, Cosmic-ray production of deuterium, He^3, lithium, beryllium, and boron in the Galaxy, *Astrophys. Space Sci.*, 17, 186, doi: 10.1007/BF00642551

Mori, K., Kusakabe, M., Balantekin, A. B., Kajino, T., & Famiano, M. A. 2021, Enhancement of lithium in red clump stars by the additional energy loss induced by new physics, *Mon. Not. Roy. Astron. Soc.*, 503, 2746, doi: 10.1093/mnras/stab595

Mosser, B., Dréau, G., Pinçon, C., et al. 2024, Locked differential rotation in core-helium burning red giants, *Astron. Astrophys.*, 681, L20, doi: 10.1051/0004-6361/202348338

Mosser, B., Benomar, O., Belkacem, K., et al. 2014, Mixed modes in red giants: a window on stellar evolution, *Astron. Astrophys.*, 572, L5, doi: 10.1051/0004-6361/201425039

Muthumariappan, C., Kwok, S., & Volk, K. 2006, Subarcsecond Mid-Infrared Imaging of Dust in the Bipolar Nebula Hen 3-401, *Astrophys. J.*, 640, 353, doi: 10.1086/500041

Nagarajan, N., Sneden, C., Afsar, M., & Pilachowski, C. 2023, in American Astronomical Society Meeting Abstracts, Vol. 241, American Astronomical Society Meeting Abstracts, 367.01

Noyes, R. W., Hartmann, L. W., Baliunas, S. L., Duncan, D. K., & Vaughan, A. H. 1984, Rotation, convection, and magnetic activity in lower main-sequence stars., *Astrophys. J.*, 279, 763, doi: 10.1086/161945

Nucci, M. C., & Busso, M. 2014, Magnetohydrodynamics and Deep Mixing in Evolved Stars. I. Two- and Three-dimensional Analytical Models for the Asymptotic Giant Branch, *Astrophys. J.*, 787, 141, doi: 10.1088/0004-637X/787/2/141

Obrien, George T., J., & Lambert, D. L. 1986, The 10830 Angstrom Chromospheric Line of Helium in Bright Stars, *Astrophys. J. Suppl.*, 62, 899, doi: 10.1086/191160

Palacios, A., Charbonnel, C., & Forestini, M. 2001, The Lithium Flash. Thermal instabilities generated by lithium burning in RGB stars, *Astron. Astrophys.*, 375, L9, doi: 10.1051/0004-6361:20010903

Paxton, B., Bildsten, L., Dotter, A., et al. 2011, Modules for Experiments in Stellar Astrophysics (MESA), *Astrophys. J. Suppl.*, 192, 3, doi: 10.1088/0067-0049/192/1/3

Pilachowski, C. A., Sneden, C., & Booth, J. 1993, The Abundance of Lithium in Metal-poor Subgiant Stars, *Astrophys. J.*, 407, 699, doi: 10.1086/172551

Pinsonneault, M. H., Charbonnel, C., & Deliyannis, C. P. 2000, in IAU Symposium, Vol. 198, The Light Elements and their Evolution, ed. L. da Silva, R. de Medeiros, & M. Spite, 74

Placco, V. M., Sneden, C., Roederer, I. U., et al. 2021, Linemake: An Atomic and Molecular Line List Generator, Research Notes of the American Astronomical Society, 5, 92, doi: 10.3847/2515-5172/abf651

Ramírez, I., & Allende Prieto, C. 2011, Fundamental Parameters and Chemical Composition of Arcturus, *Astrophys. J.*, 743, 135, doi: 10.1088/0004-637X/743/2/135

Ramírez, I., Meléndez, J., Bean, J., et al. 2014, The Solar Twin Planet Search. I. Fundamental parameters of the stellar sample, *Astron. Astrophys.*, 572, A48, doi: 10.1051/0004-6361/201424244

Reddy, B. E., & Lambert, D. L. 2005, Three Li-rich K Giants: IRAS 12327-6523, 13539-4153, and 17596-3952, *Astron. J.*, 129, 2831, doi: 10.1086/430190

Reddy, B. E., Lambert, D. L., Laws, C., Gonzalez, G., & Covey, K. 2002, A search for ^{6}Li in stars with planets, *Mon. Not. Roy. Astron. Soc.*, 335, 1005, doi: 10.1046/j.1365-8711.2002.05682.x

Reddy, B. E., Tomkin, J., Lambert, D. L., & Allende Prieto, C. 2003, The chemical compositions of Galactic disc F and G dwarfs, *Mon. Not. Roy. Astron. Soc.*, 340, 304, doi: 10.1046/j.1365-8711.2003.06305.x

Refsdal, S., & Weigert, A. 1970, Shell Source Burning Stars with Highly Condensed Cores, *Astron. Astrophys.*, 6, 426

Reimers, D. 1975, Circumstellar absorption lines and mass loss from red giants., Memoires of the Societe Royale des Sciences de Liege, 8, 369

Richard, O., Michaud, G., & Richer, J. 2005, Implications of WMAP Observations on Li Abundance and Stellar Evolution Models, *Astrophys. J.*, 619, 538, doi: 10.1086/426470

Ricker, G. R., Winn, J. N., Vanderspek, R., et al. 2015, Transiting Exoplanet Survey Satellite (TESS), Journal of Astronomical Telescopes, Instruments, and Systems, 1, 014003, doi: 10.1117/1.JATIS.1.1.014003

Romano, D., Matteucci, F., Ventura, P., & D'Antona, F. 2001, The stellar origin of ^{7}Li. Do AGB stars contribute a substantial fraction of the local Galactic lithium abundance?, *Astron. Astrophys.*, 374, 646, doi: 10.1051/0004-6361:20010751

Ruchti, G. R., Fulbright, J. P., Wyse, R. F. G., et al. 2011, Metal-poor Lithium-rich Giants in the Radial Velocity Experiment Survey, *Astrophys. J.*, 743, 107, doi: 10.1088/0004-637X/743/2/107

Rüdiger, G., Gellert, M., Spada, F., & Tereshin, I. 2015, The angular momentum transport by unstable toroidal magnetic fields, *Astron. Astrophys.*, 573, A80, doi: 10.1051/0004-6361/201424060

Rutten, R. G. M. 1984, Magnetic structure in cool stars. VII. Absolute surface flux in CA IIH and K line cores., *Astron. Astrophys.*, 130, 353

Sanna, N., Franciosini, E., Pancino, E., et al. 2020, The Gaia-ESO Survey: an extremely Li-rich giant in globular cluster NGC 1261, *Astron. Astrophys.*, 639, L2, doi: 10.1051/0004-6361/202038435

Sanz-Forcada, J., & Dupree, A. K. 2008, Active cool stars and He I 10 830 Å: the coronal connection, *Astron. Astrophys.*, 488, 715, doi: 10.1051/0004-6361:20078501

Scargle, J. D. 1982, Studies in astronomical time series analysis. II. Statistical aspects of spectral analysis of unevenly spaced data., *Astrophys. J.*, 263, 835, doi: 10.1086/160554

Schröder, K. P., & Cuntz, M. 2005, A New Version of Reimers' Law of Mass Loss Based on a Physical Approach, *Astrophys. J. Lett.*, 630, L73, doi: 10.1086/491579

Schwab, J. 2020, A Helium-flash-induced Mixing Event Can Explain the Lithium Abundances of Red Clump Stars, *Astrophys. J. Lett.*, 901, L18, doi: 10.3847/2041-8213/abb45f

Sharma, S., Stello, D., Bland-Hawthorn, J., Huber, D., & Bedding, T. R. 2016, Stellar Population Synthesis Based Modeling of the Milky Way Using Asteroseismology of 13,000 Kepler Red Giants, *Astrophys. J.*, 822, 15, doi: 10.3847/0004-637X/822/1/15

Shetrone, M., Tayar, J., Johnson, J. A., et al. 2019, Constraining Metallicity-dependent Mixing and Extra Mixing Using [C/N] in Alpha-rich Field Giants, *Astrophys. J.*, 872, 137, doi: 10.3847/1538-4357/aaff66

Simon, T., & Drake, S. A. 1989, The Evolution of Chromospheric Activity of Cool Giant and Subgiant Stars, *Astrophys. J.*, 346, 303, doi: 10.1086/168012

Singh, R., Mallick, A., Reddy, B. E., Pandey, J. C., & Zhao, G. 2024, Study of a Red Clump Giant, KIC 11087027, with High Rotation and Strong Infrared Excess—Evidence of Tidal Interaction for High Lithium Abundance, *Astrophys. J. Lett.*, 971, L3, doi: 10.3847/2041-8213/ad62f6

Singh, R., Reddy, B. E., Campbell, S. W., Kumar, Y. B., & Vrard, M. 2021, Tracking the Evolution of Lithium in Giants Using Asteroseismology: Super-Li-rich Stars Are Almost Exclusively Young Red-clump Stars, *Astrophys. J. Lett.*, 913, L4, doi: 10.3847/2041-8213/abfa24

Singh, R., Reddy, B. E., & Kumar, Y. B. 2019, Spectroscopic study of two new super Li-rich red clump K giants, *Mon. Not. Roy. Astron. Soc.*, 482, 3822, doi: 10.1093/mnras/sty2939

Smith, G. H., Dupree, A. K., & Strader, J. 2004, He I λ10830 Absorption in Metal-Poor Red Giants: Probing Fast Chromospheric Outflows, *Pub. Astron. Soc. Pac.*, 116, 819, doi: 10.1086/423988

Smith, G. H., & Martell, S. L. 2003, Comparing Deep Mixing in Globular Cluster and Halo Field Giants: Carbon Abundance Data from the Literature, *Pub. Astron. Soc. Pac.*, 115, 1211, doi: 10.1086/378078

Smith, J. C., Stumpe, M. C., Van Cleve, J. E., et al. 2012, Kepler Presearch Data Conditioning II - A Bayesian Approach to Systematic Error Correction, *Pub. Astron. Soc. Pac.*, 124, 1000, doi: 10.1086/667697

Sneden, C., Lucatello, S., Ram, R. S., Brooke, J. S. A., & Bernath, P. 2014, Line Lists for the A $^2\Pi$-X $^2\Sigma^+$ (Red) and B $^2\Sigma^+$-X $^2\Sigma^+$ (Violet) Systems of CN, $^{13}C^{14}N$, and $^{12}C^{15}N$, and Application to Astronomical Spectra, *Astrophys. J. Suppl.*, 214, 26, doi: 10.1088/0067-0049/214/2/26

Sneden, C., Afşar, M., Bozkurt, Z., et al. 2021, Chemical Compositions of Red Giant Stars from Habitable Zone Planet Finder Spectroscopy, *Astron. J.*, 161, 128, doi: 10.3847/1538-3881/abd7ee

—. 2022, The Active Chromospheres of Lithium-rich Red Giant Stars, *Astrophys. J.*, 940, 12, doi: 10.3847/1538-4357/ac922e

Sneden, C. A. 1973, PhD thesis, THE UNIVERSITY OF TEXAS AT AUSTIN.

Soares-Furtado, M., Cantiello, M., MacLeod, M., & Ness, M. K. 2021, Lithium Enrichment Signatures of Planetary Engulfment Events in Evolved Stars, *Astron. J.*, 162, 273, doi: 10.3847/1538-3881/ac273c

Spite, F., & Spite, M. 1982, Abundance of lithium in unevolved stars and old disk stars : Interpretation and consequences., *Astron. Astrophys.*, 115, 357

Stello, D., Chaplin, W. J., Basu, S., Elsworth, Y., & Bedding, T. R. 2009, The relation between $\Delta\nu$ and ν_{max} for solar-like oscillations, *Mon. Not. Roy. Astron. Soc.*, 400, L80, doi: 10.1111/j.1745-3933.2009.00767.x

Suto, Y., Sasaki, S., Nakagawa, Y., & Benomar, O. 2022, Analytic model for photometric variation due to starspots on a differentially rotating star, *Pub. Astron. Soc. Japan*, 74, 857, doi: 10.1093/pasj/psac039

Sweigart, A. V., & Mengel, J. G. 1979, Meridional circulation and CNO anomalies in red giant stars., *Astrophys. J.*, 229, 624, doi: 10.1086/156996

Takeda, Y., Ohkubo, M., & Sadakane, K. 2002, Spectroscopic Determination of Atmospheric Parameters of Solar-Type Stars: Description of the Method and Application to the Sun, *Pub. Astron. Soc. Japan*, 54, 451, doi: 10.1093/pasj/54.3.451

Takeda, Y., & Tajitsu, A. 2017, On the observational characteristics of lithium-enhanced giant stars in comparison with normal red giants, *Pub. Astron. Soc. Japan*, 69, 74, doi: 10.1093/pasj/psx057

Tassoul, M. 1980, Asymptotic approximations for stellar nonradial pulsations., *Astrophys. J. Suppl.*, 43, 469, doi: 10.1086/190678

Ting, Y.-S., Hawkins, K., & Rix, H.-W. 2018, A Large and Pristine Sample of Standard Candles across the Milky Way: ∼100,000 Red Clump Stars with 3% Contamination, *Astrophys. J. Lett.*, 858, L7, doi: 10.3847/2041-8213/aabf8e

Tsantaki, M., Andreasen, D. T., Teixeira, G. D. C., et al. 2018, Atmospheric stellar parameters for large surveys using FASMA, a new spectral synthesis package, *Mon. Not. Roy. Astron. Soc.*, 473, 5066, doi: 10.1093/mnras/stx2564

Tsantaki, M., Delgado-Mena, E., Bossini, D., et al. 2023, Search for lithium-rich giants in 32 open clusters with high-resolution spectroscopy, *Astron. Astrophys.*, 674, A157, doi: 10.1051/0004-6361/202244374

Valenti, J. A., & Fischer, D. A. 2005, Spectroscopic Properties of Cool Stars (SPOCS). I. 1040 F, G, and K Dwarfs from Keck, Lick, and AAT Planet Search Programs, *Astrophys. J. Suppl.*, 159, 141, doi: 10.1086/430500

Vaughan, A. H., Preston, G. W., & Wilson, O. C. 1978, Flux measurements of Ca II and K emission., *Pub. Astron. Soc. Pac.*, 90, 267, doi: 10.1086/130324

Vaughan, Arthur H., J., & Zirin, H. 1968, The Helium Line λ 10830 Å in Late-Type Stars, *Astrophys. J.*, 152, 123, doi: 10.1086/149531

Vida, K., & Roettenbacher, R. M. 2018, Finding flares in Kepler data using machine-learning tools, *Astron. Astrophys.*, 616, A163, doi: 10.1051/0004-6361/201833194

Vrard, M., Mosser, B., & Samadi, R. 2016, Period spacings in red giants. II. Automated measurement, *Astron. Astrophys.*, 588, A87, doi: 10.1051/0004-6361/201527259

Walker, G., Matthews, J., Kuschnig, R., et al. 2003, The MOST Asteroseismology Mission: Ultraprecise Photometry from Space, *Pub. Astron. Soc. Pac.*, 115, 1023, doi: 10.1086/377358

Wallerstein, G., & Sneden, C. 1982, A K giant with an unusually high abundance of lithium : HD 112127., *Astrophys. J.*, 255, 577, doi: 10.1086/159859

Wang, C., Huang, Y., Zhou, Y., & Zhang, H. 2023, Precise masses and ages of 1 million RGB and RC stars observed by LAMOST, *Astron. Astrophys.*, 675, A26, doi: 10.1051/0004-6361/202245809

Wiese, W. L., Fuhr, J. R., & Deters, T. M. 1996, Atomic transition probabilities of carbon, nitrogen, and oxygen : a critical data compilation (American Institute of Physics)

Xiang, M. S., Liu, X. W., Yuan, H. B., et al. 2015, The LAMOST stellar parameter pipeline at Peking University - LSP3, *Mon. Not. Roy. Astron. Soc.*, 448, 822, doi: 10.1093/mnras/stu2692

Yan, H. L., & Shi, J. R. 2022, A Review to the Studies of Lithium-Rich Giants, Acta Astronomica Sinica, 63, 2

Yan, H.-L., Zhou, Y.-T., Zhang, X., et al. 2021, Most lithium-rich low-mass evolved stars revealed as red clump stars by asteroseismology and spectroscopy, Nature Astronomy, 5, 86, doi: 10.1038/s41550-020-01217-8

Yu, J., Bedding, T. R., Stello, D., et al. 2020, Asteroseismology of luminous red giants with Kepler I: long-period variables with radial and non-radial modes, *Mon. Not. Roy. Astron. Soc.*, 493, 1388, doi: 10.1093/mnras/staa300

Yu, J., Huber, D., Bedding, T. R., et al. 2018, Asteroseismology of 16,000 Kepler Red Giants: Global Oscillation Parameters, Masses, and Radii, The Astrophysical Journal Supplement Series, 236, 42, doi: 10.3847/1538-4365/aaaf74

Zacharias, N., Finch, C., & Frouard, J. 2017, UCAC5: New Proper Motions Using Gaia DR1, *Astron. J.*, 153, 166, doi: 10.3847/1538-3881/aa6196

Zhang, J., Bi, S., Li, Y., et al. 2020a, Magnetic Activity of F-, G-, and K-type Stars in the LAMOST-Kepler Field, *Astrophys. J. Suppl.*, 247, 9, doi: 10.3847/1538-4365/ab6165

Zhang, X., & Jeffery, C. S. 2013, White dwarf-red giant mergers, early-type R stars, J stars and lithium, *Mon. Not. Roy. Astron. Soc.*, 430, 2113, doi: 10.1093/mnras/stt035

Zhang, X., Jeffery, C. S., Li, Y., & Bi, S. 2020b, Population Synthesis of Helium White Dwarf-Red Giant Star Mergers and the Formation of Lithium-rich Giants and Carbon Stars, *Astrophys. J.*, 889, 33, doi: 10.3847/1538-4357/ab5e89

Zhao, G., Chen, Y.-Q., Shi, J.-R., et al. 2006, Stellar Abundance and Galactic Chemical Evolution through LAMOST Spectroscopic Survey, *Chin. J. Astron. Astrophys.*, 6, 265, doi: 10.1088/1009-9271/6/3/01

Zhou, Y., Wang, C., Yan, H., et al. 2022, Li-rich Giants in LAMOST Survey. III. The Statistical Analysis of Li-rich Giants, *Astrophys. J.*, 931, 136, doi: 10.3847/1538-4357/ac6b3a